TECHNICAL UNIVERSITY OF MOLDOVA

JOURNAL OF ENGINEERING SCIENCE

Technical and applied scientific publication founded on 9 February 1995
Alternative title: Meridian ingineresc

2023
Vol. XXX (2)

ISSN 2587-3474
eISSN 2587-3482

TECHNICAL UNIVERSITY OF MOLDOVA (PUBLISHING HOUSE)
„TEHNICA UTM" (PRINTING HOUSE)

According to the Decision of the NAQAER No. 19 from 06.12.2019, JES is classified as B+ journal

Main subjects areas of the Journal of Engineering Science:

A. Industrial Engineering

- Mechanical Engineering and Technologies
- Applied Engineering Sciences and Management
- Materials Science and New Technologies
- Electrical Engineering and Power Electronics
- Energy systems
- Light Industry, New Technologies and Design
- Industrial and Applied Mathematics
- Vehicle and Transport Engineering

B. Electronics and Computer Science

- Electronics and Communication
- Microelectronics and Nanotechnologies
- Biomedical Engineering
- Computers and Information Technology
- Automation

C. Architecture, Civil and Environmental Engineering

- Architecture, Urbanism and Cadaster
- Civil Engineering and Management
- Energy Efficiency and New Building Materials
- Environmental Engineering

D. Food Engineering

- Food Technologies and Food Processes
- Food Industry and Management
- Biotechnologies, Food Chemistry and Food Safety
- Equipment for Food Industries

The structure of the journal corresponds to the classification of scientific publications: ***Engineering, Multidisciplinary.***

How to publish a paper:

1. Send the manuscript and information about the author to the **Editorial Board address:** jes@meridian.utm.md
2. Manuscripts are accepted only in English, by e-mail, in template file (www.jes.utm.md)
3. After a review, you will be notified of the editorial board's decision.
4. After the Journal has been published, we will send it to you immediately by mail.

Editor-in-Chief
Dr. hab. prof. univ. Viorel BOSTAN
Technical University of Moldova
viorel.bostan@adm.utm.md

Editorial Board

Responsible Editor
Dr. hab. Rodica STURZA
Editorial Board address: jes@meridian.utm.md

Editorial Production:
Dr. hab. Aliona Ghendov-Moșanu
Dr. Nicolae Trifan
Dr. Țurcan Iuliu
Dr. Svetlana Caterinciuc
Dr. Rodica Cujba

CONTENT

CONȚINUT

A. Industrial Engineering

B. Electronics and Computer Science

C. Architecture, Civil and Environmental Engineering

Journal of Engineering Science *Vol. XXX, no. 2 (2023), pp. 8 - 22*
Fascicle *Industrial Engineering* *ISSN 2587-3474*
Topic *Mechanical Engineering and Technologies* *eISSN 2587-3482*

https://doi.org/10.52326/jes.utm.2023.30(2).01
UDC 621.671

DETERMINING OPTIMAL SIMULATION SETTINGS FOR THE CENTRIFUGAL PUMP PARTS OPTIMIZATION PROCESS

Viorel Bostan[1], ORCID: 0000-0002-2422-3538,
Andrei Petco[1,2*], ORCID: 0009-0004-0577-3296

[1] *Technical University of Moldova, 168 Stefan cel Mare Blvd., Chisinau, Republic of Moldova*
[2] *S.R.L. "CRIS" 68/2-69 Albisoara str., Chisinau, Republic of Moldova,*
**Corresponding author: Andrei Petco, andrei.petco@tcm.utm.md*

Received: 05. 17. 2023
Accepted: 06. 20. 2023

Abstract. This paper explores the optimal simulation settings required by the optimization process of centrifugal canned motor pump parts using the CH 6,3/32-2,2-2 pump as an example. The optimization of centrifugal pump parts is particularly important in order to increase pump characteristics: pump efficiency, net positive suction head, as well as other optimization criteria. The optimal conditions to obtain a geometric model and optimal mesh properties, initial and boundary conditions, solver settings were investigated. The mathematical models used in the simulation were also presented. In conclusion, there have been revealed optimal simulation settings.

Keywords: *Centrifugal pumps, Numerical analysis and optimization methods, Computational Fluid Dynamics, Ansys CFX.*

Rezumat. Articolul explorează setările optime de simulare necesare procesului de optimizare a pieselor pompei centrifuge cu motor capsulat, folosind pompa CH 6,3/32-2,2-2 ca exemplu. Optimizarea pieselor pompei centrifuge este deosebit de importantă pentru a crește caracteristicile pompei: randamentul, rezerva de cavitație, precum și alte criterii de optimizare. Au fost investigate condițiile optime pentru obținerea unui model geometric și proprietățile optime ale rețelei de discretizare, condițiile inițiale și la limită, setările solutorului. Au fost prezentate și modelele matematice utilizate în simulare. În concluzie, au fost relevate setările optime de simulare.

Cuvinte cheie: *Pompe centrifuge, Analiza numerică și metode de optimizare, Dinamica fluidelor computaționale, Ansys CFX.*

1. Introduction

The use of Computational Fluid Dynamics (CFD) methods in the pump manufacturing industry is becoming an industry standard. CFD tools are used to obtain geometry of the pump pieces, in the optimization process or in the case of applying reverse engineering to investigate the parameters of the already produced pump.

This study presents the investigations on the optimal simulation settings in order to increase the efficiency of the optimization process of the centrifugal pump main parts, whose generalized optimization algorithm is presented in Figure 1.

We can notice that optimization is an iterative process, so choosing the optimal simulation settings is crucial to obtain an optimized geometric model with minimum wasted resources.

The methodology is presented based on the geometry of the canned motor hermetic centrifugal pump CH 6,3/32-2,2-2 (Figure 2).

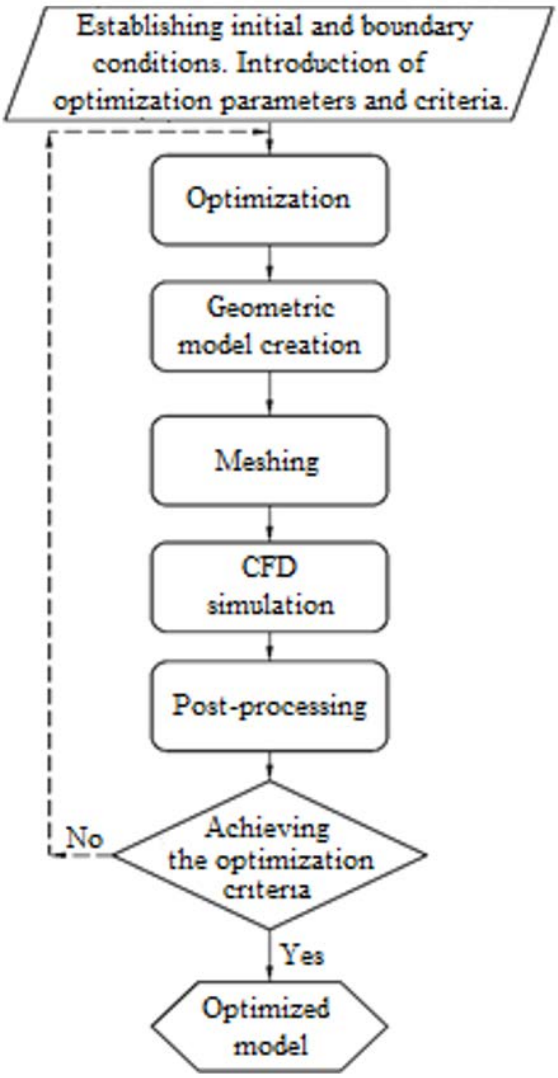

Figure 1. Optimization scheme.

2. Creating a geometric model

Geometric model is performed by "extracting" the geometry of the flow zone from the geometric model of the pump. Figure 3 shows that the CH-type hermetic pump is a monobloc construction composed of two parts [1]:

- single-stage pumping part;
- three-phase asynchronous canned electric motor.

The liquid is pumped into the pumping part, the fluid passes inside the pump casing through the suction connection, enters the impeller, where by transforming the kinetic energy of rotation into hydrodynamic energy, the fluid pressure increases, the liquid being transported to the discharge connection of pump casing. On the front and back side of the impeller, there are two cavities necessary to balance the axial forces.

A part of the pumped liquid from the discharge zone passes through the sealing slot behind the impeller, thus the lubrication, the cooling of the bearings and the inner cavity of the electric motor are carried out by means of the pumped liquid. A cooling jacket can also be used to cool the stator.

As we can see from Figure 2, a centrifugal pump is a complex hydraulic system. Due to the large difference in the ratio between the thicknesses of the flow channels in the pump it can be approx. 10^2-10^3 (between the sealing gap and the diameter of the pump casing), it is difficult to achieve the simulation of the flow in the entire pump.

To make the optimization process more efficient, it is reasonable to exclude from the calculation secondary circuit (the flow of the internal cavity of the electric motor), „balancing" cavities, the cooling circuit of the motor, etc. The exclusion will not significantly influence the calculation results [1].

The simulation is carried out in the following areas: the suction connection, the internal volume of the pump impeller, the area of the volute and the area of the discharge connection (Figure 3).

In order to represent correctly the velocity and pressure field, the area of discharge and suction connection is elongated by approx. 3-5 Dy(dy), as it is necessary for the true modeling of pump work within a hydraulic system [1].

When researching the flow of fluid through the pump, the following approaches can be applied: the pump impeller can be divided axially symmetrically, in relation to the axis of rotation. The contact between the dividing surfaces being joined by the Periodic Interface or undivided impeller. In the first case, the volume of the researched domain is reduced, which leads to an increase in the calculation speed, but may reduce its accuracy. The first approach is used in the preliminary phase of the process optimization, when the rotor can be investigated separately from the other working organs of the pump, and the second in the final phase, when maximum calculation accuracy is required. In this study, optimal parameters of the undivided impeller simulation were investigated.

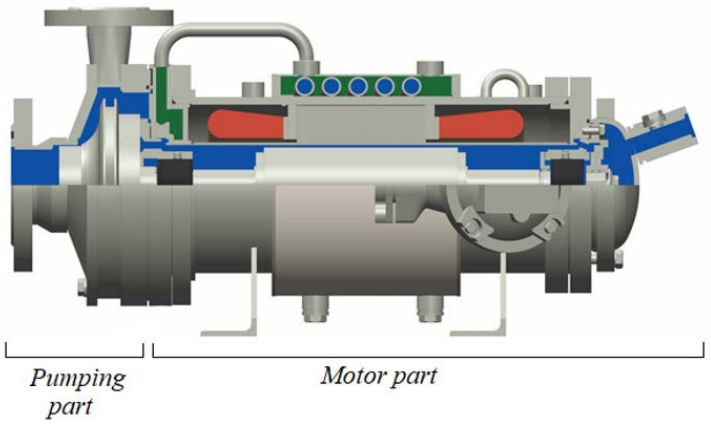

Figure 2. Canned motor pump of CH series (axial section).

It should be mentioned that the exposed algorithm is valid only if we already have the geometric model of the pump, otherwise we need to obtain some initial geometry intended for optimization. In this case we can apply simplified calculation methods, namely:

The two-dimensional calculation (ANSYS Vista CCD) simplified approach considering the impeller geometry in two dimensions, frequently used on first calculation iteration, to obtain, primarily, the meridian section of the impeller. This approach, unfortunately, may not capture all the three-dimensional flow phenomena accurately, but requires minimal computation.

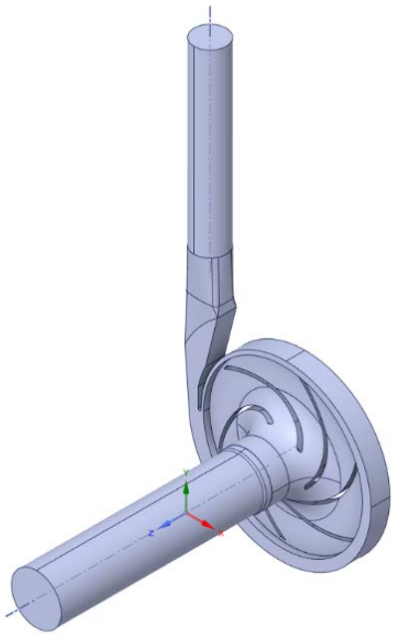

Figure 3. CH 6,3/32-2,2-2 pump geometry, represented in the Ansys SpaceClaim module.

The quasi-three-dimensional calculation (ANSYS BladeModeler, CFturbo), represents a two-dimensional method, with the application of some assumptions intended for the description of the flow in the channels between the blades, taking into account the effects formed in the boundary layer of the flow. This method is more accurate than the two-dimensional method, which allows to obtain quickly the initial geometry of the pump parts, but in turn is inferior to *the three-dimensional simulation method* (ANSYS CFX, Fluent, Poliflow, etc.) used for calculations in the final phase of the optimization process to receive the precise image of the flow in boundary layers, secondary torrents, etc., an example of the use of which is given below.

3. Discretization methods selection The fluid flow inside the pump represents a complex hydrodynamic phenomenon, described by Navier-Stokes equations, which cannot be

solved analytically in general. An alternative is to numerically solve these equations by dividing the domain into finite elements or volumes. In the numerical simulation of fluid flow processes in pumps, through ANSYS CFX, used as a solver in the case of the given study, the Finite Volume Method (FVM) is used as a discretization method.

The ANSYS Workbench environment has several modules for obtaining a finite volumes mesh: ANSYS Meshing, ANSYS TurboGrid, ANSYS ICEM CFD, ANSYS Fluent Meshing, ANSYS HFSS Meshing. In this stud

y, the optimal parameters of unstructured meshes obtained by ANSYS Meshing were considered and compared with the structured mesh obtained in conjunction with ANSYS TurboGrid and ANSYS ICEM CFD.

ANSYS Meshing is a universal mesh generator (Figure 4) used to create structured and unstructured meshes for various simulation applications (computational fluid dynamics, solid mechanics, electromagnetism and heat transfer, etc.). ANSYS Meshing is the most frequently applied mesh generator due to ease of use, as it allows for convenient customization and control over mesh parameters such as mesh density, element sizing, and boundary layer resolution. However, when studying the flow in a pump, ANSYS Meshing is used to form an unstructured grid consisting of tetrahedral elements occupying the internal volume of the flow path and a boundary layer consisting of prisms which allow to make a more correct description of the flow in the immediate vicinity of the wall, namely, a strong change in velocity caused by the phenomenon boundary layer [2]. Also, this combination allows to achieve a high degree of automation to the meshing procedure.

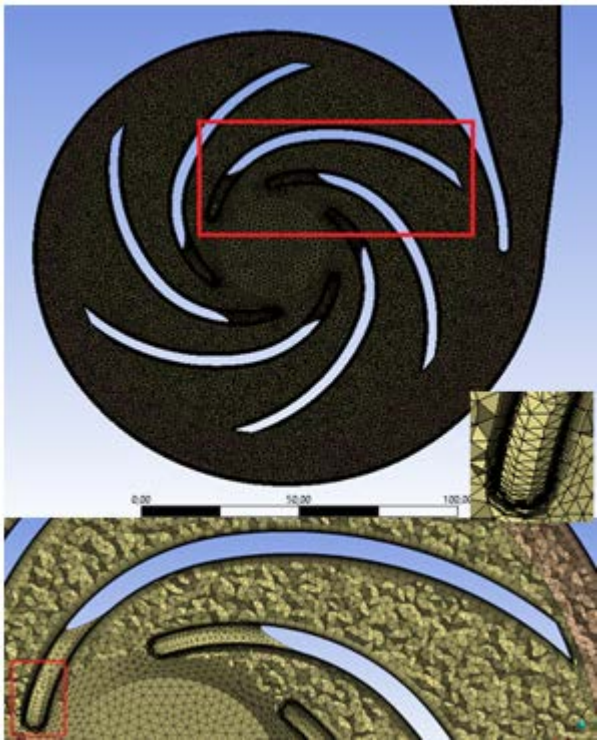

Figure 4. Unstructured mesh, obtained in ANSYS Meshing [1].

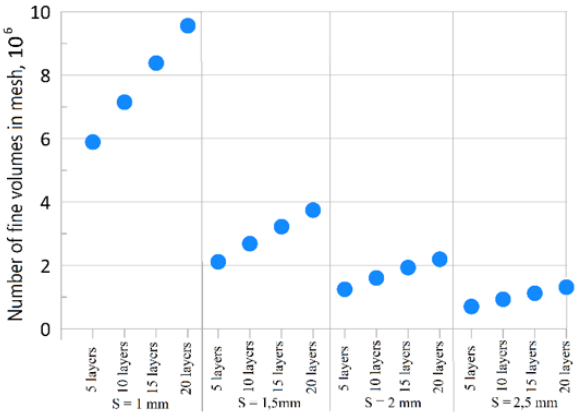

Figure 5. Correlation between fine volume size, number of inflation layers, and number of final volumes in the mesh.

Figure 5 highlights that the size of the finite volumes of the mesh is uniform in all three domains of the geometric model. To establish the optimal parameters of the mesh, a series of simulations was performed on different sizes of the finite volume, at different number of layers at the boundary surfaces. 16 unstructured discretization grids were created with finite volume size 1÷2.5 mm and 5÷20 inflation layers.

For advanced control of the distribution of finite volumes, the option Advanced Size Function: On Proximity and Curvature was applied, an option that is applied to increase the resolution of the network in the area with large curvature and in narrow areas.

The Inflation process was applied to the surface of the walls with the setting of the Total Thickness option, the Growth Rate growth coefficient of 1.2 and the thickness of the inflation layers proportional cell finite volume size.

ANSYS ICEM and ANSYS TurboGrid were used to construct a structured grid.

ANSYS TurboGrid is a powerful meshing tool specifically designed for turbomachinery applications (pumps, axial compressors and turbines). It offers an automated mesh generation of algorithms that can generate complex blade geometries mesh of inducers, impellers, vanes etc. Figure 6 shows the mesh generated in ANSYS TurboGrid. The desired achievable parameter y+ equal to 1 was used as the meshing parameters, with the assumed Reynolds number of fluid flow in the impeller equal to $5x10^5$.

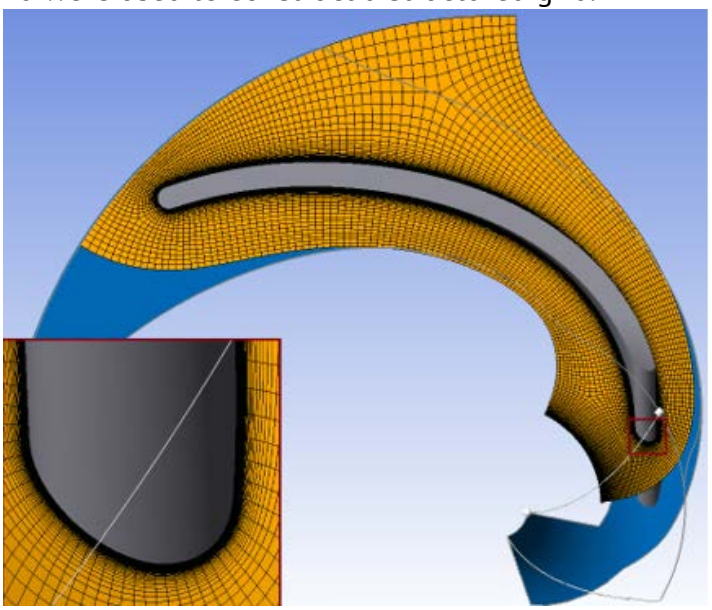

Figure 6. Structured Mesh, obtained in ANSYS TurboGrid.

The *ANSYS ICEM* tool is the most finely tuned mesh generator, primarily designed to generate high quality structured hexahedral meshes, includes a wide range of methods for creating various types of mesh models. The module is difficult to master, while having the most extensive toolkit of all modules provided by ANSYS. It should be noted that if TurboGrid has a ready-made topological set that determines the distribution of volumes, in turn, to build a mesh in ICEM, the block structure must be built manually. This greatly increases the time to get the finished mesh and increases the requirements for the skills of the engineer.

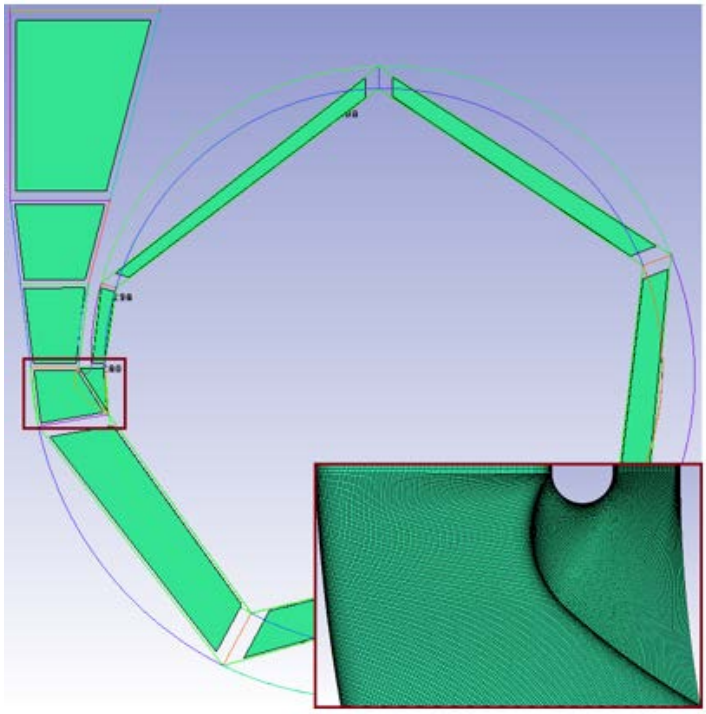

Figure 7. A block system that defines the distribution of elements and a fragment of a structured grid obtained in ANSYS ICEM.

Figure 7 shows the block system on which the finite volumes mesh is built. A fragment of the grid built in ICEM is also shown, the boundaries of the transition between the blocks associated with the geometry are visible. Since the spiral of the pump housing has a complex geometry, the engagement becomes a difficult task, so the use of a block structured mesh cannot be used only in the final optimization phase, when validating the results.

4. Establishing the mathematical model

Centrifugal pumps work by converting the mechanical energy of a rotating impeller into the energy of a fluid flow, such a complex flow is described by the Navier-Stokes equations, used to model the fluid motion inside the pump, considering complex physical phenomena such as vortex formation, reverse flows, turbulence and predict flow characteristics such as pressure and velocity field distribution, hydrodynamic losses etc. The Navier-Stokes equations represent a set of partial differential equations consisting of mass conservation and conservation of momentum equation.

The differential form of the continuity equation is:

$$\frac{\partial u}{\partial x} + \nabla(\rho u) = 0 \tag{1}$$

where: ρ is the density of the fluid, u - the velocity of the fluid and t - denotes the time.

Conservation of Momentum equation, in three dimensions are form:

$$\frac{\partial u}{\partial x} + \mathrm{u} \cdot \nabla \mathrm{u} = f - \frac{1}{\rho}\nabla p + \nu \cdot \Delta u \tag{2}$$

where: p – the pressure, f – the mass unit force, related to the mass, τ – the viscous stress tensor, defined by the constructive equation of the Newtonian fluid:

$$\tau = 2\nu(S - \frac{1}{3}(\nabla \cdot u)I)$$

ν – the kinematic viscosity, I- the unit tensor of the second order, and S is the strain rate tensor:

$$\mathrm{S} = 2\nu(\nabla u + \nabla u^T)$$

The left-hand side of Equation (2) represents the unitary inertial forces, and the terms on the right-hand side represent the mass forces, pressure forces, and viscous friction forces, respectively. [2].

Nonlinear character of equations system with partial derivatives (1) and (2), is due to the inertia term u·∇u. This nonlinear term introduces complex interactions between structures of different scales in the fluid motion, being considered the primary source of turbulence. The nonlinearity can become relatively weak, if the inertial forces, which have a destabilizing role, are small in relation to the frictional forces. In this case, the Navier-Stokes equations can be solved exactly or integrated numerically without additional simplifying assumptions. Generally, solving the Navier-Stokes equations is extremely difficult. At present, only the existence of weak solutions has been demonstrated, and the presence of strong solutions being valid only for small time intervals. Therefore, various simplifications are considered to facilitate finding the solutions, if not exact, at least approximate [2].

Since an analytical solution of the Navier-Stokes equations, representing an exact mathematical description of the flow, cannot be achieved, these equations can be solved in an approximate manner, dividing a complex flow domain into a multitude of small cells, by numerical methods [3]. The numerical solution, although it is only a numerical approximation of real physical processes in a fluid flow, it is still the most rational approach both for solving problems of calculating the theoretical characteristics of a pump and for solving the problem of optimizing pump parts.

It should also be noted the main problem in the calculation of the fluid flow, namely, modeling the turbulent process, which consists in pronounced fluctuations of the flow field in time and space, which can have a significant impact on the flow characteristics. Turbulence occurs when the inertia forces in the fluid become significant compared to viscous forces, and is characterized by a high Reynolds Number. It is a complex process, mainly because it is three dimensional, unsteady and consists of many scales [3, 4].

If the velocities in equation (1) are considered as unsteady, the Navier-Stokes equations would be sufficient to calculate turbulent flows. This *Direct Numerical Simulation* (*DNS)* of turbulent flows in pump components is, however, beyond present computing capabilities. In order to exactly describe all turbulent fluctuations, extremely fine calculation grids and excessive computing times are required. Number N of elements needed in a grid for DNS can be estimated from $N \approx Re^{9/4}$. For the liquid flowing through the pump impeller, the $Re = 10^6$, the recommended number of finite volumes is $N= 10^{13}$ [3].

Turbulence models are used to correctly describe the turbulent flow. These models are needed to simplify mathematical representation of the turbulent flows through numerical methods, which simulate the behavior of turbulent fluid. This allows to describe the interaction between turbulent eddies and the averaged parameters of the flow. The choice of the turbulence model and the pertinent turbulence parameters thus harbors one of the main uncertainties of Navier-Stokes calculations of turbomachines [3].

It should be noted that in the case of simulating the flow of fluids through the pump flow section, the Navier-Stokes equations are simplified by adopting a series of simplifying assumptions: treating the fluid as a Newtonian fluid, in an incompressible, isothermal flow with a constant fluid dynamic viscosity [1].

The most commonly used modeling approach is *RANS (Reynolds-Averaged Navier-Stokes)* allowing to modeling turbulent flows based on averaging the Navier-Stokes equations over time. The main difference of the approach is that the averaged velocity and pressure are divided into averaged components and turbulent components. The application of the averaging of the Navier-Stokes equations requires the introduction of additional terms that are interpreted as apparent stresses and apparent thermal fluxes associated with the turbulent motion, being formulated depending on the average parameters through the turbulence models that are necessary to close the system of averaged Reynolds equations [2].

Turbulence models introduce additional assumptions, which, as a rule, are no longer a strict reflection of general conservation principles. One of these assumptions being: the linear Boussinesq approximation $\tau_{ij}^R = \nu_T \cdot S_i$, which describes the linear dependence of the Reynolds tensor τ_{ij}^R and the strain rate tensor S_i, then equations (3) and (4) can be reformulated as follows:

$$\frac{\partial \overline{u_i}}{\partial x_j} = 0 \tag{3}$$

$$\overline{u_j}\frac{\partial \overline{u_i}}{\partial x_j} - \frac{\partial}{\partial x_j}\left[(\nu - \nu_T)\left(\frac{\partial \overline{u_i}}{\partial x_j} - \frac{\partial \overline{u_j}}{\partial x_i}\right)\right] + \frac{1}{\rho}\frac{\partial \overline{p}}{\partial x_j} = 0 \tag{4}$$

Turbulence models based on the RANS equations (3) and (4) are known as Statistical Turbulence Models due to the statistical averaging procedure employed to obtain the equations. Due to the use of averaging procedures, we are forced to introduce additional unknown terms containing products of fluctuating quantities that act as additional stresses in the fluid. These terms are called Reynolds stresses.

Reynolds stresses need to be modeled by additional equations of known quantities in order to achieve "closure." Closure implies that there is a sufficient number of equations for all the unknowns, including the Reynolds-Stress tensor resulting from the averaging procedure. The equations used to close the system define the type of turbulence model [4].

It should be noted that in addition to the RANS approach (Reynolds Navier-Stokes averaging) used in steady-state calculation, there are modified URANS models (Unsteady Reynolds-Averaged Navier-Stokes) used for transient calculation. Unlike the RANS model, which averages flow variables over time, URANS models take into account unsteady flow phenomena by including time-dependent terms in the governing equations, which allows the simulation of a time-varying flow pattern.

The turbulence models which can be used to simulate the fluids flow of the pump's parts are:

- *Standard k-ε model*: one of the most prominent turbulence models, is considered the industry standard model [5]. This is the baseline turbulence model in CFX, which solves transport equations for turbulent kinetic energy (k) and its dissipation rate (ε). This model is widely used because convergence is better than with other turbulence models. Standard k-ε model is a universal model suitable for a wide range of turbulent flows, but its use due to the overestimation of the turbulent kinetic energy in places with a strong velocity gradient, the flow pattern is distorted [6]. The use of this model may lead to loss of accuracy on flows on curved paths, in geometries such as bends or diffusers. Also, the k-epsilon model does not describe well the swirling flows and the strong secondary flows. It may be difficult to simulate the flow through rotating pumps components, since the body forces influence the boundary layers. These phenomena can be found in such parts of the pump as impellers, diffusers, volutes, etc. [3].
- *Standard k-ω Model*: a common two-equation turbulence model, used as an approximation for the RANS equations, involves solving the transport equations of the turbulent kinetic energy k and the specific dissipation rate ω. Advantages of this model is the near wall flow treatment [2]. The model does not involve the complex nonlinear damping functions required for the k- ε model and is therefore more accurate and more robust [4]. This model was developed specifically for flows against strong pressure gradients (a similar flow pattern appears diffuser) [3]. The model is used mainly for historical reasons, since it has been supplanted by modified k-ω models such as Menter's SST and BSL models due to the strong dependence of the solution on free flow ω values outside the shear layers [6].
- *SST (Menter's Shear Stress Transport) k-omega model*: This hybrid model combines the k-ε and k-ω models to capture the advantages of both models [2]. The SST model is the most commonly used turbulence simulation model due to the simultaneous combination of the strengths of the k-ω (description of the flow near walls) and k-ε (description of the free flow of fluids) models [7]. The advantage of the SST model over the above models is its high accuracy for flows with unfavorable pressure gradients and separation, [6] which offers improved predictions of the turbulent shear stress in regions with high shear and adverse pressure gradients [4], but flows on curved paths are still not well simulated [3].

In addition to stationary calculations, if it is necessary to describe complex flows whose parameters are difficult to average over time, transient modeling is used. In this case, the following models' groups and hybrids models are used:

— *Unsteady Reynolds Averaged Navier-Stokes (URANS)*, a time-averaged approach that solves the Reynolds-averaged Navier-Stokes equations, listed above.

— *Scale-Resolving Simulation (SRS)* is a CFD approach, i.e. an intermediate approach between URANS simulations and Direct Numerical Simulation DNS, which aims to describe both the large-scale and small-scale turbulent flow structures. Although the URANS models perform well in calculating the flow confined by walls, it should still be noted that the use of such models is important in solving complex multi-physics problems of turbomachinery, such as thermal calculations in zones of non-stationary mixing of flows at different temperatures, when simulating vortex cavitation, which is caused by a non-stationary turbulent pressure field, modeling acoustics in hydraulic systems when turbulence creates noise sources, etc [8-14]. These models include Large Eddy Simulation (LES), a model that decomposes the flow into large-scale vortex structures and models the small-scale turbulent eddies and its hybrids with RANS models. The above are extremely sensitive to mesh density and therefore cannot be used in the optimization process.

We can see that the optimization process described in figure 1 is a multi-iteration one, the calculation time problem is a decisive one. It can be mentioned that the description of the geometry of the pumps parts can be done in dozens of parameters, which leads to the increase of the number of calculation cycles to hundreds of iterations. Therefore, we cannot use computationally expensive turbulence models. Figure 8 shows the study of the effect of two different RANS models on the accuracy of measuring the pump head, taking into account the maximum size of the final mesh element. When comparing, it can be seen that the *SST model* gives a more accurate result in comparison with the *k-ε model*, both at nominal feed, and at minimum and maximum feed.

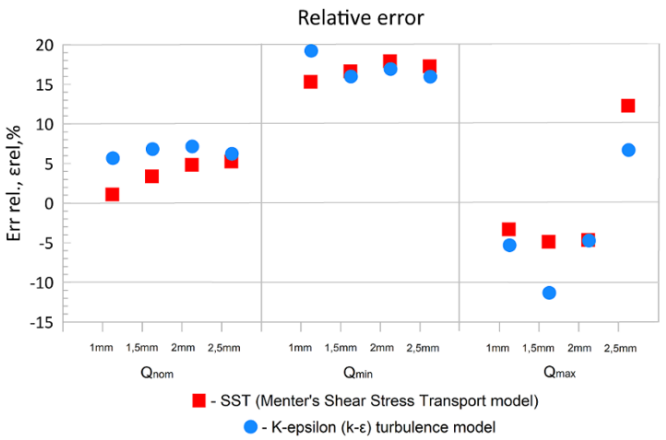

Figure 8. Comparison of the precision of calculating the head of the pump CH 6,3/32-2,2-2 using k-ε and SST turbulence models.

As already mentioned, three-dimensional simulation can be performed in two approaches: Steady-state and Transient. Steady simulations compute a solution with time-averaged values, and dynamic simulation computes instantaneous values in each time unit for each finite volume. Transient simulation considerably increases the resources required for simulation, but provides a complete picture of the processes taking place in the working organs of the pump.

Both approaches were compared and as a result, the difference between the researched parameters, under nominal flow conditions, with a discretization grid having a relatively small finite volume size, is not considerable. Although URANS transient simulations provide a more accurate picture, they are more time consuming than steady state simulations. So, we can state that in the final phase of the process optimization it is favorable to apply steady-state simulations to a fine discretization network.

It should be noted that the geometric model consists of three domains (Figure 3), so it is necessary to apply the transition model between the domains: the Stage (mixing plane) model – averaging the velocities on the interface surface and the Frozen rotor model – which better models' interaction between different domains. The Frozen rotor model additionally adds the Navier-Stokes equations, written for the mobile domain to the rotation tensor, thus virtually simulating its relative rotation. The GGI (General Grid Interface) method is used as the connection method of the finite volumes.

The comparison between the Stage and Frozen rotor models was performed. We can see that when simulating the flow through a centrifugal pump, the Frozen rotor model provides true results compared to the Stage (mixing plane) model, in relation to the size of the finite volume, with approx. 2-5% relative error (calculated as a function of pumps head).

The mass transfer model represents the cavitation model, defined by the Rayleigh-Plesset equation, which is used to model the cavitation process [7]:

The Rayleigh-Plesset equation (5) derives from the Navier-Stokes equations and represents a differential equation that governs the dynamics of a spherical bubble (formed as a result of the cavitation process inside the pump) in an incompressible fluid.

$$R\frac{d^2R}{\partial t^2}+\frac{3}{2}\left(\frac{dR}{dt}\right)^2+\frac{4\nu}{R}\frac{dR}{dt}+\frac{2\gamma}{\rho_L R}+\frac{\Delta P(t)}{\rho_L}=0 \tag{5}$$

where: ρ_L is the density of the liquid, R(t) - radius of the bubble, ν – kinematic viscosity of the liquid, γ being the surface tension between the bubble and the liquid, $\Delta P(t)=P_\infty(t)-P_B(t)$, where $P_B(t)$ - pressure in bubble, and $P_\infty(t)$ - liquid pressure.

The cavitation model used is the Zwart, Gerber and Belamri model based on the Rayleigh-Plesset equation [4]:

$$\dot{S}_{lv}=\begin{cases}Fvap\dfrac{3r_{nuc}(1-r_v)\rho_v}{R_B}\sqrt{\dfrac{2}{3}\dfrac{P_v-P}{\rho_l}}, & P<P_v\\ Fcond\dfrac{3r_v\rho_v}{R_B}\sqrt{\dfrac{2}{3}\dfrac{P-P_v}{\rho_l}}, & P>P_v\end{cases}$$

The model assumes that the overall rate of multiphase mass transfer per unit volume $\dot{S}_{lv}$ is calculated using the nucleation site volume fraction r_{nuc}, assuming all bubbles in the system are the same size [9].

In present research, the nucleation site radius R_B is $1\cdot10^{-6}$, the vapor saturation pressure P_v is chosen to be 3170 Pa.

5. Establishing initial and boundary conditions

The following initial conditions were applied in the study (Figure 9):

- The impeller area rotates at a speed of 2950 min-1.
- Zero reference pressure (Pref = 0 atm).
- Isothermal flow (t = 25˚C).
- Minimal inlet turbulence (1%).
- In the initial state, the fluid consists entirely of water in liquid form.

• Walls type boundary conditions are applied to the walls with the "no slip" specification - as a wall that does not allow mass or energy transfer, the velocity on these surfaces is considered zero, which allows the simulation of flow in the area near the wall.

It should be noted that the model does not take into account the gravitational forces and the roughness of the contact surfaces.

The simulation is based on the biphasic continuous fluid model, consisting of:

• water in liquid form at 25° C;

• water vapor at 25° C.

The choice of the time step size is made due to the use of a static calculation model. The Timescale Control function allows you to adjust the size of the time step during simulation to ensure calculation convergence and accuracy. As the Timescale Control model, we selected the *Physical Timescale* option.

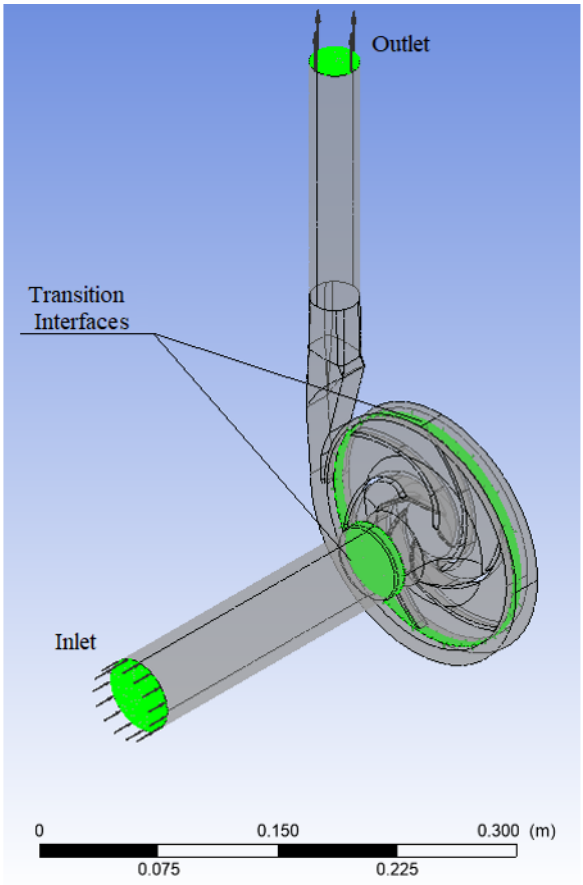

Figure 9. Application of boundary and initial conditions in ANSYS CFX pre.

Since the main movement under the study is the rotational movement of the impeller at a constant speed, in the search for the optimal step, we tie it to the angular velocity. The following cases were investigated: 2⁄ω, 1⁄ω, ...,1⁄8ω, where: ω=2πn - angular velocity. The optimal time step was equal to 1⁄ω = 0.003237 s, decreasing the step below this level does not bring tangible results.

At the *Inlet* in the flow area, Total Pressure (Stable), $P_{inlet} = 10^6$ Pa is indicated, the flow direction being normal. The character of the domain is indicated – Subsonic and the state of low turbulence (1%). It is assumed that at the entrance to the system the flow consists entirely of water in liquid form.

At the *Outlet* from the flow area, the Flow (Bulk Mass Flow Rate) is indicated, for a nominal flow rate of 1.75 kg/s. At the system output, the flow characteristics related to turbulence and cavitation are calculated by the solver (Zero gradient).

6. Establishing the calculation parameters

Calculation parameters are also important as they allow to ensure numerical convergence, optimization of computational resources, such as allocated memory and execution time.

For the Stage and Frozen rotor models, the final number of calculation iterations of 400 was selected, also the calculation is completed when the residual error tolerance of 10^{-5} is reached during the simulations.

To monitor the convergence, the following indicators were selected: static and absolute pressure at the inlet and outlet, as well as the torsional moment relative to the axis of rotation applied to the pump impeller and domain imbalance.

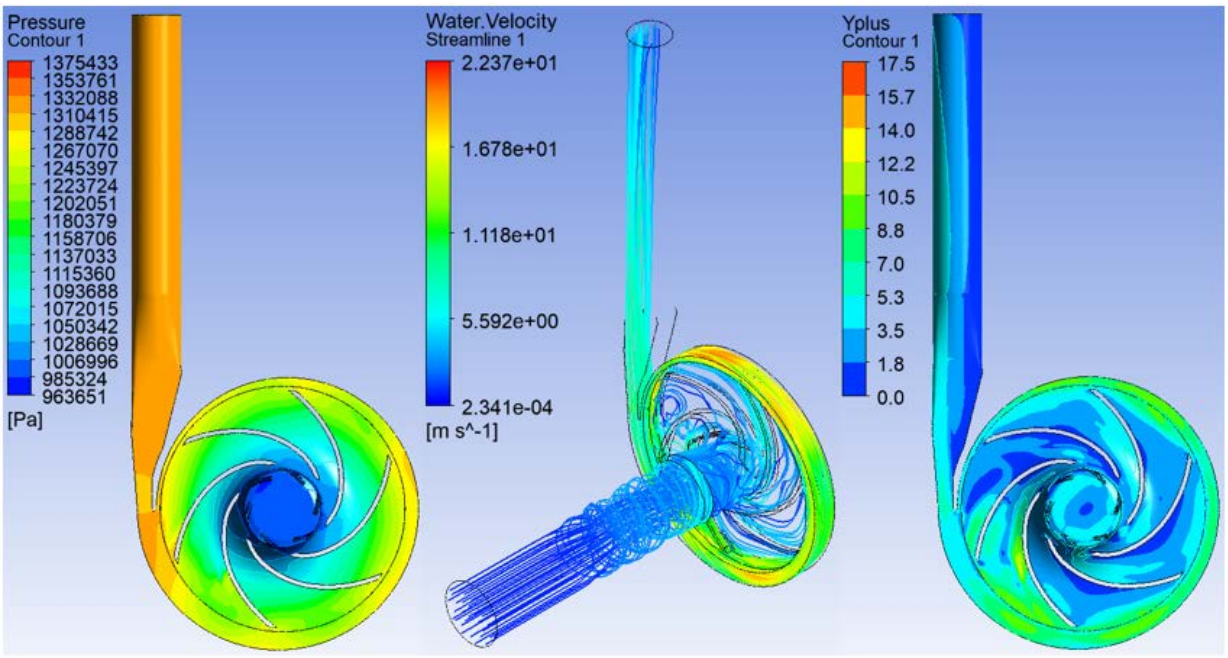

Figure 9, a. Representation of the pressure and velocity field, as well as the distribution of the y+ parameter in ANSYS CFX post.

7. The results of the simulations

Throughout this study, 128 simulations were performed on different discretization grids, with the size of the finite volume 1÷2.5 mm and with 5÷20 layers of inflation, at different flow regimes: minimum flow (Q_{min} = 2 m^3/h), Best Efficiency Point nominal flow (Q_{nom} = 6.3 m^3/h) and at maximum flow (Q_{max} = 9.5 m^3/h), also the k-ε and SST turbulence models at nominal flow were compared.

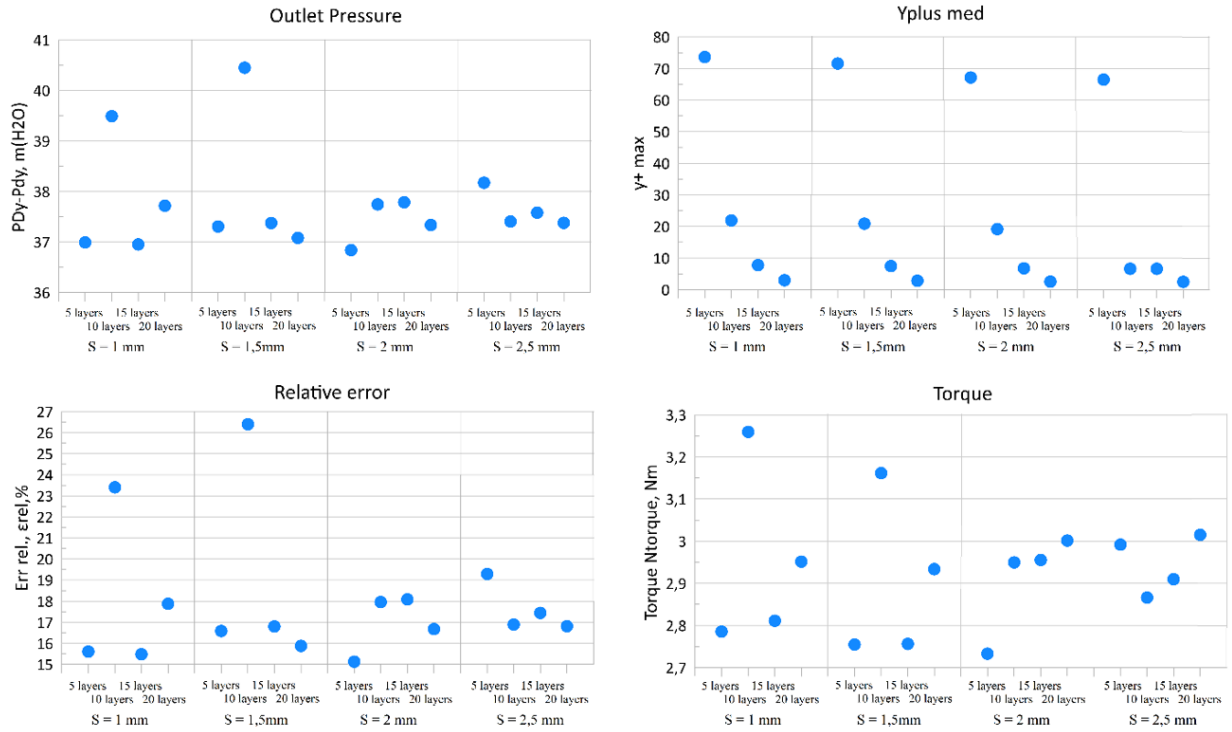

Figure 10. Simulation results (pump: CH-6,3-32; Qmin = 2 m^3/h, Frozen rotor, SST model).

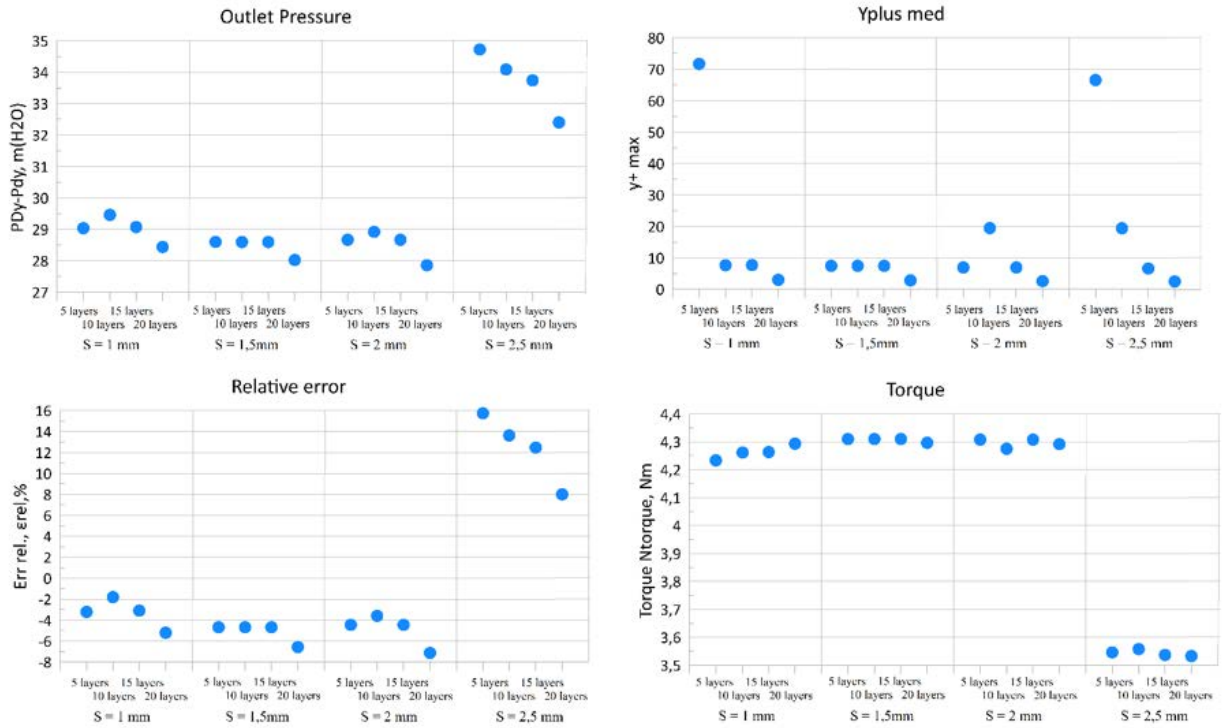

Figure 11. Simulation results (pump: CH-6,3-32; Q_{nom} = 6,3 m^3/h, Frozen rotor, SST model).

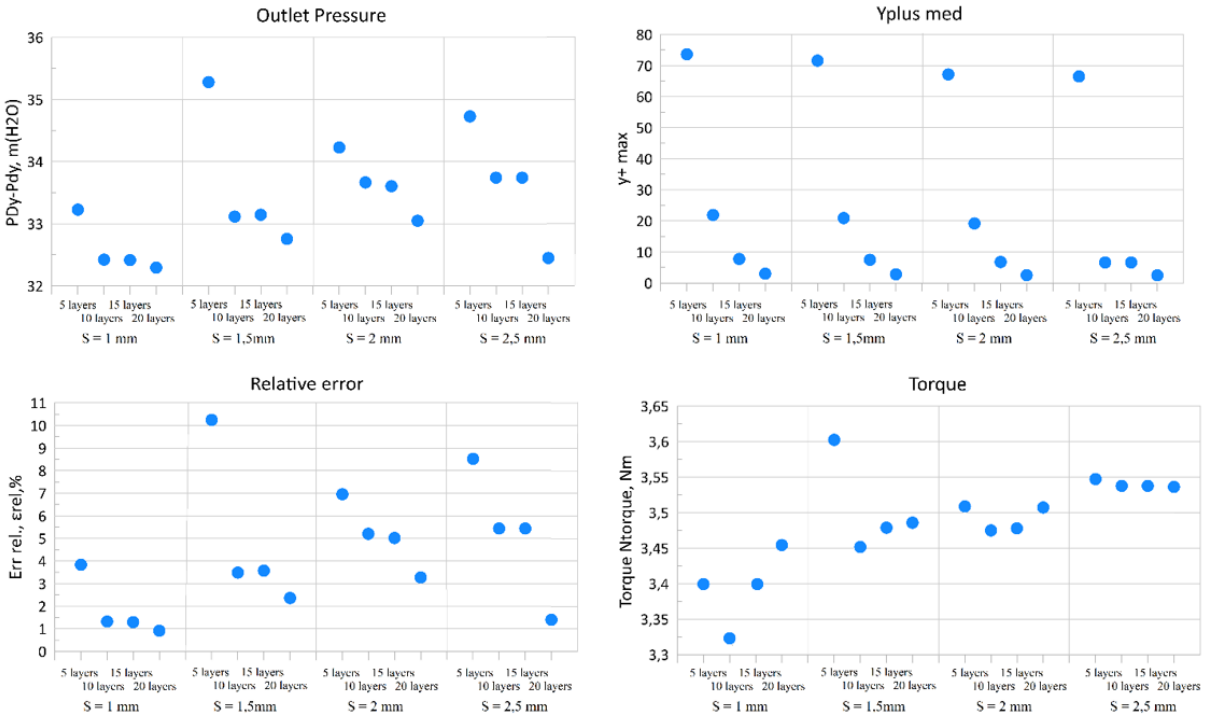

Figure 12. Simulation results (pump: CH-6,3-32; Q_{max} = 9,5 m^3/h, Frozen rotor, SST model).

8. Conclusions

A series of simulations was carried out on different grids, with different sizes of the finite element (S = 1÷2.5 mm), with a different number of pumping layers (5÷20 layers). Unstructured and structured meshes were also compared, when carrying out process optimization. It is recommended to use an unstructured mesh obtained in ANSYS Mesher and

a structured mesh obtained in ANSYS TurboGrid, due to the high degree of automation of mesh generation.

The accuracy of the calculation increases proportionally to the decrease in size of the fine volume and the increase in the number of layers of inflation describing the boundary layer. The best option is to choose the size of the final volume of the order of 1.5 mm and the order of 15-20 layers of inflation, because the difference in the number of final volumes between the mesh of the volume size of the order of 1.5 mm and 1 mm is more than 2 times (Fig. 5), and the available computing resources are limited.

The numerical convergence of the results is obtained. As the size of the final volume decreases, the parameter y+ drops to the region of units.

It can be noted that the accuracy of the SST model is higher, and is optimal for the optimization procedure of parts of centrifugal pumps. This fact is due to the simultaneous combination of the strengths of k-ω and k-ε.

The results of applying the SST RANS and URANS models were also compared. It was found out that the use of transient calculation significantly increases the consumed computing resources, which is unacceptable for building process optimization.

Conflicts of Interest: The authors declare no conflict of interest.

References

1. Petco, A. Numerical simulation of liquid flow in the working organs of the centrifugal pump by means of Ansys CFX. In: Technical-Scientific Conference of Students, Masters and Doctoral Students, Technical University of Moldova, Chisinau, 23-25 March, 2021. [in Romanian].
2. Bostan, V. Mathematical models in engineering: contact problems: modeling and numerical simulations in aero-hydrodynamics. Chisinau, 2014, 456 p. [in Romanian].
3. Gülich, J.F. Centrifugal Pumps. Springer International Publishing, Cham, 2020, 966 p.
4. Ansys CFX Solver Theory Guide. Release 2021 R2. ANSYS, Inc., 2021.
5. Ansys CFX-Solver Modeling Guide. Release 2021 R3. ANSYS, Inc., 2021.
6. Menter, F.R., Sechner, R., Matyushenko, A. Best Practice: RANS Turbulence Modeling in Ansys CFD. Available online: https://semiengineering.com/best-practice-rans-turbulence-modeling-in-ansys-cfd/ (accessed on 12.03.2023).
7. Petco, A. Constructive-functional development of centrifugal pumps through multiparametric optimization and CFD simulations. In: Technical-Scientific Conference of Students, Masters and Doctoral Students, Technical University of Moldova, Chisinau, 26-29 March, 2019.
8. Best Practice: Scale-Resolving Simulations in Ansys CFD. Available online: https://www.ansys.com/resource-center/technical-paper/best-practice-rans-turbulence-modeling-in-ansys-cfd (accessed on 12.03.2023).
9. Zwart, P.; Gerber, A.G.; Belamri, T. A two-phase flow model for predicting cavitation dynamics. In: Fifth International Conference on Multiphase Flow, 2004.
10. Matlakala M.E.; Daramy V. K. Optimization of the Pumping Capacity of Centrifugal Pumps Based on System Analysis. MATEC Web of Conferences 347, 00024 (2021) SACAM2020.
11. Lomakin, V.O. ; Chaburko, P.S.; Kuleshova, M.S. Multi-criteria Optimization of the Flow of a Centrifugal Pump on Energy and Vibroacoustic Characteristics, Procedia Engineering, Volume 176, 2017, 476-482.
12. Zhenwang L.; James D.; Shen K.; Man J. Performance Optimization of High Specific Speed Centrifugal Pump Based on Orthogonal Experiment Design Method. October 2019, Processes 7(10):728
13. Pouria H.; Shahriyar M. Modeling and optimization of centrifugal pumps using ansys fluent® and genetic algorithm analysis. International Transaction Journal of Engineering, Management, & Applied Sciences & Technologies, 2019, p. 903-911.
14. Ling Z.; Weidong S.; Suqing Wu. Performance Optimization in a Centrifugal Pump Impeller by Orthogonal Experiment and Numerical Simulation. Advances in Mechanical Engineering 2013, p.1-7.

Citation: Bostan, V.; Petco, A. Determining optimal simulation settings for the centrifugal pump parts optimization process. *Journal of Engineering Science* 2023, 30 (2), pp. 8-22. https://doi.org/10.52326/jes.utm.2023.30(2).01.

Submission of manuscripts: jes@meridian.utm.md

Journal of Engineering Science *Vol. XXX, no. 2 (2023), pp. 23 - 33*
Fascicle *Industrial Engineering* *ISSN 2587-3474*
Topic *Mechanical Engineering and Technologies* *eISSN 2587-3482*

https://doi.org/10.52326/jes.utm.2023.30(2).02
UDC 539.3:004.42

APPLICATION OF DISCONTINUOUS SOLUTIONS IN BOUNDARY ELEMENT METHOD FOR THE BENDING PROBLEMS OF KIRCHHOFF PLATES WITH AN ARBITRARY CONTOUR

Sergiu Galbinean*, ORCID: 0009-0000-9876-492x

Technical University of Moldova,168 Ștefan cel Mare Blvd., Chișinău, Republic of Moldova
*Corresponding author: Sergiu Galbinean, *sergiu.galbinean@cms.utm.md*

Received: 05. 15. 2023
Accepted: 06.12. 2023

Abstract. The discontinuous solutions represent a new direction for the indirect Boundary Element Method (BEM) in the indirect formulation. Discontinuous solutions represent those functions, which when crossing certain lines, the transverse deflection, the slope angle, the bending moment and the generalized shear force may have jumps. These can be used to solve important problems for which the existing methods do not have solutions or a satisfactory accuracy, such as: plates of arbitrary contour, presence of defects, mixed boundary conditions, contact problems, infinite domains etc. In this paper, we describe the methodology of application and the numerical implementation of discontinuous solutions for the bending problems of plates with an arbitrary contour in the classical theory (Kirchhoff). For this purpose, programming codes were developed in the Matlab language, which allowed to calculate the displacements and efforts in the plate. The obtained results were compared with the Finite Element Method (FEM) for different mesh densities.

Keywords: *Boundary Element Method; discontinuous solution; Green function; Kirchhoff plate.*

Rezumat. Soluțiile discontinue reprezintă o nouă direcție pentru Metoda Elementelor de Frontieră (MEFr) în formularea indirectă. Soluțiile discontinue reprezintă acele funcții, care la traversarea anumitor linii, săgeata, unghiul de rotire, momentul de încovoiere și forța tăietoare generalizată pot căpăta salturi. Acestea pot fi utilizate la rezolvarea unor probleme importante pentru care metodele existente nu au soluții sau o acuratețe satisfăcătoare, precum: plăci de contur arbitrar, prezența defectelor, condiții mixte la limită, probleme de contact, domenii infinite etc. În această lucrare este descrisă metodologia de aplicare și implementare numerică a soluțiilor discontinue la calculul plăcilor de un contur arbitrar în teoria clasică (Kirchhoff). În acest scop, au fost elaborate coduri de programare în limbajul Matlab, care au permis de a calcula deplasările și eforturile în placă. Rezultatele obținute au fost comparate cu Metoda Elementelor Finite (FEM) pentru diferite densități ai rețelei de discretizare.

Cuvinte cheie: *Metoda elementelor de Frontieră; soluții discontinue; funcția Green; placă Kirchhoff.*

1. Introduction

Plates are important elements for different resistance structures. Although computational theory has a history of more than 200 years, until now there are no methods that would solve all types of plate bending problems encountered. Some solutions for rectangular and circular plates are presented in weakly convergent Fourier series, but these cannot be used for all boundary conditions and loading cases. Along with the development of the computational techniques, numerical calculation methods were developed. The most used are: the Finite Element Method (FEM) [1, 2] and the Boundary Element Method (BEM) [3-4].

The Finite Element Method (FEM) has become widely used in recent times. It is commonly acknowledged that the majority of FEM programs do not contain plate finite elements with more than three degrees of freedom in the nodes, that could satisfy all boundary conditions. The process of discretization of the entire surface of the plate into finite elements, it usually leads to: a massive system of linear equations, necessity of big initial data, big volume of computer memory. There are, also, difficulties in solving problems that present: stress concentrations, defects, contact problems, plate-bar connections etc.

In recent years the boundary elements method (BEM) intensively develops. In BEM the discretization is applied only to the edge of the plate. Therefore, the number of nodes and elements is reduced compared to FEM, and this also implies the reduction of the system of linear equations by one unit. In BEM we have numerical solution only at the edge of the plate, while in the interior the solutions are analytical and provide more accurate results. In the theory of plates and shells there are two approaches to obtain the integral equations: direct [5, 6] and indirect [7, 8].

For the indirect BEM is offered a new approach which is based on discontinuous solutions. These solutions were obtained by Prof. Moraru Gheorghe [9, 10] for an infinite domain by applying the generalized Fourier transform to the differential equation of plates. Using them as Green Functions [11-13] of influence we can solve a variety of plate bending problems.

2. Materials and Methods

2.1. Governing equation in Kirchhoff plate theory

The differential equation of the deformed median surface of the plate has the form:

$$\Delta\Delta w = \frac{p(x,y)}{D}, \tag{1}$$

where Δ is the Laplace operator, p is the the external load distributed on area;
$D = Eh^3/12(1-\nu^2)$ is the flexural rigidity, E and ν are Young's modulus and Poisson's ratio.

This differential equation allows to satisfy two boundary conditions for each side.

2.2. Discontinuous solutions for an infinite plate

Consider that in an infinite plate on the axis y ($x = 0$) (Figure 1) there is a defect (crack, plastic hinge, rigid inclusion etc.). When passing from one side of the defect $x = -0$ to the other $x = +0$ the deflection w, the slope angle ϑ_x, the bending moment M_x, and the generalized shear force V_x may obtain jumps (Figure 2). In the local system of coordinates (x, y) we introduce the following notation for the jump of functions:

$$\begin{aligned} w(-0,y) - w(+0,y) &= \langle w(y)\rangle; \\ \theta_x(-0,y) - \theta_x(+0,y) &= \langle \theta_x(y)\rangle; \\ M_x(-0,y) - M_x(+0,y) &= \langle M_x(y)\rangle; \\ V_x(-0,y) - V_x(+0,y) &= \langle V_x(y)\rangle. \end{aligned} \tag{2}$$

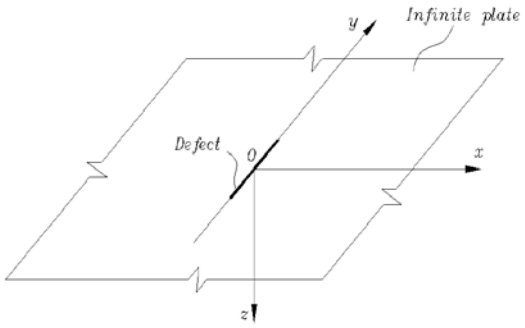

Figure 1. Infinite plate with a defect.

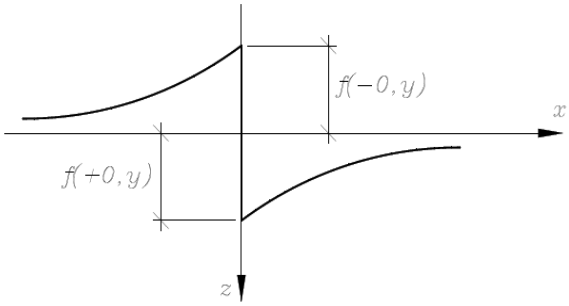

Figure 2. The jump of function *f* when passing through the defect.

We can obtain the solutions for these jumps by applying the generalized Fourier transform [14] to the differential equation of plates (1), assuming that $q(x, y) = 0$. The relations between concentrated jumps and displacements can be written in the following form:

$$\begin{Bmatrix} w(x,y) \\ \theta_x(x,y) \\ \theta_y(x,y) \end{Bmatrix} = \begin{bmatrix} g_{11} & g_{12} & g_{13} & g_{14} \\ g_{21} & g_{22} & g_{23} & g_{24} \\ g_{31} & g_{32} & g_{33} & g_{34} \end{bmatrix} \begin{Bmatrix} \langle w(y) \rangle \\ \langle \theta_x(y) \rangle \\ \langle M_x(y) \rangle \\ \langle V_x(y) \rangle \end{Bmatrix}, \tag{3}$$

where elements g_{ij} are given [8]:

$$g_{11} = -\frac{1}{4\pi}\frac{x}{r^4}[(3-\nu)x^2 + (1+\nu)y^2]; \quad g_{12} = -\frac{1}{4\pi}\left[(1+\nu)\ln r + (1-\nu)\frac{x^2}{r^2}\right];$$

The relations between jumps and efforts are given by:

$$\begin{Bmatrix} M_x(x,y) \\ M_y(x,y) \\ M_{xy}(x,y) \\ Q_x(x,y) \\ Q_y(x,y) \end{Bmatrix} = \begin{bmatrix} t_{11} & t_{12} & t_{13} & t_{14} \\ t_{21} & t_{22} & t_{23} & t_{24} \\ t_{31} & t_{32} & t_{33} & t_{34} \\ t_{41} & t_{42} & t_{43} & t_{44} \\ t_{51} & t_{52} & t_{53} & t_{54} \end{bmatrix} \begin{Bmatrix} \langle w(y) \rangle \\ \langle \theta_x(y) \rangle \\ \langle M_x(y) \rangle \\ \langle V_x(y) \rangle \end{Bmatrix}, \tag{4}$$

where elements t_{ij} are given [8]:

$$t_{11} = \frac{3(1-\nu)^2 D}{2\pi}\frac{x}{r^8}(x^4 - 6x^2y^2 + y^4);$$

$$t_{21} = \frac{(1-\nu)D}{2\pi}\frac{x}{r^8}[-(5-\nu)x^4 + 2(11-7\nu)x^2y^2 + 3(1+3\nu)y^4];$$

The relations between jums and the generalized shear force [8]:

$$\begin{Bmatrix} V_x(x,y) \\ V_y(x,y) \end{Bmatrix} = \begin{bmatrix} l_{11} & l_{12} & l_{13} & l_{14} & l_{15} \\ l_{21} & l_{22} & l_{23} & l_{24} & l_{25} \end{bmatrix} \begin{Bmatrix} \langle w(y) \rangle \\ \langle \theta_x(y) \rangle \\ \langle M_x(y) \rangle \\ \langle V_x(y) \rangle \end{Bmatrix}, \tag{5}$$

where elements l_{ij} are given:

$$l_{11} = \frac{3(1-\nu)D}{2\pi r^{10}}[(7-3\nu)x^6 - 5(11-7\nu)x^4y^2 + 5(1-5\nu)x^2y^4 + (3+\nu)y^6];$$

$$l_{12} = -\frac{3(1-\nu)^2 D}{2\pi}\frac{x}{r^8}(x^4 - 6x^2y^2 + y^4); \quad \cdots$$

2.3. The efforts in plates with arbitrary boundary

If we consider the obtained solutions as Green functions of influence [11-13] and applying the principle of superposition we can write the discontinuous solutions for the defect located on an arbitrary contour *L* (Figure 3).

If we use coordinate transformation from one local system $(\bar{x},\bar{y})$ to another local system (*n*,*t*), then we obtain:

$$w^*(P)=\int_L \bar{w}\,(P,Q)ds_Q; \qquad \theta_n^*(P)=\int_L\left[\bar{\theta}_x(P,Q)\cos\gamma+\bar{\theta}_y(P,Q)\sin\gamma\right]ds_Q;$$

$$M_n^*(P)=\int_L\left[\bar{M}_x(P,Q)\cos^2\gamma+\bar{M}_y(P,Q)\sin^2\gamma+2\bar{M}_{xy}(P,Q)\cos\gamma\sin\gamma\right]ds_Q;$$

$$M_{nt}^*(P)=\int_L\left\{\left[\bar{M}_y(P,Q)-\bar{M}_x(P,Q)\right]\cos\gamma\sin\gamma+M_{xy}(P,Q)(\cos^2\gamma-\sin^2\gamma)\right\}ds_Q;$$

$$Q_n^*(P)=\int_L\left[\bar{Q}_x(P,Q)\cos\gamma+\bar{Q}_y(P,Q)\sin\gamma\right]ds_Q; \qquad V_n^*(P)=Q_n^*+\frac{\partial M_{nt}^*}{\partial t}, \tag{6}$$

where $\gamma=\beta-\alpha$.

The discontinuous solutions can also be applied to solve fundamental plate bending problems. In such cases, the edge is treated as a defect within an infinite plate. As we approach the edge from within the region occupied by the plate, the jumps are assumed to be equal to the values on the boundary. On the other hand, as we approach the edge from outside, these jumps are considered equal to zero.

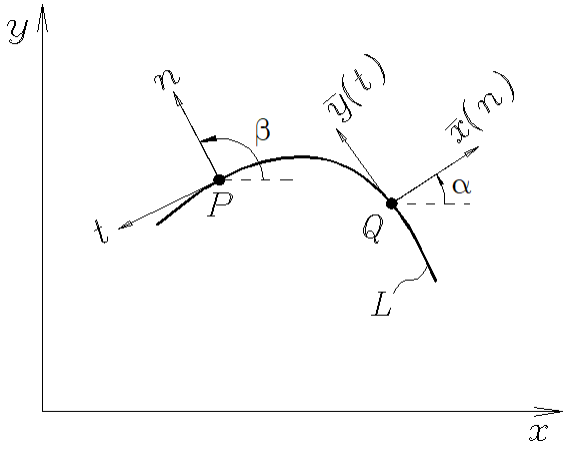

Figure 3. Local systems of coordinates on contour *L*.

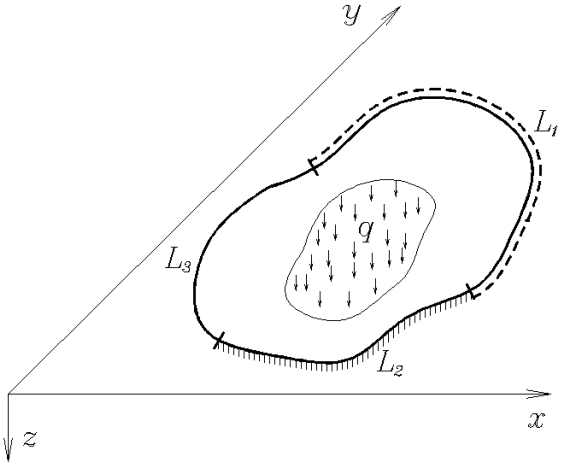

Figure 4. Plate of arbitrary shape.

2.4. Numerical implementation of discontinuous solutions in BEM

Consider a plate of arbitrary shape (Figure 3). On the edge L_1 the plate is simply supported, on L_2 – clamped and on L_3 – free.

To write the boundary integral equations, the deformable state of the plate is expressed as a combination of two states: the first one (marked with an asterisk) corresponds to the concentrated jumps on the line *L* of the defect, while the second one (marked with a circle) – to the external loads.

The boundary conditions are:

– for simply supported edge (L_1)

$$w^*+w^o=0; \qquad M_n^*+M_n^o=0; \qquad (\langle\theta_n\rangle\neq 0; \quad \langle V_n\rangle\neq 0);$$

– for clamped edge (L_2)

$$w^* + w^o = 0; \qquad \theta_n^* + \theta_n^o = 0; \quad (\langle M_n \rangle \neq 0; \quad \langle V_n \rangle \neq 0);$$

– for free edge (L_3)

$$M_n^* + M_n^o = 0; \qquad V_n^* + V_n^o = 0; \quad (\langle w \rangle \neq 0; \quad \langle \theta_n \rangle \neq 0).$$

For example, if the plate is subjected to a point force F with coordinates a_0, b_0, the solutions due to the external load have the form:

$$\begin{aligned} w_i^o &= F \cdot g_{14}(x_i^m - a_0, y_i^m - b_0); \\ \theta_{ni}^o &= F\left(n_x\theta_{xi}^o + n_y\theta_{yi}^o\right) = F\left[n_x g_{24}(x_i^m - a_0, y_i^m - b_0) + n_y g_{34}(x_i^m - a_0, y_i^m - b_0)\right]; \\ M_{ni}^o &= F\left(n_x^2 M_{xi}^o + n_y^2 M_{yi}^o + 2n_x n_y M_{xyi}^o\right) = F[n_x^2 t_{14}(x_i^m - a_0, y_i^m - b_0) + \\ &+ n_y^2 t_{24}(x_i^m - a_0, y_i^m - b_0) + 2n_x n_y t_{34}(x_i^m - a_0, y_i^m - b_0)]; \\ V_{ni}^o &= F\left(n_x V_{xi}^o + n_y V_{yi}^o\right) = F\left[n_x l_{14}(x_i^m - a_0, y_i^m - b_0) + n_y l_{24}(x_i^m - a_0, y_i^m - b_0)\right] \end{aligned} \quad (7)$$

where $n_x = \cos\alpha$ şi $n_y = \sin\alpha$.

For other loading types the solutions can be obtained by integrating the expressions (7) on the line or on the area of the load distribution.

If we discretize the contour L into a set of constant elements we can obtain the following system of equations:

$$\left.\begin{array}{l} \sum_{j=n_{L3}} w_{ij}^1\langle w_j\rangle + \sum_{j=n_{L1},n_{L3},n_{Ld}} w_{ij}^2\langle\theta_{nj}\rangle + \sum_{j=n_{L2}} w_{ij}^3\langle M_{nj}\rangle + \sum_{j=n_{L1},n_{L2}} w_{ij}^4\langle V_{nj}\rangle = -w_i^o; \quad (i = n_{L1}, n_{L2}) \\ \sum_{j=n_{L3}} \theta_{ij}^1\langle w_j\rangle + \sum_{j=n_{L1},n_{L3},n_{Ld}} \theta_{ij}^2\langle\theta_{nj}\rangle + \sum_{j=n_{L2}} \theta_{ij}^3\langle M_{nj}\rangle + \sum_{j=n_{L1},n_{L2}} \theta_{ij}^4\langle V_{nj}\rangle = -\theta_{ni}^o; \quad (i = n_{L2}) \\ \sum_{j=n_{L3}} m_{ij}^1\langle w_j\rangle + \sum_{j=n_{L1},n_{L3},n_{Ld}} m_{ij}^2\langle\theta_{nj}\rangle + \sum_{j=n_{L2}} m_{ij}^3\langle M_{nj}\rangle + \sum_{j=n_{L1},n_{L2}} m_{ij}^4\langle V_{nj}\rangle = -M_{ni}^o; \quad (i = n_{L1}, n_{L3}, n_{Ld}) \\ \sum_{j=n_{L3}} v_{ij}^1\langle w_j\rangle + \sum_{j=n_{L1},n_{L3},n_{Ld}} v_{ij}^2\langle\theta_{nj}\rangle + \sum_{j=n_{L2}} v_{ij}^3\langle M_{nj}\rangle + \sum_{j=n_{L1},n_{L2}} v_{ij}^4\langle V_{nj}\rangle = -V_{ni}^o; \quad (i = n_{L3}) \end{array}\right\} \quad (8)$$

where: n_{L1}, n_{L2}, n_{L3} – the index number of the boundary elements on the edge: L_1, L_2 and L_3, respectivly.

By solving the system of equations (8) all the jumps on the boundary will be known, so that the displacements and the efforts in any point inside the plate can be calculated, these being expressed by the obtained jumps. For example, if it is necessary to calculate the displacement at any point k from the interior of the plate (Figure 5), the expression take the form:

$$w_k = \sum_{j=n_{L3}} g_{11}\langle w_j\rangle + \sum_{j=n_{L1},n_{L3},n_{Ld}} g_{12}\langle\theta_{nj}\rangle + \sum_{j=n_{L2}} g_{13}\langle M_{nj}\rangle + \sum_{j=n_{L1},n_{L2}} g_{14}\langle V_{nj}\rangle + w_k^o. \quad (9)$$

The bending moment at the point k, acting in direction d (Figure 5):

$$\begin{aligned} M_k^d = &\sum_{j=n_{L3}} (c^2 t_{11} + s^2 t_{21} + 2\,cs\,t_{31})\langle w_j\rangle + \sum_{j=n_{L1},n_{L3},n_{Ld}} (c^2 t_{12} + s^2 t_{22} + 2\,cs\,t_{32})\langle\theta_{nj}\rangle + \\ &\sum_{j=n_{L2}} (c^2 t_{13} + s^2 t_{23} + 2\,cs\,t_{33})\langle M_{nj}\rangle + \sum_{j=n_{L1},n_{L2}} (c^2 t_{14} + s^2 t_{24} + 2\,cs\,t_{34})\langle V_{nj}\rangle + \\ &n_x^2 M_{x,k}^o + n_y^2 M_{y,k}^o + 2n_x n_y M_{xy,k}^o.^* \end{aligned} \quad (10)$$

The terms g_{11}, g_{12}, ... , t_{54} from relations (9) and (10) will be calculated using the solutions from (3) and (4) substituting: x_i with x_k and y_i with y_k.

Where: x_k and y_k represent the coordinates of point k in the global system;

$c = \cos(\beta_k - \alpha_j)$; $s = \sin(\beta_k - \alpha_j)$; $n_x = \cos(\beta_k)$; $n_y = \sin(\beta_k)$;

w_k^o, $M_{x,k}^o$, $M_{y,k}^o$, $M_{xy,k}^o$ represent the solutions at the point k due to the external loads. For example, in case of a point force these solutions can be obtained from (7) substituiting x_i^m with x_k and y_i^m with y_k. For other loading types – by integrating the expressions (7) on the line or on the area of the load distribution.

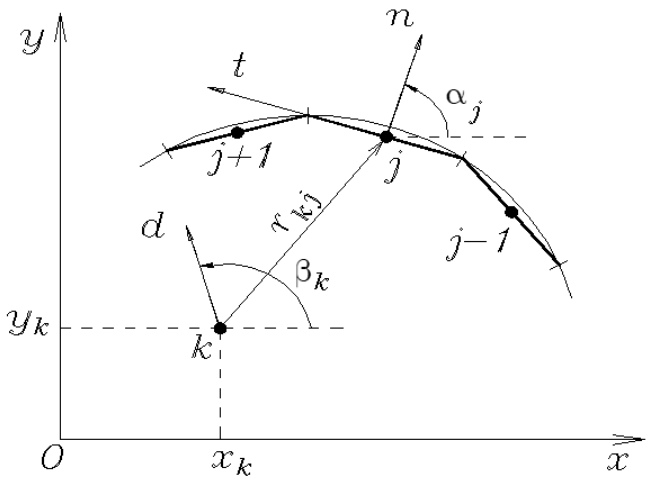

Figure 5. The position of the interior point *k* relative to the constant boundary elements.

In the same maner, at any point, we can calculate the expresions for slope angles and shear forces. For BEM analysis based on discontinuous solutions we developed a computational program DISSOL using Matlab programming language and sources from specialized literature [15, 16], that allowed us to calculate the deflections and stresses in every point of the plate.

3. Results and Discussion

We propose to examine a plate of an arbitrary contour having one part of the contour simply supported and the another – clamped. Two loading cases are proposed: first – point force loading (Figure 6, a); second – uniform load distributed on a rectangular area (Figure 6, b).

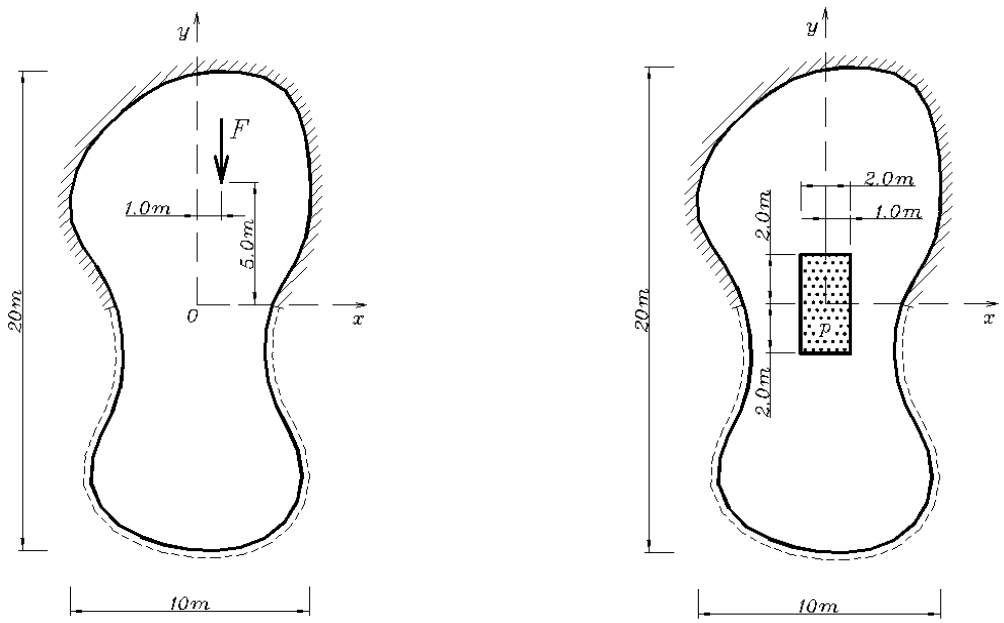

Figure 6. Plate of arbitrary contour loaded with: a) point force; b) area load.

For plates with an arbitrarily complicated contour, which cannot be described by a mathematical equation, analytical solutions cannot be found in the specialized literature. This type of problem can only be solved by numerical methods such as FEM [1, 2] or BEM [3, 4]. The most popular is FEM, but, as is well known, the accuracy of this method depends a lot on the

mesh density and the types of finite elements used (triangular, rectangular, trapezoidal, etc.). Another alternative would be the use of BEM based on discontinuous solutions, described in this paper and in other works [9, 10, 17].

In order to validate and demonstrate the efficiency of the proposed method, we will analyze a plate with an arbitrary contour by building BEM models (with the application of discontinuous solutions) and FEM models, and we will compare the results obtained by both numerical methods.

For BEM model we used the previously mentioned program (DISSOL) to calculate the deflections and stresses in every point of the plate. For this purpose, the contour of the plate was discretized into 50 constant boundary elements (Figure 7, a).

For FEM analysis we built 3 models: i) 165 elements and 182 nodes (Figure 7, b); ii) 321 elements and 320 nodes (Figure 7, c); iii) 641 elements and 663 nodes (Figure 7, d).

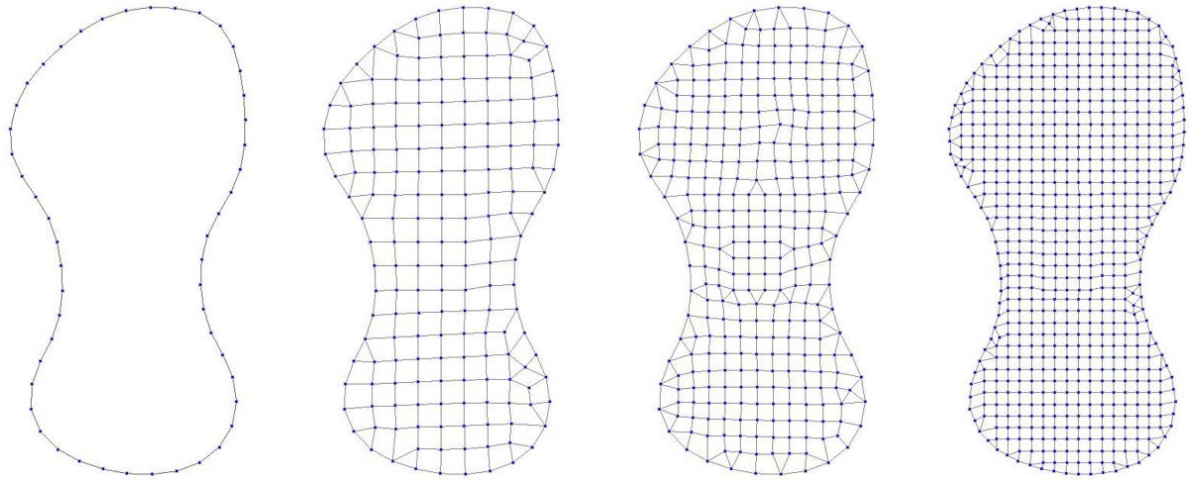

a) b) c) d)

Figure 7. Plate models: a) BEM – 50 elem.; b) FEM – 165 elem. (182 nodes); c) FEM – 321 elem. (320 nodes); d) FEM – 641 elem. (663 nodes).

Case 1. We obtained the deflection field due to a point force DISSOL (Figure 8, a) and also, using a FEM program (SCAD Office) for 3 models of mesh discretization (Figure 8, b, c, d).

The obtained results were introduced in the table below. It contains the maximal values of deflection and the deviations of the results in FEM models compared to BEM model.

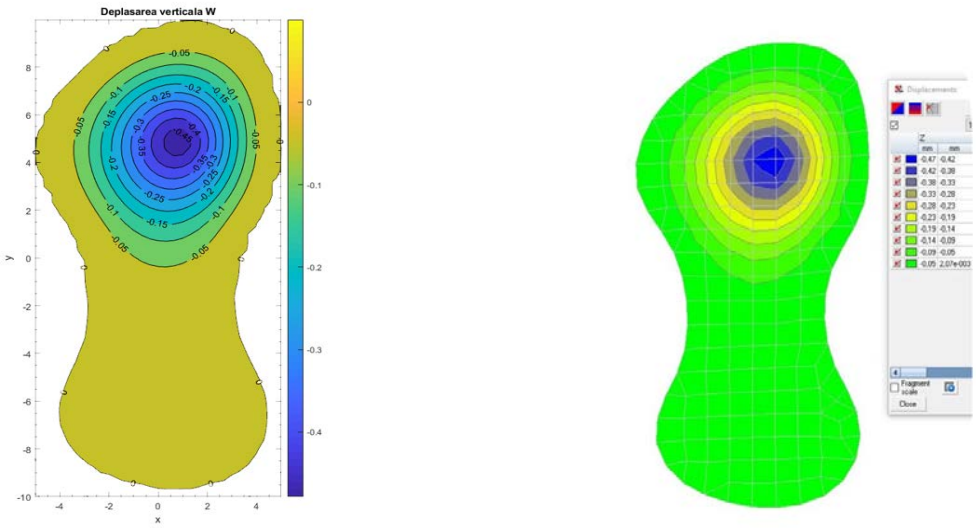

a) b)

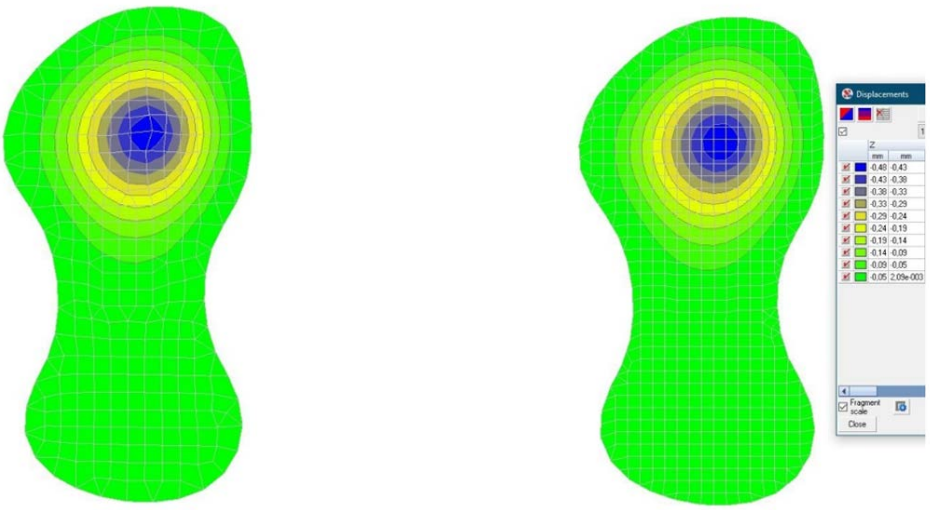

c) d)

Figure 8. Deflection field due to a point force: a) BEM – 50 elem.; b) FEM – 165 elem.; c) FEM – 321 elem.; d) FEM – 641 elem.

Table 1

The maximal deflection W_{max} due to a point force applied on a plate with arbitrary contour

Numerical method	Nr. of elements	Dimension of the global matrix	Max. deflection W_{max} [mm]	Deviations compared to BEM model [%]
BEM	50	100	0.4783	-
FEM (i)	165	840	0.4702	1.69
FEM (ii)	321	1668	0.4738	0.94
FEM (iii)	641	3476	0.4767	0.33

Case 2. We obtained the deflection field due to a uniform load distributed on a square area using the developed Matlab codes (Figure 9, a) and also, using a FEM program (SCAD Office) for 3 models of mesh discretization (Figure 9, b, c, d).

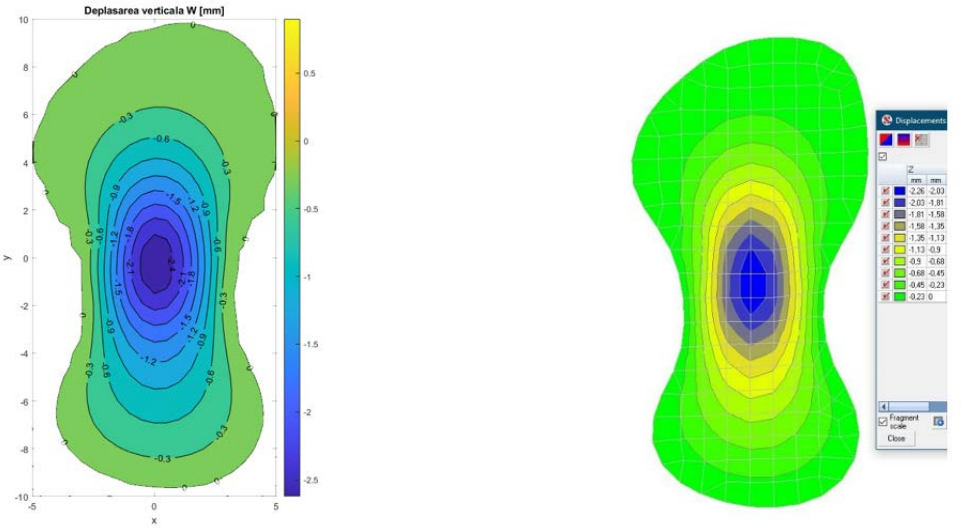

a) b)

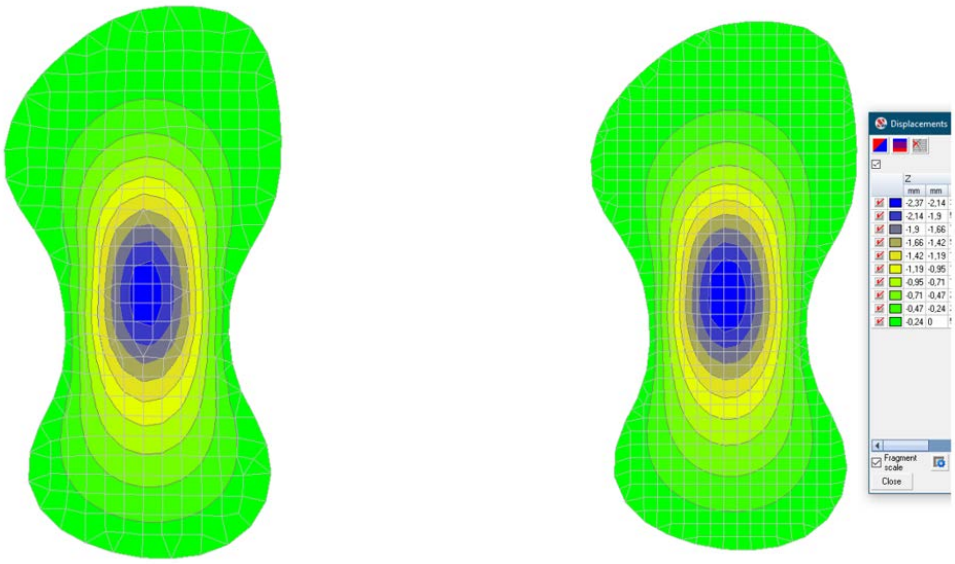

c) d)

Figure 9. Deflection field due to a uniform load distributed on a square area: a) BEM – 50 elem.; b) FEM – 165 elem.; c) FEM – 321 elem.; d) FEM – 641 elem.

The obtained results were introduced in the table below. It contains the maximal values of deflection and the deviations of the results in FEM models compared to BEM model.

Analyzing the obtained results illustrated in Figure 8 and Figure 9, we observe that for the FEM models with a relatively reduced number of elements, the deflection curves, especially in the areas of load action, show some polygonal shapes, and for the FEM models with denser mesh, the deflection curves become more regularized, acquiring more curvilinear shapes and the results approach those obtained in BEM models [18].

Table 2

The maximal deflection W_{max} due to a distributed load

Numerical method	Nr. of elements	Dimension of the global matrix	Max. deflection W_{max} [mm]	Deviations compared to BEM model [%]
BEM	50	100	2.520	-
FEM (i)	165	840	2.258	10.0
FEM (ii)	321	1668	2.300	8.70
FEM (iii)	641	3476	2.375	5.75

As we can observe in Table 2, for the second case of loading distributed on a rectangular area, to obtain an acceptable precision FEM models require solving a massive system of linear equations (3476 eq.), tens of times larger than BEM models (100 eq.). Also, in the discretization process of the curvilinear contour, the problem of geometry approximation appears, which involves the use of irregular elements (triangular, quadrilateral, etc.) for the mesh, that can affect the accuracy of the results in the neighboring elements. In BEM due to the fact that the solutions at the edge are described numerically, and in the interior – analytically, this influence has a local effect present only at the edge of the plate and does not spread in interior. The problem of approximating the curvilinear

contour can be improved using higher-order boundary elements (linear, quadratic, cubic etc.). We mention that in the BEM models presented in this paper, constant boundary elements of the lowest precision were used, which still provide results quite close to the analytical ones [17].

4. Conclusions

The Boundary Element Method based on discontinuous solutions, described in this paper, represents a new direction in the solid mechanic. These solutions were applied to the calculation of a plate with an arbitrary contour, different modes of support and loads. The obtained results were compared to FEM, demonstrating a good accuracy and applicability.

One of the main advantages of the BEM is that the discretization is applied only to the edge of the plate reducing the size of the system of linear equations by one unit and leading to a minimal use of computer resources. The numerical implementation of the proposed method offered us the possibility to develop Matlab codes for solving practical problems, which cannot be solved using analytical methods.

Acknowledgments: This paper is dedicated to the memory of Prof. Gheorghe Moraru, my first scientific coordinator for my doctoral thesis.
Special thanks to my wife Tatiana Galbinean who helped me translate and edit the text.

Conflicts of Interest: The authors declare no conflict of interest.

References

1. Moraru, G.A. *Introducere în metoda elementelor finite şi de frontieră*. UTM, Chisinau, 2002, 176 p.
2. Zienkiewicz, O.C. *The Finite Element Method in Engineering Science*. McGraw-Hill, London, UK, 1971, 521 p.
3. Brebbia, C.A.; Walker, S. *Boundary Element Techniques in Engineering*. Butterworths, London, UK, 1980, 220 p.
4. Katsikadelis, J.T. *Boundary Elements. Theory and Applications*. Elsevier, UK, 2002, 448 p.
5. Jaswon, M.A; Maiti, M. An integral equations formulation of plate bending problems. *J. Engng Math* 1968, 2, pp. 83-93.
6. Rizzo, F.J. An integral equation approach to boundary value problem of classical elastostatics. *Q. Appl. Math*. 1967, 25, pp. 83-95.
7. Ventsel, E. An indirect boundary element method for plate bending analysis. *Int. J. Numer. Meth. Engng*. 1997, 40, pp. 1597-1610.
8. Muskhelishvili, N.I. *Singular Integral Equations: Boundary Problems of Function Theory and Their Applications to Mathematical Physics*. Dover Publications, New York, SUA, 2011, 464 p.
9. Moraru, G.A. *Discontinuous solutions in the statics of deformable bodies*. Tehnica-Info, Chisinau, 2015, 398 p.
10. Moraru, G.A. BEM based on discontinuous solutions in the theory of Kirchhoff plates on an elastic foundation. *Eng. Anal. Bound. Elem*. 2006, 30, pp. 382-390.
11. Sheremet, V.D. *Handbook of Greens Functions and Matrices*. WIT Press, Southampton, UK, 2003, 304 p.
12. Melnikov, Y.A. *Influence Functions and Matrices*. Marcell Dekker, New York, SUA, 1998, 488 p.
13. Duffy, D.G. *Green's Functions with Applications*. 2nd Edition, Chapman & Hall/CRC, New York, SUA, 2015, 685 p.
14. Sneddon, I.N. *Fourier Transforms*. McGraw-Hill Book Co, New York, SUA, 1951, 560 p.
15. Beer, C.; Smith, I.; Duenser, C. *The Boundary Element Method with Programming for Engineers and Scientists*. Springer, Viena, Austria, 2010, 512 p.
16. Pozrikidis, C.A. *Practical Guide to Boundary Element Methods with the Software Library BEMLIB*. CRC Press, Boca Raton, SUA, 2002, 440 p.
17. Galbinean, S.G. Soluţii discontinue pentru calculul plăcilor în teoria clasică. *Akademos* 2018, 1, pp. 31-35.
18. Galbinean, S.G. Calculation errors of the plates using finte element method. *Meridian Ingineresc* 2013, 2, pp. 64-66.

Citation: Galbinean, S. Application of discontinuous solutions in boundary element method for the bending problems of Kirchhoff plates with an arbitrary contour. *Journal of Engineering Science* 2023, 30 (2), pp. 23-33. https://doi.org/10.52326/jes.utm.2023.30(2).02.

Submission of manuscripts: jes@meridian.utm.md

Journal of Engineering Science *Vol. XXX, no. 2 (2023), pp. 34 - 46*
Fascicle *Industrial Engineering* *ISSN 2587-3474*
Topic *Applied Engineering Sciences and Management* *eISSN 2587-3482*

https://doi.org/10.52326/jes.utm.2023.30(2).03
UDC 624.21:69.059(498)

TECHNIQUES FOR SPECIAL FOLLOWING OF THE DEGRADATIONS DEVELOPMENT FOR A RAILWAY PASSAGE

Gheorghiță Boacă*, ORCID: 0000-0002-0938-1503,
Maria-Cristina Scutaru, ORCID: 0000-0002-7077-340X,
Cristian-Claudiu Comisu, ORCID: 0000-0001-5446-7229,
Răzvan-Gelu Gimiga, ORCID: 0000-0002-6798-1793

Gheorghe Asachi Technical University of Iasi-Romania, 1 Mangeron Blvd., 700050, Iasi, Romania
*Corresponding author: Gheorghiță Boacă, *gheorghita.boaca@academic.tuiasi.ro*

Received: 04. 02. 2023
Accepted: 05. 13. 2023

Abstract. Nowadays, most of the transportation infrastructure is already built, the main challenge being the maintenance of these structures in optimal conditions of safety and comfort for users. Therefore, in recent years, research in the field of bridge maintenance has focused on the development and implementation of special monitoring programs that can identify and warn transportation infrastructure managers of the appearance and development of degradation, and especially the possibility of collapse of the construction element in the near future. In addition to familiarizing readers with the structural design of the Constanta Bridge, this work proposes the presentation of the main technologies used for implementing the in-service behavior monitoring program, along with the arrangement of data acquisition units and a brief interpretation of the information provided by the monitoring system. In the conclusions of the article, the authors will draw attention to the bearing capacity of the structure, affected by the development of degradation processes and the need for emergency implementation of rehabilitation and strengthening works of the passage.

Keywords: *bridges, monitoring, rehabilitation, structural analysis, structural health monitoring.*

Rezumat. În zilele noastre, cea mai mare parte a infrastructurii de transport este deja construită, provocarea principală fiind reprezentată de menținerea acestor structuri în condiții optime de siguranță și confort a utilizatorilor. De aceea, în ultimii ani, cercetările în domeniul întreținerii structurilor de poduri s-au canalizat pe dezvoltarea și implementarea unor programe de urmărire specială, ce reușesc să identifice și să atenționeze administratorii infrastructurii de transport de apariția și dezvoltarea degradărilor, și, mai ales, de posibilitatea cedări elementului de construcție în viitorul apropiat. Prezenta lucrare își propune, pe lângă familiarizarea cititorilor cu structura constructivă a Podului Constanței, prezentarea principalelor tehnologii utilizate pentru implementarea programului de urmărire a comportării în exploatare, alături de modul de dispunere a unităților de captare a datelor și de o scurtă interpretare a informațiilor oferite de sistemul de monitorizare. În concluziile articolului, autorii vor trage un semnal de alarmă privitor la capacitatea portantă a structurii,

influențată de dezvoltarea proceselor de degradare și a necesității implementării în regim de urgență a lucrărilor de reabilitare și consolidare a pasajului.

Cuvinte cheie: *poduri, monitorizare, reabilitare, analiză structurală, monitorizarea stării tehnice.*

1. Introduction

With time, constructions show various degradation due to environmental conditions and exploitation, primarily degradation of the materials used in the structure. Today, one of the biggest challenges for administrators is maintaining existing infrastructure [1, 2]. Thus, administrators and designers seek the best solutions for performing maintenance and repair work on bridges and overpasses on time [3, 4]. The solutions must also not be too costly, given the limited budget. For bridges that have been open for a long time, or whose age is approaching its maximum service life, or for those structures of particular importance for traffic flow, special monitoring programs have been recommended in recent years [5]. These aim to monitor the in-service behavior of structures, track the evolution of degradation, and alert the responsible staff in case of exceeding alarm thresholds, along with emergency remediation measures. Therefore, the Romanian National Railways Company (CFR S.A) has decided to implement a special monitoring program for the overpass on line 800, at km 6+645, which provides a crossing over the railway line, in Bucharest. The overpass was built in 1938, providing continuity of a highly important railway line, the CF 800 Bucharest Nord-Constanta, in the heart of the capital, over a major traffic artery, Calea Griviței. It carries traffic from two major national roads, DN 1A Bucharest-Ploiesti and DN 7 Bucharest-Pitesti, providing access to the city center. In 2014, after identifying potentially dangerous degradation during daily inspections, the administrator contracted a technical expertise. Its conclusions revealed a series of degradation affecting the structure, recommending the implementation of a long-term monitoring program.

The article aims to present the main technologies used for the implementation of the behavior monitoring program for the developed Constanța Bridge, along with the arrangement of data acquisition units. The main purpose of the article is to provide a solid starting point for future bridge and overpass monitoring projects, with the hope of increasing the use of this practice in the country's management system.

This work is part of a comprehensive research program in the field of development and implementation of modern bridge monitoring systems at a national level. The program is developed by the Faculty of Construction and Installations at the Technical University "Gheorghe Asachi" in Iași.

2. The Constanța Bridge presentation

Although the structure that is the subject of this study is known as the Constanța Bridge, it is actually a passageway that provides continuity for the Bucharest-Constanța railway 800 line, over one of the most important road arteries in Bucharest, namely Calea Griviței. Due to its location in the middle of a curve, the passageway's length is 28.70 m, a measurement taken along the left side of the railway line's parapet. If we measure the distance between the joints located approximately in the middle of the longitudinal support walls' coronations, the result is a significantly shorter length of 18.35 m.

If we analyze the passageway from the perspective of its distance between the infrastructures, the result is a distance between the vertical faces of the two portals of 17.89 - 17.93 m (Figure 1). This light is divided symmetrically in relation to the pier located in the central section of the passageway.

Figure 1. The Constanța Bridge.

Figure 2. The railway line

In order to ensure maximum railway transport capacity and due to the high importance of the served line, the passageway was built with a total width measured between the parapets, at the joint level on portal C1, of 32.42 m, a width that corresponds to the service of 5 railway tracks (Figure 2).

In terms of building material, the passageway is made of reinforced concrete. An interesting feature is that the superstructure is composed of two asymmetric structures next to each other (Figure 3). This composition can demonstrate the importance given to this structure, highlighting the need to increase the capacity of circulation, with industrial development and the significant increase in railway traffic on the Bucharest-Constanța direction.

Analyzing the structure in cross-section, we notice the presence of 20 main girders (Figure 3) connected by means of a reinforced concrete slab placed at the level of the upper flanges of the beams. Due to the specificity of the communication path, the slab supports the 5 railway lines through a reinforced concrete trough.

Figure 3. The superstructure.

Each structure is composed of 9 main beams, located in the railway lines area. In the center of the viaduct there are 2 adjacent beams, separated by a longitudinal groove. The main beams have a width of 50 cm and a height of 1.20 m, dimensions that were measured between the intrados plane and the lower flange of the beams.

All 10 beams of each structure rest directly on the three piers, being connected at the support level and in the central section through the cross-girders. These have an average width of 30 cm, maintaining the same height as the beams.

The infrastructures of the viaduct, consisting of two abutments and one pier (Figure 1), are founded directly. According to the existing documentation in the Technical Construction Book, the foundation base has a width of 5.50 m and a thickness of 1.50 m.

The abutments are massive, built of concrete, their elevation is plastered, with coping, at the base there is a plastered plinth.

The pier of the viaduct (Figure 4) has a length of approximately 34.00 m, measured at the level of the plinth. The elevation of the pier is composed of 20 columns built of reinforced concrete. In the central area of the pier, there are 8 columns for each superstructure, with a polygonal section, similar to that of a circle with a diameter of 50 cm. The columns in the end areas have an oval section, with dimensions of 50×100 cm, developed along the pier.

As it is a viaduct, it is also important to mention the configuration of the crossed communication path. Thus, the clearance between the abutments' elevations is 17.89-17.93 m, it includes 2 sidewalks with a width of approximately 1.00 m each and 2 areas for road and tram traffic with a width of 7.78 m each, separated from the pier elevation by a 0.70 m wide area.

Figure 4. The Constanța Bridge pier before rehabilitation works.

Figure 5. Traffic jam at the entrance of passage.

3. Reasons for the special following of the degradations

In February 2014, the facility administrator conducted a routine inspection on the site, identifying a series of deteriorations whose arrangement and extent could have endangered the safety of both railway, on the railway 800 line, and road traffic, on Griviței Road.

The first step in launching the rehabilitation works was the contracting of a specialized Technical Expertise, which identified and thoroughly described the deterioration state of the structure in August of the same year.

According to the Expertise, although the conclusions were that the structure was in good technical condition, the passage presented a series of degradations and deteriorations whose extent could lead to the imposition of traffic restrictions and even endanger the safety of users.

Some of the largest problems identified were:

-The road traffic is very heavy (Figure 5), this being due to the clear passage height under the bridge, and the passage lighting is only designed for 2 lanes of road traffic in each direction and 2 tram lines. On the passage area, Griviței Road has undergone a series of expansions over time, currently having 3 lanes of traffic in each direction and 2 tram lines.

- The tram traffic (Figure 6) through the passage generates strong vibrations in the immediate vicinity of the pile, which has led to multiple deteriorations, including the safety structure of the passage.

Figure 6. The tram traffic in the passage.

Figure 7. The marginal girder.

The following degradations were identified at the superstructure level:

-The marginal beams have numerous signs of impact due to the violation of the safety height (Figure 7).

-Due to advanced age and repeated impacts, the reinforcement at the bottom fiber of the girder is exposed, rusty, some of the reinforcing bars are even broken, which leads to a pronounced decrease in the carrying capacity of the girder and, implicitly, the entire structure.

Figure 8. Degradations of the pillar support [6].

The infrastructure was also found to have significant degradation issues, including:

-The pillar supports show severe degradation of the concrete cover layer, with reduction in section, complete corrosion of reinforcing steel, cracks oriented along the elements, and friable concrete (Figure 8).

-The elevations of the piers and abutments are severely degraded, with extensive areas of fallen plaster, segregated concrete, voids, and exposed reinforcement.

The civil society has raised concerns about the structure through articles in local and central press, presenting the situation in an exaggerated manner (Figure 9). This has led to expedited procedures for rehabilitation works and a special monitoring process was instituted to keep track of the real-time appearance of the danger of collapse and the progression of the degradation.

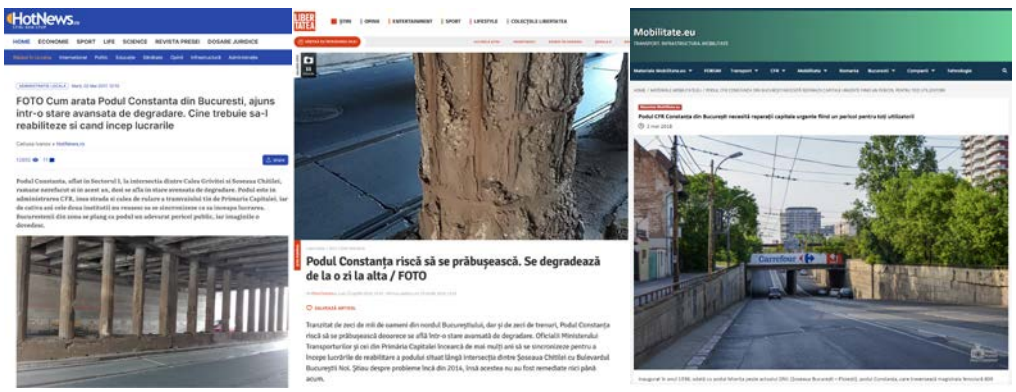

Figure 9. The impact of the mass-media [7-9].

4. Behavior tracking technologies in operation

The behavior monitoring of the bridge during operation was carried out on the piles and girders. The following activities were undertaken:

- periodic visual inspections;
- installation of markers at the level of cracks in piles, girders and abutments;
- installation of a video system with cameras at the level of each ramp, with the purpose of monitoring railway and road traffic;
- determination of the position of the reinforcement, the distances between bars and the concrete coverage;
- determination of the concrete resistance of the main structural elements;
- determination of the corrosion of the reinforcement;
- installation of sensors at the level of piles and abutments for identification of the structure's vibration modes in static and dynamic regime.

Due to the specificity of the structure and the identified degradation, the team of specialists responsible for designing the behavior monitoring system decided to install multiple types of technology, targeting the following aspects:

- video monitoring of railway traffic and how the structure reacts to different loads;
- monitoring the evolution of cracks;
- establishment of the reinforcement scheme, this aspect becoming important after the finding of the small volume of information available from the construction of the bridge;
- determination of concrete strength;
- recording of deformations through modern systems that use precision fiber optics.

4.1. Monitoring the evolution of cracks in the bridge's structural resistance

This stage will focus on carrying out a crack survey. This survey was used as input data for the analysis of crack opening, position, and length, and also indicating their evolution over time.

The survey methods were purely visual, with the infrastructure, superstructure, and access ramps area being analyzed up close. Additionally, in this stage, glass markers were installed (Figure 10), readings being taken at least once a week.

Figure 10. Glass marker for monitoring crack evolution.

4.2. Video surveillance of the structure

The purpose of this technology is to monitor the real-time flow of traffic through the bridge and on the railway. Video cameras were mounted on each access ramp. The captured data was transmitted in real-time to a control center.

In addition to the continuous monitoring of the structure, another advantage of this technology is the minimization of response times by competent authorities to any incidents or accidents that occur in the area, as the system instantly alerts of their occurrence.

4.3. The position determination of the reinforcement, the distance between bars, and the concrete cover for the reinforcement

In areas of the passage with major degradation and pronounced cracks in the structural integrity, non-destructive tests have been carried out. These aimed to locate the

reinforcement, determine the position, the diameters of the bars used in the construction of the targeted element, and measure the remaining concrete cover layer after degradation occurred.

The non-destructive testing was performed using a Profomet 5+ model Scan Log5+ (Figure 11), consisting of a display unit, scanner, and universal probe.

Figure 11. ScanLog 5+ profometer [10].

Figure 12. Digi Schmidt hardness tester [11].

The measurement was performed by positioning the probe parallel to the direction of the targeted reinforcement. In this way, 3 successive passes were made over each set area. The displayed data includes the diameter of the reinforcement, the concrete cover of each bar, and the distance between it and the point of origin of the measurement.

4.4. Determination of the compressive concrete strength

Another important parameter for the viability of the structure is the value of the compressive strength of the concrete in the main load-bearing elements. This parameter has undergone various changes over the period of operation, mainly due to environmental and usage factors of the structure.

The test targeted the concrete in the bridge piles, main beams, and columns. Given the specificity of the targeted monitoring, the tests performed were non-destructive. The determination was made using a Digi Schmidt (Figure 12) hardness tester.

The device consists of the hardness tester itself and a display and data storage unit. The measuring technology is based on recording the rebound distance. With the help of internal conversion curves, the device converts the rebound value into the compressive strength of the concrete and displays its f_{ck}value.

4.5. Determination of the reinforcing steel corrosion

Corrosion is the chemical process that occurs at the surface of reinforcing steel and results in a substantial reduction of the affected steel bars' cross-section. This phenomenon is especially common in construction elements where the minimum concrete coverage of reinforcing bars was not respected during construction, where the concrete has a high degree of porosity, or where the element has cracks with openings exceeding 0.3 mm.

Thus, in the site, areas with rust stains were identified, the main sign given by the structure of corrosion occurrence.

The determination was non-destructive, using the CANIN+ (Figure 13) system for measuring the potential electromagnetic fields of affected concrete elements. The system determines changes in potential grades per unit length, drawing attention to different affected areas.

Unidentified and unmitigated, the corrosion process can ultimately lead to structural failure.

Figure 13. CANIN+ measurement system [12].

4.6. Structural Deformation Monitoring

During the design of the entire structural monitoring system, the issue of using high-precision topographical methods was raised. After analyzing the possibility, it was concluded that due to the high rigidity of the elements and their small dimensions, these systems would not be capable of providing the necessary information regarding the time behavior of the passage under traffic.

Thus, the specialist staff sought other solutions, focusing their attention on interferometric fiber optic sensors installed on the piles.

The system consisted of 12 sensors each mounted on a pile column and 6 sensors mounted at the level of the main girders (Figure 14). The length of each sensor was a minimum of 2 meters for each column and a minimum of 5 meters for those mounted at the girder level.

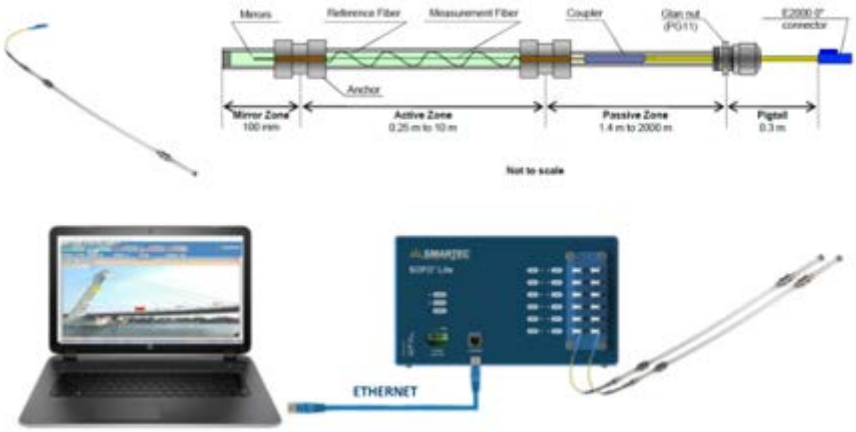

Figure 14. Fiber Optic Sensor-Based Monitoring System [13-15].

Also, for increased data accuracy, 4 triaxial accelerometers were installed. They monitored the vibration mode of the piles, especially in dynamic regime, under the useful loads. The accelerometers were triaxial with a data capture range of +/-4 G, sensitivity of 1μG, and operating frequency of 0 + 500 Hz.

5. Data capture units arrangement

During the design of the monitoring works, the exact installation points of all the data capture units were selected (Figure 15), regardless of their specificities. By closely analysing, the degradation state of the structure and its evolution over time, it was determined that data should be recorded from the main load-bearing elements with the highest depreciation in the technical state evaluation, namely the main beams and pier piles.

For crack monitoring, glass indicators were installed as follows:

- At the location of cracks affecting the pier piles (Figure 10), to highlight the stress state and crack evolution over time, determining if the crack is active or passive. For better data accuracy, at least 50% of cracks will be monitored.
- In the case of cracks affecting the main beams, due to their importance, all cracks will be monitored, following their evolution under traffic, regardless of the cause of appearance and position (cracks in the bearing area due to shear force or cracks in the central area due to bending moment).

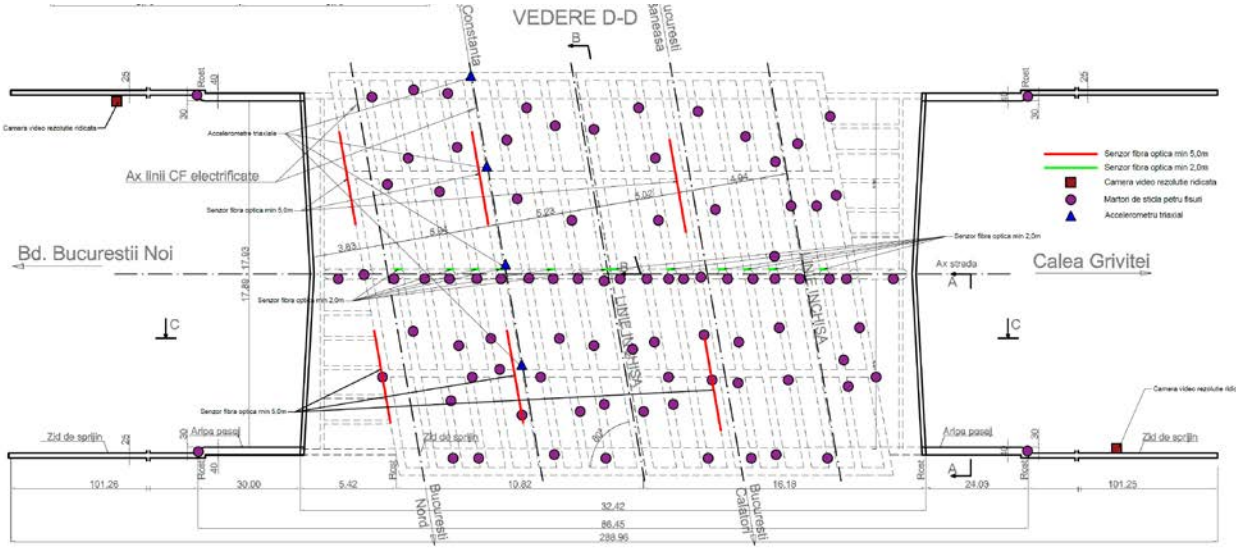

Figure 15. Position of the principal monitoring sensors.

To monitor how the structure reacts as a whole, in terms of temperature variation and horizontal forces from rail traffic, two indicators will be installed at each joint level between the elevation of the arches and the wings of the bridge and between the wings and the retaining walls.

The necessary video cameras for monitoring the traffic served by the structure, both road and rail, will be installed on each ramp. The cameras have opposing directions, thus ensuring high clarity of the recorded data.

The ScanLog5+ level was used for all piles (Figure 16), one of the columns, and a beam, easily analysing the structure's reinforcement, degree of degradation, and concrete coverage. The determination took place during a site visit on 12/19/2018, targeting the structure's characteristic areas.

Figure 16. Data capture for structural reinforcement.

The concrete compressive strength was determined for all piles, 2 main girders, column elevations (Figure 17) and bridge wings. This determination becomes a key factor in decision-making regarding the rehabilitation work to be performed, as concrete is one of the most important building materials and the available strength determines the chosen rehabilitation solution and type of materials to be used.

Figure 17. Determination of the compressive strength of concrete in pile columns.

Figure 18. Installation of optical fiber at the pile column.

As previously noted in the previous chapter, to ensure a high level of quality in rehabilitation work, corrosion of the reinforcement must be identified and eliminated. The testing was performed using the CANIN+ system during the same site visit. The targeted areas were the pile column pilings and the most severely degraded girder.

To monitor the evolution of structure deformations over time, the 4 triaxial accelerometers were mounted on main beam no. 6, positioned as follows:

- 2 accelerometers were placed in the center of the opening;
- 1 accelerometer was placed at the pile level;
- 1 accelerometer was placed at the column level.

Optical fiber was installed at each pile column (Figure 18). The main goal was to record the structure's behavior under traffic.

6. Data recorded during the monitoring of behavior in operation

With the installation of the entire operation behavior monitoring system for the Constanta overpass in Bucharest, a comprehensive monitoring process was launched. It lasted throughout the first half of 2019, with the behavior in operation of the structure being highlighted from the first days of monitoring.

The monitoring system for the vibration evolution of the bridge under traffic loads has revealed serious resistance problems of the bridge. The vibration modes varied from the expected and calculated ones during the design phase of the system.

The main causes of structural vibrations were the trams and trolleybuses passing through the bridge. These generated the largest dynamic loads that propagated to all structural elements, as seen in Figure 19.

Additionally, the monitoring system was able to capture the structure's reaction to an earthquake recorded on January 31st, 2019. As such, the evolution of vibration mode graphs (Figure 20) shows a significant jump. At the same time, the monitoring system alerted the monitoring team about the situation.

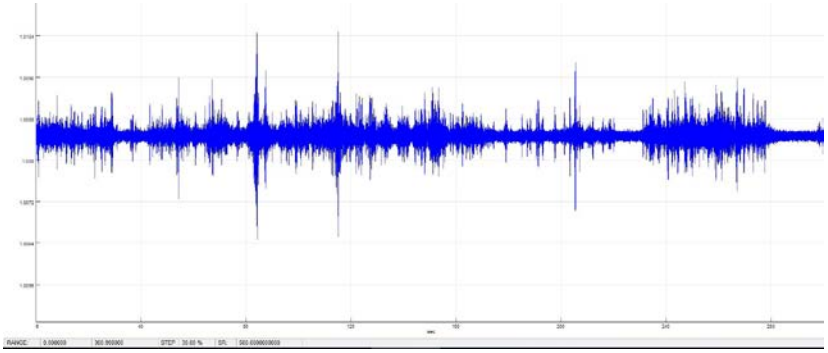

Figure 19. Evolution of structural vibrations.

After analysing the cause of the jump, the monitoring team was unable to find any structural explanation, learning from the media that the earthquake occurred in the Vrancea area and the waves propagated towards Bucharest. Thus, the effectiveness of the concept in alerting the occurrence of situations with a high potential risk for users was demonstrated.

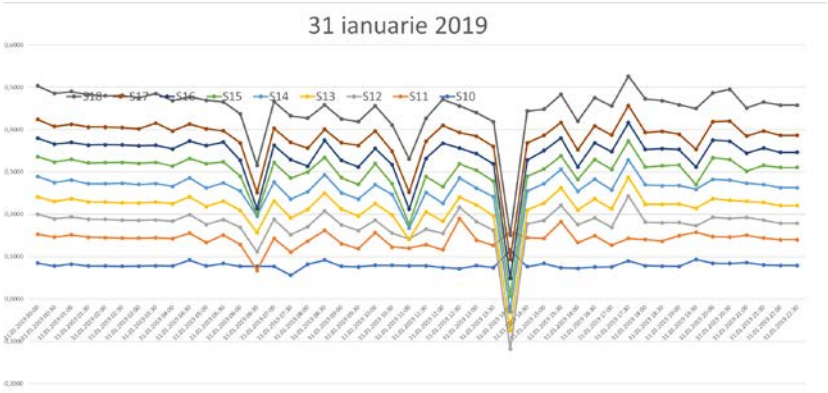

Figure 20. Recording of the earthquake on 01.31.2019.

Regarding the monitoring of crack evolution, as shown in Figure 21, it was identified a significant settling at both piers, on the side towards Calea Griviței, highlighted by the opening of cracks on the right side of the piers and their ascending evolution. The settling occurred immediately after the earthquake on 01.31.2019.

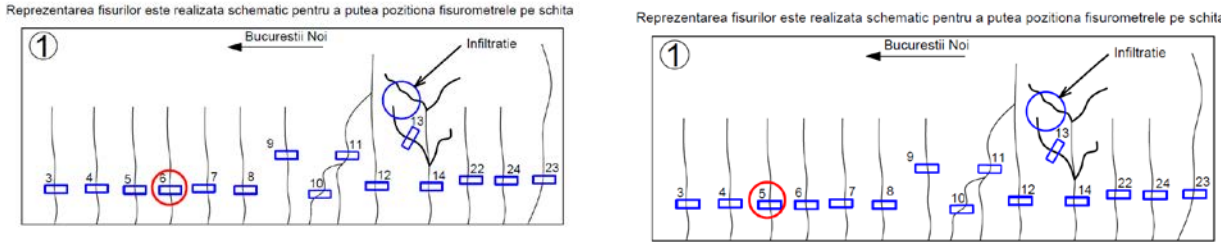

Figure 21. Evolution of cracks.

7. Conclusions

The purpose of this article is to familiarize readers with the tracking technologies of the behavior during operation used in the Constanta Passage in Bucharest. This article can be a solid starting point for future bridge and overpass tracking projects.

Following a thorough analysis of the recorded data, the following conclusions can be drawn regarding the targeted structure:

1. After a service life of over 80 years, despite no repair, reinforcement, or rehabilitation works, the carrying capacity of the entire structure is visibly reduced but does not exceed the limit threshold imposed by standards for user safety, thus not posing a threat to the structural integrity of the bridge.

2. The analysis of the cracking state of the structure shows the presence of degradation processes in advanced stages of development, which significantly contribute to the reduction of the overall resistance and stability of the bridge.

3. The current state of degradation, at time T=0, does not immediately and directly threaten the local resistance and stability of the pier piles or the bridge as a whole structure of resistance.

4. The identified state of degradation at the level of the pylon elevation columns does not immediately and directly endanger the local resistance and stability of the pylon.

5. Graphs of variation will be prepared, at times T=1...T=n, in which the evolution of degradation processes (cracking state, static and dynamic behavior of the bridge structure) will be analyzed. Based on the analysis of the time variation of the general degradation state of the structural resistance, after at least 3-4 measurement stages, conclusions can be drawn and conclusions regarding the viability of the structure can be issued with certainty.

6. In case of a strong earthquake, the widespread cracking at the level of the resistance structure will be the main source that can severely affect the functionality of the bridge, which will not collapse, but in this case, the immediate closure of railway, road and pedestrian traffic in the bridge will be required to avoid serious accidents.

7. It is recommended to carry out the consolidation and rehabilitation works of the bridge as soon as possible to avoid severe degradation of the structure in case of a strong earthquake that would force the closure of the bridge's circulation.

This work is part of a complex research program developed by the Faculty of Construction and Utilities at the "Gheorghe Asachi" Technical University in Iasi. The research focuses on the study of bridge maintenance methods, the development of modern systems for monitoring their behavior in use, and the adaptation and application of these systems to bridges in our country.

Conflicts of Interest: The authors declare no conflict of interest.

References

1. Comisu, C.C.; Țăranu, N.; Boacă, G.; Scutaru, M.C. Structural health monitoring system of bridges. *Procedia Engineering* 2017, 199, pp. 2054-2059.
2. Scutaru, M.C.; Țăranu, N.; Comisu, C.C.; Chingălată, C. Development of bridge structural health monitoring. *Bult. Inst. Polit. Iasi* 2017, 63 (67), pp. 105-120.
3. Gimiga, G.R.; Iriciuc, S.C. Workability of storable asphalt mixtures, measuring devices. *Bult. Inst. Polit. Iasi* 2012, 58 (63), pp. 175-180.
4. Scutaru, M.C.; Țăranu, N.; Comisu, C.C.; Boacă, G.; Ungureanu D.; Hudișteanu I. Numerical study of the dynamic characteristics of a hybrid steel-concrete bridge. In: *IOP Conf. Series: Materials Science and Engineering*, 2019, 591, 012030.
5. Simeng, L.; Liangliang, Z.; Zengshun, C.; Jianting, Z.; Chao, Z. Mode-Specific Demage Identification Method for Reinforced Concrete Beam: Concert, Theory and Experiments. *Construction and Building Materials* 2016, 124, pp. 1090-1099.
6. Digi24.ro Available online: https://www.digi24.ro/stiri/economie/transporturi/podul-constanta-folosit-de-o-treime-dintre-bucuresteni-in-pericol-sa-se-prabuseasca-917901 (accessed on 17.04.2023).
7. Hotnews.ro Available online: https://www.hotnews.ro/stiri-administratie_locala-21743753-foto-cum-arata-podul-constanta-din-bucuresti-ajuns-intr-stare-avansata-degradare-cine-trebuie-reabiliteze-cand-incep-lucrarile.html (accessed on 12.04.2023).

8. Libertatea.ro Available online: https://www.libertatea.ro/stiri/podul-constanta-risca-sa-se-prabuseasca-2226763 (accessed on 12.04.2023).
9. Mobilitate.ro Available online: https://mobilitate.eu/podul-cfr-constanta-bucuresti/ (accessed on 12.04.2023).
10. Manualslib.com Available online: https://www.manualslib.com/manual/1393068/Proceq-Profometer-5Plus.html (accessed on 12.04.2023).
11. Indiamart.com Available online: https://www.indiamart.com/proddetail/digi-schmidt-test-hammer-2799448833.html (accessed on 12.04.2023).
12. Urbipedia.org Available online: https://www.urbipedia.org/hoja/Corros%C3%ADmetro (accessed on 17.04.2023).
13. Technovolt.ro Available online: http://www.technovolt.ro/senzori-de-deformare-sofo (accessed on 12.04.2023).
14. Waterpowermagazin.com Available online: https://www.waterpowermagazine.com/features/featuredam-monitoring-with-fibre-optics-4264695/ (accessed on 12.04.2023).
15. Telemac.fr Available online: https://telemac.fr/en/product/sofo-lite-reading-unit/attachment/sofolite-scheme_medium/ (accessed on 12.04.2023).

Citation: Boacă, Gh.; Scutaru, M.-C.; Comisu, C.-C.; Gimiga, R.-G. Techniques for special following of the degradations development for a railway passage. *Journal of Engineering Science* 2023, 30 (2), pp. 34-46. https://doi.org/10.52326/jes.utm.2023.30(2).03.

Submission of manuscripts: jes@meridian.utm.md

Journal of Engineering Science *Vol. XXX, no. 2 (2023), pp. 47 - 58*
Fascicle *Industrial Engineering* *ISSN 2587-3474*
Topic *Applied Engineering Sciences and Management* *eISSN 2587-3482*

https://doi.org/10.52326/jes.utm.2023.30(2).04
UDC 662.753:621.43

PROCESSES OF CHANGING THE PHYSICO-CHEMICAL PROPERTIES OF AUTOMOBILE MOTOR OILS DURING OPERATION

Olivian Pădure*, ORCID: 0000-0002-6024-3763,
Iurie Tezec, ORCID: 0009-0005-9788-1899,
Victor Ceban, ORCID: 0000-0002-2013-5055,
Vasile Plămădeală, ORCID: 0000-0003-1722-2649,
Alexandru Buga, ORCID: 0000-0002-4342-0502

Technical University of Moldova, 168 Stefan cel Mare Blvd., Chisinau, Republic of Moldova
Corresponding author: Olivian Pădure, *olivian.padure@tran.utm.md*

Received: 03. 25. 2023
Accepted: 04. 19. 2023

Abstract. Mathematical modeling of the operation processes of automotive engine oils allows to optimize the time of their use during operation. A certain significance for changing the qualitative properties of motor oils is introduced by such an operational indicator as „waste" oil consumption. The article describes the causes and parameters of engine oil consumption, as well as the mathematical model of changes in the physico-chemical properties of engine oil during operation. The one that will allow us to optimize the periodicity of replacing the engine oil, as a result this fact will allow us to increase the distance between the interventions of the corrective maintenance works of the means of transport.

Keywords: *internal combustion engine, cylinder-piston group, cylinder head, fuel and lubricants, automotive engine oils, technical operation of the car, engine lubrication system, consumption of engine oil for waste, refilling („refreshing") engine oil.*

Rezumat. Modelarea matematică a proceselor de funcționare a uleiurilor de motor pentru automobile permite optimizarea timpului de utilizare a acestora în procesul exploatării. O anumită semnificație asupra proceselor de modificare a proprietăților calitative ale uleiurilor de motor este introdusă de un astfel de indicator de explaotare, precum consumul de ulei la „ardere". În articol sunt descrise cauzele și parametrii de consum a uleiului de motor, precum și modelul matematic de modificare a proprietăților fizico-chimice ale uleiului de motor în timpul exploatării.

Cuvinte cheie: *motor cu ardere internă, grupul cilindru-piston, chiulasă, combustibil și lubrifianți, uleiuri de motor pentru automobile, exploatarea tehnică a automobilului, instalația de ungere a motorului; consumul uleiului de motor la ardere; umplerea („împrospătarea") cu ulei de motor.*

1. Introduction

Currently, the main source of obtaining motor oils is crude oil, which is a liquid with a complex chemical composition. It contains 84...87% carbon, 12...14% hydrogen, the rest, 1...5% sulfur, 1...3% oxygen, 0...1% nitrogen [1].

The physico-chemical properties of engine oils largely depend on the type of base oil (petroleum or synthetic elements), the technology used in manufacturing, as well as the type and nature of the additives introduced into the base oil. The oils used in the lubrication systems of thermal engines work in extremely difficult conditions and have a complex composition. All engine oils contain two components (Figure 1) [2]. The main component is the base oil, which represents 80...85% of the final product and the additive package, which constitutes up to 15...20% respectively [1, 3].

Mineral base oils are the purified form of crude oil and have been used as a base for obtaining automotive lubricants since the beginning of their production, and synthetic base oils are chemical products obtained in the laboratory with the specific purpose of lubrication. Synthetic oils are obtained from pure compounds that do not contain contaminating agents.

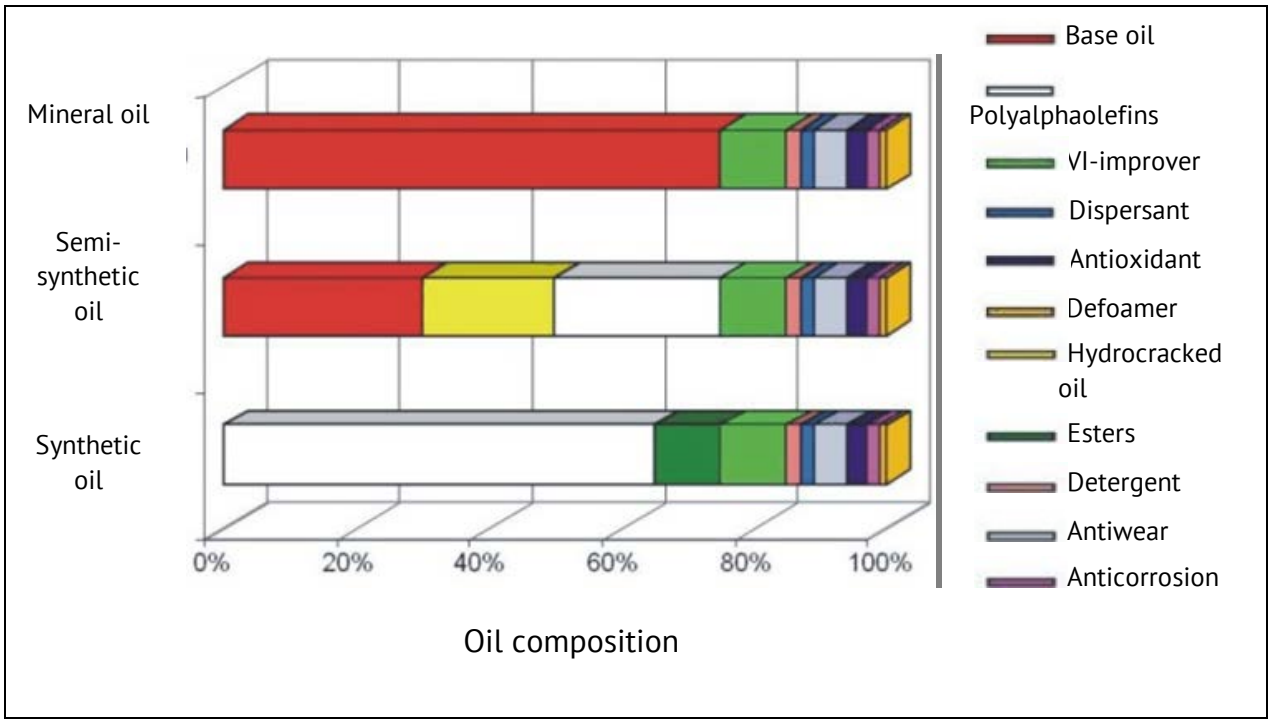

Figure 1. The composition of motor oils [2].

Additives are chemical substances (organic compounds, based on metals or polymers), which, by combining with the base oil, have the role of improving certain characteristics of the oils used in the lubrication systems of thermal engines[4].

Depending on the origin of the base, the oils can be: vegetable, mineral, synthetic and semi-synthetic. Vegetable oils were widely used in technology, starting from the Bronze Age until the 60s of the 20th century. Mineral oils are obtained from crude oil by different methods. Synthetic oils are organic compounds or organic elements, obtained from different types of raw material – crude oil, coal, gas, esters etc. Dozens of types of synthetic oils are known, of which the most widespread are synthetic hydrocarbons (polyalphaolefins, olefin oligomers), dialkylbenzenes (alkylated aromatics, alkylbenzenes), neopentyls (polyol esters), diesters, polyalkylene glycols (polyglycols, polyesters), fluorocarbons, organophosphorus (esters of phosphoric acid), silicones (siloxanes, polysiloxanes, polyorganosiloxanes) [1].

Mineral oils are themselves natural oils mixed with additives. Base oil is a refined oil. Semi-synthetic oils are based on refined oil, but it is an oil that has gone through a hydrogenated refining process. After this process, the oil is obtained, which has the qualities of a synthetic oil.

Synthetic oils represent oils obtained in laboratories from synthesized base oils. Due to the stable and well-calculated molecular structure, it presents a higher quality. It presents an advance over natural oils, because they are designed from the beginning for lubrication, so the manufacturer can focus better on the finished product than on natural oil products.

2. Working conditions and functions of engine oils

Permanent engine oils are subject to quite high thermal and mechanical loads due to the multiple couplings, which have different lubrication conditions. For example, the pressure in the oil film between the surface of the cylinder and the working surface of the segment varies sharply within the limits of 0.15...0.30 MPa, in the area of the compression segment and within the limits of 0.5...1.3 MPa, in the lubrication segment area, and the piston speed varies from 0 to about 15 m/s. In some circumstances the pressure in the oil film can reach the value of 2.0 MPa. The temperature of the lubricant film varies within the limits of 270...280 ^{o}C, in the channel of the upper compression segment, and during supercharging this temperature can reach 300...350 ^{o}C. If the „cylinder-piston segment" coupling is worn, gas leaks are greater and, then, the temperature can reach 450 ^{o}C for SIE (spark ignition engines) and 500...700 ^{o}C for CIE (compression ignition engines). Crank shaft spindles and bearings work under heavy conditions at oil film temperatures of 150...160 ^{o}C and very high specific pressures. The temperature of the oil in the oil bath, under such operating conditions, does not drop below 80...100 ^{o}C [1,5,6].

At the same time, the oil is chemically reacted with the oxygen in contact with the air, it is contaminated by the combustion gases, other gases and the fuel infiltrated into the oil bath, due to the pumping of the segments. In such „uncomfortable" conditions, the oil must perform, over a long period of operation, the following functions [1,3,7]:

- the formation of a stable unctuous film (a film) on the surfaces of the contacted parts, excluding a metal contact at the micro-aspirator level (surface adhesion) and ensuring the reduction of surface wear;
- efficient sealing of the combustion chamber, excluding or reducing to a minimum gas leaks to the oil bath;
- heat removal, released from fuel combustion and friction between parts, cooling of parts surfaces;
- prevention of calamine deposits and lake formations;
- prevention of the corrosion process of the parts;
- prevention of decanting, maintaining deposits from aging and wear in the form of a stable emulsion, evacuation of these deposits from the friction zone;
- neutralization of acids, formed during oil oxidation and fuel combustion.

The lubrication function consists in creating a film of lubricant between the parts in relative motion in order to reduce frictional forces, wear and prevent seizure.

The cooling function consists in evacuating, with the help of the lubricant, a quantity of heat from the friction area of the parts' surfaces.

The function of removing (cleaning) the wear products of the parts, mechanical impurities that may come from the environment.

The chemical protection function is manifested by the property of lubricants to form on the surface of the parts, with which they come into contact, an adherent and persistent film, which also has the role of protecting the metal surfaces from the corrosive action of external and internal factors.

The sealing function that manifests itself on the one hand by protecting the bearings against abrasive particles, and on the other hand by sealing the combustion chamber more firmly due to the oil film between the segments and the cylinder.

The function of engine oil additives [8-10]:

1. To protect metal surfaces:
   - ✓ anti-wear and anti-seize additives – adhere to metal surfaces, forming a protective film between the components;
   - ✓ anti-rust and anti-corrosive additives – additives that protect metal surfaces from corrosion from the chemical attack of water or other contamination agents. When the components have ferrous metals in their structure, this corrosion is called rust;
   - ✓ friction modifiers – to reduce the friction coefficient;
   - ✓ oxidation and corrosion inhibitors;
   - ✓ detergents – form the oil's ability to prevent impurities from sticking to the surface of the parts;
   - ✓ dispersants – form the ability of the oil to maintain in suspension the products of oil degradation and fuel oxidation with the action against the formation of any deposits in the engine, with the exception of calamine.
2. To protect the gaskets – they prevent the gaskets and semi-rings from being attacked.
3. To protect the oil:
   - ✓ antifoams – contain silicone to prevent the formation of air bubbles;
   - ✓ antioxidants - limit the effect of high temperatures, which lead to burning (oxidation) of the oil.
4. To expand the field of use:
   - ✓ depressants (antifreezes) – protect the oil at low temperatures, preventing its solidification;
   - ✓ viscosity modifiers (thickeners) – to increase the viscosity index.
5. Multifunctional additives for the simulant improvement of several properties.

3. Oil consumption by burning

It is known that any engine consumes oil. To understand how much the engine should consume, engine oil consumption rates will help us. They are different for various engines and are almost always determined by construction [11,12].

Usually, in terms of fuel consumption, for gasoline engines of cars, the norm can be taken as 0.005...0.025 L of oil per hundred liters of fuel. For V6 or V8 engines, the flow rate will be higher – up to 0.030...0.040 L per hundred liters of fuel. In engines with significant mileage, engine oil consumption increases steadily and reaches one liter per 1000 km or more. For gasoline turbine engines, the minimum engine oil consumption is 0.8 L per change interval of 6...7 thousand km [13,14].

Truck engines use more oil, usually 0.7...1.2 liters per 1000 kilometers. A high-mileage diesel engine can burn up to 0.8% oil per 100 liters of fuel (0.2...0.250 L per 1000 km). At the same time, oil consumption in engines after a major overhaul, as a rule, increases. Light diesel engines consume less oil. The norm will be within the limit of

0.5 liters per 10.000 km. The amount of oil consumption when the alarm should be sounded is the same – 2 liters per 100 liters of diesel [14]. During the operation of the engine, the oil undergoes several physico-chemical transformations due to various phenomena that occur in it. These transformations lead to the loss of the qualities of performing the necessary functions and subsequently to its degradation. One of the main causes is oil burning.

Oil consumption for waste in an internal combustion engine of a car is a process of reducing the volume of oil in the lubrication system, caused by the features of the power unit, internal malfunctions, defects and other reasons. Internal combustion engines always use engine oil. Engine oil consumption is influenced by a large number of factors. These are engine design features (diesel engines consume more oil) and operational features (high speeds, heavy engine loads), weather and climatic conditions, etc.

Examples include: turbocharged engines Audi, BMW, Subaru, individual models of Mercedes, Porsche, Ford, Mazda, Mitsubishi and Toyota engines, which show excellent appetite for engine oil (Table 1) [11,15].

Table 1

Causes of oil consumption

Car brand	Engine model	Engine oil consumption	Causes of oil consumption
VW	TSI, TFSI, TDI, CAWA, BRZ	up to 1 L/1000 km	Constructive particularities
BMW	Twin Turbo, V8, M54	1 L/1000 km	Engine overheating, crankcase ventilation entanglement, twin turbine
Porsche	3,2 V6	1 L/2000 km	Constructive particularities
Mercedes	OM 606, M112	1 L/10000 km	Engine overheating, water in fuel
Ford	Duratec	1 L/1000 km	Blocked segments. Fuel quality
Mazda	FP 1,8	up to 5 L/1000 km	Wear of lubrication segments
Mitsubishi	4G 64	1 L/1000 km	Constructive particularities
Subaru	EJ20, EJ25, V6R	1 L/1000 km	Constructive particularities
Toyota	4A-FE	2. L/10000 km	Wear of lubrication segments

The problem of increased oil consumption is associated not only with additional costs for the operation of equipment, but is also fraught with the risk of damage and premature failure of the engine. The stability of the oil level in the engine crankcase is the key to its reliable and long-term operation.

Causes of engine oil fumes. Increased oil consumption in the engine can manifest itself for several reasons [16]:

- natural waste, the normative indicators of which are approved by engine manufacturers;
- low quality motor oils;
- use of engine oils not suitable for this type of engine;
- unsatisfactory technical condition of the engine (wear of the cylinder-piston group);
- faulty turbocharged compressor;
- ejection of part of the engine oil through the exhaust system or through the cooling system.

Parameters affecting oil consumption. There is not a single indicator that would show the real rate of oil waste. But two indirect parameters stand out [17]:

1. Evaporation of engine oil.
2. Flash point.

The hardest thing to know is the first indicator, because this information is nowhere to be found. As for the second parameter, it is easy to find the necessary information. These data are found in many reference books and show at what temperature the lubricant of the power unit ignites on contact with an open flame. It depends on the composition of the oil, namely the presence of light fractions in its composition. The higher their number, the lower the temperature required for ignition.

Engine oil volatility is regulated by the API (American Petroleum Institute), ACEA (Association of European Automobile Manufacturers) and OEM (Original Equipment Manufacturers) standards using a special Selby-Noack test. The Selby-Noack test is standardized in the ASTM D5800 method and consists in simulating high-temperature oil volatility in the engine by keeping the oil sample in a special device at a temperature of 250 ^{o}C for 1 hour [15, 16]. The volatility is expressed as a percentage. The lower the percentage of evaporation in the test, the more stable the oil is in terms of oil loss. Knowing the NOACK value, you can predict the intensity of oil consumption in your engine. The most „liberal" – at about 15% – evaporation rate requirements are shown by the API standard. More stringent – about 13% – requirements are imposed by engine manufacturers (OEMs).

On average, mineral lubricating compositions lose about 22...25%, and modern synthetic oils – no more than 8...10% [15].

To compensate for oil consumption for waste, periodic topping up of fresh engine oil (preferably of the same type and brand) is used to maintain the appropriate level in the engine crankcase.

To develop a reasonable frequency of changing the engine oil in engines with a different degree of oil consumption for burnout and, accordingly, the frequency of refilling (freshening), consider the following model of the processes of its operation.

4. Mathematical model of changes in the physical and chemical properties of engine oil during operation

The empirical character of dependence of alkaline number of engine oil (y) on the mileage or operating time (x) suggests that it refers to the type of exponential, monotonically decreasing to a certain limit. This assumption agrees with the equations obtained by a number of authors on the basis of theoretical considerations [6,17,18]. In addition, in favor of such an assumption indicates a simplified representation of the chemical transformations occurring as a result of interaction of oil with air oxygen and exhaust gases[19]. Let's assume that the chemical transformation can be interpreted by the simplest scheme:

$$A_1 \underset{k_2}{\overset{k_1}{\rightleftharpoons}} A_2 \tag{1}$$

where: A_1, A_2 – substance reaction component;

k_j – the rate constant of the j-th stage of a complex reaction.

Then, denoting the current concentration of the initial substance expressed in moles by the letter C, the initial letter C_0 and, considering the conditions of the material balance,

from which it follows that the concentration $A_2 = C_0 - C$, we can obtain a differential kinetic equation in the form:

$$\frac{dC}{dt} + (k_1 + k_{-1}) \cdot C = k_{-1} \cdot C_0 \tag{2}$$

where: t – the current time with initial conditions:

$$C(0) = C(t) \Big|_{t=0} = C_0 \tag{3}$$

The solution of equation (2) under condition (3) can be represented as:

$$C = C_0 - \alpha \cdot (1 - e^{-bx}) \tag{4}$$

where:

$$a = \frac{k_1 \cdot C_0}{k_1 + k_{-1}} \tag{5}$$

$$b = k_1 + k_{-1} \tag{6}$$

By analogy with (4), the dependence of the base number of engine oil (y) on the mileage (x) can be postulated as:

$$y = y_0 - \alpha(1 - e^{-bx}) \tag{7}$$

This equation corresponds to the differential equation:

$$\frac{dy}{dx} + by = b(y_0 - \alpha) = c \tag{8}$$

with initial conditions:

$$y(0) = y_0 \tag{9}$$

The general solution of the inhomogeneous linear ordinary differential equation (LODE) (8) is:

$$y(x) = y_0 \cdot a^{-bx} + \frac{c}{b}(1 - e^{-bx}) = y_0 \cdot e^{-bx} + (y_0 - a) \cdot (1 - e^{-bx}) = y_0 - a \cdot (1 - e^{-bx}) \tag{10}$$

Equations (7) and (8) can only be used if there is no oil in the considered mileage interval, adding fresh engine oil to compensate for its waste during operation.

If we mean the mode with topping up („refreshing") oil at some point in time, then this situation requires special consideration.

Let: m_0 – the initial volume of oil in the engine crankcase, expressed in liters;

Δm – oil waste in liters per car mileage in thousand km;

y_0 – base number of fresh engine oil, expressed in mg KOH/g;

$y(x)$ – base number of oil in the crankcase before topping up, expressed in mg KOH/g;

Δy – increase in the base number of oil as a result of topping up, mg KOH/g.

Based on the condition of the need to maintain the volume of oil in the crankcase at a constant level, we will compose an equation for calculating the increase in base number:

$$\frac{m_0 - \Delta m}{m_0} \cdot y(x) + \frac{\Delta m}{m_0} \cdot y_0 = y(x) + \Delta y \tag{11}$$

From this expression we have:

$$\frac{\Delta m}{m_0}(y_0 - y) = \Delta y \tag{12}$$

An analysis of experimental data allows us to judge that oil waste is linearly expressed in terms of vehicle mileage, i.e.:

$$\Delta m = \gamma \cdot \Delta x \tag{13}$$

where: γ – the rate of oil burning, related to the unit of the mileage scale, l/ths. km.

Substitution of expression (13) into (12) will lead to the relation:

$$\Delta y = \frac{\gamma \cdot \Delta x}{m_0}\left(y_0 - y\right) \tag{14}$$

This expression allows the increase in base number due to topping up (refreshing) engine oil. It is appropriate to note that the interval Δx is calculated either from the start of engine operation (if we are talking about the first topping up), or from the moment of the previous topping up.

Let us now return to the differential equation (8), bearing in mind the need to correct it if the oil is topped up once and instantly at $\Delta x = x_1 - x_0$, when the base number (before topping up) is determined by equation (7).

It is known from the theory of linear differential equations that in such a case the right side of equation (8) must be supplemented by a „control" in the form:

$$\begin{cases} \dfrac{dy}{dx} + by = b(y_0 - a) + \Delta y_1 \cdot \delta(x - x_1) \\ y(0) = y_0 \end{cases} \tag{15}$$

This equation describes the change in base number, taking into account the fact that at the moment $x = x_1$ oil is added, leading to an instantaneous jump in base number Δy_1.

Equation (15) is a typical equation of a linear dynamic system with a perturbing function in the form of an instantaneous impulse $\delta(x - x_1)$ - an impulse function ($\delta(\cdot)$ is the Dirac delta function [9]) that has the following properties:

$$\delta(x - x_1) = 0 \quad npu \quad -\infty < x < \infty, \quad x \neq x_1$$

$$\int_{-\infty}^{\infty} \delta(x - x_1)dx = 1$$

To obtain the general solution of equation (15), it suffices to add to solution (10) of equation (8) a particular solution of the equation:

$$\begin{aligned} &\frac{dy}{dx} + by = \Delta y_1 \cdot \delta(x - x_1) \\ &y(0) = y_0 \end{aligned} \tag{16}$$

The general solution of equation (10 and 15) can be written as a composite function:

$$y(x) = y_0 - \alpha(1-e^{-bx}) \left| \begin{matrix} +\Delta y_1 \cdot e^{-b(x-x_1)} \\ x \geq 0 \end{matrix} \right| x \geq x_1 \tag{17}$$

Note also that the second and third terms on the right side of the equation are not equivalent. The second term $\left[-\alpha(1-e^{-bx})\right]$ „acts" on the entire interval of existence of the argument (x), i.e. from (0) to (∞) (theoretically). The third term „acts" only for $x \geq x_1$, and besides $x \geq x_1$, for it gives a jump on a curve different from Δy_1. In other words, it is a composite function. Figure 2 shows a dependency graph for a function of the form (17), where: $y_1 = y(x_1) = y_0 - \alpha(1-e^{-bx_1})$, and the jump Δy_1 is calculated by the equation:

$$\Delta y_1 = \frac{\gamma x_1}{m_0}\left[y_0 - y(x_1)\right] \tag{18}$$

The graft section at is $x > x_1$ described by a composite function:

$$y = y_0 - \alpha(1-e^{-bx}) \left| \begin{matrix} +\Delta y_1 \cdot e^{-b(x-x_1)} \\ x \geq 0 \end{matrix} \right| x \geq x_1 \tag{19}$$

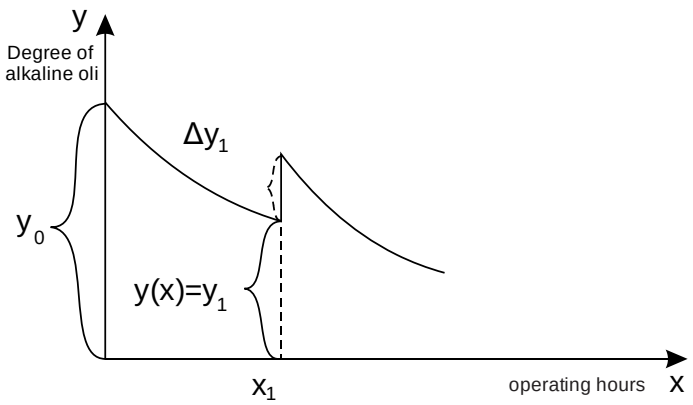

Figure 2. Diagram of the change in the alkaline number of the engine oil as a function of the operating hours in the presence of an instantaneous pulse refill oil [9].

Now let's consider a more complicated case, when oil is topped up many times in portions at different mileage values $x_1, x_2, ..., x_k$. Obviously, in this case, the „jumps" of the base number, due to the addition of oil at will $x = x_1; x = x_2; .....x = x_k;$ be expressed by equations of the form:

$$\begin{cases} \Delta y_1 = \dfrac{\gamma \cdot x_1}{m_0}\left[y_0 - y(x_1)\right] \\ \Delta y_2 = \dfrac{\gamma \cdot (x_2 - x_1)}{m_0}\left[y_0 - y(x_2)\right] \\ - - - - - - - - - - - - - - - - - \\ \Delta y_k = \dfrac{\gamma \cdot (x_k - x_{k-1})}{m_0}\left[y_0 - y(x_k)\right] \end{cases} \tag{20}$$

It should be borne in mind that the values $y(x_2), y(x_3), ..., y(x_k)$ must be calculated taking into account previous jumps.

If multiple impulse actions are performed on the system (multiple impulse oil topping up), then the differential equation can be written in the form:

$$\begin{cases} \dfrac{dy}{dx} + by = C + \sum_{i=1}^{k} \Delta y_i \cdot \delta(x - x_i) \\ y(0) = y_0 \end{cases} \tag{21}$$

The solution of such an equation (provided that $x_{i+1} > x_i$) is constructed similarly to the previous case and is expressed as a function:

$$y(x) = y_0 - \alpha(1 - e^{-bx}) \left| \begin{matrix} +\Delta y_1 \cdot e^{-b(x-x_1)} \\ x \geq 0 \end{matrix} \right| \begin{matrix} +\Delta y_2 \cdot e^{-b(x-x_2)} \\ x \geq x_1 \end{matrix} \left| \begin{matrix} +... + \Delta y_k \cdot e^{-b(x-x_k)} \\ x \geq x_2 \end{matrix} \right| x \geq x_k \tag{22}$$

The dependency graph for such a composite function is shown in figure 3.

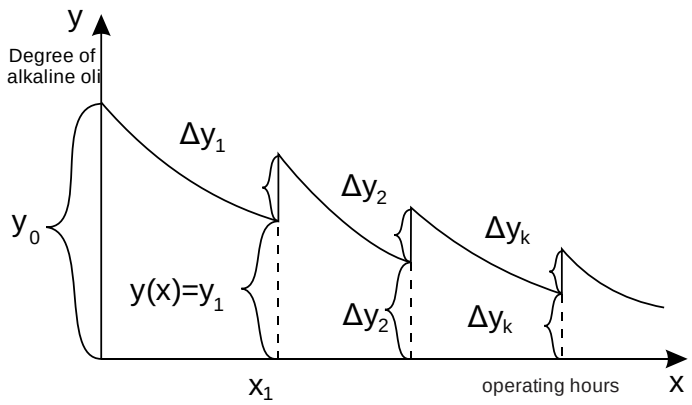

Figure 3. Diagram of the relationship between the alkaline number of the engine oil and the operating hous in the presence of multiple pulse refills during operation motor vehicle[9].

It is appropriate to note that the jumps, even with the same intervals between topping up, $x_1 - 0 = x_2 - x_1 = ... = x_k - x_{k-1} = \Delta x$ will not be equal to each other.

To describe the process of changing the physical, chemical and operational properties of the engine oil depending on the mileage, technical condition of the engine and the degree of "freshening" of the oil, you can use a mathematical model of the form:

$$y = y_0 \pm a(1 - e^{-bx}) \pm \sum_{i=1}^{k} \Delta y_i \cdot e^{-b(x-x_i)}$$

where: y_0 – the initial value of the quality indicator of fresh (commercial) motor oil;

x – the current value of the car's mileage;

$x - x_i$ – the mileage interval between the moment of topping up engine oil, which compensates for oil consumption for waste;

k – the number of top-ups made during the period of operation of the oil in the engine.

Parameters „*a*" and „*b*" in the mathematical model can be described depending on the technical state of the engine using the formulas:

$$\begin{cases} a = \alpha_0 + \alpha_1 Q + \alpha_2 Q^2 \\ b = \delta_0 + \delta_1 Q + \delta_2 Q^2 \end{cases}$$

where: Q – oil pumpability through the engine lubrication system, l/min;

$\begin{cases} \alpha_0, \alpha_1, \alpha_2 \\ \delta_0, \delta_1, \delta_2 \end{cases}$ – the coefficients of the system of equations.

In operating conditions, the process of „refreshing" the engine oil can be regarded as a repeated pulse refill and described by the equation of the form:

$$\Delta y_i = \frac{\gamma(x - x_i)}{m_0}\left[\pm y_0 \mp y(x_i)\right]$$

where: m_0 – the amount of engine oil in the engine crankcase, set by the manufacturer;

$y(x_i)$ – the current value of the oil quality index at the time of the next oil top-up;

γ – engine oil burn rate.

The rate of engine oil burnout during operation is described by an equation of the form:

$$\gamma = \gamma_0 + k\bar{x}$$

where: γ_0 – oil burn rate corresponding to the technical condition of the new engine;

$\bar{x}$ – vehicle mileage since the start of operation;

k – an empirical coefficient that takes into account the wear of engine parts.

5. Conclusions

In the given article the peculiarities of engine oil combustion are analyzed, taking into consideration the renewal of engine oil due to the addition of oil up to the necessary limits of engine operation, the physical-chemical properties of engine oil are maintained at an optimal level necessary for the proper functioning of internal combustion engines. This allows us to increase the time between corrective maintenance interventions. One of the main parameters of the maintenance work is the oil change, which increases the vehicle ride periodicity.

Conflicts of Interest: The authors declare no conflict of interest.

Bibliography

1. Corpocean, A.; Ene, V.; Pădure, O. *Exploitation materials*. University course. Tehnica-UTM, Chisinau, Republic of Moldova 2008, 141 p. [in Romanian].
2. Oils; from which, from where, how many km, when? Copyright © 2004 - 2023 ClubOpel.com Romania. Available online: https://www.clubopel.com/viewtopic.php?t=132115 (accessed on 10.04.2023) [in Romanian].
3. Engine oil: composition and physical-chemical characteristics. ©2018-2023 LUBRIFIANT.MD - Calbor Grup SRL. Available online: https://lubrifiant.md/blog/articol/d86ee0cf/ (accessed on 10.04.2023) [in Romanian].
4. Additives to engine oil. Available online: https://neftegaz.ru/tech-library/energoresursy-toplivo/474570-prisadki/ (accessed on 14.04.2023) [in Russian].
5. Amariei, V.; Jomiru, V. *System of technical revision and repair of motor vehicles*. UTM, Chisinau, Republic of Moldova, 1999, 84 p. [in Romanian].

6. Ene, V. *Theoretical foundations of the technical operation and repair of automobiles. Availability. Fiability*. University course. UTM, Chisinau, Republic of Moldova, 2005, 232 p. [in Romanian].
7. Pădure, O.; Pădure, D. *The Automobile Dictionary*. ARC, Chisinau, Republic of Moldova, 2013, 132 p. [in Romanian].
8. Goian, V.; Ene, V.; Padure, O. *Technical diagnosis of automobiles*. U.T.M., Chisinau, Republic of Moldova, 2010, 297 p. [in Romanian].
9. The role of additives in engine oil. Available online: https://rolfoil.ru/rol-prisadok-v-motornom-masle.html (accessed on 14.04.2023) [in Russian].
10. Modern Automotive Technology-Fundamentals, service, diagnostics. 2nd edition, Xmeditor Adverstising SRL, Berceni, Ilfov, Romania, 2020, 788 p. [in Romanian].
11. Kanarchuk, V.E.; Ludchenko, A.A. Curnicov I.P.; Luic A.I. *Maintenance, repair and storage of motor vehicles*. Vyshcha shkola, Kiev, Ukraine, 1991, vol. 1, 359 p. [in Russian].
12. Avdonkin, F.N. *Theoretical bases of technical operation of automobiles*: Textbook for universities. Transport, Moscow, 1985, 215 p. [in Russian].
13. Oprean, I. M. *The Modern Automobile*. Romanian Academic, Bucharest, Romania, 2003, 271 p. [in Romanian].
14. Oil-eater. Why does engine oil burn out? Causes of oil consumption in a car engine. © 2007 GT OIL. Available online: https://gtoil.ru/materials/articles/maslozhor-pochemu-ugaraet-motornoe-maslo (accessed on 14.04.2023) [in Russian].
15. Ene, V. *Fiability and maintainability of automobiles*. Evrica, Chisinau, Republic of Moldova, 2007, 344 p. [in Romanian].
16. Oil burning in the engine or how to reduce the „oil burn" of the motor. © 2010 – 2023 AUTOTOPIK. Available online: https://autotopik.ru/dvigatel/ugoranie-masla-v-dvigatele.html [accessed 14.04.2023] [in Russian]. Waste of motor oils. NOACK test. Available online: https://mosksm.ru/ugar-motornyh-masel/ (accessed on 12.04.2023) [in Russian].
17. Tezec, Iu. M. Development of a method for optimizing the use of engine oil in KamAZ-740 engines depending on their technical condition. Diss. for the competition Ph.D. – Chisinau.: CAI, 1996. - 183 p. [in Russian].
18. Kuzmin, N.A. *Causes and regularities of changes in the technical condition of cars in operation*. NHSAA, Nizhny Novgorod, 2011, 79 p. [in Russian].
19. Fastovtsev, G.F. *Organization of maintenance and repair of cars: Textbook for students of automobile transport vocational schools*. 2nd edition, revised. and supplementary, Transport, Moscow, 1989, 240, p. [in Russian].

Citation: Pădure, O.; Tezec, Iu.; Ceban, V.; Plămădeală, V.; Buga, A. Processes of changing the physico-chemical properties of automobile motor oils during operation. *Journal of Engineering Science* 2023, 30 (2), pp. 47-58. https://doi.org/10.52326/jes.utm.2023.30(2).04.

Submission of manuscripts: jes@meridian.utm.md

Journal of Engineering Science *Vol. XXX, no. 2 (2023), pp. 59 - 71*
Fascicle *Industrial Engineering* *ISSN 2587-3474*
Topic *Applied Engineering Sciences and Management* *eISSN 2587-3482*

https://doi.org/10.52326/jes.utm.2023.30(2).05
UDC 656.05625.74(498)

IMPROVING ROAD SAFETY ON THE NATIONAL ROAD NETWORK IN ROMANIA THROUGH PILOT SOLUTIONS

Flavius-Florin Pavăl*, ORCID: 0000-0002-9105-2134,
Ilie Bricicaru, ORCID: 0000-0002-2342-5760

Technical University of Moldova, Chisinau, 168 Stefan cel Mare Blvd., Republic of Moldova
*Corresponding author: Flavius-Florin Pavăl, *flavius.paval@iit.utm.md*

Received: 03. 22. 2023
Accepted: 04. 26. 2023

Abstract. In recognition of outstanding work in the field of road safety, especially for the implementation of road safety pilot projects, N.C.R.I.A.-S.A. was declared the winner. The road safety pilot projects that have attracted the attention of the IRF, being a model to follow for all road administrations are: Roller Barriers; Impact attenuators; Road sector 2+1; Cable Road barriers; Illumination of dangerous sectors with light assemblies; Projects to increase road safety by creating elevated road crossings. The International Road Federation (IRF) encourages all companies and organizations in the road development sector to get involved in the awards program it grants, because by promoting innovative ideas a positive and motivating influence can be created. The National Company for Road Infrastructure Administration S.A, Traffic Safety Service participated in the "Find a Way Global Road Safety Award" organized by IRF. In this article, the road safety projects are presented, with their results and the road safety measures implemented by the national roads and highways administrator in Romania, so that other road administrations to be encouraged to implement as many road safety measures as possible.

Keywords: *Road Safety, Pilot Solutions, „Find a Way" IRF Prize.*

Rezumat. Pentru recunoașterea muncii remarcabile în domeniul siguranței rutiere, în special pentru implementarea proiectelor-pilot de siguranță rutieră, C.N.A.I.R.-S.A. a fost desemnată câștigătoare. Proiectele pilot de siguranță rutieră care au atras atenția IRF, fiind un model de urmat pentru toate administrațiile rutiere sunt: Parapetele rutier pe rulouri; Atenuatori de impact; Sector de drum 2+1; Parapete cu cablu; Iluminarea sectoarelor periculoase prin intermediul ansamblurilor luminoase; Proiecte de creștere a siguranței rutiere prin realizarea de pasaje rutiere. Federația Internațională a Drumurilor (FID) încurajează toate companiile și organizațiile din sectorul de dezvoltare rutieră să se implice în programul de premii pe care le acorda, pentru ca prin promovarea ideilor inovatoare se poate crea o influenta pozitiva si motivatoare. Compania Națională de Administrare a Infrastructurii Rutiere din România, Serviciul Siguranța Traficului a participat la "Premiul Global pentru Siguranța Rutieră Find a Way" decernat de IRF. În cadrul acestui articol sunt prezentate rezultatele și măsurile de siguranță rutieră implementate de administratorul drumurilor naționale și autostrăzilor din

România, astfel încât și alte administrații rutiere să fie impulsionate să implementeze cât mai multe măsuri de siguranță rutieră.

Cuvinte cheie: *Siguranța Rutieră, Soluții Pilot, Premiul IRF „Find a Way”.*

1. Introduction

The public road network in Romania totalled 86,199 km on 31.12.2021, of which national roads represent 16,599 km and motorways 931 km. National roads, express roads and motorways are owned by the Ministry of Transport and Infrastructure, which manages them through the largest road network administrator in Romania, the National Company for Road Infrastructure Administration.

The National Company for Road Infrastructure Administration S.A. (N.C.R.I.A.-S.A.) is a company of national strategic interest whose mission is to implement programmes to develop the public road network and to maintain and increase road safety on the existing road network under its management.

The following figure shows the road network managed by N.C.R.I.A.-S.A.

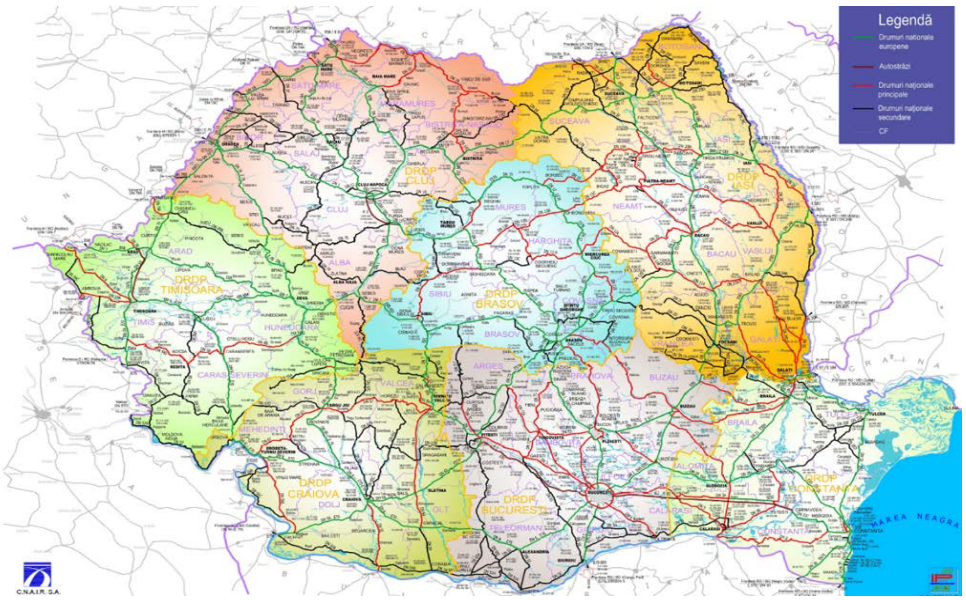

Figure 1. The road network managed by N.C.R.I.A.-S.A. [1].

In view of the commitment reaffirmed in December 2020 by the European Commission on the long-term goal of achieving almost zero road deaths by 2050 - "Vision Zero" and, as an intermediate step, reducing by a further 50% the number of people killed in road accidents and by 50% the number of people seriously injured in the period 2021-2030, Romania joins the European effort and takes over the European target.

Road safety is a priority at both global and European level and the reduction of road fatalities has been set as a target by N.C.R.I.A.-S.A. due to the need to get as close as possible to zero road fatalities by 2050.

N.C.R.I.A.-S.A. is involved in activities to improve traffic safety by promoting traffic safety programmes and projects and implementing technical measures to reduce accidents.

2. Current road safety situation

The European Commission has set an ambitious target of a 50% reduction in the number of road fatalities for the period 2010-2020, which it is maintaining for the next decade, 2020-2030 [2].

In terms of the results achieved, the target was not met, the European average was 37%, from 29,691 to 18,844 people killed, and for Romania, on all public roads there was only a 31% reduction, from 2,377 to 1,646 people killed in road accidents [3].

The road safety measures implemented by N.C.R.I.A.-S.A. have led to positive results on the national road network in terms of reducing the number of fatalities, i.e. a reduction of 43.9%, well above the European average and close to the target set by the Commission.

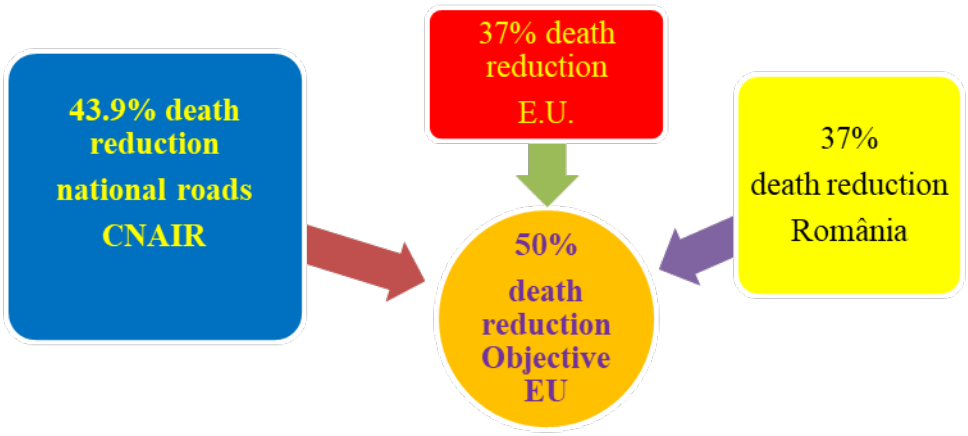

Figure 2. Road safety situation in 2020 compared to 2010 [2].

Even if at national level, the target set by the European Commission of reducing by 50% the number of road fatalities has not been met, when analysing the causes behind the results recorded, it is imperative to take into account the increase in the number of vehicles and licence holders.

Thus, between 2010 and 2020, there was a massive annual increase in the number of vehicles registered in Romania, both in terms of cars and vehicles in general.

At the end of 2020 the car fleet was 68.9% (2,968,445 units) larger than in 2010, and the overall registered vehicle fleet at the end of 2020 was 70.2% (3,803,099 units) larger than in 2010. The evolution of the car fleet in the period 2010-2020 is shown in the following Table 1 [2].

Table 1

Evolution of the car fleet between 2010-2020

Year	Automobiles	Vehicles	Annual evolution	Evolution since the reference year (2010)
2010	4,306,283	5,419,181		
2011	4,321,584	5,482,746	1.2%	1.2%
2012	4,485,148	5,710,773	4.2%	5.4%
2013	4,695,660	5,985,085	4.8%	10.4%
2014	4,907,564	6,270,582	4.8%	15.7%
2015	5,155,059	6,600,325	5.3%	21.8%
2016	5,472,423	7,010,608	6.2%	29.4%
2017	5,998,194	7,635,775	8.9%	40.9%
2018	6,452,536	8,193,278	7.3%	51.2%
2019	6,902,984	8,708,863	6.3%	60.7%
2020	7,274,728	9,222,280	5.9%	70.2%

The evolution of the car fleet in the period 2010-2020 is shown in the following Figure 3.

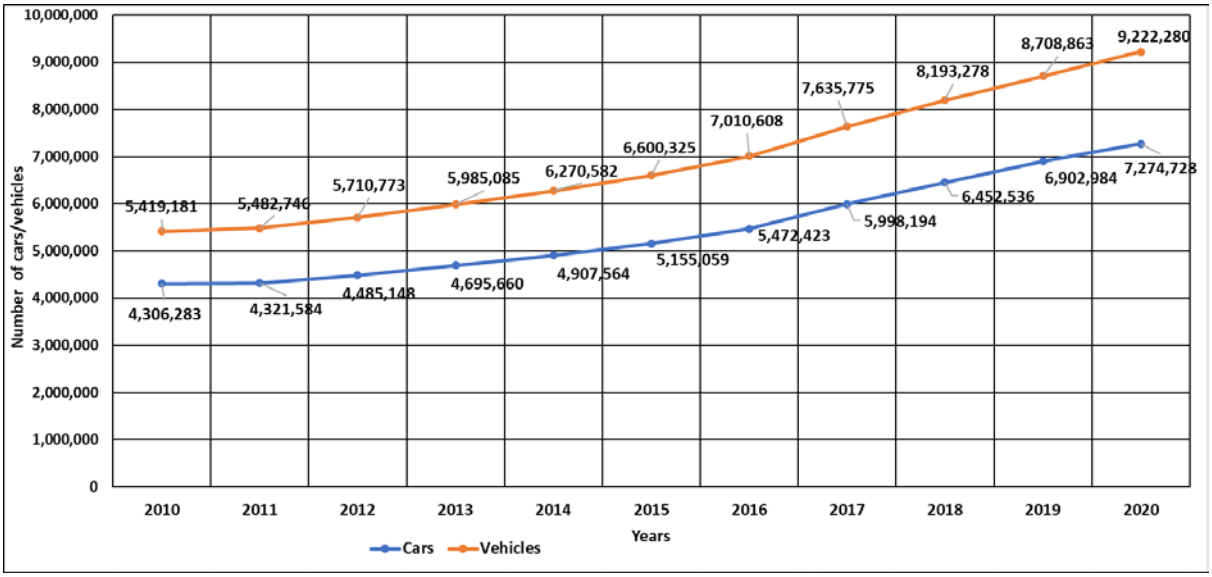

Figure 3. Evolution of the car fleet between 2010-2020 [2].

Thus, between 2010 and 2020 there was a massive annual increase in the number of vehicles registered in Romania, both in terms of passenger cars and vehicles in general.

As regards the number of holders of driving licences, there is a continuous increase from 6,431,415 holders of driving licences in 2011 to 8,065,846 licence holders in 2020, representing an increase of 25.4%, as can be seen in the following Table 2 [2].

Table 2

Evolution of the number of drivers between 2010-2020

Year	No. Permits	Annual evolution	Evolution since the reference year (2011)
2011	6,431,415		
2012	6,806,045	5.8%	5.8%
2013	6,791,626	-0.2%	5.6%
2014	6,967,034	2.6%	8.3%
2015	7,142,478	2.5%	11.1%
2016	7,347,009	2.9%	14.2%
2017	7,554,743	2.8%	17.5%
2018	7,721,323	2.2%	20.1%
2019	7,907,928	2.4%	23.0%
2020	8,065,846	2.0%	25.4%

In order to improve road safety, Romania has taken the necessary legislative measures by adopting Law 265/2008 „Road infrastructure traffic safety management" [3] which is the transposition into national law of Directive 2008/96/EC „Road infrastructure safety management" [4].

Starting from 2016 the National Company for Road Infrastructure Administration contracted:

- around 470 Road Safety Impact Assessments and Road Safety Audits. Road Safety Impact Assessments and Road Safety Audits (for all stages) for all new road infrastructure projects and for the projects that makes substantial changes to existing road network.

- road safety inspections on 2,994 km of roads under its management. Road safety inspections are carried out on deficiencies of existing roads, that can lead to road accidents.

3. Road safety pilot projects

From its role as the largest road administrator, N.C.R.I.A.-S.A. has a moral obligation to implement the latest and most effective solutions so that by the power of example, efficient pilot projects can be transformed into a normality in terms of the chosen technical solutions [5].

Starting from the database of road accidents where analyzes are performed on homogeneous road sectors, the causes that were the basis for the occurrence of road accidents, N.C.R.I.A.-S.A. road safety specialists choose the latest technical solutions on the profile market and implement pilot projects in order to track the behavior of these technical solutions.

After implementation, the pilot projects that prove their benefits and meet the expectations of specialists, become a norm in terms of technical solutions that they will use in the current activity.

Successful road safety pilot projects implemented by N.C.R.I.A.-S.A.:

- *Roller barriers (*guardrails on rollers).
- *Impact attenuators*.
- *Road sector 2+1*.
- *Cable barriers*.
- *Illumination of dangerous sectors by means of light assemblies.*
- *Projects to increase road safety by building road overpasses.*

3.1. Roller barriers

In 2019, the pilot project to increase road safety by placing rollers barriers was implemented, which consisted of installing 1,000 m of guardrails on 5 sectors where accidents were frequent. The sectors where these barriers were installed are shown in the Table 3.

Table 3

Implementation of the roller guardrail pilot project

National Road (number)	Installed sector (km+m – km+m)	Placement (right/left/axial)	Quantity (m)
7	14+700 - 14+920	Right edge	220
7	14+750 - 14+920	Left edge	170
7	18+700 - 18+820	Left edge	120
2	51+670 - 51+900	Left edge	230
2	51+690 - 51+950	Right edge	260
		TOTAL	**1,000**

Due to the positive results obtained, namely a reduction in the number of serious accidents and the need to stop intervening on the barrier sectors, the use of this barrier has been extended and the pilot project has become normal practice, as can be seen in the Figure 4.

As it can be seen in the Figure 5, serious accidents have turned into minor accidents, with an increase in the number of minor accidents.

Figure 4. Sections of guardrails on rollers on national roads.

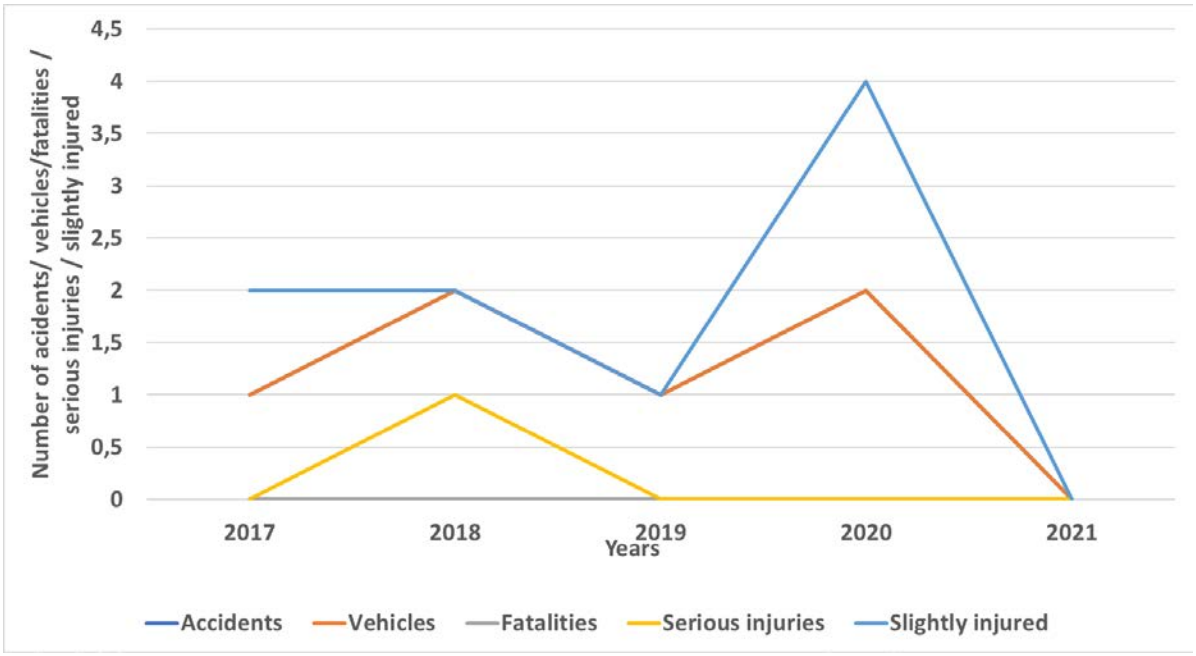

Figure 5. Results of a sector with roller barrier.

A major advantage of this type of guardrail is that, on the sectors where it has been installed, the road accidents that have subsequently occurred have been transformed from major to minor and the guardrail has not suffered degradation requiring replacement, thus increasing the efficiency of the road administrator's activity of increasing road safety and ensuring a climate of safety for drivers, due to the fact that this protection system fulfils its role repeatedly and consecutively.

Figure 6. Roller guardrails that took over the road event.

In the following figure, it can be seen that the crash barrier has taken up loads from accidents that have occurred but have not affected the structure of this protection system.

Thus, in 2021 and 2022, the campaign of installing roller barriers was continued, being installed on other sectors as follows, Tables 4 and 5.

Table 4

Sectors with roller barriers installed in 2021

National Road (number)	Installed sector (km+m – km+m)	Placement (right/left/axial)	Quantity (m)
71	21+200	Left marginal	70
72	5+676- 5+900	Right marginal	224
72	5+400 - 5+544	Left marginal	144
2	48+400 - 49+022	Axial	622
1	31+500 - 31+600	Right marginal	100
1	31+450 - 31+600	Left marginal	150
6	32+242 - 32+392	Right marginal	150
6	32+112 - 32+188	Left marginal	70
6	32+088 - 32+188	Right marginal	100
1	205+800 - 205+950	Left marginal	150
1	206+050 - 206+200	Left marginal	150
1A	171+450 - 171+550	Left marginal	150
		TOTAL	**2,080**

Table 5

Sectors with roller barriers installed in 2022

National Road (number)	Installed sector (km+m – km+m)	Placement (right/left/axial)	Quantity (m)
1	147+080 - 147+200	Right marginal	120
1	146+820 - 146+870	Right marginal	50
1	145+250 - 145+470	Right marginal	220
1	144+500 - 144+550	Right marginal	50
VOBV	2+440 - 2+600	Right marginal	160
28	33+620 - 34+287	Axial	630
22	255+000 - 255+200	Right marginal	200
22	256+450 - 256+650	Right marginal	200
2	262+000 - 262+500	Axial	500
2	254+800 - 255+300	Axial	500
		TOTAL	**2,630**

Note: VOBV- Brașov Bypass Variant.

The sectors installed in 2021 and 2022 are under observation in order to follow the results to be obtained.

3.2. Impact attenuators

In order to achieve „friendly roads" that will lead to a reduction in the severity of road accidents resulting in leaving the road surface for various reasons, during the period (2017-2020) N.C.R.I.A.-S.A. has installed a number of approximately 150 impact attenuators.

Impact attenuators are installed on road sections with a high risk of frontal vehicle collisions. The purpose is to protect vehicle passengers when they leave the road and collide with a rigid object outside the carriageway.

Attenuators are designed to gradually absorb the kinetic energy of the vehicle at the moment of collision, thereby bringing the vehicle to a controlled stop, which may result in avoiding collision with the obstacle, while maintaining a limited amount of deceleration on the vehicle occupants.

The performance evaluation of impact attenuators is carried out according to the European standard EN 1317-3 based on various speed limits and impact angles.

The following figure (Figure 7) shows a damaged crash attenuator which has fulfilled its purpose and resulted in a serious accident being transformed into a minor one, resulting only in material damage to the car involved.

Figure 7. Degraded impact attenuator.

3.3. Road sector 2+1

In 2019, was implemented a pilot project, transforming a sector with 2 lanes and 2 big shoulders in 2 + 1 solution (traffic lanes) on the sector is between km 30 + 605 (Sinești) - 40 + 240 (Movilița) with a length of 9.6 km.

Before the implementation of this system, in the previous 5 years, there were 43 serious road accidents resulting in 14 deaths and 70 injuries. From implementation, only 2 serious accident occurred.

The following figure (Figure 8) shows the 2+1 sector.

Figure 8. Sector on DN 2 in 2+1 traffic system.

3.4. Cable parapet

In the Figure 9 we can see the implementation of the pilot cable barrier project, mounted within the range of Afumati village, between km 12+500 and km 14+500, is a road sector of DN 2 with 4 lanes, each the traffic lane having of 3.5 meters width and a speed limit of 50 km/h, due to the location of the sector, inside the locality [6].

Figure 9. Sector on DN 2 with the cable parapet pilot project.

No deaths have been reported since implementation:

- **Before: 3 or 4 serious accidents (every year).**
- **After: 0 serious accidents (in 3 years).**

On the most beautiful road in the world, namely Transfagarasan, from the Figure 10, It was decided to install cable road barriers.

Figure 10. Transfagarasan road.

This decision was taken, to ensure a level of road safety during the summer, when traffic is allowed and in winter when traffic is closed, the railing allows it to be placed on the ground so as not to suffer damage due to avalanches.

3.5. Illumination of hazardous areas by lighting assemblies

To increase the visibility of dangerous points on the road network, light assemblies consisting of 5 light poles powered by photovoltaic panels were used to provide increased visibility at night.

In the last 2 years, about 700 light sets have been installed to illuminate traffic lights, entrance/exit islands and pedestrian crossings, examples in Figure 11.

Figure 11. Lighting assemblies mounted on hazardous sectors.

3.6. Projects to increase road safety through the construction of road overpasses

In order to reduce the number of road events and at the same time to ensure the traffic flow on the busiest national road sector in Romania, which connects the South and the North, the capital (Bucharest) and a very large city Brasov, as well as the connection with the mountain resorts of the Prahova Valley, N.C.R.I.A.-S.A. has also started road safety projects that will also have European funding, namely the Large Infrastructure Operational Programme, as follows:

Road overpasses – 4 buc – amounting to 225,606,567.06 lei without VAT.

Elaboration of feasibility study and technical execution project for:

- Construction of a road overpass at the intersection of DN 1 and Republicii Boulevard (Sinaia South).
- Construction of a road overpass at the intersection of DN 1 and Ferdinand Boulevard (Sinaia Nord).
- Construction of a road overpass at the intersection DN 1 with Prahovei street (Azuga).
- Construction of a road overpass at the intersection DN 1 with DN 73A (Predeal).

The road overpasses are shown in Figure 12.

Figure 12. Road overpass.

Underground pedestrian passages – 5 buc amounting to 32,646,020.74 lei without VAT

Elaboration of feasibility study and technical execution project for:

- Construction of the pedestrian underpass in the Central Square of Comarnic - intersection DN 1 with Ghiosesti street.
- Construction of pedestrian underpass at Comarnic Town Hall.
- Construction of pedestrian underpass - intersection DN 1 with Urlatoarei, Gloriei and Nicolae Balcescu streets (Poiana Tapului).
- Construction of pedestrian underpass - intersection DN 1 with Telecabinei street (Busteni).
- Construction of pedestrian underpass - intersection DN 1 with Panduri street (Predeal).

The pedestrian underpasses are shown in Figure 13.

Figure 13. Pedestrian underpass.

As far as the expected benefits are concerned, the feasibility study has shown in the Table 6.

Table 6

Benefits from road overpasses [7-10]

Benefits	Overpass Sinaia S	Overpass Sinaia N	Overpass Azuga	Overpass Predeal
Improving the average speed of traffic, %	81	90	27.9	79 %
Reducing the average delay of a vehicle, s	47.37	55.89	20.00	48.62
Decrease maximum queue length, m	504	442	150	560
Reduce traffic flow density, %	43	43	42	54
Reducing the total duration of road journeys, hours	441	394	102	351

In the Comarnic area, where 2 pedestrian crossings will be built, the following benefits is expected, shown in the Table 7.

Table 7

Benefits from pedestrian underpasses [11,12]

Pedestrian underpass	Expected benefits	
	Improving average road speeds, %	**reduction of average delay per vehicle, s/vehicle**
Underground pedestrian passage Central Market Comarnic - intersection DN 1 with Ghioseşti street	2	3.57
Construction of pedestrian underpass Comarnic Town Hall	5	3.78

4. Discussion

The IRF encourages all companies and organisations in the road development sector to get involved in its awards programme, as promoting innovative ideas can create a positive and motivating influence. The spread area of the IRF affiliated states is shown in the Figure 14.

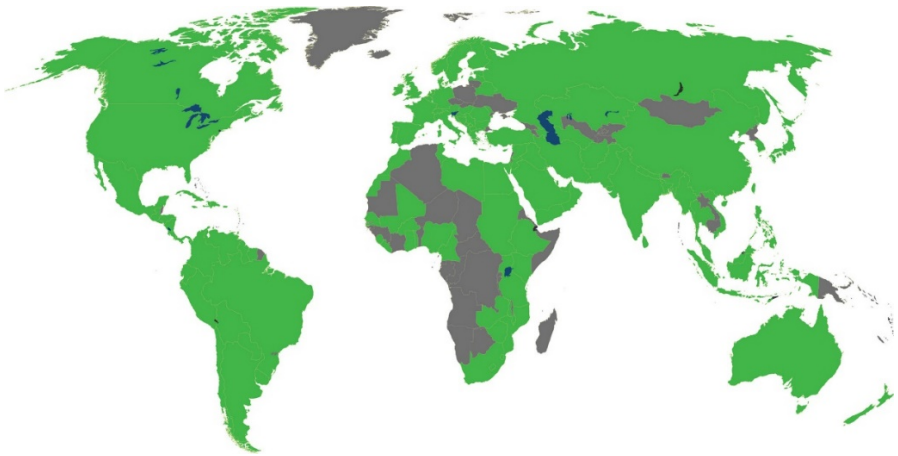

Figure 14. International Road Federation members (with green) [13].

In 2012, recognizing the value of political leadership to drive road safety strategies, His Excellency Abdullah Al-Mogbel, President of the International Road Federation (IRF), established an annual IRF Global "Find a Way" Road Safety Award, which recognizes outstanding commitment to safer roads by national, regional or city governments. Starting in

2021, this award is given to one agency per IRF region. At the recommendation of IRF representatives who were aware of the projects carried out in the field of road safety by N.C.R.I.A.-S.A., the Traffic Safety Service participated in the "Global Road Safety Award Find a Way" organized by the IRF, in recognition of our company's outstanding work in the field of road safety, especially for the implementation of road safety pilot projects, for which it was named winner.

The Figure 15 shows the award information letter, the IRF "Find a Way" award plaque and a picture of the award ceremony.

Figure 15. IRF "Find a Way" award, N.C.R.I.A.-S.A. winner of 2022.

5. Conclusions

The results obtained from the implementation of road safety pilot projects were presented for each solution and the conclusion was that those projects with positive results were transformed into a common practice.

Road safety pilot projects that can serve as a model for all road administrations are:

- Roller Barriers.
- Impact attenuators.
- Road sector 2+1.
- Cable Road barriers.
- Illumination of dangerous sectors with light assemblies.
- Projects to increase road safety by creating elevated road crossings.

From N.C.R.I.A.'s point of view, as the largest administrator, the road safety projects that have been implemented since 2019 have led to a 43.9% reduction in the number of road fatalities, (on its network) leading to positive results on the national road network, close to the target imposed by the Commission, even though Romania is at the bottom of the European ranking when we refer to the entire public road network.

References

1. Site of The National Company for Road Infrastructure Administration S.A. Available online: http://www.cnadnr.ro/ (accessed on 25.10.2022).
2. Road Safety Bulletin 2020 published by the Road Directorate Institute for Crime Research and Prevention. Available online: https://www.politiaromana.ro/ro/prevenire/buletinul-sigurantei-rutiere (accessed on 20.10.2022).

3. Law 265/2008 "On Road Infrastructure Traffic Safety Management. Available online: https://www.arr.ro/Files/uploads/173-Legea%20265-2008%20actualizata.pdf (accessed on 20.11.2022).
4. Directive 2008/96/EC On Road Infrastructure Safety Management, published by the European Comission. Available online: https://eur-lex.europa.eu/legal-content/EN/ALL/?uri=celex% 3A32008L0096 (accessed on 27.10.2022).
5. Andrei, C.; Paval, F. F. Road safety - Modern measures implemented by CNAIR. In: *16th National Congress of Roads and Bridges in Romania*, Timisoara, Romania, 2022.
6. Paval, F.F.; Toma, M.G. Pilot project for road safety in Romania using the cable road barrier. In: *5th International Conference on Road and Rail Infrastructure, CETRA*, Zadar, Croatia, 2018.
7. Feasibility Study and Technical Execution Project for - Construction of road overpass at the intersection of DN 1 with Prahovei Street (Azuga), 2021.
8. Feasibility Study and Technical Execution Project for - Construction of road overpass at the intersection of DN 1 with DN 73A (Predeal), 2021.
9. Feasibility Study and Technical Execution Project for - Construction of a road overpass at the intersection of DN 1 with Republicii Boulevard (Sinaia Sud), 2021.
10. Feasibility Study and Technical Execution Project for - Construction of a road overpass at the intersection of DN 1 with Ferdinand Boulevard (Sinaia Nord), 2021.
11. Feasibility Study and Technical Execution Project for - Construction of an underground pedestrian passage / above ground pedestrian passage in Comarnic central square - intersection DN 1 with Ghiosesti Street; - Construction of an underground pedestrian passage above ground Comarnic Town Hall, 2021.
12. Feasibility Study and Technical Execution Project for: - Underground/underground pedestrian passage - intersection DN 1 with Crinului Street (Poiana Tapului); - Underground pedestrian passage - intersection DN 1 with Telecabinei Street (Busteni); - Underground pedestrian passage - intersection DN 1 with Panduri Street (Predeal), 2021.
13. Recognizing Outstanding Achievement in Delivering "Vision Zero" Road Traffic Injuries. Available online: https://www.irf.global/find-a-way-award/ (accessed on 20.11.2022).
14. Annual statistical report on road safety in the EU 2021 published by the European Road Safety Observatory Available online: https://eur-lex.europa.eu/legal-content/EN/ALL/ ?uri=celex% 3A32008L0096 (accessed on 20.10.2022).
15. Valletta Declaration on Road Safety from 29 March 2017, Valletta, the published by the European Comission. Available online: https://road-safety.transport.ec.europa.eu/news-events/news/ valletta-declaration-road-safety-2017-03-29_en (accessed on 21.10.2022).
16. National Strategy for Road Safety 2021 - 2030 approved by Government Decision no. 682 of 25.05.2022. Available online: https://www.google.ro/url?sa=i&rct=j&q=&esrc= s&source= web&cd=&cad=rja&uact=8&ved=0CAIQw7AJahcKEwjYgJzhh8X_AhUAAAAAHQAAAAQAw&url=https%3A%2F%2Fwww.mt.ro%2Fweb14%2Fdocumente%2Facte_normative%2F2022%2F04_16%2FStrategia%2520Nationala%2520pentru%2520Siguranta%2520Rutiera%2520-%25202022-2030% 2520Anexa%25201.docx &psig =AOvVaw3HBFHJ0QRQ_rerOd4ooTBv&ust=1686910975121515&cshid=1686824624526338 (accessed on 20.10.2022).
17. Site of European Comission about EU Road Safety policy. Available online: https://road-safety.transport.ec.europa.eu/eu-road-safety-policy_en (accessed on 26.10.2022).

Citation: Pavăl, F.F.; Bricicaru, I. Improving road safety on the national road network in Romania through pilot solutions. *Journal of Engineering Science* 2023, 30 (2), pp. 59-71. https://doi.org/10.52326/jes.utm.2023.30(2).05.

Submission of manuscripts: jes@meridian.utm.md

Journal of Engineering Science *Vol. XXX, no. 2 (2023), pp. 72 - 80*
Fascicle *Industrial Engineering* *ISSN 2587-3474*
Topic *Materials Science and New Technologies* *eISSN 2587-3482*

https://doi.org/10.52326/jes.utm.2023.30(2).06
UDC 548:535

OPTICAL PROPERTIES OF $HgGaInS_4$ CRYSTALS

Andrei Tiron, ORCID: 0000-0003-2077-4014

Technical University of Moldova, 168 Stefan cel Mare Blvd., Chisinau, Republic of Moldova
*Corresponding author: Andrei Tiron, *andrei.tiron@scec.utm.md*

Received: 05. 15. 2023
Accepted: 06. 10. 2023

Abstract. Luminescence, transmission, reflection, and wavelength modulation transmission and wavelength modulation reflection spectra of $HgGaInS_4$ crystals were researched in the temperature range of 300-10 K. This article discusses the various features observed in the spectra of $HgGaInS_4$ crystals. The dependence on temperature of the energy gap is shown. Spectra of wavelength modulation transmission have minima a_1, a_2, and a_3, which vary with temperature and are caused by indirect transitions L-Γ with phonon absorption and emission. Spectra of thicker crystals have more features caused by the same indirect transitions. The photoluminescence show a strong maximum at 2.43 eV, attributed to radiative recombination of free excitons. These various features have significant implications for the understanding of the electronic and optical properties of $HgGaInS_4$ crystals.

Keywords: *Photouminescence, transmission, reflection, wavelength modulation transmission and reflection, absorption, emission.*

Rezumat. Au fost cercetate spectrele de luminescență, de transmisie, de reflexie și modulate în funcție de lungimea de undă a transmisiei și reflexiei ale cristalelor $HgGaInS_4$ în intervalul de temperatură 300-10 K. În acest articol se discută diferite caracteristici observate în spectrele cristalelor $HgGaInS_4$. Este prezentată dependența de temperatură a energiei de bandă. Spectrele de modificare a transmisiei în funcție de lungimea undei, cu minime a_1, a_2 și a_3, care variază cu temperatura și sunt cauzate de tranziții indirecte L-Γ cu absorbție și emisie de fononi. Spectrele cristalelor mai groase au mai multe caracteristici cauzate de aceleași tranziții indirecte. Spectrele de fotoluminescență arată un maxim puternic la 2.43 eV, atribuit recombinării radiative a excitonilor liberi. Aceste diferite caracteristici au implicări semnificative pentru înțelegerea proprietăților electronice și optice ale cristalelor $HgGaInS_4$.

Cuvinte cheie: *Luminescență, transmisie, reflexie, transmisie și reflexie modulate în funcție de lungimea de undă, absorbție, emisie.*

1. Introduction

Crystals $HgGaInS_4$ formed when defect chalcopyrite $HgGa_2S_4$ interacts with spinel $HgIn_2S_4$ and has layered structure. The lattice structure of $HgGaInS_4$ crystals consists of an arrangement of anions in a hexagonal close-packed structure, with layers of cations occupying particular arrangement both voids in the shape of tetrahedrons and octahedrons [1].

The hexagonal lattice of $HgGaInS_4$ crystals has unit cell parameters (lengths of the cell edges) of a = b = 0.39 nm and c = 3.14 nm [1]. $HgGaInS_4$ crystals exhibit similar chemical, crystalline and electrophysical properties compared to $ZnIn_2S_4$, $CdGaInS_4$, $CdIn_2S_2Se_2$ crystals [2].

The highly pronounced layered structure of $ZnIn_2S_4$ crystals, which belong to the $A^{II}B_2^{III}C_4^{VI}$ group of ternary semiconducting compounds, makes them particularly interesting and has attracted the attention of researchers, leading to numerous experimental studies [3-4]. These crystals possess photo-sensitivity and exhibit photoluminescence [5-6], showcasing intriguing optical properties.

The classic thiospinel structure is the crystalline form of $HgIn_2S_4$ compounds. The optical properties of compounds in this group have been predominantly studied using crystals like $ZnIn_2S_4$, $ZnAl_2Se_4$, and $CdGa_2S_4$ [7-13]. These crystals are utilized in various optical filters and nonlinear optical devices. Investigated materials such as $HgIn_2S_4$ and $HgGa_2Se_4$ are intriguing due to their linear and nonlinear optical characteristics, as well as their narrow band gap of 1.2-1.6 eV [9,14].

2. Materials and Methods

The single crystals of $HgGaInS_4$ were grown by the gas transport method in ampoules. The material was grown with mirror-like surfaces with dimensions of ~10x7 mm^2. The plates had different thicknesses (0.01-3 mm) and were easily cleavable. Monocrystals of nanoscale thickness (50 nm) were visually distinguishable by their color. The spectra at low temperatures of the material placed in a helium cryostat LTS-22 C 330 cryogenic optical system were obtained using an MDR-2 spectrometer with an aperture with a ratio of 1:2 and a linear dispersion of 0.7 nm/mm. The optical system of the MDR-2 spectrometer is shown in Figure 1.

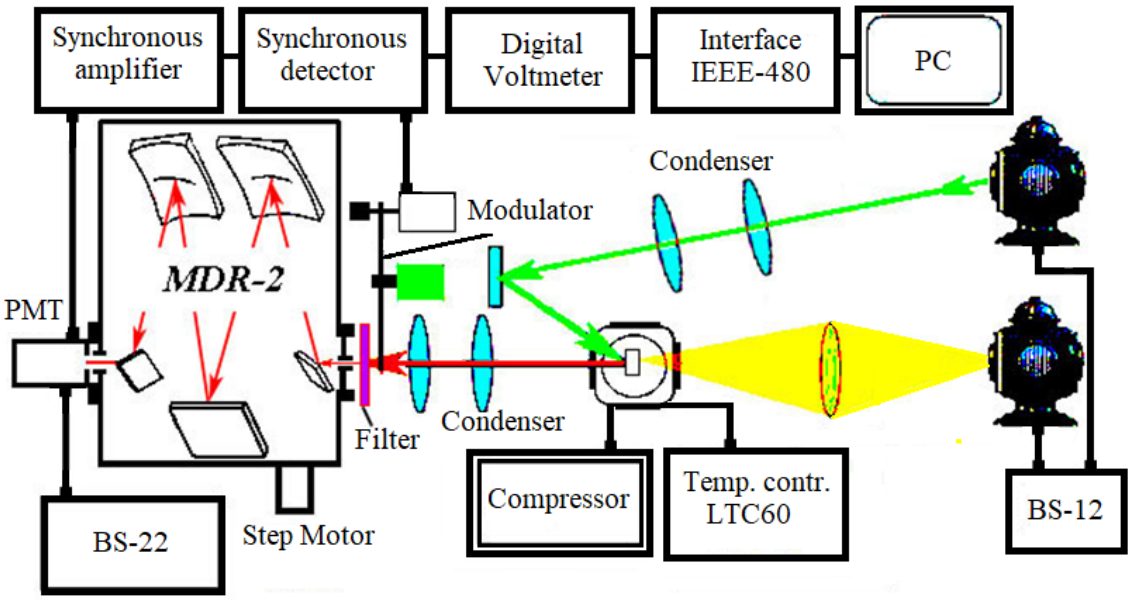

Figure 1. Schematic representation of set-up based on single spectrometer MDR-2 for transmission and reflection spectra registration.

The photoluminescence spectra were measured using the double-beam spectrophotometer SDL-1 with a light amplification ratio of 1:2 and a linear dispersion of 0.7 nm/mm. The optical system of SDL-1 is shown in Figure 2.

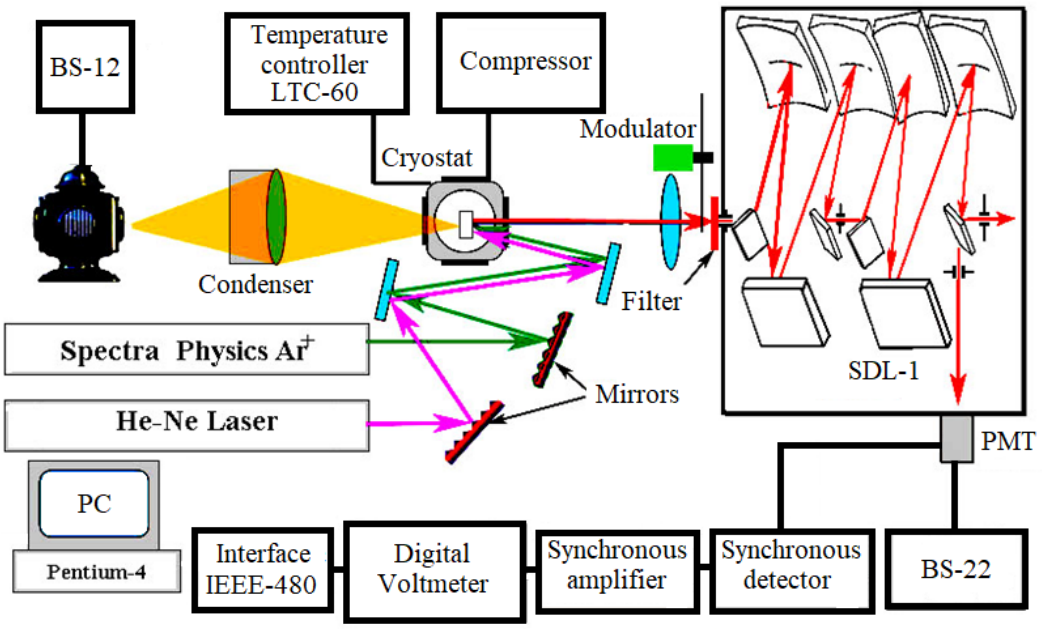

Figure 2. Scheme of measurement installation based on double spectrometer SDL-1 for photoluminescence spectra registration.

3. Results

Initial results on the absorption and photoluminescence of $HgGaInS_4$ crystals have been previously investigated [2]. The energy gap of $HgGaInS_4$ is equal to 2.41 eV at temperature 300 K and 2.46 eV at 80 K [2]. It was also noted that the exponential tail of the absorption edge is caused by the existence of states that are distributed quasi-continuously [15].

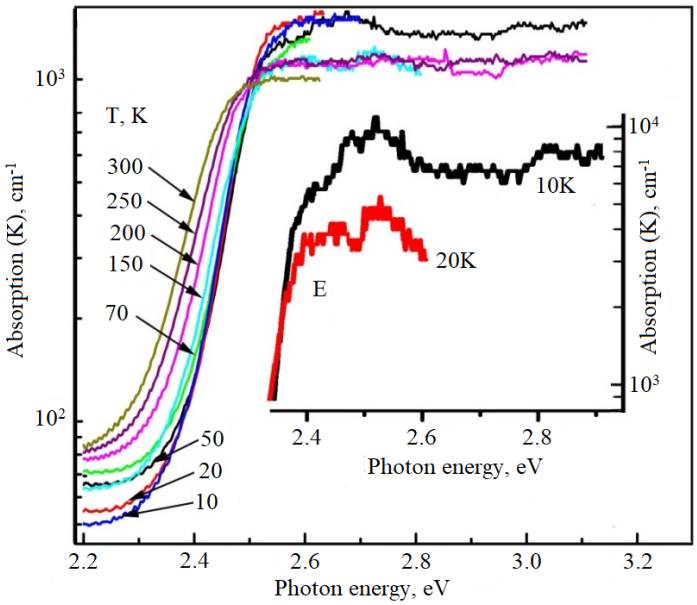

Figure 3. Absorption edge of $HgGaInS_4$ crystals, with thicknesses 0.1-0.6 μm within the temperature interval of 300-10 K and with a thickness of 1.2 μm (insert).

The newly discovered layered phase of $HgGaInS_4$ has a crystalline structure that includes empty spaces or vacancies within the cation lattice and the atoms in the cation sublattice are randomly distributed. This material is an electron semiconductor, with a band gap of 2.41 eV, high sensitivity to light, strong photoluminescence. In the band gap, there are exponentially distributed electron traps (with a characteristic energy of about 65 meV) near the conduction band bottom, and several distinct energy levels positioned roughly at 0.01, 0.11, and 0.2 eV above the top of the valence band. The initial two levels are associated with radiative electron transitions from donor-like states that are exponentially distributed. The third level is a sensitizing level. The slope of electron transitions from the valence band to quasi-

continuously distributed states in the exponential region of the absorption edge remains constant regardless of temperature.

Figure 3 shows the spectra of absorption of $HgGaInS_4$ thicknesses of crystals 0.1-0.6 μm at different temperatures in the interval of 300-10 K. Decreasing temperature leads to the absorption edge shifts towards higher energies. Measurements were conducted also on crystals with thicknesses of 1-1.2 μm in the range where absorption coefficients are higher than 10^3 cm^{-1} (see insert from Figure 3). Maxima can be detected on the spectra at energies of 2.42-2.53 eV.

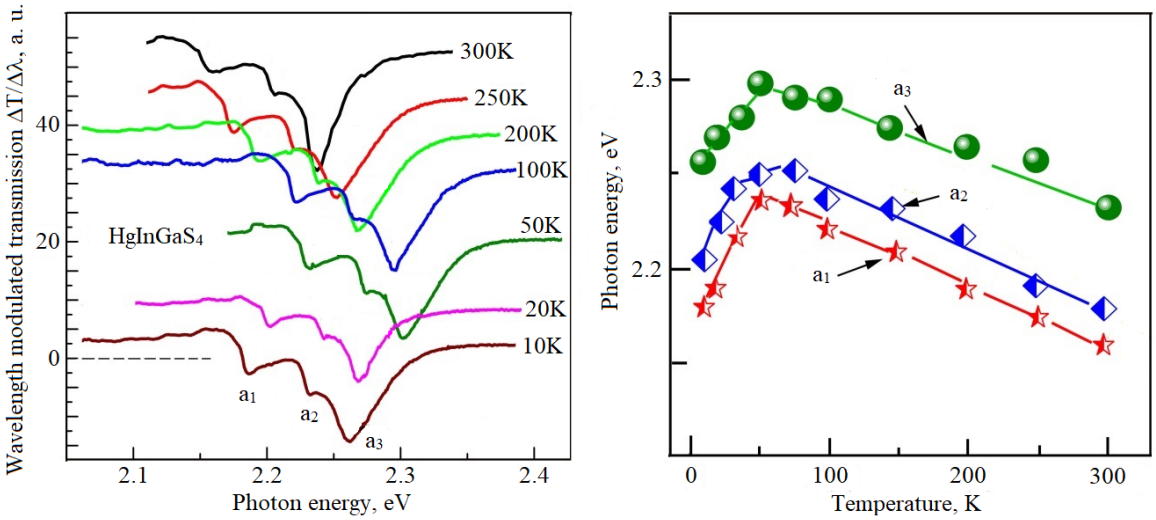

a) b)

Figure 4. Temperature dependence of wavelength modulation transmission (ΔT/Δλ) (a) and of a_1, a_2 and a_3 minima positions (b).

The spectra of the wavelength modulation transmission change ΔT/Δλ of $HgGaInS_4$ crystals at temperatures of 10-300K exhibit features (minima) a_1, a_2, and a_3, the energy positions of which vary with temperature, as shown in Figure 4a and Figure 4b, positions of peaks is shown in table 1.

Table 1

Temperature values and peak positions used in the research

Temperature, K	Peak position, eV
10	a_1 – 2.188
	a_2 – 2.231
	a_3 – 2.261
20	a_1 – 2.191
	a_2 – 2.242
	a_3 – 2.269
50	a_1 – 2.232
	a_2 – 2.273
	a_3 – 2.303
100	a_1 – 2.222
	a_2 – 2.267
	a_3 – 2.295
200	a_1 – 2.193
	a_2 – 2.241

Continuation Table 1

	a_3 – 2.269
250	a_1 – 2.175
	a_2 – 2.224
	a_3 – 2.252
300	a_1 – 2.161
	a_2 – 2.206
	a_3 – 2.237

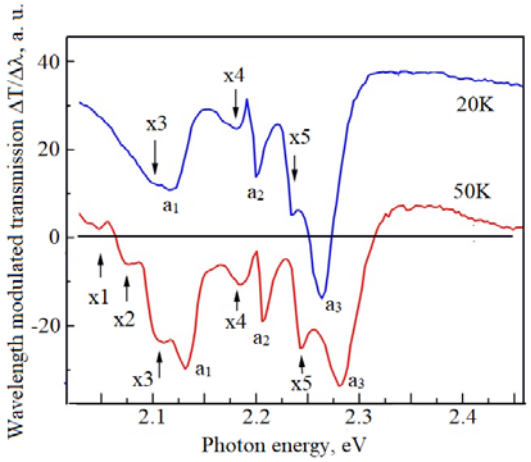

Figure 5. Spectra of wavelength modulation transmission (ΔT/Δλ) for $HgGaInS_4$ crystals with a thickness of 600μm at temperatures of 20 and 50K.

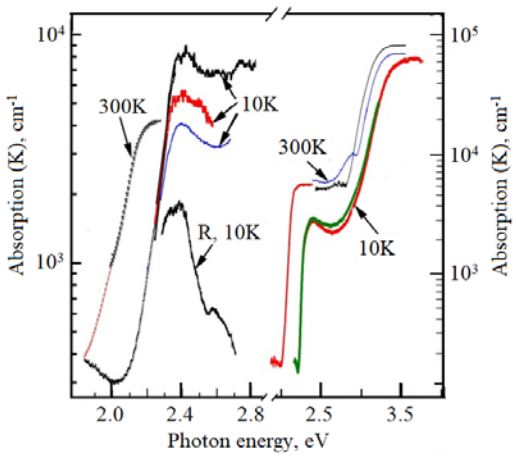

Figure 6. Spectra of absorption (K) of $HgGaInS_4$ with different thicknesses (right side – 0.5mm, left side - 0.1mm), at temperatures of 10 K and 300 K.

On the other hand, massive crystals with thickness about (600 μm) exhibit minima x1-x5, as shown in Figure 5. We assume that x1-x5 and a_1-a_3 are caused by indirect transitions L-Γ (E_g^{ind}-2.2-2.3 eV) with phonon absorption and emission. Thicker crystals and additional investigations are required for a more accurate determination of this interval.

Figure 6 shows the shift of the absorption edge spectra of $HgGaInS_4$ crystals with a thickness of 0.5 mm in the temperature interval of 300-10 K. As seen from the spectra, at temperature 300K the absorption edge starts at 1.9 eV, at temperature 10 K, at 2.08 eV. At an absorption coefficient of 10^3 cm^{-1}, the temperature coefficient of the absorption edge shift (ΔEg/ΔT) equal to $8.1 \cdot 10^{-4}$ eV/K. Decreasing temperature leads to a shift of the absorption edge towards higher energies. At absorption coefficients of $3 \cdot 10^3$ cm^{-1}, coefficient of the temperature shift of the absorption edge (ΔEg/ΔT) is $6 \cdot 10^{-4}$ eV/K, and at an absorption coefficient of $3 \cdot 10^4$ cm^{-1}, *β*(ΔEg/ΔT) is twice as small and equal to $-3 \cdot 10^{-4}$ eV/K. These data practically confirm the concept that changes in temperature have a weaker effect on deep energy levels and high-energy electronic transitions.

Figure 7 shows the reflection spectra of 0.5 mm thick $HgGaInS_4$ crystals at temperature 10 K in the high absorption region. In the energy interval of 2.4-2.6 eV, a weak change in reflection spectra is observed with a maximum at 2.4 eV. The change in intensity from the maximum to the minimum occurs within 6-7%. This characteristic is more clearly distinguished in the reflection spectra wavelength modulation. The observed R feature is due to direct electronic transitions into the exciton zone at the Γ point.

Measured excitonic reflection ($R_{exper.}$) and calculated using a one-oscillator model ($R_{calc.}$) spectra is presented in Figure 5.

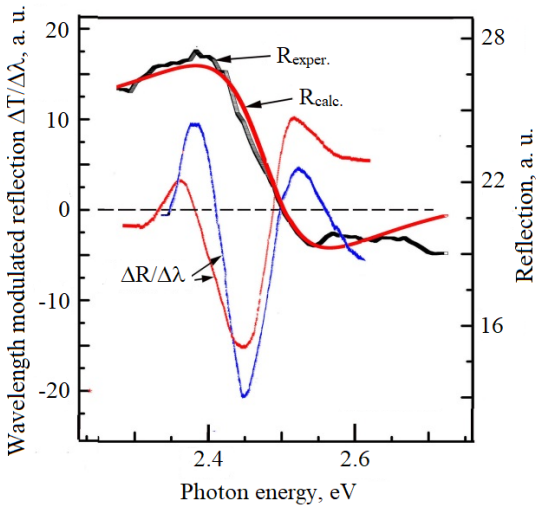

Figure 7. Reflection spectra and spectra of wavelength modulation reflection (ΔR/Δλ) of $HgGaInS_4$ crystals with a thickness of 0.5mm at temperature 10K.

The resonant value of the excitonic transition is 2.43 eV, the background dielectric constant is 9.83, the splitting between longitudinal and transverse components is 13 meV, and the factor of damping is about 187. Naturally, with such a large damping factor, the excitonic reflection spectra contour is weakly distinguished.

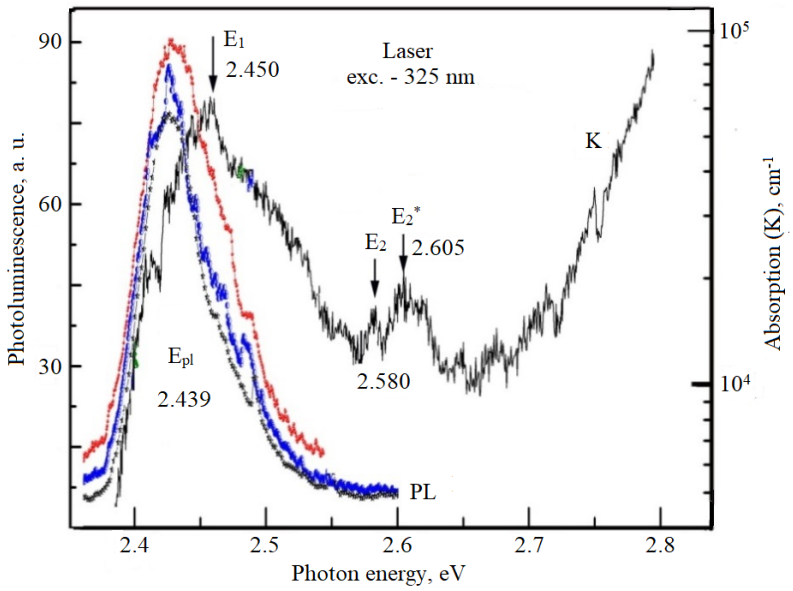

Figure 8. Absorption spectra of $HgGaInS_4$ crystals with a thickness of 0.1 μm and photoluminescence spectra with excitation wavelength 325 nm laser at 10 K.

Absorption spectra of crystals with a thickness of 0.1 μm clearly show peaks at E_1 (2.450 eV), E_2 (2.580 eV), and E_2^* (2.605 eV), as shown in Figure 8. The photoluminescence spectral dependence of $HgGaInS_4$ crystals with excitation wavelength 325 nm at temperatures of 20 K and 10 K shows an intense peak at 2.439 eV, as can be seen Figure 8. The comparison of the absorption and photoluminescence peaks suggests that the E_1 absorption peak and E_{PL} photoluminescence peak are associated with the excitonic transition. The E_2 and E_2^* absorption peaks are associated with the n=2 and n=3 states, respectively. In this case, the exciton binding energy (Rydberg constant) is 180 meV, and the bandgap width is 2.619 eV.

The interference fringes are clearly visible in the spectra, and as can be seen, the interference spectra extend more into the short-wavelength region as the crystals become thinner. The refractive index was determined by using the relation between the energy positions of the observed maxima (or minima) and the refractive index:

$$\boldsymbol{n} = \frac{\boldsymbol{M}}{2\boldsymbol{d}\left(\frac{\boldsymbol{1}}{\boldsymbol{\lambda_1}} - \frac{\boldsymbol{1}}{\boldsymbol{\lambda_2}}\right)} \quad , \tag{1}$$

M equal to 1 for nearby maxima (minima); $\boldsymbol{\lambda_1}$ and $\boldsymbol{\lambda_2}$ position value (nm) for maxima (minima) in interference spectra.

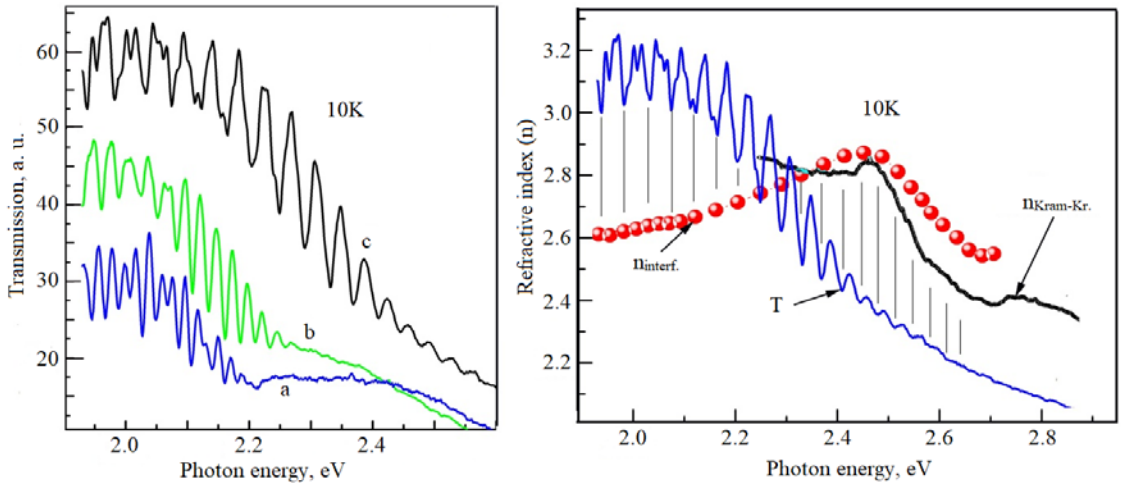

a) b)

Figure 9. Transmission spectra of crystals with different thicknesses (a-270 μm, b-120 μm, c-0.1 μm) at 10 K (a). Dependence of the refractive index n(interf.) calculated from interference transmission spectra (T) and from the Kramers-Kronig calculation of the reflection spectra (n-Kram-Kr) (b).

The spectral dependence of the refractive index $n_{interf.}$ obtained from the calculation of interference transmission spectra (T) is presented in Figure 9b. The obtained spectra are compared with the refractive index spectral dependence $n_{Kram-Kr.}$ obtained through calculations of the reflection spectra R applying the Kramers-Kronig equation. The spectral dependences of the reflection coefficient (R) and the optical constants refractive index (n), extinction coefficient (k), real part of permittivity (ε_1), imaginary part of permittivity (ε_2), and phase (ϕ) are interconnected by Kramers-Kronig relationships. These relationships allow the calculation of one parameter from another and are useful in analyzing the optical properties of materials.

$$\begin{cases} r = \dfrac{N-1}{N+1} = \dfrac{n+ik-1}{n+ik+1} \\ r = \sqrt{R}e^{-i\varphi} = \sqrt{R}\left(\cos\varphi - i\sin\varphi\right) \end{cases} \Rightarrow \begin{cases} n = \dfrac{1-R}{1-2\sqrt{R}\cos\varphi + R} \\ k = \dfrac{2\sqrt{R}\sin\varphi}{1-2\sqrt{R}\cos\varphi + R} \end{cases} \tag{2}$$

As can be seen, the refractive index values and the spectral dependence obtained by the two methods are in good agreement.

.

4. Discussion

The study of the $HgGaInS_4$ crystals revealed interesting properties related to their optical absorption, reflection, and transmission spectra. The absorption edge of the material shifts towards higher energies as the temperature decreases, indicating that the temperature has a lesser effect on deep energy levels and high-energy electronic transitions [1]. The thickness of the crystal affects the appearance of features in the absorption spectra, which may be caused by indirect transitions with phonon absorption and emission [16].

The reflection spectra of the crystals exhibit a weak change in the intensity in the energy interval of 2.4-2.6 eV, with a maximum at 2.43 eV, which is attributed to direct electronic transitions into the exciton zone at the Γ point. The photoluminescence spectra also show peaks related to exciton modes [16].

The transmission spectra exhibit interference fringes that extend more into the short-wavelength region as the crystals become thinner, and the refractive index values obtained by the two methods (refractive index obtained from the calculation of interference spectra and obtained through calculations applying Kramers-Kronig equation) are in good agreement.

Overall, the study of the $HgGaInS_4$ crystals provided valuable insights into the optical properties of the material, which could be useful for applications in optoelectronics and photonics. Further investigations on the material's properties, particularly on thicker crystals, are required for a more accurate determination of the observed features and transitions.

5. Conclusions

The study of $HgGaInS_4$ crystals' spectra has revealed several significant features. The shift in the absorption edge towards higher energies with decreasing temperature indicates a temperature dependence of the bandgap energy. The wavelength modulation transmission spectra exhibit energy minima caused by indirect transitions L-Γ with phonon absorption and emission, and the spectra of thicker crystals have additional minima due to the same transitions. The weak change in the reflection spectra at energies between 2.4-2.6 eV, with a maximum at 2.4 eV, is resulted by direct electronic transitions to excitonic zone at the Γ point. Spectra of photoluminescence with an excitation by a 325 nm show a strong maximum at 2.21 eV, resulting from the radiative recombination of free excitons. The absorption edge temperature shift coefficient varies with the absorption coefficient, indicating that temperature changes affect deep energy levels and high-energy electronic transitions to a lesser extent. Overall, these results provide valuable insights into the electronic and optical properties of $HgGaInS_4$ crystals.

Acknowledgments: The author acknowledge financial support from the Ministry of Education, Culture and Research of Moldova under the Grant #20.80009.5007.20.

Conflicts of Interest: The author declares no conflict of interest.

References

1. Moldovyan, N. A.; Pyshnaya, N. B.; Radautsan, S. I. New Multinary Layered Chalcogenides with Octahedral and Tetrahedral Cation Coordination. *Jpn. J. Appl. Phys.* 1993, 32 (3), pp. 781-783 DOI 10.7567/JJAPS.32S3.781.
2. Moldovyan, N.A.; Chebotaru, V.Z. Growth and characteristics of $HgGaInS_4$ single crystals. *Cryst. Res. Technol.* 1990, 25, pp. 997-1005 https://doi.org/10.1002/crat.2170250904
3. Vaipolin, A. A.; Nikolaev, Yu. A.; Rud, V. Yu.; Rud, Yu. V.; Terukov, E. I.; Fernelius, N. Fabrication and properties of photosensitive structures of $ZnIn_2S_4$ single crystal. *Phys. Tech. Polupr.* 2003, 37 (2), pp. 187 – 191 DOI 10.1134/1.1548661

4. Xia, Y.; Li, Q.; Lv, K.; Li, M. Heterojunction construction between TiO_2 hollowsphere and $ZnIn_2S_4$ flower for photocatalysis application. *Applied Surface Science* 2017, 398, pp. 81–88 https://doi.org/10.1016/j.apsusc.2016.12.006
5. Xia, Y.; Li, Q.; Lv, K.; Tang, D.; Li, M. Superiority of graphene over carbon analogs for enhanced photocatalytic H2-production activity of $ZnIn_2S_4$. *Applied Catalysis B: Environmental* 2017, 206, pp. 344–352 https://doi.org/10.1016/j.apcatb.2017.01.060
6. Shen, S.; Guo, P.; Zhao, L.; Du, Y.; Guo, L. Insights into photoluminescence property and photocatalytic activity of cubic and rhombohedral $ZnIn_2S_4$. *Journal of Solid State Chemistry* 2011, 184, pp. 2250–2256 https://doi.org/10.1016/j.jssc.2011.06.033
7. Jiang, X. and Walter, R. L. Lambrecht Electronic band structure of ordered vacancy defect chalcopyrite compounds with formula $II-III_2-VI_4$. *PHYSICAL REVIEW B* 2004, 69 (3-15), pp. 035201-1 – 035201-8 https://doi.org/10.1103/PhysRevB.69.035201
8. Yousaf, M.; Saeed, M. A.; Isa, A. R. M.; Aliabad, H. A. R.; Sahar, M. R. An Insight into the Structural, Electronic and Transport Characteristics of XIn_2S_4 (X=Zn, Hg) Thiospinels using a Highly Accurate All-Electron FP-LAPW+Lo Method. *CHIN. PHYS. LETT.* 2013, 30 (7), pp. 077402-1 – 077402-5 DOI 10.1088/0256-307X/30/7/077402
9. Chen, Z.; Li, D.; Xiao, G.; He, Y.; Xu, Y. J. Microwave-assisted hydrothermal synthesis of marigold-like $ZnIn_2S_4$ microspheres and their visible light photocatalytic activity. *J. Solid State Chem.* 2012, 186, pp. 247-254 https://doi.org/10.1016/j.jssc.2011.12.006
10. Chen, Y.; Huang, R.; Chen, D.; Wang, Y.; Liu, W.; Li, X. and Li, Z. Exploring the Different Photocatalytic Performance for Dye Degradations over Hexagonal $ZnIn_2S_4$ Microspheres and Cubic $ZnIn_2S_4$ Nanoparticles. *ACS Appl. Mater. Interfaces* 2012, 4, p.2273-2279 https://doi.org/10.1021/am300272f
11. Chai, B.; Peng, T.; Zeng, P. and Zhang, X. Preparation of a MWCNTs/$ZnIn_2S_4$ composite and its enhanced photocatalytic hydrogen production under visible-light irradiation. *Dalton Trans.* 2012, 41, pp. 1179 -1186 https://doi.org/10.1039/C1DT11308A
12. Xu, Z.; Li, Y.; Peng, S.; Lu, G. and Li, S. NaCl-assisted low temperature synthesis of layered Zn-In-S photocatalyst with high visible-light activity for hydrogen evolution. *RSC Adv.* 2012, 2, pp. 3458-3466 https://doi.org/10.1039/C2RA01159J
13. Shen, S.; Guo, P.; Zhao, L.; Du, Y. and Guo, L. Insights into photoluminescence property and photocatalytic activity of cubic and rhombohedral $ZnIn_2S_4$. *J. Solid State Chem.* 2011, 184, pp. 2250-2256 https://doi.org/10.1016/j.jssc.2011.06.033
14. Ding, K.; Jia, W.; Zhang, Y. Electronic Structures and Optical Properties of $HgGa_2X_4$ (X = S, Se, Te) Semiconductors. *Chinese J. Struct. Chem.* 2013, 9, pp. 1307—1315
15. Anedda, A.; Casu, M. B.; Serpi, A.; Burlakov, I. I.; Tiginyanu, I. M.; Ursaki, V. V. Recombination in $HgGaInS_4$ single crystals. *Journal of Physics and Chemistry of Solids* 1997, 58(2), pp. 325-330 https://doi.org/10.1016/S0022-3697(96)00124-2.
16. Syrbu, N. N.; Tiron, A.; Zalamai, V. V. Electronic and optical properties of $HgIn_2S_4$ thiospinels. *Materials Research Express* 2019, 6(7), pp. 1-17, DOI 10.1088/2053-1591/ab17b0.

Citation: Tiron, A. Optical properties of $HgGaInS_4$ crystals. *Journal of Engineering Science* 2023, 30 (2), pp. 72-80. https://doi.org/10.52326/jes.utm.2023.30(2).06.

Submission of manuscripts: jes@meridian.utm.md

Journal of Engineering Science *Vol. XXX, no. 2 (2023), pp. 81 - 89*
Fascicle *Industrial Engineering* *ISSN 2587-3474*
Topic *Materials Science and New Technologies* *eISSN 2587-3482*

https://doi.org/10.52326/jes.utm.2023.30(2).07
UDC 622.361.16:621.798

CLAY-STARCH NANOCOMPOSITE COATINGS ON PAPER SUBSTRATE - A PROMISING FRONTIER IN ENVIRONMENTALLY FRIENDLY PACKAGING MATERIAL

Nikita Siminel, ORCID: 0000-0002-1055-7078

Technical University of Moldova, 168 Stefan cel Mare Blvd., Chisinau, Republic of Moldova
*Corresponding author: Nikita Siminel, *siminel.n@gmail.com*

Received: 03. 17. 2023
Accepted: 04. 27. 2023

Abstract. The growing concern for environmental sustainability has created an urgent need for the development of innovative and environmentally friendly packaging materials. Among the various options available, clay-starch nanocomposites have emerged as a promising avenue for improving the barrier properties and mechanical strength of paper substrates. In this scientific paper the importance of clay-starch nanocomposite coatings on paper substrate and highlight the role of computer simulations, especially molecular dynamics, in elucidating their structural and functional properties. It has been shown that phyllosilicates with a layer charge < 0.4 electrons per stoichiometric unit can intercalate starch in the interlayer space, forming a barrier for water vapor in the covering layer. Phyllosilicates with a shell charge of > 0.4 electrons per stoichiometric unit were not able to intercalate starch. Thus, clay-starch nanocomposites can provide limited water vapor transfer rates and can be recommended as a promising material for dry food packaging.

Keywords: *Molecular dynamics, montmorillonite, clay, water, diffusion, clay-coatings.*

Rezumat. Preocuparea tot mai mare pentru sustenabilitatea mediului a creat necesitatea urgentă de dezvoltare a materialelor de ambalare inovatoare și ecologice. Printre diferitele opțiuni disponibile, nanocompozitele argilă-amidon prezintă o cale promițătoare pentru îmbunătățirea proprietăților de barieră și a rezistenței mecanice a substraturilor de hârtie. În această lucrare se evidențiază importanța acoperirilor nanocompozite argilo-amidon pe substrat de hârtie și rolul simulărilor pe computer, în special a dinamicii moleculare în elucidarea proprietăților structurale și funcționale ale acestora. S-a demonstrat, că filosilicații cu o sarcină a stratului < 0,4 electroni pe unitate stoechiometrică pot intercala amidonul în spațiul interstrat, formând o barieră pentru vaporii de apă în stratul de acoperire. Filosilicații cu o sarcină de înveliș > 0,4 electroni per unitate stoechiometrică nu au fost capabili să intercaleze amidonul. Astfel, nanocompozitele argilă-amidon pot asigura viteze limitate de transfer al vaporilor de apă și pot fi recomandate ca material de perspectivă pentru ambalarea produselor alimentare uscate.

Cuvinte cheie: *dinamică moleculară, montmorillonit, argilă, apă, difuzie, acoperiri cu argilă.*

Abbreviations;

MD – Molecular Dynamics;
NaMt – Na^{+}-Montmorillonite;
CaMt – Ca^{2+}-Montmorillonite;
Th – Tetrahedral clay sheet;
Oh – Octahedral clay sheet;
AML – Amylose;
PEG200 – Poly(ethylene) glycol, MW = 200 g/mol
ADP – Atomic density profile.

1. Introduction

The ever-increasing demand for packaging materials, driven by the global rise in consumption and e-commerce, has led to the accumulation of vast amounts of non-biodegradable waste, causing significant environmental concerns. Addressing this issue necessitates the development of sustainable packaging solutions that minimize environmental impact while maintaining the required mechanical and barrier properties [1]. In this context, clay-starch nanocomposites have garnered substantial attention due to their unique combination of renewable and abundant components, as well as their potential to improve the performance of traditional paper-based packaging materials.

In the domain of packaging applications, starch is one of the promising biopolymer materials, because it is renewable, low in price, fully biodegradable and rather importantly, approved for food contact [2-5]. Starch based paper coatings improved barrier to water vapour, reducing water vapour transmission rate (WVTR) from 800 g/m^2.day for untreated paper down to 400 g/m^2.day for paper coated with starch and poly(ethylene glycol) [6]. The incorporation of clay minerals into different polymeric matrices has drawn a particular interest due to their potential to improve the barrier properties of formulated coatings. When montmorillonite clay was added to starch polymer matrix, the barrier properties were significantly improved, reducing the WVTR to lower than 200 g/m^2.d [7]. Furthermore, adding PEG to the starch/clay nanocomposite plummet the WVTR to remarkable 10 g/m^2.d [5, 6], which is competitive with some of the conventional latexes.

Clay minerals, such as montmorillonite, possess layered structures consisting of stacked silicate sheets, with exchangeable cations in the interlayer spaces [8]. The incorporation of clay nanoparticles into starch matrices creates a synergistic effect, resulting in nanocomposites with enhanced mechanical strength, gas barrier properties, and thermal stability. These characteristics make clay-starch nanocomposites highly suitable for coating applications on paper substrates, imparting them with improved functionalities. The clay type and, in particular, layer charge distribution, however, has significant effect on the barrier properties of formulated coatings. In some studies addition of montmorillonite (Mt) sometimes had no effect or even a slight negative effect on the resultant barrier properties [9-11]. One explanation of that has been difference in the polymer intercalation dynamics for various Mts [5, 6]. It was concluded that starch-PEG/clay based coatings would have good barrier properties only when both starch and plasticiser coexist in the interlayer of clay. Adsorbed PEG onto the Mt surfaces forms a strongly constrained layer with very low oxygen permeability [6]. The organisation of plasticiser and bio-polymer in the clay interlayer, however, is not accessible through experimental techniques. Therefore, molecular simulation of PEG-starch/clay nanocomposites may provide insight on the nanocomposite interlayer

structure in relation to the clay type, and, as a result on the mechanism of the formation of coatings with high barrier properties.

Computer simulations, particularly molecular dynamics (MD), have emerged as indispensable tools for investigating the behavior and properties of materials at the atomic and molecular scales. By simulating the interactions between clay nanoparticles, starch molecules, and the paper matrix, MD simulations enable researchers to gain valuable insights into the structural organization, interfacial interactions, and mechanical behavior of clay-starch nanocomposite coatings [3, 4, 12, 13]. Furthermore, MD simulations facilitate the exploration of the effects of various processing parameters, such as temperature, humidity, and nanoparticle concentration, on the overall performance of the coating material.

In this paper, we present a comprehensive study on the computational modeling of clay-starch nanocomposite coatings. Our work aims to elucidate the mechanisms underlying the improved barrier properties and mechanical strength exhibited by these coatings. Through systematic molecular dynamics simulations, we investigate the nanoscale interactions between clay nanoparticles, starch molecules, and the paper matrix, considering different clay loadings and coating architectures. Additionally, we explore the influence of processing conditions on the structural arrangement and properties of the nanocomposite coatings.

The findings of this research will provide critical insights into the design and optimization of clay-starch nanocomposite coatings for environmentally friendly packaging materials. By harnessing the advantages of computer simulations, we can accelerate the development of novel coatings with enhanced performance, reduced environmental impact, and improved recyclability.

2. Materials and Methods

The model framework for Montmorillonite (Mt) was generated from a pyrophyllite crystal structure. A number of Mt models were investigated with a selection of charge locations and two exchange cations (Na^{+}, Ca^{2+}). Starch is one popular natural polymer material due to the fact that it can be easily produced from plants, e.g. potato, corn, cassava etc. [14]. Starch consists of two types of molecules; amylose (AML) and amylopectin. It it generally accepted that amylose is amorphous polymer whereas amylopectin has semicrystalline structure [14]. Through analysis of the XRD traces of the thermoplastic starch plasticised with urea, it was shown that freshly prepared nanocomposite contained starch in its amorphous form [15]. Therefore, for our computer simulations we created a model of amorphous amylose to represent starch/clay interactions. Amylose is a spiral polymer made up of D-glucose units. Each molecule of amylose in the developed model consisted of five D-glucose units resulting in total molecular weight of 828.7 $g \cdot mol^{-1}$. The initial binary and tri-systems were constructed by randomly distributed Amylose (AML) or AML and Poly(ethylene) glycol (PEG200) molecules with pre-equilibrated water molecules at desired ratios. Starting amylose and water content for AML/Mt system was 0.7 g_{AML}/g_{clay} and 0.07 gH_2O/gclay respectively. Water content of 7 wt% is reported from experimental observation of starch based clay nanocomposites [16]. For AML-PEG/Mt system, a broad range of PEG200 and H_2O concentrations, ranging from 0 to 0.35 g_{PEG200}/g_{clay} (0 to ~7.1 PEG200·*uc*-1) and 0 to 0.2 gH_2O/gclay (0 to ~16.5 $H_2O \cdot uc^{-1}$) respectively were used (Figure 1).

Molecular Dynamics simulation is a technique used to compute the equilibrium and transport properties of a classical many-body system by using essential information about a

system's dynamics, usually resolved at atomistic detail. Molecular dynamics simulations were performed using the Nosé-Hoover thermostat and DL_POLY simulation package [17] with a 1.0 ps relaxation time. For the NPT simulations, a Nosé-Hoover barostat was utilised to control the pressure. Interatomic interactions were evaluated using a time step of 0.001 ps, and three-dimensional periodic boundary conditions were employed with a cutoff of 15 Å for short-range interactions. Interatomic potentials for the clay and interlayer ions were obtained from the CLAYFF force field developed by Cygan et al. [18]. Each atom in CLAYFF force field has an assigned partial charge derived from DFT calculations, and the flexible TIP3P/Fs water model [19] is incorporated to describe water.

3. Results and Discussion

A. Adsorption Thermodynamics

The adsorption analysis employs a simple model of montmorillonite – amylose interface, containing one layer of Mt and one single chain of AML. MD simulations were used in order to investigate the adsorption process of AML on hydrated clays and influence of clay charge location on this process. The simulation cell of this model is shown in Figure 1. The free energy of adsorption was calculated from potentials of mean force (PMF).

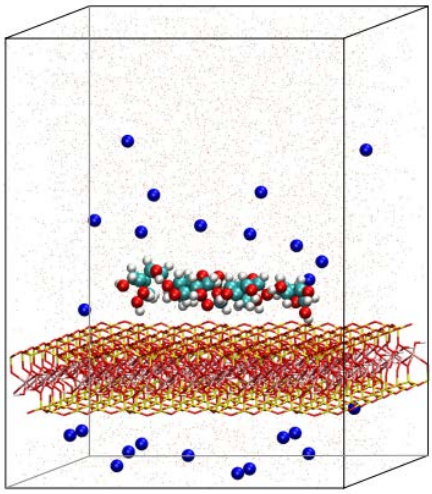

Figure 1. Starting structure of the AML/Mt adsorption model. The centre of mass of single amylose molecule in aqueous environment is positioned at 3.5 Å above the clay surface.

Each AML was placed parallel to the selected Mt surface with its centre of mass at a distance of 3.5 Å above the surface. Two main orientations of amylose molecule were considered – parallel to (100) direction (Fig. 2(a)) and parallel to (010) direction (Fig. 2(b)). Thereafter, into each system 2400 of pre-equilibrated H_2O molecules were added.

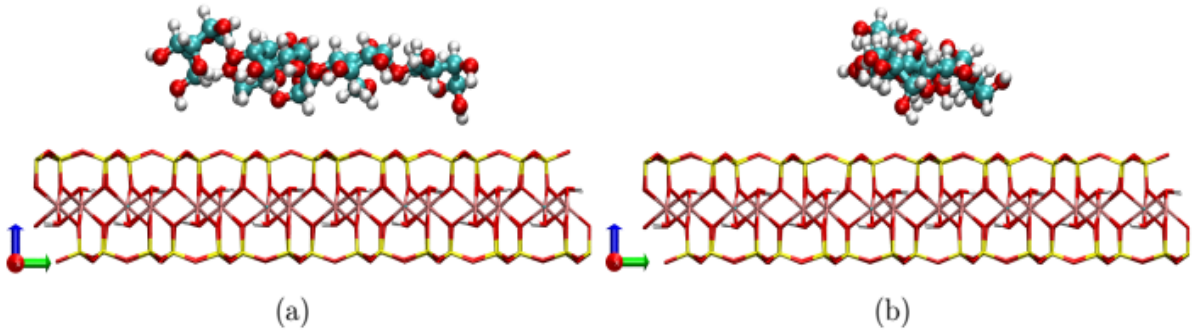

Figure 2. Definition of the AML orientations of te AML/Mt adsorption model. The amylose molecule is oriented along (a) (010) and (b) (100).

All simulations were performed in NPT ensemble at 300 K and 1 atm. The simulation timestep was 1 fs. Simulation lasted for 10 ns. The data from final 5 ns was used for analysis. All bonds were constrained. The equilibration was established through monitoring two parameters – structural and energetical stability. Structural stability of a molecule was assessed by calculating the root-mean-square deviation (RMSD) of AML molecule. Energy stability was judged by the total instantaneous interaction energy between the AML and Mt, which is defined as;

$$E_{int}(t) = E_{AML+Mt}(t) - E_{AML}(t) - E_{Mt}(t), \quad (1)$$

where E_{int} refers to the interaction energy between the AML and Mt, E_{AML+Mt} is the total energy of the AML and Mt, and E_{AML} and E_{Mt} are the internal energies of AML and Mt, respectively. The instantaneous RMSD of the AML and interaction energy between the AML and Mt are presented in Figures 3(a) and 3(b), respectively. All twelve studied models reached equilibration at around 4 ns of the MD simulation. Therefore, the data from final 5 ns was used for analyses.

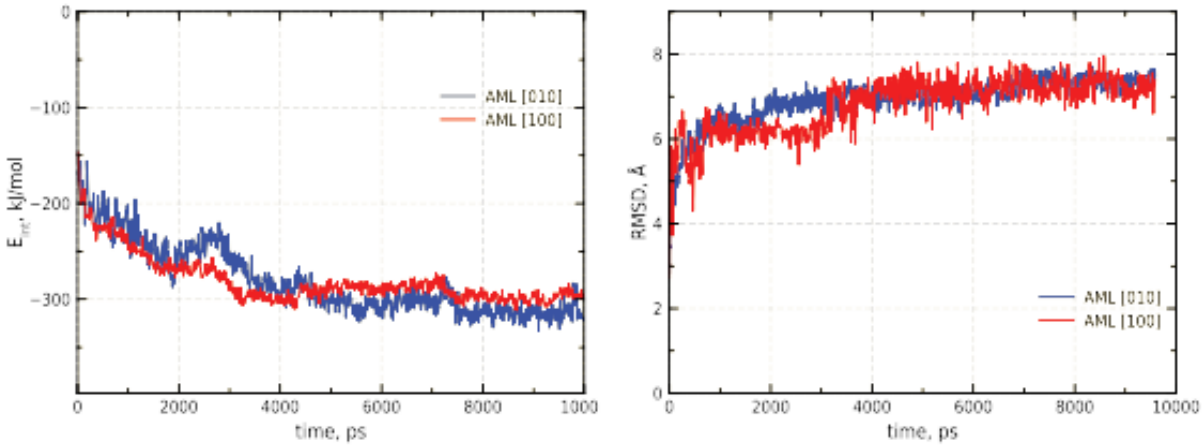

Figure 3. Variation of (a) E_{int} and (b) RMSD of amylose molecules adsorbed onto NaMt in different adsorption configurations with simulation time.

B. Swelling Dynamics and Interlayer Structure

A total of 12 simulated swelling curves for NaMt and CaMt models are shown in Figures 4 and 5, respectively. Error bars based on standard deviation calculated from block averaging over the last 1 ns of simulations are less than data symbol, therefore are not visible on the plots.

Unlike swelling curves of hydrated montmorillonite or PEG/Mt systems, intercalation of amylose in the Mt do not suggest formation of highly ordered polymer structures within the interlayer. Most simulated clays swell gradually with increase of polymer content in the interlayer until reaching an "equilibrated" basal spacing of ~21-22 Å. Similar d-spacings were observed by many experimentalists who were investigating intercalation of starch in montmorillonites under ambient conditions [6-9]. This is revealed as a plateau at higher AML content on all simulated swelling curves (Figures 4 and 5). It is very important result obtained from simulation and indicates the preferable interlayer organisation of amylose.

Distribution of carbon atoms for all studied systems suggests formation of pseudo bilayer of starch in the interlayer. Amylose can produce larger number of conformations than PEG, therefore its ADPs are so distorted (Fig. 6).

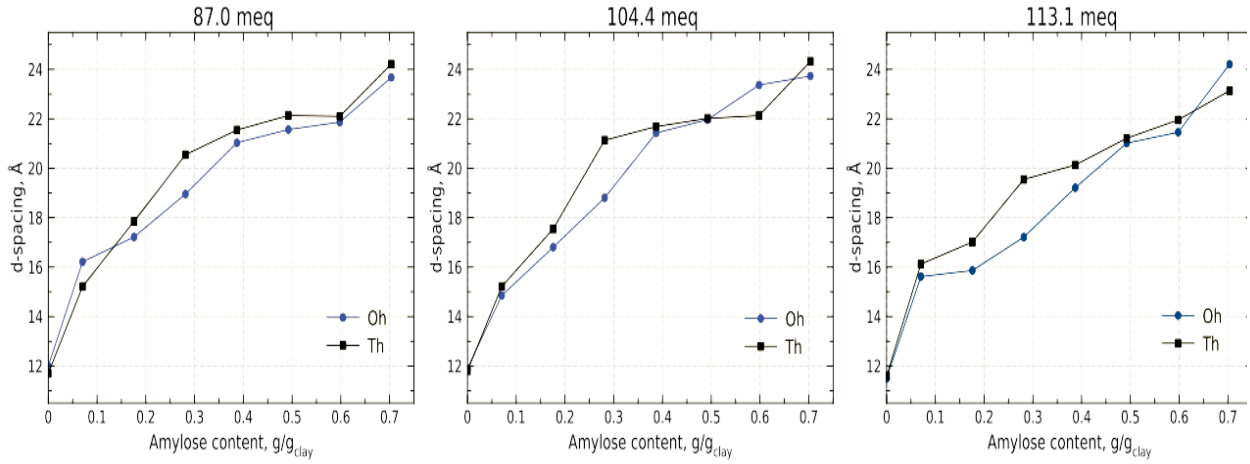

Figure 4. Swelling curves of NaMt as a function of amylose content in the interlayer from MD simulations at 300 K and 1 atm. Swelling curves are shown for clays with various net charge distribution.

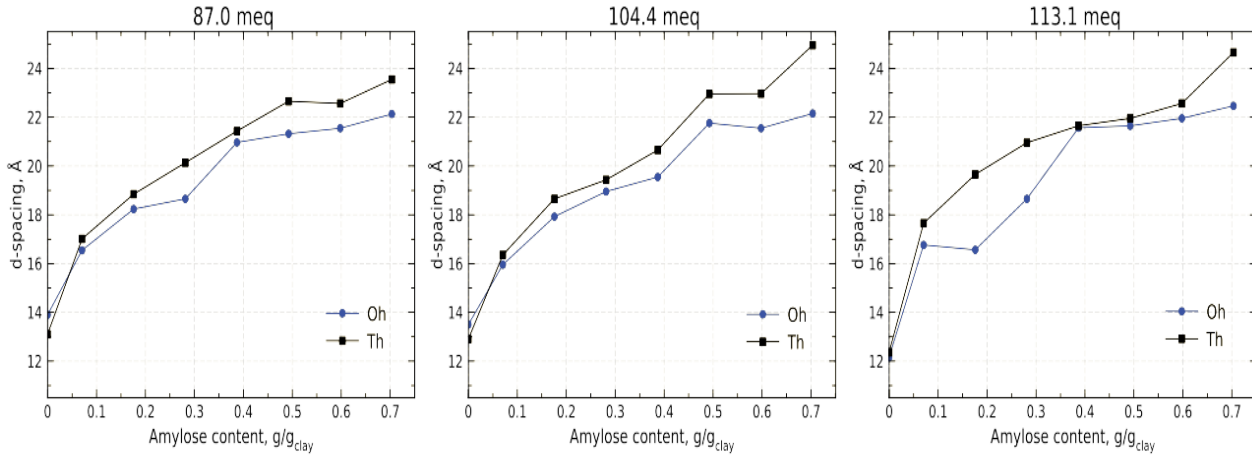

Figure 5. Swelling curves of CaMt as a function of amylose content in the interlayer from MD simulations at 300 K and 1 atm. Swelling curves are shown for clays with various net charge distribution.

Interestingly, even at relatively low water concentration (~0.07 g_{H2O}/g_{clay}), a water bilayer is found in the interlayers of all samples. It is expelled from the middle of the interlayer and distinct, sharp OW peaks are positioned between the basal surface of clay and layer of AML indicating hydrophilic nature of amylose and formation of a network of hydrogen bonds. Similar behaviour is right for the divalent exchangeable cations.

Another peculiar conclusion that can be drawn from the simulated swelling curves is that spacings of AML/Mt nanocomposites based on the low charge clays are overall higher by approximately 0.9-1.2 Å in the region of 0.3 g_{AML}/g_{clay} than those that are based on the high charge clays. Similar conclusion was drawn from investigation of barrier properties of starch-clay nanocomposites based on various clay types [4, 20, 21]. There are evidences that high charge clay do not uptake starch in the interlayer at all [8]. It is, however impossible to investigate directly by the methods presented here, as content of organic material in the interlayer is fixed and cannot escape from the clay gallery.

Clays with isomorphous substitutions occurring in tetrahedral sheet (Th charge) produce higher basal spacing compared to those with charge deficit in the octahedral sheet (Oh charge).

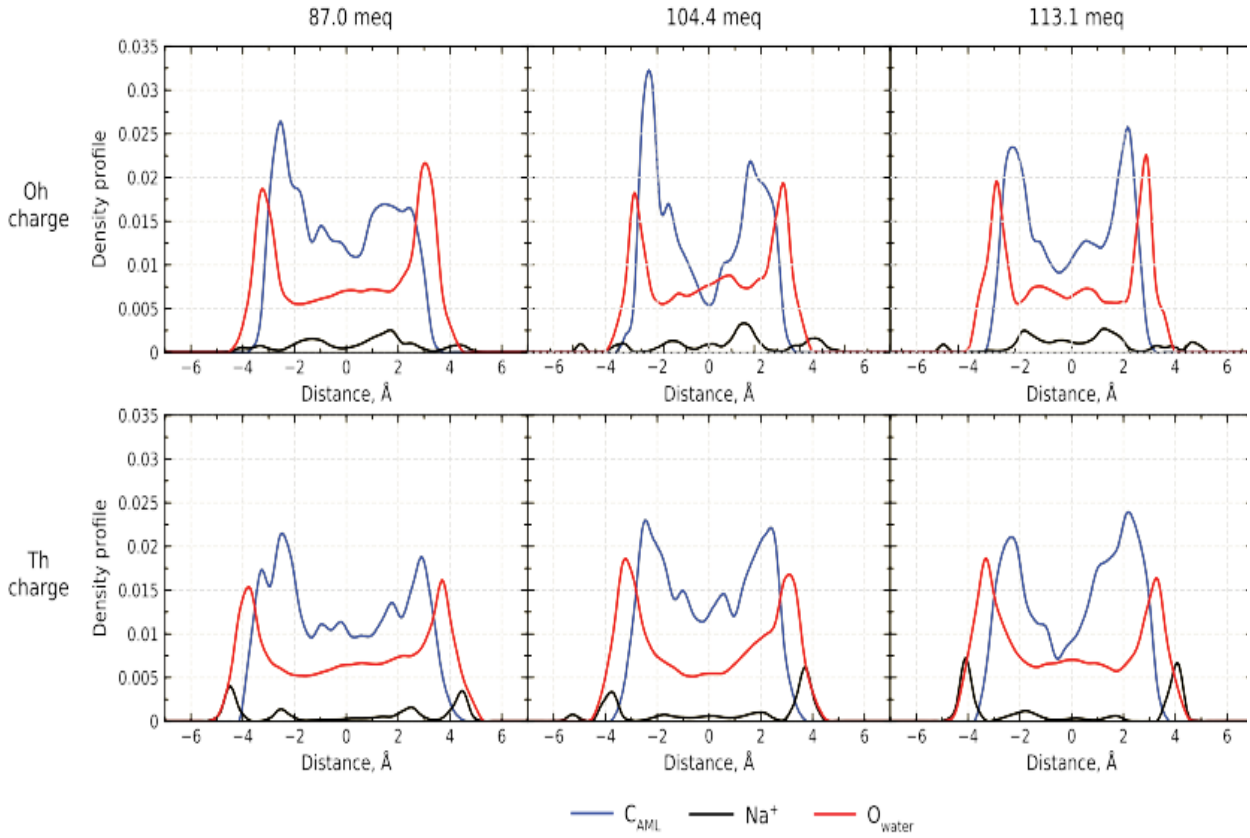

Figure 6. Atomic density profiles from MD simulations at 300 K and 1 atm for AML/NaMt nanocomposite. Amylose backbone carbon atom (C_{AML} – blue curve), sodium (Na^+ - black curve) and water (O_{water} - red curve). Left to right increases clay layer charge.

The reason for that is primarily due to the distribution of exchangeable cation within the interlayer of AML/Mt nanocomposite which is illustrated in Figure 6 as atomic density profile along the *c*-axis normal to the basal surface of clay. Strong association between exchangeable cations and substitution sites in the tetrahedral sheet of clay, and low diffusivity of cations and amylose, results in most of them being located between the clay layer and amylose molecules. Additionally, exchangeable cations in the high charge clay with charge deficit in the octahedral sheet form anhydrous adsorption complex more readily. This opens up space for organic material, leading to overall smaller basal spacing.

Conclusions

In this study, we employed molecular dynamics simulations to investigate the intercalation process and predict the structure of clay-starch nanocomposite coatings, with the aim of developing sustainable barrier materials for the packaging industry. We observed that the intercalation process occurs in distinct stages. Initially, the clay nanoparticles disperse in the starch matrix, forming stable nanocomposite structures. As the intercalation progresses, the clay particles gradually penetrate the spaces between the starch molecules, resulting in an intercalated structure. The interlayer spacing and interfacial interactions play crucial roles in determining the mechanical strength and barrier properties of the resulting coating material.

Based on our simulations, we can confidently predict the structure of the formulated clay-starch nanocomposite coatings. The intercalated structure exhibits an ordered arrangement of clay layers within the starch matrix, providing enhanced barrier properties

against gas permeation. The formulated clay-starch nanocomposite coatings hold great promise as sustainable barrier materials in the packaging industry. In conclusion, our molecular dynamics simulations have provided valuable insights into the intercalation process and predicted the structure of clay-starch nanocomposite coatings. These coatings demonstrate immense potential as sustainable barrier materials in the packaging industry, offering enhanced gas barrier properties and mechanical strength. This research paves the way for the design and optimization of environmentally friendly packaging materials, contributing to a greener and more sustainable future.

Conflicts of Interest; The author declare that they have no conflict of interest.

Acknowledgments; Author would like to express his gratitude to Dr. hab., prof.univ. Rodica Sturza for provided insight and expertise that greatly assisted the research.

References

1. Zhang, Y; Han, L; Zhang, Q. Starch-based composite films reinforced with cellulose nanocrystals modified by clay. *Carbohydr Polym.* 2018, 194, pp. 300-308.
2. Huang, M.; Yu, J., Ma, X. Studies on the properties of montmorillonite reinforced thermoplastic starch composites. *Polymer* 2004, 45(20), pp. 7017–7023.
3. Avella, M.; De Vlieger, J.; Errico, M.; Fischer, S.; Vacca, P.; Volpe, M. Biodegradable starch/clay nanocomposite films for food packaging applications. *Food Chemistry* 2005, 93(3), pp. 467–474.
4. Gao W., Dong H.; Hou H.; Zhang H. Effects of clays with various hydrophilicities on properties of starch-clay nanocomposites by film blowing. *Carbohydrate Polymers* 2012, 88(1), pp. 321–328.
5. Olsson E.; Johansson C.; Larsson J.; Järnström L. Montmorillonite for starch-based barrier dispersion coating - part 1; the influence of citric acid and poly(ethylene glycol) on viscosity and barrier properties. *Applied Clay Science* 2014, 97-98, pp. 160–166.
6. Johansson C.; Bras J.; Mondragon I.; Nechita P.; Plackett D.; Simon P.; Svetec D.; Virtanen S.; Baschetti M.; Breen C.; Clegg F.; Aucejo S. Renewable fibers and bio-based materials for packaging applications - a review of recent developments. *Bioresources* 2012, 7(2), pp. 2506–2552.
7. Olsson E.; Johansson C.; Larsson J.; Järnström L. Montmorillonite for starch based barrier dispersion coating - part 2; pilot trials and PE-lamination. *Applied Clay Science* 2014, 97-98, pp. 167–173.
8. Chen W; Zhou X; Chen P. Bio-based nanocomposite coating of corn starch/clay for improving gas barrier and mechanical properties of paper. *Ind. Crops. Prod.* 2016, 84, pp. 18-24.
9. Park H.; Li X.; Jin C.; Park C.; Cho W.; Ha C. Preparation and properties of biodegradable thermoplastic starch/clay hybrids. *Macromolecular Materials and Engineering* 2002, 287(8), pp. 553–558.
10. Park H.; Lee W.; Park C.; Cho W.; Ha C. Environmentally friendly polymer hybrids. *Journal of Materials Science* 2003, 38, pp. 909 – 915.
11. Masclaux C.; Gouanve F.; Espuche E. Experimental and modelling studies of transport in starch nanocomposite films as affected by relative humidity. *Journal of Membrane Science* 2010, 363(1-2), pp. 221–231.
12. Zhu Y.; Han S.; Hong Y. Molecular dynamics simulations on the mechanical properties of natural rubber filled with montmorillonite particles. *J Polym Sci Part B Polym Phys* 2011, 49(12), pp. 880-890.
13. Huang X.; Netravali A. Characterization of Nano-Clay Reinforced Phytagel-Modified Soy Protein Concentrate Resin. *Biomacromolecules* 2006, 7(10), pp. 2783–2789.
14. Wang Y.; Ju S.; Chen C.; Chen H.; Hsieh J. Mechanical property prediction of starch/polymer composites by molecular dynamics simulation. *RSC Advances* 2014, 4, pp. 11475
15. Ma X.; Yu J. The effects of plasticizers containing amide groups on the properties of thermoplastic starch. *Starch/Staerke* 2004, 56(11), pp. 545–551.
16. Giroto A.; de Campos A.; Pereira E.; Cruz C.; Marconcini J.; Ribeiro C. Study of a nanocomposite starch-clay for slow-release of herbicides; evidence of synergistic effects between the biodegradable matrix and exfoliated clay on herbicide release control. *Journal of Applied Polymer Science* 2014, 41188, pp. 1–9.
17. Todorov I.; Smith W.; Trachenk K. DL_POLY_3; new dimensions in molecular dynamics simulations via massive parallelism. *Journal of Materials Chemistry* 2006, 16, pp. 1911–1918.
18. Cygan R.; Liang J; Kalinichev A. Molecular models of hydroxide; oxyhydroxide, and clay phases and the development of a general force field. *The Journal of Physical Chemistry B* 2004, 108, pp. 1255–1266.

19. Wu Y.; Tepper H.; Voth G. Flexible simple point-charge water model with improved liquid-state properties. *The Journal of Chemical Physics* 2006, 124(2), pp. 024503.
20. Mbey J.; Hoppe S.; Thomas F. Cassava starch-kaolinite composite film. Effect of clay content and clay modification on film properties. *Carbohydrate Polymers* 2012, 88(1), pp. 213–222.
21. Olsson E.; Menzel C.; Johansson C.; Andersson R.; Koch K; Jarnstrom L. The effect of pH on hydrolysis, cross-linking and barrier properties of starch barriers containing citric acid. *Carbohydrate Polymers* 2013, 98(2), pp. 1505–1513.

Citation: Siminel, N. Clay-starch nanocomposite coatings on paper substrate - a promising frontier in environmentally friendly packaging material. *Journal of Engineering Science* 2023, 30 (2), pp. 81-89. https://doi.org/10.52326/jes.utm.2023.30(2).07.

Submission of manuscripts: jes@meridian.utm.md

Journal of Engineering Science *Vol. XXX, no. 2 (2023), pp. 90 - 103*
Fascicle *Industrial Engineering* *ISSN 2587-3474*
Topic *Electronics and Communication* *eISSN 2587-3482*

https://doi.org/10.52326/jes.utm.2023.30(2).08
UDC 621.311:004.94

THE USE OF SYNCHRONOUS VECTOR MEASUREMENTS IN THE CALCULATION OF STEADY-STATE MODES OF ELECTRICAL NETWORKS

Ecaterina Murdid*, ORCID: 0009-0002-3209-8148

Technical University of Moldova, 168 Stefan cel Mare Blvd., Chisinau, Republic of Moldova
*Corresponding author: Ecaterina Murdid, *ecaterina.murdid@ee.utm.md*

Received: 05. 04. 2023
Accepted: 06. 10. 2023

Abstract. Calculation of steady state mode is the most used tool of modern electrical networks' analysis. The current study is focused on the application of synchronized phasor measurements technology for steady state mode calculation. There is shown that the solely use of synchronized phasor measurements as initial information for calculating the steady state mode or in conjunction with traditional telemetry from Supervisory Control And Data Acquisition system (SCADA) has a number of advantages over classical methods, which is due to the simplification of the computational process, reduced time and required computational memory, and more reliable informational support. This paper presents the novel approach which consists in steady state mode calculations using accelerated and ultra-accelerated algorithms. These algorithms are based on the implementation of the method of determining values and special structure of the matrix of nodal admittances, what allow to reduce the number of equations, that must be solved in order to find the searched nodal voltages. Besides, there is no need to set balancing node, and dependences between searched and known nodal voltages become linear. The calculations performed for test scheme IEEE-14 demonstrate that both algorithms provide high accuracy results, increase the simplicity and speed of calculation by separate solving of linear equations.

Keywords: *nodal analysis, matrix of nodal admittances, Phasor Measurement Unit (PMU), SCADA measurements, method of determining values.*

Abstract. Calculul regimului permanent de funcționare este cel mai utilizat instrument de analiză a rețelelor electrice moderne. Studiul actual se concentrează pe aplicarea tehnologiei de măsurări fazoriale sincronizate pentru calculul regimului. Se demonstrează, că utilizarea doar a măsurătorilor fazoriale sincronizate ca informație inițială pentru calculul regimului sau simultan cu telemetria tradițională din sistemul de control și achiziții de date (SCADA) are o serie de avantaje față de metodele clasice, ceea ce se reflectă în simplificarea procesului de calcul, reducerea timpului și memoriei de calcul, asigurarea suportului informațional mai fiabil. Această lucrare prezintă o nouă abordare privind calculul regimului permanent de funcționare, care constă în utilizarea algoritmilor accelerați și ultra-accelerați. Acești algoritmi se bazează pe implementarea metodei mărimilor determinate și a structurii speciale a matricei admitanțelor nodale, ceea ce permite reducerea numărului de ecuații, care trebuie

rezolvate pentru a găsi tensiunile nodale căutate. În plus, dispare necesitatea de a seta nodul de echilibru, iar dependențele dintre tensiunile nodale căutate și cunoscute devin liniare. Calculele efectuate pentru schema test IEEE-14 demonstrează că ambii algoritmi oferă rezultate de înaltă acuratețe, măresc simplitatea și viteza de calcul prin soluționarea separată a ecuațiilor liniare.

Cuvinte cheie: *metoda tensiunilor nodali, matricea admitanțelor nodali, unitatea de măsurarea fazorilor (PMU), măsurări SCADA, metoda mărimilor determinate*.

1. Introduction

The Kirchhoff's and Maxwell's works gave a tremendous impulse to the development of the analysis of electrical circuits. The development of modern electrical power systems (EPS), which are characterized with a large segment of distributed generation, voltage and power control devices, characterized by multi-mode and complex configuration, is based on the analysis of electrical networks. Calculation of steady state is the most common task in the field of electrical systems analysis. The scope of calculating the steady state mode of an electrical network is to determine the electrical parameters of the state: voltages at the nodes, electric currents and power flows along the branches, power losses in the network, etc. The results of such calculations make it possible to find out:

• the feasibility of this mode of the electrical network (the possibility of transferring the required power from sources of electrical energy to consumers);
• admissible voltage limits in nodes;
• admissible ranges of change of current loadings of elements of electric networks in normal and post-emergency conditions.

In addition, the calculation of the steady state of power networks must be carried out when checking transient, post-emergency modes of network operation, when solving the problem of operational management and control, when calculating urgent and expected modes, when assessing and planning costs of power losses, an any other tasks, that may arise during operation, development and design of electrical systems.

The method of nodal analysis has become widely used in the calculations of steady-state conditions. The advantage of this method is explained by the fact, that this method makes it possible to form relatively simply and definitely a system of nodal equations in which the matrix of nodal admittances is easily corrected when changing the transformation ratios of transformer branches and when switching on / off the power line branches.

At present, a number of mathematical methods are used to calculate the steady state mode using the nodal analysis: simple iteration, Gauss-Seidel, Newton-Raphson, gradient method, modified Newton method (Newton-Kantorovich method), second-order Newton-Raphson methods (using the Hessian matrix), cybernetic modeling, dividing the EPS into subsystems, etc. Iterative methods are most widely used due to the fact that the mathematical description of the electrical network using the nodal analysis is performed using nonlinear dependencies between dependent and independent mode parameters. The essence of various numerical methods for solving nonlinear nodal equations is consistently refining the initial voltages at the nodes, while iterations continue until the specified calculation accuracy is reached. The iterative methods for calculating complex electrical systems require a lot of time and volatile memory even with the current level of development of computer technology.

The requirements set by modern researchers in the field of analysis of electrical modes are [1]:

– reducing the amount of computational work in order to obtain quickly calculation results;

– reducing the amount of volatile memory, which leads to the possibility of increasing the size of the problem being solved;

– solving the problem in any form of informational support for power network parameters.

The steady state of the electrical system is determined by the values of the parameters of its nodes. Each node is characterized by four regime parameters: active P and reactive Q power, module U and argument δ of the complex voltage, while in practice information is known only about two of the four parameters [1].

Depending on the nature of the assignment of the initial information, the nodes can be classified as follows [1]:

1. A node of type U - δ, for which the module and argument of the complex voltage are specified, and it is necessary to determine the active and reactive powers. As such a node, a generation node is selected, which is assigned as the base node.
2. Node of type $P – U$, for which the active power and the module of the complex voltage are specified, and it is necessary to determine the reactive power and the argument of the complex voltage. In practice, nodes of this type are usually only generation nodes.
3. Node of $P – Q$ type, for which active and reactive power are set, and it is necessary to determine the module and argument of the complex voltage. Nodes of this type can be both generation and load nodes.

If it is used the standard approach to information support for calculating the steady state using the nodal analysis, then the parameters of nodes of the type P - U and P - Q can be determined from the data of traditional measurements (telemetry of the SCADA system), while parameter identification for nodes of the type $U – \delta$ is more sophisticated problem. The feature of the nodal analysis is the mandatory determination of reference nodes. When solving problems by iterative methods, a reference node is set, this is a node in which the voltage vector is known (its modulus and phase angle which, as a rule, is equal to zero) [2].

If the voltage vector in the reference node is given, then the number of equations solved by the nodal analysis is reduced by one, and any equation can be excluded. A node whose equation is excluded from the system is called a balancing node [3, 4]. When solving a problem using Newton's method, only one reference node is specified. During iterations, the voltage vectors at the all nodes are oriented relative to the voltage vector at the reference node. Thus, from the choice of a node as a reference, balancing or reference-balancing one, the results of the calculation may change.

Classical methods for state estimation and steady state mode calculation were based on the initial data provided by SCADA [5]. Current researches in the field of solving problems of optimizing methods for calculating the steady state, as well as eliminating the disadvantages of iterative methods of nodal analysis, are focused on the application of synchronized phasor measurements technology. This technology is based on the tracking of voltage phasors in certain system nodes, correlated often with measurements of current phasors in incident branches [4]. As traditional SCADA system is built on Remote Terminal Units (RTU), so and the system of synchronized phasor measurements uses Phasor Measurement Units (PMU) as main device for informational support of the wide number of applications, one of them being state estimation and steady state calculation.

The use of synchronized phasor measurements as initial information for calculating the steady state mode independently or in conjunction with traditional telemetry has a number of advantages over classical methods, due to the simplification of the computational process, reduced time and required volatile memory, and more reliable informational support.

The author of this article showed that the methods for PMU optimal placement based on the method of determined values provide both the minimum number of nodes for installing PMU according to the criteria for complete network observability and contribute to performing steady state calculations by accelerated and super-accelerated methods [6]. Minimization of the time spent for calculating the mode is achieved with the method of determined values and the matrix-block transformation of the system of linear equations.

The informational support of the steady state calculation by the accelerated method is provided by using voltage phasors as initial information at the nodes where the PMUs are installed, as well as the scalar values of the power flows (*P* and *Q*) received from the SCADA system.

The steady state calculation by the ultra-accelerated method is achieved by using voltage phasors as initial information at nodes where PMUs are installed, as well as current phasors in all incident branches [7]. When calculating by ultra-accelerated method, scalar values of power flows (P and Q) obtained from the SCADA system can also be used [8].

This paper is dedicated to the novel approach in steady state calculations, based on the application of PMU measures. In this study, the algorithm and technique for calculating steady state by the accelerated method, as well as the ultra-accelerated method, will be described in detail. The main features of the steady state calculation technique based on these algorithms will be shown.

2. Materials and Methods

2. 1 Algorithm for accelerated steady state mode calculation (A1)

All accelerated methods for calculating the steady state mode of the EPS are based on dividing the column matrix $\left[\underline{U}_{\Sigma}\right]$ into 2 submatrices $\left[\underline{U}_{p}\right]$ and $\left[\underline{U}_{q}\right]$, respectively [9]. The first submatrix includes the determining nodal voltages, that is, independent values, and the second submatrix includes dependent variables. The submatrix $\left[\underline{U}_{q}\right]$ is determined depending on $\left[\underline{U}_{p}\right]$. After separating the matrix-column, the system of nodal voltage equations that describes the EPS mode can be written as follows [6]:

$$\begin{cases}\left[\underline{Y}_{pp}\right]\cdot\left[\underline{U}_{P}\right]+\left[\underline{Y}_{pq}\right]\cdot\left[\underline{U}_{q}\right]=\left[\underline{J}_{p}\right];\\ \left[\underline{Y}_{qp}\right]\cdot\left[\underline{U}_{P}\right]+\left[\underline{Y}_{qq}\right]\cdot\left[\underline{U}_{q}\right]=\left[\underline{J}_{q}\right].\end{cases} \quad (1)$$

If the elements of the submatrix $\left[\underline{U}_{p}\right]$ are known, then they can be considered independent variables (these are the determining nodal voltages), then the dependent variables of the submatrix $\left[\underline{U}_{q}\right]$ are determined from the second equation of system Eq.(1) using the expression:

$$\left[\underline{Y}_{qq}\right]\cdot\left[\underline{U}_{q}\right]=\left[\underline{J}_{q}\right]-\left[\underline{Y}_{qp}\right]\cdot\left[\underline{U}_{P}\right]. \quad (2)$$

Reducing the matrix $\left[\underline{Y}_{qq}\right]$ to a diagonal form ($\left[\underline{Y}_{qq}\right]=\left[\underline{Y}_{d}\right]$) makes it possible to obtain easily its inverse matrix and to find the required nodal voltages using the formula:

$$\left[\underline{U}_{q}\right]=\left[\underline{Y}_{d}\right]^{-1}\left\|\left[\underline{J}_{q}\right]-\left[\underline{Y}_{qp}\right]\cdot\left[\underline{U}_{P}\right]\right\|. \quad (3)$$

It is recommended to reduce the matrix $\left[\underline{Y}_{qq}\right]$ to a lower triangular or band form, since in this case the number of PMU devices will be minimal. Thus, on the basis of the matrix-block transformation, it is possible to solve 2 problems at once: the problem of the optimal placement of the PMU in the EPS, as well as the problem of calculating the steady state by a simplified method.

There are presented below the rules of the algorithm for the formation of the matrix of nodal admittances, in which the submatrix $\left[\underline{Y}_{qq}\right]$ has a band structure.

The illustration of the specified algorithm is based on a dot diagram, which is a conditional form of representation of the matrix of nodal admittances. In it, non-zero elements of the matrix are replaced by dots.

The following steps must be performed to divide the nodes of the EPS into two subsets:

1. The ranks of all nodes of the system are determined, i.e. the number of incident branches for each node.

2. The node of maximum rank is excluded from the scheme, as well as all branches adjacent to it. In the case when there are several nodes with the maximum rank, the first node is selected in the order of numbering of nodes in the scheme. Moving a node of maximum rank *q* to a subset *P* leads to the maximum decomposition of chains *g-1* at this step.

3. After the elimination of any node, the ranks of the nodes remaining in the scheme are recalculated.

4. The presence of looped circuits in the studied scheme is checked. If so, steps 2 and 3 are repeated until the scheme has been converted to a tree or multiple trees.

5. First, the nodes of the subset *P* are randomly numbered, which, in addition to the nodes selected for the installation of the PMU, will also include one node each from the obtained trees and leaf nodes. (Leaf nodes are nodes associated with a tree with only one branch).

6. Then the nodes of the subset *Q* are numbered, which includes the remaining nodes of the tree, as well as isolated nodes. Isolated nodes are numbered last.

Figure 1 shows the IEEE-14 test network [5], where nodes were renumbered (numbers after transformation are indicated in brackets) according to this algorithm. Figure 2 shows dot diagram of the matrix of nodal admittances obtained by this algorithm.

To the right of the dot diagram (figure 2), the sequence for determining the voltages of dependent nodes is indicated. If the voltage vectors of these nodes are known from the PMU measurements installed at nodes 1, 2, 3 and 4, then, first of all, the voltage of node 5 can be determined by the expression:

$$\underline{U}_{5calc}=\frac{\underline{Y}_{44}\underline{U}_{4}-\underline{Y}_{42}\underline{U}_{2}+\frac{\overset{*}{\underline{S}}_{4,G}}{\overset{*}{\underline{U}}_{4}}}{\underline{Y}_{45}}. \quad (4)$$

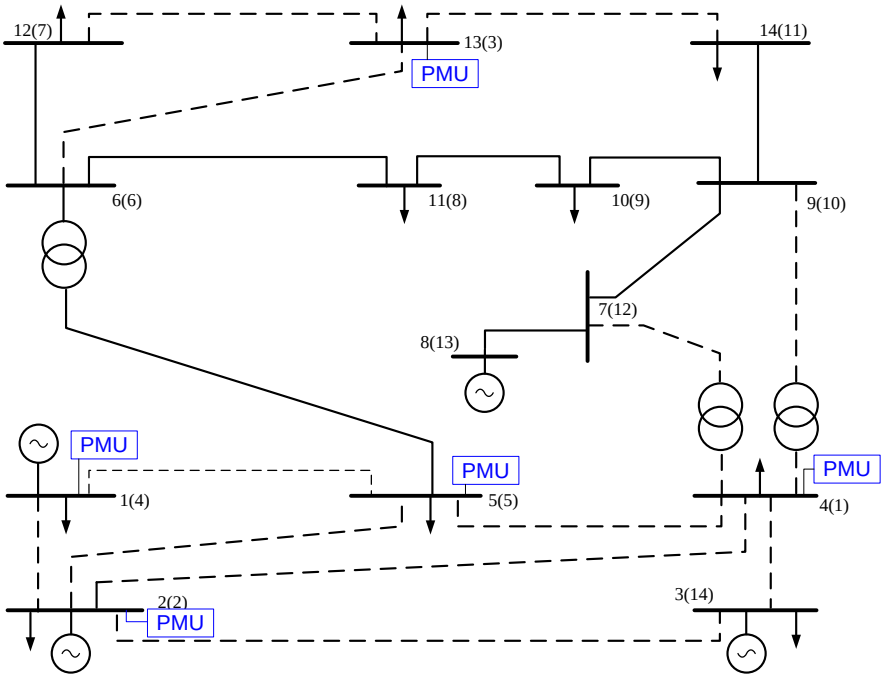

Figure 1. Single-line diagram of 14 nodes network, IEEE-14 using the A1 algorithm for arranging PMU in four nodes.

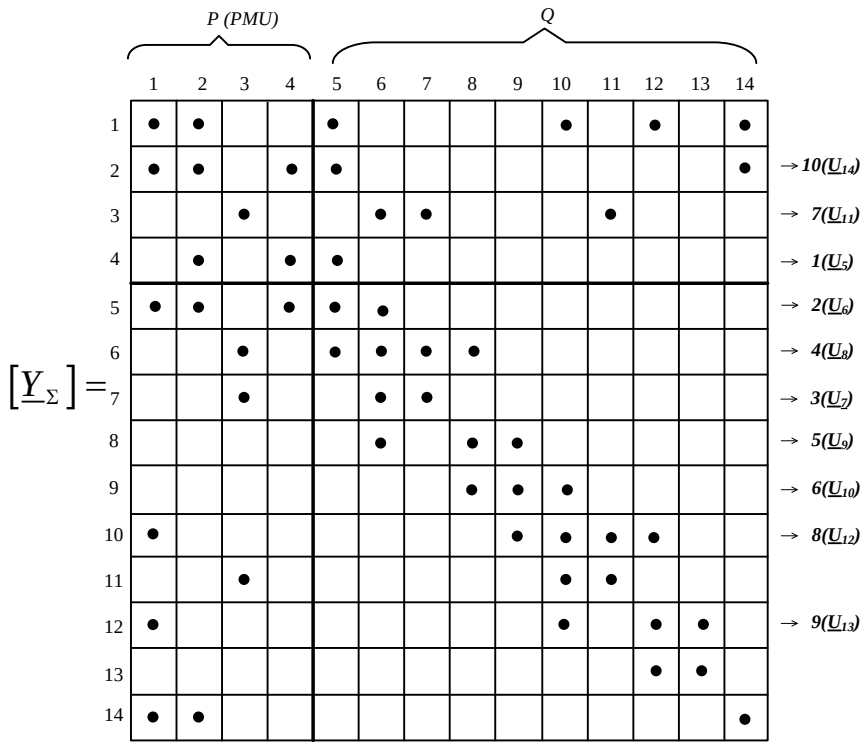

Figure 2. Matrix of nodal admittances corresponding to the IEEE-14 scheme according to Algorithm A1 with 4 PMU, in which the submatrix $\left[\underline{Y}_{qq}\right]$ is reduced to a band form.

Similarly, the voltage of node 6 is determined:

$$\underline{U}_{6calc} = \frac{\underline{Y}_{55}\underline{U}_{5calc} - \underline{Y}_{54}\underline{U}_4 - \underline{Y}_{52}\underline{U}_2 + \frac{\overset{*}{\underline{S}}_5}{\underline{U}^*_{5calc}}}{\underline{Y}_{56}}. \quad (5)$$

The voltage of node 7 is determined from the equation for node 7 by the expression:

$$-\underline{Y}_{73}\underline{U}_{3}-\underline{Y}_{76}\underline{U}_{6calc}+\underline{Y}_{77}\underline{U}_{7calc}+\frac{\overset{*}{\underline{S}}_{7}}{\overset{*}{\underline{U}}_{7calc}}=0. \quad (6)$$

As it can be seen from Eq. (6), the voltage of node 7 is in a non-linear dependence on the voltage values of nodes 3 and 6. The voltage value of node 7 is determined iteratively using the Newton-Raphson method. In this case, it took 4 iterations to numerically determine the desired value.

Node 8 voltage is determined from the expression:

$$\underline{U}_{8calc}=\frac{\underline{Y}_{66}\underline{U}_{6calc}-\underline{Y}_{63}\underline{U}_{3}-\frac{\underline{Y}_{65}}{k_{56}}\underline{U}_{5calc}+\frac{\overset{*}{\underline{S}}_{6}}{\overset{*}{\underline{U}}_{6calc}}}{\underline{Y}_{68}}. \quad (7)$$

Further, according to Eq. (8) - (13), the voltages at nodes 9, 10, 11, 12, 13 and 14 are determined.

$$\underline{U}_{9calc}=\frac{\underline{Y}_{88}\underline{U}_{8calc}-\underline{Y}_{86}\underline{U}_{6calc}+\frac{\overset{*}{\underline{S}}_{8}}{\overset{*}{\underline{U}}_{8calc}}}{\underline{Y}_{89}}. \quad (8)$$

$$\underline{U}_{10calc}=\frac{\underline{Y}_{99}\underline{U}_{9calc}-\underline{Y}_{98}\underline{U}_{8}+\frac{\overset{*}{\underline{S}}_{9}}{\overset{*}{\underline{U}}_{9calc}}}{\underline{Y}_{9.10}}. \quad (9)$$

$$\underline{U}_{11calc}=\frac{\underline{Y}_{33}\underline{U}_{3}-\underline{Y}_{37}\underline{U}_{7calc}-\underline{Y}_{36}\underline{U}_{6calc}+\frac{\overset{*}{\underline{S}}_{3}}{\overset{*}{\underline{U}}_{3}}}{\underline{Y}_{311}}. \quad (10)$$

$$\underline{U}_{12calc}=\frac{\underline{Y}_{10.10}\underline{U}_{10calc}-\underline{Y}_{10.9}\underline{U}_{9calc}-\frac{\underline{Y}_{10.1}}{k_{10.1}}\underline{U}_{1}-\underline{Y}_{10.11}\underline{U}_{11calc}+\frac{\overset{*}{\underline{S}}_{10}}{\overset{*}{\underline{U}}_{10calc}}}{\underline{Y}_{10.12}}. \quad (11)$$

$$\underline{U}_{13calc}=\frac{\underline{Y}_{12.12}\underline{U}_{12calc}-\underline{Y}_{12.10}\underline{U}_{10calc}-\frac{\underline{Y}_{12.1}}{k_{12.1}}\underline{U}_{1}+\frac{\overset{*}{\underline{S}}_{12}}{\overset{*}{\underline{U}}_{12calc}}}{\underline{Y}_{10.12}}. \quad (12)$$

$$\underline{U}_{14calc}=\frac{\underline{Y}_{22}\underline{U}_{2}-\underline{Y}_{21}\underline{U}_{1}-\underline{Y}_{24}\underline{U}_{4}-\underline{Y}_{25}\underline{U}_{5calc}+\frac{\overset{*}{\underline{S}}_{2}}{\overset{*}{\underline{U}}_{2}}}{\underline{Y}_{2.14}}. \quad (13)$$

It should be noted that if the voltage of node *i* is determined from the expression for the current balance of node *j*, then it is necessary to solve a linear equation in function of $\underline{U}_i$. If the voltage of node *i* is determined from the expression for the current balance of the same node *i*, then $\underline{U}_i$ is determined by solving a non-linear equation by the iterative method, as was done for node 7.

If the number of nodes in which PMUs must be installed is increased, the values of nodal voltages can be determined from linear dependencies. So, if for the IEEE-14 test circuit, the PMU devices are located in 5 nodes, as shown in Figure 3, a matrix of nodal admittances of the band form shown in Figure 4 will be obtained.

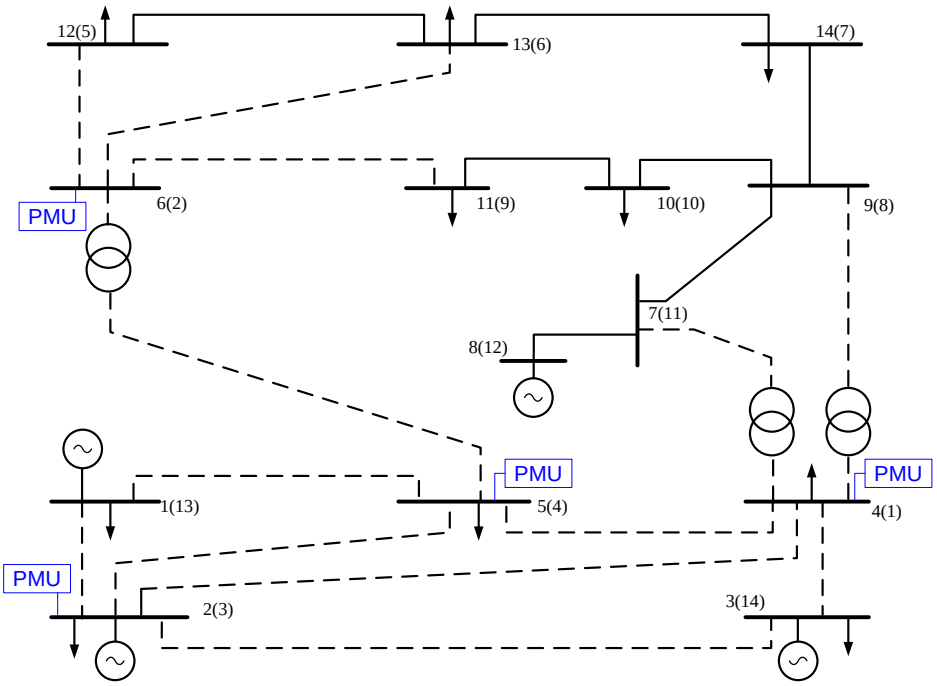

Figure 3. Single-line diagram of 14 nodes network, IEEE-14 using the A1 algorithm for arranging PMU in five nodes.

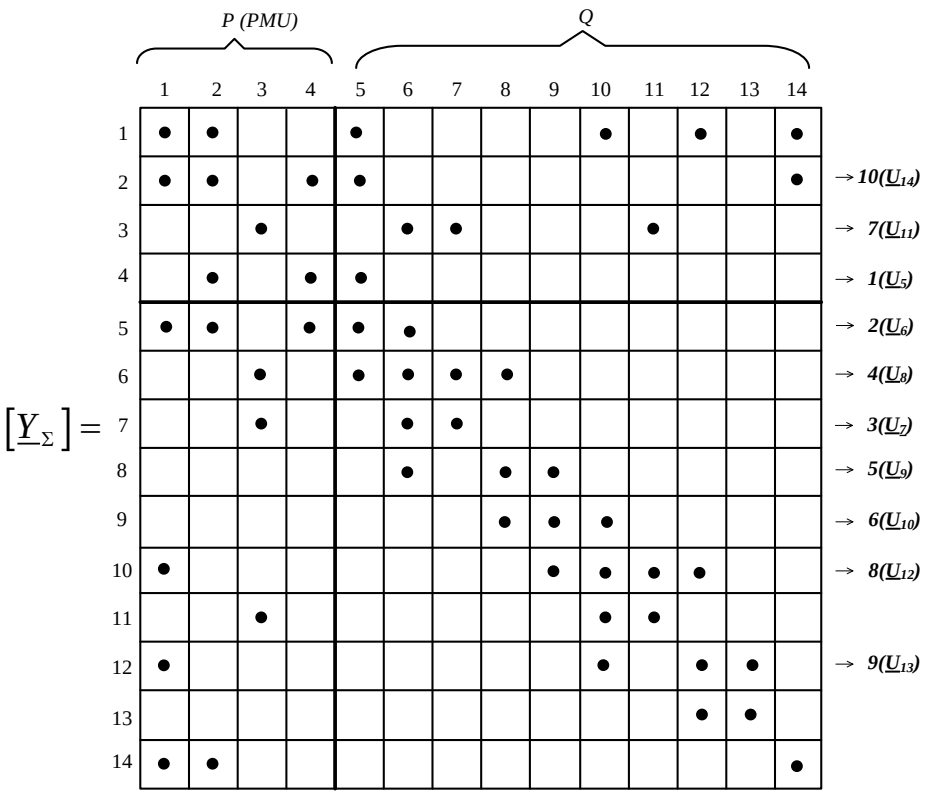

$[\underline{Y}_{\Sigma}] =$

Figure 4. Matrix of nodal admittances corresponding to the IEEE-14 scheme according to Algorithm A1 with 5 PMU, in which the submatrix $[\underline{Y}_{qq}]$ is reduced to a band form.

To the right of the dot diagram (Figure 4), the sequence for determining the voltages of dependent nodes is indicated. In this case, the voltages of all nodes are determined by solving linear equations.

2.2 Algorithm for ultra-accelerated steady state mode calculation (A2)

This algorithm is based on the joint use of both the voltage vector in the node and the current vectors of all branches connected to the node. This amount of data can be obtained from the PMU system installed in the one node. At the same time, using Ohm's law, it is possible to determine the voltages of adjacent nodes as pseudo-measurements [10]. Pseudo-measurements are determined with the help of current phasors and known branch parameters [11]. Figure 5 and Eq. (14)-(17) illustrate how the voltage vector of node 2 can be calculated with the help of given voltage phasor of node 1 and the current phasor in line 1-2.

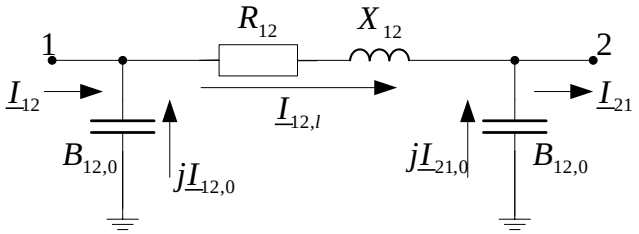

Figure 5. Equivalent circuit of power lines connecting nodes 1 and 2.

The voltage drop in branch 1-2 is calculated by the expression:

$$\Delta \underline{U}_{12} = \sqrt{3}\underline{I}_{12,I}\underline{Z}_{12}. \quad (14)$$

The current phasor $\underline{I}_{12,I}$ at the beginning of the line is determined by the expression:

$$\underline{I}_{12,I} = \underline{I}_{12} + \underline{I}_{12,0}, \quad (15)$$

where value of current vector $\underline{I}_{12,0}$ is calculated as follows:

$$\underline{I}_{12,0} = j\frac{B_{12,0}\cdot U_1}{\sqrt{3}}. \quad (16)$$

If the voltage drop in section 1-2 is known, the voltage of node 2 can be calculated (pseudo measurement):

$$\underline{U}_2 = \underline{U}_1 - \Delta\underline{U}_{12}. \quad (17)$$

The essence of the algorithm for ultra-accelerated calculation of the steady state is to form a matrix of nodal admittances, in which nodes will be divided into three subsets: a subset of *P* nodes in which PMUs are installed, a subset of *PP* nodes in which pseudo-measurements are calculated, and also a subset of *Q*, containing all other nodes of the circuit. The following steps must be performed for dividing the nodes of the power system into three subsets:

1. The ranks (*R*) of all nodes of the system are determined, i.e. the number of incident branches for each node.
2. The node of maximum rank, as well as all branches adjacent to it, are excluded from the scheme. In the case when there are several nodes with the maximum rank, the first node is selected in the order of numbering of nodes in the scheme.
3. After eliminating any node, the ranks of the remaining nodes in the scheme are recalculated. Nodes whose ranks have decreased are listed as pseudo-PMUs (a subset of *PP*).
4. Steps 2 and 3 are repeated until all nodes with rank *R*>=3 transform into nodes, that provide PMUs or pseudo-PMUs measurements.

5. If the rank of a node is equal to 1 and 2, then the node is included in the subset *Q*, and the complex value of the voltage in this node, as well as the complex values of the currents of the incident branches, will be determined linearly through the voltage drops in the branches and the current balance equations.

6. The nodes of each subset are numbered in direct but random order.

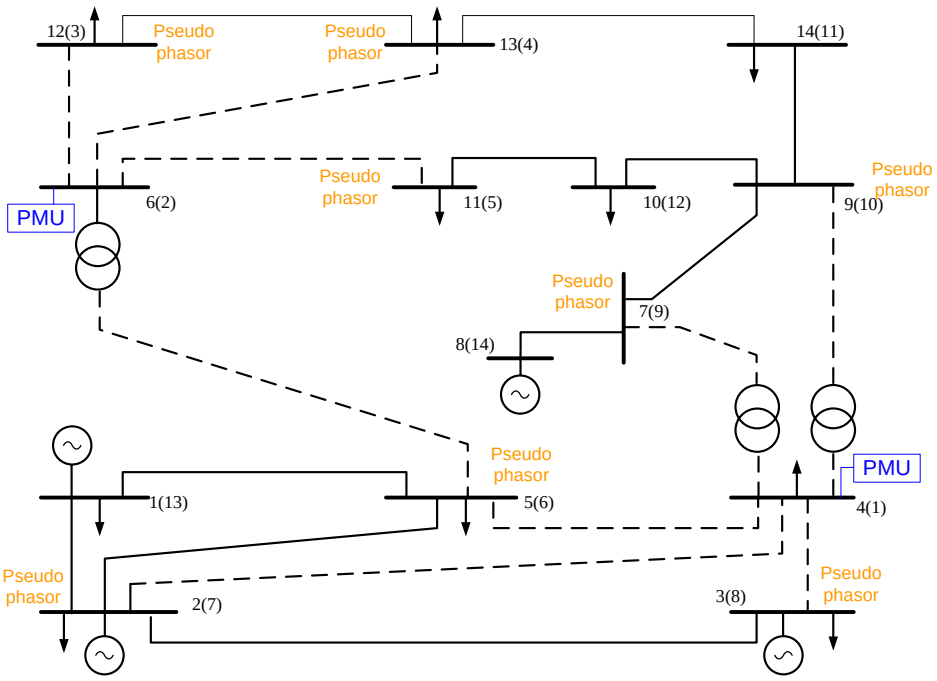

Figure 6. Single-line diagram of 14 nodes network, IEEE-14 using the A2 algorithm for arranging PMU in two nodes and having pseudo-measurements in 8 nodes.

Figure 6 shows the IEEE-14 test circuit, for which nodes were renumbered (numbers after transformation are indicated in brackets) according to the algorithm A2. Figure 7 shows a dot diagram of the matrix of nodal admittances obtained by this algorithm.

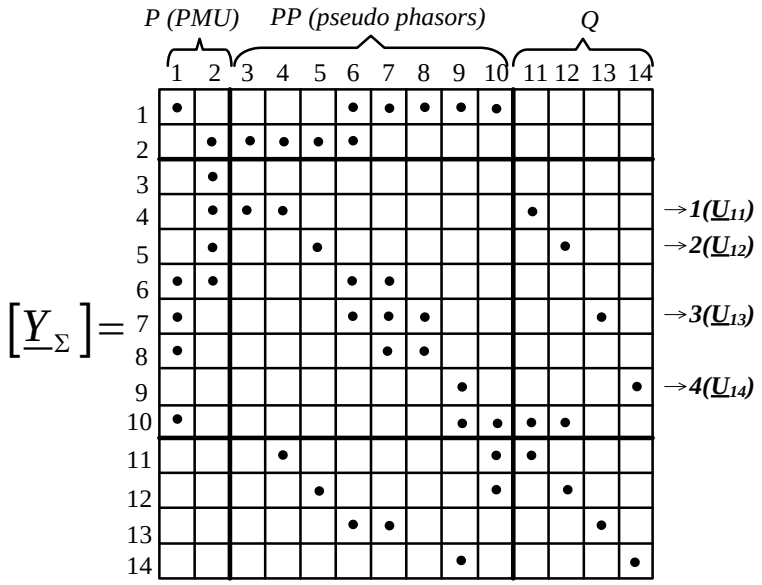

Figure 7. Matrix of nodal admittances corresponding to the IEEE-14 scheme according to Algorithm A2.

The calculation of the steady state according to the A2 algorithm contains two stages. At the first stage, using the above formulas, the nodal voltages of the nodes adjacent to the PMU installation site are calculated (pseudo-measurements), and the second stage, the voltage phasors in the dependent nodes are determined from the current balance equations with the help of the PMU data and pseudo-measurements. At the same time, it is important to satisfy condition described for the Algorithm A1, the voltage phasor for node *i* is determined from the expression for the current balance of node *j*. Then it will be necessary to solve linear equation in function of searched value $\underline{U}_i$.

The progress of the calculation according to the A2 algorithm can be described as follows:

1. The PMU installed in node 1 measures and provide the following information: $\underline{U}_1^{PMU}$, $\underline{I}_{1-6}^{PMU}$, $\underline{I}_{1-7}^{PMU}$, $\underline{I}_{1-8}^{PMU}$, $\underline{I}_{1-9}^{PMU}$ и $\underline{I}_{1-10}^{PMU}$. Then the voltage drops in branches adjacent to node 1 are determined: $\Delta\underline{U}_{1-6}$, $\Delta\underline{U}_{1-7}$, $\Delta\underline{U}_{1-8}$, $\Delta\underline{U}_{1-9}$ and $\Delta\underline{U}_{1-10}$.

2. The PMU installed in node 2 measures and provide the following information: $\underline{U}_2^{PMU}$, $\underline{I}_{2-3}^{PMU}$, $\underline{I}_{2-4}^{PMU}$, $\underline{I}_{2-5}^{PMU}$, $\underline{I}_{2-6}^{PMU}$. Then the voltage drops in branches adjacent to node 2 are determined: $\Delta\underline{U}_{2-3}$, $\Delta\underline{U}_{2-4}$, $\Delta\underline{U}_{2-5}$, $\Delta\underline{U}_{2-6}$.

3. There are calculated the pseudo-measurements of voltage phasors in nodes, 4, 5, 6, 7, 8, 9 and 10: $\underline{U}_3^{pP}$, $\underline{U}_4^{pP}$, $\underline{U}_5^{pP}$, $\underline{U}_6^{pP}$, $\underline{U}_7^{pP}$, $\underline{U}_8^{pP}$, $\underline{U}_9^{pP}$, $\underline{U}_{10}^{pP}$.

4. After calculation of the phasors at nodes 1-10, knowing traditional SCADA power flow measurements at nodes 4, 5, 7 and 9, the voltage vectors for dependent nodes 11, 12, 13, 14 are determined.

Thus, there is no need to solve a system of equations with size 14x14 within the steady state mode calculation. Within joint application of PMU data, pseudo-measurements and traditional SCADA measurements, it is necessary to solve only four linear equations similar to Eq. (7)-(13).

3. Results and discussion

The placement of PMU in nodes of EPS makes the system model observable and as a result ensures the linear dependence between unknown and measured node voltages. Although, in [12] there are indicated sites, where PMU must be installed obligatory (intersystem lines, generation nodes, plants of frequency control, etc.), it is unfeasible to install PMU in each node of the network. Thus, many studies deal with the searching of the minimal number of PMU that should be placed in EPS' nodes to ensure the complete observability. As it was noted in [13] and developed in [8] and [14], the optimal placement of PMU implies the existence of at least one spanning tree in each network, which connects all the nodes trough branches with measured or calculated phasors. This principle underlies the rules of the accelerated algorithm for the formation the matrix of nodal admittances, which are specified in this paper.

In [15] there is clearly described main data necessary for steady state mode calculation: topology data, data about parameters of the branches and nodes. All these data are used within the process of accelerated calculation of steady state mode.

There is noted in [16] the feasibility of partition of nodal admittances matrix in some regions (submatrices). According to described here algorithms this partition and matrix transformation bring to the possibility to reduce the calculation time. Both proposed algorithms A1 and A2 are based on transformation of nodal admittance matrix. But essential difference in comparison with [13] is that there are developed specific rules for implementation and the nodes in the graph of EPS are renumbered. These algorithms can be applied without considering the presence of reference or reference-balancing nodes.

For the IEEE-14 test circuit, the steady state calculation was performed using the A1 and A2 algorithms proposed in this paper. The similar calculation of the mode was performed for the IEEE-14 model in the specialized program RastrWIN in order to demonstrate the correctness of the calculations and compare the results. Table 1 presents the summary results of steady state calculations for the IEEE-14 scheme.

Table 1

Results of the calculation of the steady state by the accelerated and ultra-accelerated methods and performed in RastrWIN software

Node	RastrWIN	Algorithm A1		Algorithm A2
		4 PMU	5 PMU	
1	$243.8 \cdot e^{j0^\circ}$	$243.8 \cdot e^{j0^\circ}$	$243.8 \cdot e^{j0^\circ}$	$243.262 \cdot e^{j0.6^\circ}$
2	$230 \cdot e^{-j4.433^\circ}$	$230 \cdot e^{-j4.433^\circ}$	$230 \cdot e^{-j4.433^\circ}$	$230.075 \cdot e^{-j4.43^\circ}$
3	$224.521 \cdot e^{-j13.095^\circ}$	$224.523 \cdot e^{-j13.098^\circ}$	$224.523 \cdot e^{-j13.098^\circ}$	$224.937 \cdot e^{-j12.99^\circ}$
4	$223.202 \cdot e^{-j10.234^\circ}$	$223.202 \cdot e^{-j10.234^\circ}$	$223.202 \cdot e^{-j10.234^\circ}$	$223.202 \cdot e^{-j10.234^\circ}$
5	$224.409 \cdot e^{-j8.609^\circ}$	$224.409 \cdot e^{-j8.608^\circ}$	$224.409 \cdot e^{-j8.609^\circ}$	$224.409 \cdot e^{-j8.61^\circ}$
6	$115 \cdot e^{-j14.681^\circ}$	$114.998 \cdot e^{-j14.681^\circ}$	$115 \cdot e^{-j14.681^\circ}$	$115 \cdot e^{-j14.681^\circ}$
7	$113.94 \cdot e^{-j13.666^\circ}$	$113.928 \cdot e^{-j13.681^\circ}$	$113.942 \cdot e^{-j13.669^\circ}$	$113.929 \cdot e^{-j13.66^\circ}$
8	$115 \cdot e^{-j13.666^\circ}$	$114.975 \cdot e^{-j13.706^\circ}$	$115.006 \cdot e^{-j13.675^\circ}$	$115.03 \cdot e^{-j11.55^\circ}$
9	$113.353 \cdot e^{-j15.483^\circ}$	$113.344 \cdot e^{-j15.49^\circ}$	$113.353 \cdot e^{-j15.483^\circ}$	$113.353 \cdot e^{-j15.48^\circ}$
10	$112.728 \cdot e^{-j15.669^\circ}$	$112.72 \cdot e^{-j15.675^\circ}$	$112.728 \cdot e^{-j15.669^\circ}$	$112.746 \cdot e^{-j15.65^\circ}$
11	$113.423 \cdot e^{-j15.326^\circ}$	$113.418 \cdot e^{-j15.329^\circ}$	$113.423 \cdot e^{-j15.326^\circ}$	$113.423 \cdot e^{-j15.32^\circ}$
12	$113.176 \cdot e^{-j15.659^\circ}$	$113.174 \cdot e^{-j15.659^\circ}$	$113.176 \cdot e^{-j15.659^\circ}$	$113.176 \cdot e^{-j15.66^\circ}$
13	$112.588 \cdot e^{-j15.751^\circ}$	$112.588 \cdot e^{-j15.751^\circ}$	$112.588 \cdot e^{-j15.751^\circ}$	$112.588 \cdot e^{-j15.75^\circ}$
14	$110.794 \cdot e^{-j16.752^\circ}$	$110.798 \cdot e^{-j16.749^\circ}$	$110.794 \cdot e^{-j16.752^\circ}$	$110.794 \cdot e^{-j16.75^\circ}$

Taking into account the obtained results, it can be concluded that the proposed algorithms don't concede the results obtained by the iterative Newton method in the RastrWIN software package in terms of the accuracy of calculating the steady state mode. It is worth mentioning that the results in the RastrWIN were performed after 4 iterations.

4. Conclusions

In the context of using the technology of synchronized vector measurements in conjunction with traditional SCADA measurements, new algorithms for calculating the steady state mode were proposed. These algorithms have a number of advantages over the widely used iterative calculation methods:

- there is no need to select a balancing node (although it must be performed in iterative methods),

- minimizes or completely eliminates the necessity of solving nonlinear equations,

- in the process of selecting nodes for PMU placement, a matrix of nodal admittances is formed, which is easy to correct in case of a change in the transformation ratio of transformer branches or switching lines,

- minimizing the amount of time and the amount of volatile memory required to perform calculations using these specified algorithms.

The acceleration of the calculation process is achieved by reducing the number of calculations, since the values of the voltage phasors are known in advance for the nodes in which PMUs are installed. For other nodes, for which only information about traditional measurements is available, voltages are calculated using the current balance equations (algorithm A1), or partially according to Ohm's law and current balance equations (algorithm A2). Calculations are mainly performed by solving linear equations. In order to obtain a linear relationship between the known and searched voltages, it is necessary to calculate the unknown voltage according to the balance equation, compiled not for one's own, but for an adjacent node.

A significant reduction in the number of calculations is achieved by using the method of determining values and matrix-block transformation of the system of linear equations, according to which the matrix of nodal admittances includes a submatrix of a band or lower triangular structure. This in turn ensures that there is a minimum set of nodes where a PMU needs to be installed, and also provides accelerated or ultra-accelerated way to calculate steady state mode by reducing the number of required variables, whose dependence on known parameters is predominantly linear.

The proposed algorithms for accelerated and ultra-accelerated steady state mode calculation based on the joint use of PMU and SCADA measurements might become a convenient tool for analyzing the operating modes of modern EPS.

The findings of this research were presented at the International Conference on Electromechanical and Energy Systems (SIELMEN) in 2021.

Acknowledgments: The research was performed within the institutional project Nr. 20.80009.7007.18 „Soluţii tehnice ecoiNovative de Eficientizare a consumului de energie în clădiri şi elaborarea opţiunilor de dezvoltare a reţelelor inteligente cu integrare avansată a energiei regenerabile în R.M. (SINERGIE)" running at the Technical University of Moldova.

Conflicts of Interest: The author declares no conflict of interest.

References

1. Badalyan, N. *Analiz i raschyot metodov korrekcii ustanovivshihsya rezhimov elektricheskih system*. 1st ed., VIGU, Vladimir, Russia, 2017, pp. 9-38 [in Russian].
2. Presada, V.; Toma, L.; Eremia, M. An algorithm for improving the power system state estimation using PMU measurements. In: *Proceedings of IEEE Grenoble Conference PowerTech*, Grenoble, France, 2013.
3. Merkuriev, G.; Shargin, I. *Ustojchivost' energosistem. Raschety*. 1st ed., NOU Centr podgotovki kadrov energetiki, Sankt-Petersburg, Russia, 2006, pp. 38-69 [in Russian].
4. Gavrilash, M. *Modern aspects in the modeling of power systems*. 1st ed., Venus, Iasi, Romania, 2008, pp. 229-254 [in Romanian].
5. Sun, H.; Wang, Z.; Nikovski, D. Two-level state estimation method for power systems with SCADA and PMU measurements. In: *Proceedings of IEEE Innovative Smart Grid Technologies*, Asia, 2012.
6. Murdid, E.; Stratan, I. Optimal PMU Placement and Algorithms' Development of Accelerated Calculations of State Estimation Performance in Power Systems. In: *Proceedings of International Conference on Electromechanical and Energy Systems (SIELMEN)*, Iasi, Romania, 2021, pp. 115-120.

7. Xu, B.; Abur, A. Observability analysis and measurement placement for system with PMUs. In: *Proceedings of IEEE PES Power Systems Conference and Exposition*, New York, NY, USA, 2004.
8. Gamm, A.; Grishin, Y.; Glazunova, A.; Kolosok, I.; Korkina, E. New EPS state estimation algorithms based on the technique of test equations and PMU measurements. In: *Proceedings of the International Conference PowerTech*, Lausanne, Switzerland, 2007.
9. Jukov, L.; Stratan, I. *Ustanovivishiesya rezhimy slozhnyh elektricheskih setej i sistem. Metody raschetov*. 1st ed.; Energiya, Moscow, Russia, 1979, 415 p.
10. Rahman, N.H., Zobaa, A.F. Optimal PMU Placement using Topology Transformation Method in Power Systems. *J. Adv. Res.* 2016, 7 (5), pp. 625-634.
11. Chakrabarti, S.; Kyriakides, E.; Ledwich, G.; Ghosh, A. Inclusion of PMU current phasor measurements in a power system state estimator. *IET Generation, Transmission & Distribution* 2009, 4, pp. 1104 - 1115.
12. Glazunova, A.; Kolosok, I.; Korkina, E. Monitoring of EPS Operation by the State Estimation Methods. In: *Proceedings of IEEE PES ISGT Europe*, Manchester, United Kingdom, 05-07 December 2011.
13. Baldwin, L.; Mili, L.; Boisen, M.B.; Adapa, Jr.R. Power System Observability with Minimal Phasor Measurement Placement. *IEEE Transactions on Power Systems* 1993, 8 (2), pp. 701-715.
14. Bartolomey, P.; Eroshenko, S.; Semenenko, S.; Suvorov, A. PMU-based informational support of power system control tasks. *WIT Transactions on Ecology and the Environment* 2014, 190, pp. 307-318.
15. Presadă, V., Eremia, M., Toma, L. Modified state estimation in presence of PMU measurements. *UPB Scientific Bulletin, Series C: Electrical Engineering* 2014, 76, pp. 237-248.
16. Adebayo, I.; Abdul-ganiyu, J.; Adedayo, Y. An alternative method for voltage stability assessment in power system. In: *Proceedings of IEEE Africon*, Cape Town, South Africa, 2017.

Citation: Murdid, E. The use of synchronous vector measurements in the calculation of steady-state modes of electrical networks. *Journal of Engineering Science* 2023, 30 (2), pp. 90-103. https://doi.org/10.52326/jes.utm.2023.30(2).07.

Submission of manuscripts: jes@meridian.utm.md

Journal of Engineering Science *Vol. XXX, no. 2 (2023), pp. 104 - 116*
Fascicle *Electronics and Computer Science* *ISSN 2587-3474*
Topic *Electronics and Communication* *eISSN 2587-3482*

https://doi.org/10.52326/jes.utm.2023.30(2).09
UDC 004.021:004.89:629.78

ATTITUDE CONTROL OF THE NANOSATELLITE USING A HYBRID FUZZY ALGORITHM BY MEANS OF THE REACTION WHEELS

Vladimir Melnic*, ORCID: 0000-0003-4180-3654

Technical University of Moldova, 168, Stefan cel Mare Blvd., Chisinau, Republic of Moldova
* Corresponding author: Vladimir Melnic, *vladimir.melnic@mate.utm.md*

Received: 05. 16. 2023
Accepted: 06. 13. 2023

Abstract. Numerous application fields of automation the industrial processes have demonstrated favorable outcomes with modern control algorithms that rely on artificial intelligence. Therefore, some researchers have endeavored to implement these algorithms in the attitude control of satellites by evaluating their performance in simulated scenarios. However, due to the associated cost and risks, there is a scarcity of experimental data available for testing new attitude control algorithms on a real satellite. To address this issue, simulation of satellite positioning based on the dynamic model of the satellite with reaction wheels was carried out to perform a comparative analysis of a hybrid proportional integral and derivative (PID) fuzzy control algorithm and a classical PID control algorithm, regarding the analysis of the obtained performances. The obtained results indicate that using a Hybrid Fuzzy PID control algorithm produces better performances, than the PID control algorithm.

Keywords: *PID controller, fuzzy logic, attitude control, satellites, Hybrid Fuzzy PID controller.*

Rezumat. Numeroase domenii de automatizare a proceselor industriale au demonstrat rezultate favorabile în utilizare a algoritmilor moderni de control, care se bazează pe inteligența artificială. Prin urmare, unii cercetători au implementat acești algoritmi în controlul atitudinii sateliților prin evaluarea performanței acestora în scenarii simulate. Cu toate acestea, din cauza costurilor și riscurilor asociate, există un deficit de date experimentale disponibile pentru testarea noilor algoritmi de control al atitudinii pe un satelit real. Pentru a rezolva această problemă, a fost efectuată simularea poziționării satelitului în baza modelului dinamic al satelitului cu roți de reacție pentru a efectua o analiză comparativă a unui algoritm de reglare fuzzy proporțional integral și derivativ (PID) hibrid și a unui algoritm de reglare clasic PID, în ceea ce privește analiza de performanțe obținute. Rezultatele simulării au demonstrat că utilizarea algoritmului de reglare fuzzy PID hibrid asigură performanțe mai ridicate în comparație cu algoritmul de reglare clasic PID.

Cuvinte-cheie: *regulator PID, logica fuzzy, controlul atitudinii, satelit, fuzzy PID hibrid regulator.*

1. Introduction

Classical Proportional Integral and Derivative (PID) control algorithm is one of the most common control algorithms used in satellite positioning systems [1]. It can be used to control the movement of the satellite in real time, adjusting its desired orientation in the orbit as needed. In general, classical PID control algorithm is based on three components:

proportional, integral, and derivative. PID control algorithm can be effective for satellite positioning, especially for slow moving satellites. However, there are also situations where a more complex and advanced approach may be required, such as, the use of adaptive controller or other more sophisticated control methods are necessary. The concept of fuzzy controller for orbit and attitude control is a new approach that allows meeting different control requirements with mission specific redesign effort of the satellite.

The concept relies on membership functions and logic rules to analyze the observed state and take appropriate control actions without the need for complex dynamic models. One of the key features of the fuzzy controller is its ability to control the satellite at all stages of the mission without support from ground stations [2]. Classical and state-space satellite attitude control techniques use a linear approach, which is only valid for nominal inertia tensors and small perturbations. Other more complex control techniques, such as adaptive controller or nonlinear controller, better fit the idea of robust control of a system, where the system parameters are not well known, however, these techniques are quite complicated and expensive.

The hybrid fuzzy PID attitude controller provides robust and non-linear control with the ability to be easily adapted to different satellite configurations and missions [3]. Hybrid fuzzy control algorithm represents a more advanced approach to PID control algorithm, which uses fuzzy logic to improve the performance of the control system and reduce errors, and allows a fine adjustment of control parameters according to the specific conditions and requirements. This approach combines the advantages of PID controller, such as the ability to react quickly to the changes in position, with fuzzy logic, which can take into account more factors and provide a more precise and robust control approach.

All critical maneuvers low orbit missions require a high level of autonomy due to reduced visibility from the control station. This means that all onboard operations will be performed on a scheduled basis. To maintain autonomy, an attitude controller must perform all maneuvers without any ground support based only on the initial and final states. The purpose of this paper is to show the characteristics and functional performance of the hybrid fuzzy PID controller in a satellite mission.

2. Structure of satellite

The model of satellite studied in this paper is the CubeSat type. For the correct execution of the missions, the need arises for the correct orientation of the satellites to orient the antennas, to orient a camera, to give a rotational movement to the satellite to avoid overheating of a surface etc. The system that controls the attitude of the satellite is called the Attitude Determination and Control System (ADCS).

The characteristics of the studied satellite are presented in Table 1.

Table 1

Satellite structure characteristics

Description	Value	Unit
Mass	1.00	kg
Moments of inertia I_{xx}, I_{yy}, I_{zz}	0.00235; 0.00235; 0.00166	kg·m^2
Location of center of mass relative to geometrical center (x, y, z)	0.0023; 0.0034; 0.0025	m
Dimensions	0.1×0.1×0.1135	m

The positioning method is assumed to be realized by the reaction wheels [4], where the axis of rotation of each wheel corresponds to the axis of the satellite frame. The configuration of the reaction wheels relative to the satellite reference system is schematically presented in Figure 1.

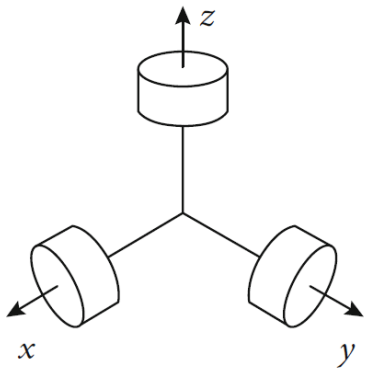

Figure 1. Diagram of the positioning of the reaction wheels in relation to the reference system of the satellite.

The characteristics of the reaction wheels together with the DC motor to which they are coupled are indicated in Table 2.

Table 2

Motor with reaction wheel characteristics

Description	Value	Unit
Moment of inertia about spin axis	1.25	kg·mm^2
Armature current	0.41	A
Speed	9000	min^{-1}

In any typical ADCS system, there are basically two parts: actuators (reaction wheels described above) and sensors. In case, studied in this paper, there are used the following sensors:

1. Microgyros - for determination of rotation velocity of the satellite.
2. Hall sensors - for determination of reaction wheel velocity.
3. Other IMUs for attitude determination.

3. Dynamics and kinematics of the satellite with reaction wheels

The equations that govern the attitude of a satellite can be represented by equations related to angular kinematics [5]. Knowing Euler's moment equation (1) [6]

$$\dot{h}_{tot} = N_e - \omega \times h_{tot}, \tag{1}$$

where $h_{tot} = \sum_j^N (\mathrm{I}_j\, \omega_j)$ is the sum of all parts (*N*) of the satellite, N_e is the total external impulse, ω angular velocity of the satellite.

The kinematics of the body is described by the attitude quaternion, in equation (2) below [6,7]

$$\dot{q} = \frac{1}{2}\Omega q \equiv \frac{1}{2}\begin{bmatrix} 0 & \omega_3 & -\omega_2 & \omega_1 \\ -\omega_3 & 0 & \omega_1 & \omega_2 \\ \omega_2 & -\omega_1 & 0 & \omega_3 \\ -\omega_1 & -\omega_2 & -\omega_3 & 0 \end{bmatrix} q, \tag{2}$$

where and ω_1 is the rotation speed of the satellite relative to the *x*-axis, ω_2 relative to the *y*-axis and ω_3 respectively relative to the *z*-axis, *q* is the attitude quaternion. The attitude quaternion $\mathrm{q} = [q_1, q_2, q_3, q_4]^T$ is used to describe the kinematics of the satellite. The quaternion components are explicitly represented using Euler rotation angles in the sequence 3-1-3, the representation of quaternions by Euler angles is shown below [8].

$$q_1 = \cos(\varphi/2)\cos(\theta/2)\cos(\psi/2) - \sin(\varphi/2)\cos(\theta/2)\sin(\psi/2),$$
$$q_2 = \cos(\varphi/2)\sin(\theta/2)\cos(\psi/2) + \sin(\varphi/2)\sin(\theta/2)\sin(\psi/2),$$
$$q_3 = \cos(\varphi/2)\sin(\theta/2)\sin(\psi/2) - \sin(\varphi/2)\sin(\theta/2)\cos(\psi/2),$$
$$q_4 = \cos(\varphi/2)\cos(\theta/2)\sin(\psi/2) + \sin(\varphi/2)\cos(\theta/2)\cos(\psi/2).$$

The rotation of the satellite was further described using the rotation matrix [6], in which the elements of the attitude quaternion are used as parameters. Being known as I_S as the inertia matrix of the satellite, h_ω being the total angular momentum of the flywheels, *ω* as the angular velocity of the satellite, N_e as the total external impulse, all in the coordinate system attached to the satellite, the dynamics of the satellite is described by the following relations..

Thus, the dynamic equation is (3), or it can be written in the form (4):

$$\frac{d}{dt}(\mathrm{I}_S\,\omega) + \dot{\mathrm{h}}_\omega = N_e - \omega \times \mathrm{I}_S\,\omega - \omega \times \mathrm{h}_\omega, \tag{3}$$

$$\dot{\omega} = -\mathrm{I}_S^{-1}(\omega \times \mathrm{I}_S\,\omega) - \mathrm{I}_S^{-1}\,\omega \times \mathrm{h}_\omega - \mathrm{I}_S^{-1}\,\dot{\mathrm{h}}_\omega + \mathrm{I}_S^{-1}\,\mathrm{N}_e. \tag{4}$$

If the cross product is written as a matrix operation using $\mathrm{S}(\omega)$, then a simpler form is obtained (Equation (5))

$$\mathrm{S}(\omega) = \begin{bmatrix} 0 & -\omega_3 & \omega_2 \\ \omega_3 & 0 & -\omega_1 \\ -\omega_2 & \omega_1 & 0 \end{bmatrix}, \tag{5}$$

is obtained (Equation (6)):

$$\dot{\omega} = -\mathrm{I}_S^{-1}\,\mathrm{S}(\omega)\,\mathrm{I}_S\,\omega - \mathrm{I}_S^{-1}\,\mathrm{S}(\omega)\mathrm{h}_\omega - \mathrm{I}_S^{-1}\,\dot{\mathrm{h}} + \mathrm{I}_S^{-1}\,\mathrm{N}_e. \tag{6}$$

The combined nonlinear dynamic model of the satellite is complemented by the fact that the control torque in the satellite coordinate system is N_c and provides a rate of change of the total angular momentum from the reaction wheels (Equation (7)):

$$\dot{h} = -N_C, \tag{7}$$

and therefore the dynamics of the satellite driven by the reaction wheels is described by equation (8)

$$\dot{\omega} = -\mathrm{I}_S^{-1}\,S(\omega)\,\mathrm{I}_S\,\omega - \mathrm{I}_S^{-1}\,S(\omega)h + \mathrm{I}_S^{-1}\,N_C + \mathrm{I}_S^{-1}\,N_e. \tag{8}$$

The satellite position is obtained by rotating the satellite frame with respect to the inertial frame by means of the matrix of director cosines A_{SI} [9]. The rotation matrix is parametrized by quaternions and denoted by $A_{SI}(q)$. The vector measured in the inertial frame is a_I, and the vector measured within the satellite frame has the coordinates a_S, so $\mathrm{a}_S = A_{SI}(q)\,\mathrm{a}_I$. The kinematics of the satellite is described by Equation (9)

$$\frac{d}{dt}\begin{bmatrix} q_1 \\ q_2 \\ q_3 \\ q_4 \end{bmatrix} = \frac{1}{2}\begin{bmatrix} 0 & \omega_3 & -\omega_2 & \omega_1 \\ -\omega_3 & 0 & \omega_1 & \omega_2 \\ \omega_2 & -\omega_1 & 0 & \omega_3 \\ -\omega_1 & -\omega_2 & -\omega_3 & 0 \end{bmatrix}\begin{bmatrix} q_1 \\ q_2 \\ q_3 \\ q_4 \end{bmatrix}. \quad (9)$$

For simplicity it will be represented as follows (Equation (10))

$$\dot{q} = \frac{1}{2}\Omega(\omega)q\,. \quad (10)$$

A For a later analysis, another detailed form of kinematics is considered. For this, Equation (9) is rewritten to a form that separates the terms containing q_4 from the other elements of the attitude quaternion. Thus the vector formed by the elements q_1, q_2, q_3 of the attitude quaternion is denoted by g.

$$\mathrm{g}=\begin{bmatrix} q_1 \\ q_2 \\ q_3 \end{bmatrix}.$$

Hence equation (10) takes the form (11-12)

$$\dot{\mathrm{g}} = -\frac{1}{2}\omega \times g + \frac{1}{2}q_4\omega\,, \quad (11)$$

$$\dot{q}_4 = -\frac{1}{2}\omega^T \mathrm{g}\,. \quad (12)$$

The full form of the model is (Equation (13))

$$\frac{d}{dt}\begin{bmatrix} q_1 \\ q_2 \\ q_3 \\ q_4 \end{bmatrix} = -\frac{1}{2}\begin{bmatrix} 0 & -\omega_3 & \omega_2 \\ \omega_3 & 0 & -\omega_1 \\ -\omega_2 & \omega_1 & 0 \\ \omega_1 & \omega_2 & \omega_3 \end{bmatrix}\begin{bmatrix} q_1 \\ q_2 \\ q_3 \end{bmatrix} + \frac{1}{2}\begin{bmatrix} q_4 & 0 & 0 \\ 0 & q_4 & 0 \\ 0 & 0 & q_4 \\ 0 & 0 & 0 \end{bmatrix}\begin{bmatrix} \omega_1 \\ \omega_2 \\ \omega_3 \end{bmatrix}. \quad (13)$$

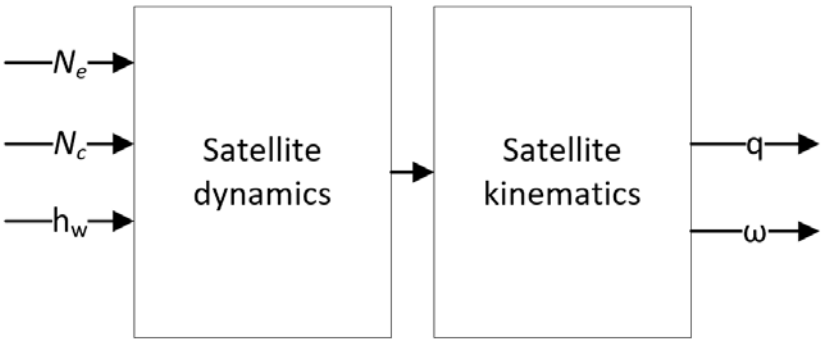

Figure 2. Satellite model with nonlinear dynamics and kinematics, where N_e - an external torque, N_c - control torque from reaction wheels, $\underline{h_\omega}$ – angular momentum of wheels and output is q and ω.

So, it is obtained, that the kinematic equation is written using $q = \left[g^T, q_4 \right]$, where g is the q_1, q_2, q_3 components of the quaternion (Eq. 14)

$$\frac{d}{dt}\begin{bmatrix} g \\ q_4 \end{bmatrix} = \frac{1}{2}\begin{bmatrix} -S(\omega) \\ -\omega^T \end{bmatrix} g + \frac{1}{2} q_4 \begin{bmatrix} I_{3\times 3} \\ 0 \end{bmatrix} \omega . \quad (14)$$

In this operation it preserves the unit length of the quaternion. The satellite model includes the dynamics in Equation (4) and the kinematics in Equation (10), that can be presented by the model presented in the Figure 2.

4. Attitude control system

The attitude control process is carried out according to the following scheme:

1. Only enabled with the permission of the mission planning process. As a rule, it will be requested at the moment of capturing the image and transmitting the data to the ground station.
2. It is checked if the stabilization and orientation of the satellite can be achieved, otherwise the process of combating hijacking/uncontrolled running will be activated.
3. The current attitude (current position) of the satellite will be determined.
4. The reference position of the nanosatellite will be obtained from the mission planning process or by telemetry command from the ground station (usually the requested position or "nadir" of the satellite).
5. The difference between the current position and the reference one is calculated and the error is transmitted to the controller.
6. Motors with reaction wheels shall be actuated according to the control law.
7. Steps 2-6 will be repeated, until the current position does not coincide with the reference one.

The orientation of the satellite is determined by interrogating the set of magnetometers, accelerometers, microgyroscopes and IGRF modeling (IGRF - International Geomagnetic Reference Field - the set of spherical harmonic coefficients, which can be entered into a mathematical model to describe the Earth's internal magnetic field).

The positioning of the nanosatellite is achieved by driving the reaction wheels, which are embedded on three axes *X, Y* and *Z*, which operate based on the principle of conservation of angular momentum. A reaction wheel is essentially a spinning wheel mounted on a satellite that can change its orientation by changing the speed and direction of the wheel's rotation. When a reaction wheel spins in one direction, the spacecraft will begin to rotate in the opposite direction, due to the conservation of angular momentum.

In this article, Figure 3 illustrates the overall design of a satellite attitude control system that was studied.

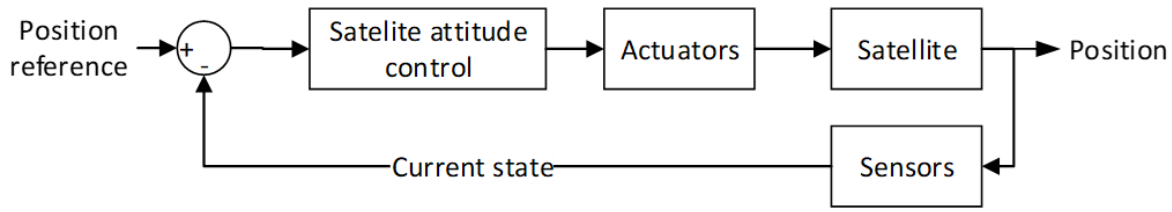

Figure 3. Design of a satellite attitude control system.

The simulation model utilized the models described earlier, namely the "Actuators" and "Satellite" blocks. However, the "Sensors" block was not included in this particular research. The "Current state" data block includes the state variables of the satellite, reaction wheels and the quaternion $q = [q_1, q_2, q_3, q_4]^T$.

5. Synthesis of the hybrid attitude control algorithm

The synthesis of a hybrid fuzzy PID control algorithm for satellite attitude control is an algorithm that combines the strengths of both fuzzy logic and proportional-integral-derivative (PID) control algorithm, to improve the performance of satellite attitude control. Fuzzy logic, which is based on fuzzy set theory, is well-suited for handling uncertainty and imprecision in the system and is effective in modeling complex and nonlinear systems.

On the other hand, PID control is a widely used as control algorithm, that is simple to implement and has good robustness and stability. By combining these two methods, a hybrid fuzzy PID control algorithm can achieve improved control accuracy and robustness over using either method alone. Synthesizing such a control algorithm is a challenging task that requires a deep understanding of the system dynamics and a combination of analytical and simulation-based approaches. It involves designing a fuzzy logic controller, a PID controller and then integrating them to achieve optimal control performance. This integration takes place using a set of instructions or functions, that set some rule to transmit the command from the PID or Fuzzy controller, or modify the command according to some function.

The PID control algorithm

The three parameters of the PID control algorithm are the proportional (P), integral (I), and derivative (D) components. The P component relies on the current error, the I component on the accumulated past error, and the D component on the anticipated future error, based on the current rate of error change, Figure 4 shows the block scheme of the automatic control system [10, 11].

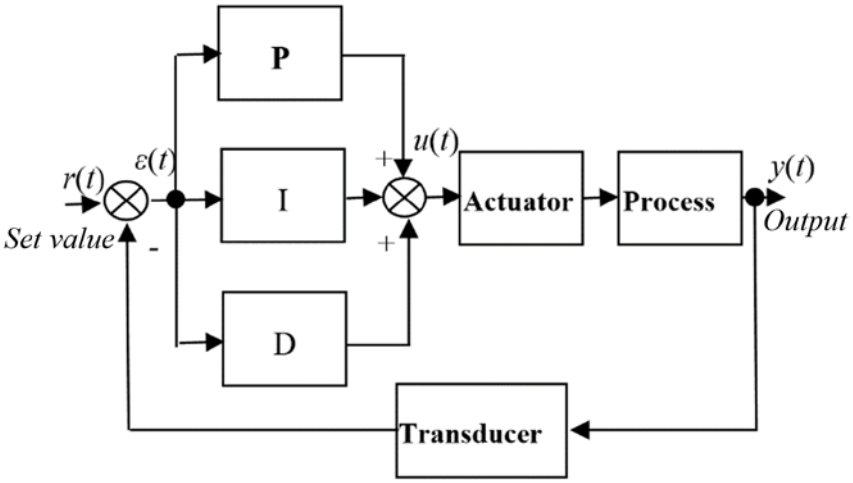

Figure 4. Block scheme of the automatic control system.

Various techniques exist for generating control algorithms, including experimental methods, graphic-analytical methods that rely on knowledge of the mathematical model approximating the process, optimization methods, and artificial intelligence approaches such as evolutionary algorithms, which are commonly employed in optimizing the PID control algorithm synthesis problem.

Fuzzy controller

Fuzzy Logic Control (FLC) is a type of control method that uses fuzzy set theory to represent data and interpret human experience in real-world scenarios. It operates based on a set of rules and has gained the attention of numerous researchers over the past few decades as an innovative and effective control approach for a variety of applications. One of the key advantages of FLC is its independence from the plant model, making it a popular choice for

systems where the precise mathematical model of the object is unknown or contains significant nonlinearities. This characteristic has led to its widespread adoption and investigation [12].

The fuzzy controller is composed of the following three elements:

1. **Fuzzification stage:** the initial data is transformed into linguistic variables, where the values are determined based on the input membership functions. Specifically, for this paper, the input data for the Fuzzy Logic Controller (FLC) will consist of the error signal (e(t)) and the rate of change of the error signal (de/dt) [13]. The most commonly used input membership function to represent linguistic variables in this stage is the triangular membership function, but other types of membership functions can also be used, such as trapezoidal or gaussian. The linguistic variables can receive different values labeled as - Large Negative, Medium Negative, Small Negative, Zero, Small Positive, Medium Positive, Large Positive and labeled as (NB, NM, NS, Z, PS, PM, PB) respectively [14].
2. **Rule base:** the rule base is a method of decision-making that mimics the human thought process. It comprises the definitions of fuzzy membership functions allocated to each control variable, along with the essential rules that articulate the control's objectives through the use of linguistic variables. The rules are usually designed using natural language, making it easy for non-experts to understand and modify the controller. The rule base is a crucial component of the fuzzy controller, as it determines the behavior of the controller based on the input data.
3. **Defuzzification:** the decision deduced is converted back into numerical values. The input for defuzzification is the membership (certainty) in the implicit fuzzy sets resulting from the premise rules, and the output is a crisp number [15].

The membership functions for the input and output variables are presented in the Figure 5.

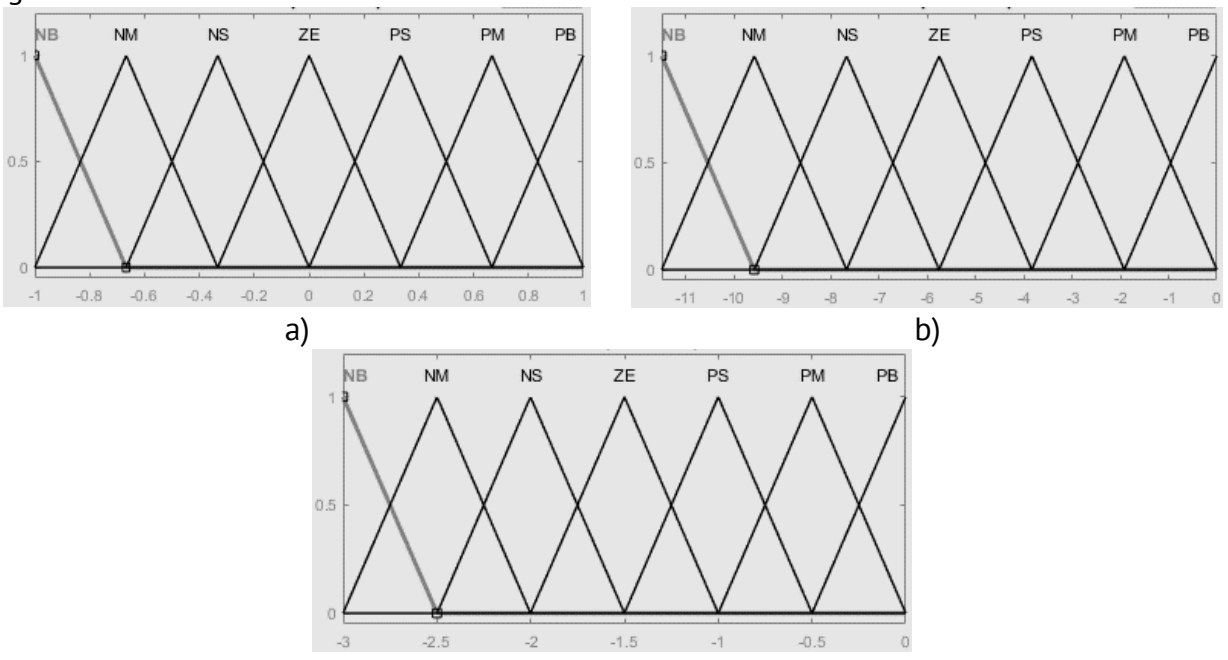

Figure 5. The membership functions: a) error signal; b) rate of change of the error signal; c) command signal.

The fuzzy rules for the two input variables as: error signal - $e(t)$ and the variation of the error $\Delta e(t)$, based on which the attitude of the satellite is controlled are presented in Table 3.

Table 3

The base of the fuzzy rules

Δe(t) \ e(t)	NL	NM	NS	ZR	PS	PM	PL
NL	NL	NL	NL	NM	NS	ZR	PS
NM	NL	NL	NM	NS	ZR	PS	PM
NS	NL	NM	NS	ZR	PS	PM	PL
ZR	NM	NS	ZR	PS	PM	PL	PL
PS	NS	ZR	PS	PM	PL	PL	PL
PM	ZR	PS	PM	PL	PL	PL	PL
PL	PL	PL	PL	PL	PL	PL	PL

Note: NL-Large Negative, NM-Medium Negative, NS-Small Negative, ZR-Zero, PS-Small Positive, PM-Medium Positive, PL-Large Positive.

The Hybrid control algorithm

A hybrid fuzzy PID controller combines the concepts of fuzzy logic control and PID control to achieve better control performance in a system. The fuzzy logic component helps handle nonlinearities and uncertainties in the system, while the PID component provides robust and accurate control. the block diagram of the hybrid fuzzy PID controller is shown in Figure 6. It works in the following way: Fuzzy and PID controllers receive the error signal and perform some correction according to the control algorithm. After the correction performed at the output of the fuzzy and PID controllers, the signal is passed to the mixing block u_FUZZY and u_PID.

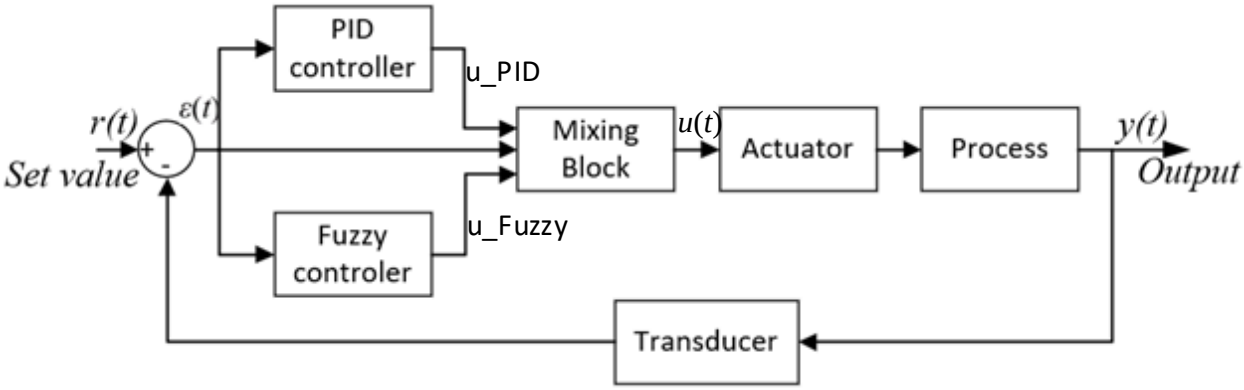

Figure 6. Control scheme of the hybrid controller.

The combination function is initially declared as a function with three inputs and one output, then a coefficient f is equal to the error value to the power of 2, $f(e) = e^2$, and the output variable is equal to 0.

Depending on the response of the Fuzzy controller and PID we have three cases:

1. If the response of the Fuzzy controller is faster than the response of the PID controller, then the command value *u* is calculated using the relation:
$$u_{hibrid} = f(e) * u_{PID} + \big(1 - f(e)\big) * u_{Fuzzy}$$
2. If the response of the PID controller is faster than the response of the Fuzzy controller, the command value *u* is calculated using the relation:
$$u_{hibrid} = (1 - f(e)) * u_{PID} + f(e) * u_{Fuzzy}$$
3. If the response of the PID controller is equal to the response of the Fuzzy controller, the command value u remains that of the PID controller.

6. Simulation

The hybrid fuzzy PID controller has undergone testing using a realistic simulation environment that incorporates a satellite model and attitude dynamics. This simulation was realized using the simulation software MATLAB/Simulink. The tool was utilized to construct the entire control loop and manage the integration of differential equations of continuous variables and output calculation of sensors. Customized attitude functions were also incorporated. The Simulink tool was employed to model the kinematics, mass properties, and motion of the satellite around its center of mass.

To control the rotations of the reaction wheels, the mathematical model of the reaction wheel engine was identified. The mathematical model of the direct current motor was experimentally identified using the System Identification Toolbox in Matlab. The identification process involved analyzing the experimental speed variation data of the DC motor at a reference speed of 7330 rpm.

The speed variation experimental data of the DC motor was modeled as a second-order inertial system [11]:

$$H(s)=\frac{k}{(T_1 s+1)(T_2 s+1)}=\frac{1.0069}{3.1695s^2+5.0289s+1}.$$

In this work, the Genetic Algorithm was used for the synthesis of the PID control algorithm for the speed control of the direct current motor (reaction wheels), depending on the imposed performance.

The PID control algorithm in the standard form was utilized, which is characterized by the following transfer function:

$$H_{PID}(s)=k_p+\frac{k_i}{s}+k_d s=\frac{k_d s^2+k_p s+k_i}{s},$$

where k_p, k_i, k_d – are the tuning parameters of the PID control algorithm.

The PID controller was tuned by the genetic algorithm and there are obtained the following values of the tuning parameters: $k_p=20.402$, $k_i=4.58$, $k_d=9.12$, It was obtained the transient response with following performance: t_r=0,55, t_s=2,00, σ=3,99, λ=*1,* [11].

The obtained simulation result of tuning the PID controller is presented in the Figure 7.

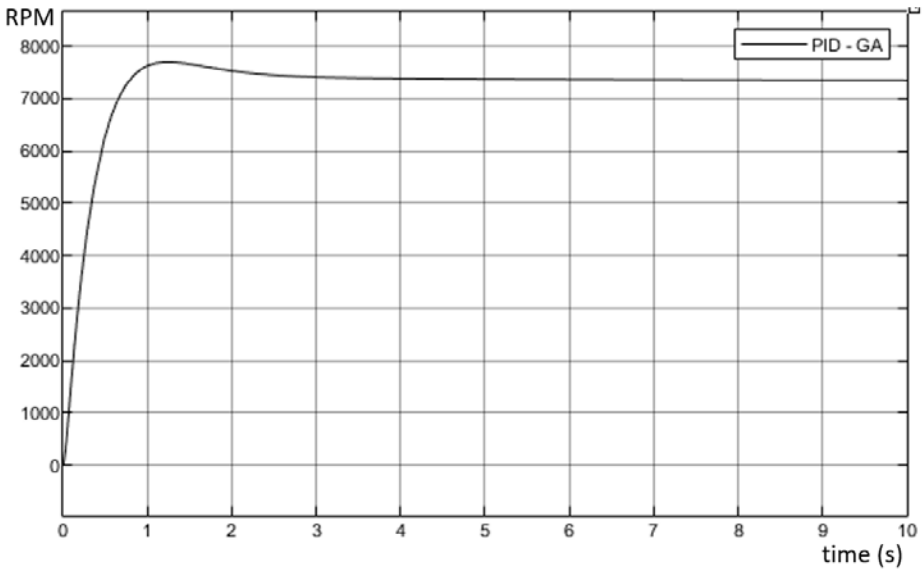

Figure 7. The transient responses of the control system with PID controller.

The transient responses of the satellite positioning control system using the PID control algorithm is presented in Figure 8. This algorithm ensures the settling time equal with 2.5 seconds.

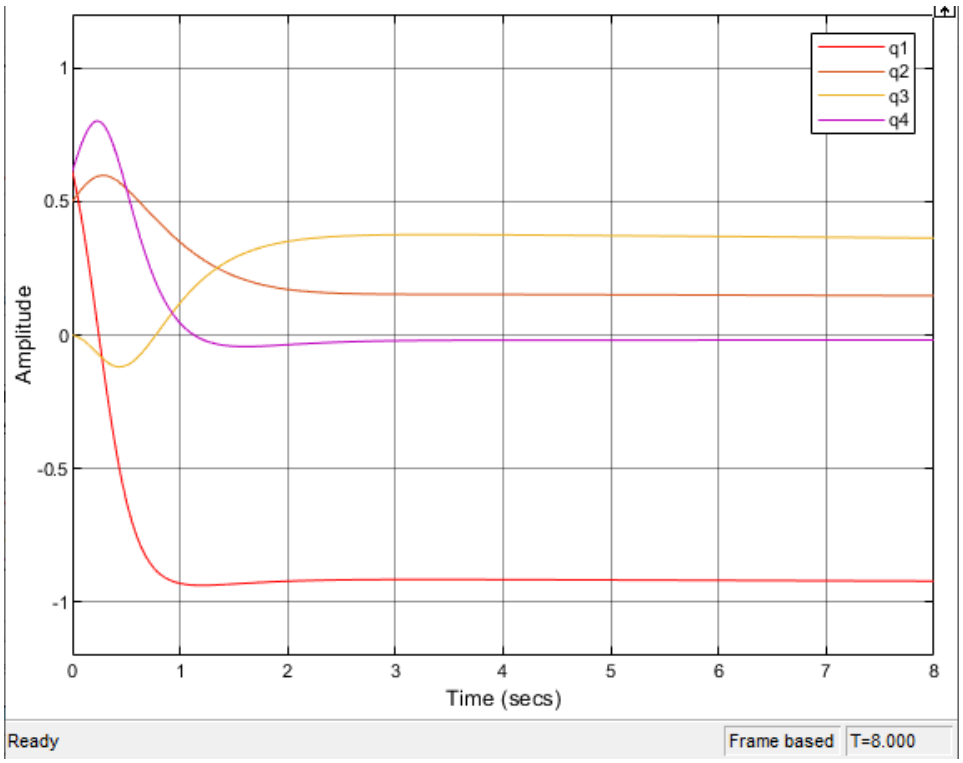

Figure 8. The transient responses of the control system with PID controller.

The transient responses of the satellite positioning control system using the hybrid fuzzy PID controller is presented in Figure 9. This algorithm ensures settling time equal with 2 seconds.

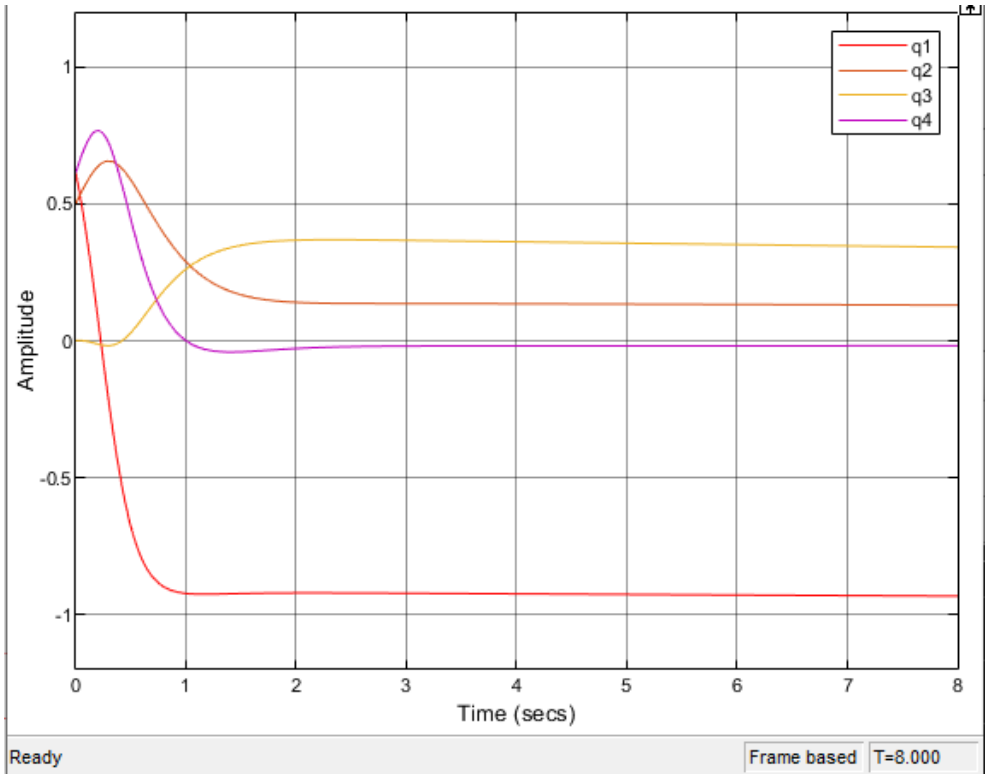

Figure 9. The transient responses of the control system with hybrid fuzzy PID controller.

From the simulation results, it can be observed, that using the hybrid fuzzy PID controller system has better performance than system with PID controller.

Conclusion

The paper compared the effectiveness of a hybrid fuzzy PID control algorithm with a classical PID control algorithm in process of controlling the attitude of a nanosatellite, by using a simulation of the system with a reaction wheels for positioning. Results indicated that artificial intelligence strategies, specifically fuzzy logic, could improve the attitude control of nanosatellites. The comparison also revealed that the hybrid fuzzy PID controller outperformed the PID controller in terms of settling time, with up to 20% faster. This is illustrated in Figure 10. Finally, the obtained results contribute to the development of an ADCS with 3 axes, which will also allow experimental testing of control algorithms.

Acknowledgment

This work was supported by the project „Research and synthesis of efficient attitude control algorithms for nanosatellites".

Conflicts of Interest: The author declares no conflict of interest.

Reference

1. Bello, Á.; Olfe, K.; Ezquerro, J. M.; Rodríguez, J.; Lapuerta, V. Experimental comparison of attitude controllers for nanosatellites. In: *8Th European Conference for Aeronautics and Space Sciences (EUCASS)*, Published by the EUCASS Madrid 2019, pp. 15.
2. Bello, Á.; Olfe, K.; Rodríguez, J.,; Ezquerro, J. M.; Lapuerta, V. Experimental verification and comparison of fuzzy and PID controllers for attitude control of nanosatellites. *Advanced in Space Research,* COSPAR 2022, pp. 18.
3. Erenoglu, I.; Eksin, I.; Yesil, E.; Guzelkaya, M. An Intelligent Hybrid Fuzzy PID Controller. In: *Proceedings 20th European Conference on Modelling and Simulation*, 2006, pp. 62-66.
4. Ge, S.; Cheng, H. A Comparative Design of Satellite Attitude Control System with Reaction Wheel. In: *First NASA/ESA Conference on Adaptive Hardware and Systems*, Istanbul, Turkey, 2006, pp. 4.
5. Nudehi, S.; Farooq, U.; Alasty, A.; Issa, J. Satellite attitude control using three reaction wheels. In: *American Control Conference*, Seattle, Washington, USA, 2008, pp. 4850-4855.
6. Sidi, M. Spacecraft Dynamics and Control. In: *A practical Engineering Approach*. Cambridge University Press, New York, USA, 1997, pp. 95-97.
7. Wertz, J. *Spacecraft Attitude Determination and Control*. Kluwer Academic Publishers, Dordrecht, The Netherlands, 1984, pp. 510-514.
8. Diebel, J. Representing Attitude: Euler Angles, Unit Quaternions, and Rotation Vectors. *Matrix, 2006,* pp. 35.
9. Roubache, R.; Benyettou, M.; Simohammed, A.M.; Boudjemai, A.; Bellar A. Extended Kalman filter for attitude determination of an elliptical orbit satellites. In: *The 6th International Conference on Recent Advances in Space Technologies (RAST)*, Istanbul, Turkey, 2013, pp. 17.
10. Borase, R.P.; Maghade, D.K.; Sondkar, S.Y.; et al. A review of PID control, tuning methods and applications. *International Journal of Dynamics and Control 9*, 2021, pp. 818–827.
11. Melnic, V.; Cojuhari, I. Synthesis the PID Control Algorithm for Speed Control of the DC Motor based on the Genetic Algorithm. In: *The 12th International Conference on Electronics, Communications and Computing*, Chisinau, Republic of Moldova, 2021, pp. 148-151.
12. Yassin, M. Y.; Mahallawy, A.; El-Sharkawi, A. Real time prediction and correction of ADCS problems in LEO satellites using fuzzy logic. *The Egyptian Journal of Remote Sensing and Space Sciences*, 2017, pp 11-19.
13. Chekenbah, H.; Maataoui, Y.; Lasri, R.; Choukri, L. Application of an adaptive fuzzy logic controller to optimize the performances of the P&O algorithm. *In: Conference on Computer Science and Engineering Technology*, 2020, pp. 8. doi:10.1088/1757-899X/1088/1/012051.
14. Calvo, D.; Aviles, T.; Lapuerta, V.; Laverón-Simavilla, A. Fuzzy attitude control for a nanosatellite in low Earth orbit. *Expert Systems with Applications*. 2016, pp. 102-118.

15. Melnic, V.; Cojuhari, I.; Tuning the Fuzzy Controller for Speed Control of the DC Motor. In: *The 12th International Conference on Electronics, Communications and Computing,* Chisinau, Republic of Moldova, 2022, pp. 240-243.

Citation: Melnic, V. Attitude control of the nanosatellite using a hybrid fuzzy control algorithm by means of the reaction wheels. *Journal of Engineering Science* 2023, 30 (2), pp. 104-116. https://doi.org/10.52326/jes.utm.2023.30(2).09.

Submission of manuscripts: jes@meridian.utm.md

Journal of Engineering Science *Vol. XXX, no. 2 (2023), pp. 117 - 125*
Fascicle *Architecture, Civil and Environmental Engineering* *ISSN 2587-3474*
Topic *Architecture, Urbanism and Cadaster* *eISSN 2587-3482*

https://doi.org/10.52326/jes.utm.2023.30(2).10
UDC 528.9:004(478)

LAND USE WEB MAP OF MOLDOVA CREATING USING WEB-BASED MAPPING SOFTWARE ARCGIS ONLINE

Ioana Chiriac*, ORCID: 0000-0003-4684-0243

Technical University of Moldova, 168 Stefan cel Mare Blvd., Chisinau, Republic of Moldova
*Corresponding author: Ioana Chiriac, *ioanna.chiriac@gmail.com*

Received: 04. 11. 2023
Accepted: 05. 26. 2023

Abstract. The motivation for creating of an interactive map for school is the desire to collect all the necessary information from different sources into one web map to facilitate and standardize the process of teaching geography of the Republic of Moldova, and due to the interactivity of the map to increase student academic achievement and motivation. In the article the methodology of the research, which is carried out within scientific project, the creation of Land Use Web school map of Moldova is considered. The content of the Land Use Web Map and interface screenshots showing functions of interactive map are presented in the article. In the main part of the article, the technology of the creation of Land Use map is described developed by means of work with spatial data of Laboratory of Geomorphology and Ecopedology of Institute of Ecology and Geography and using tools of Web-based mapping software ArcGIS Online. The first result of the study is the description of the technology by which any other thematic web map can be created. The second result is the Land Use web map of Moldova, which through the Internet can be used in any country of the world by students and school teachers.

Keywords: *Interactive map, Geographic Information System, secondary school education.*

Rezumat. Motivarea în realizarea unei hărți interactive pentru școală este dorința de a colecta toate informațiile necesare din diferite surse într-o hartă web pentru a facilita și standardiza procesul de predare a geografiei Republicii Moldova, iar datorită interactivității hărții - a motiva pe elevi de a multiplica cunoștințele în domeniu. În articol se ia în considerare metodologia cercetării, care se desfășoară în cadrul proiectului științific, realizarea hărții interactive Utilizarea terenurilor în Republica Moldova. În articol dat este descrisă tehnologia de creare a hărții web utilizând datele spațiale din Laboratorul de Geomorfologie și Ecopedologie al Institutului de Ecologie și Geografie și folosind instrumentele ArcGIS Online. Conținutul hărții tematice și capturile de ecran ale hărții web sunt prezentate în articol. În urma cercetării au fost stabilite două rezultate. Primul rezultat al cercetării este descrierea tehnologiei pentru crearea altor hărți tematice interactive. Al doilea rezultat al cercetării este harta web de utilizare a terenurilor în Republica Moldova, care poate fi accesată prin intermediul Internetului în orice țară de către elevi și profesori.

Cuvinte cheie: *Hartă interactivă, Sistem Informațional Geografic, învățământ secundar.*

1. Introduction

For centuries, maps were routinely printed on paper. Although useful and aesthetically pleasing, paper maps were not always easily accessible and were often too expensive for the map consumer. In many cases, university libraries were the best places to locate paper maps. But the Web has fundamentally changed how maps are accessed, distributed, and produced [1, p.442]. According to Michael Peterson, the Web has evolved over three distinct periods that have fundamentally changed how maps are distributed. During the Web's early years, existing paper maps were digitally converted into .jpg or .gif images that were stored and retrieved via Web. As the Web matured, developments in technology and the evolution in computer languages allowed interactivity and animation to take place via the Web. In its current state, the Web has potential to deliver a considerable range of mapping products [2, p. 357].

Web map is an interactive display of geographic information that can be used in school education successfully. Using specific mapping-based Web site, teachers can individually tailor data sets, symbolization, data classes, color schemes and to produce maps to suit their individual mapping requirements in real time. In addition, an interactive school web map maybe used on the white board. To clarify, organize and prioritize learning, teacher can resize map, pan, zoom in or zoom out, highlight some objects in different ways, select areas, add or hide geographical elements, create geospatial tests for students. Students can search geographical objects on digital maps using spatial data tools, measure distances on interactive map, to color digital contour maps, to analyze statistics data from different sources, to create thematic map using geospatial analyze, to save digital map, to export it like an image or to print it.

Thanks to the presence of interactive maps at school, students will grow up with the understanding that GIS is an information and scientific complex for studying the dynamics and predicting landscape changes and its main components - relief, climate, soil, water and forest resources; impact anthropogenic impact on the landscape. [3, p. 82].

Currently, at the secondary education institutions (gymnasiums, high schools) of the Republic of Moldova on the Geography lessons only paper Geography Atlases are used. These atlases do not correspond to modern GIS (Geographic Information System) and are not convenient for online lessons in quarantine or homeschooling [4].

For example, "Physical and Social Geography of Republic of Moldova" Atlas is available to students during their grade 8 year. This Atlas been elaborated with the participation of the author of this article, published in 2015 by Institute "INGEOCAD", consists of two sections: physical geography and social geography of Republic of Moldova. Of particular interest is the map of the structure of the land fund, because agriculture has traditionally been and remains the main pillar of the economy of Moldova. This map shows by diagrams the percentage of arable land, orchards, vineyards and pastures in each district of Republic [5, p. 23]. The Land Use map [6, p. 149] from Atlas of History and Geography of Romania was used as an example. There is one more map from another section of Atlas, the cartogram [7, p. 248] in which districts are coloured by means of erosion degree. The impact of soil loss is one of the most pressing environmental problems. With a very slow rate of soil formation, any soil loss above 1 ton/ha/year is considered irreversible within a time span of 50-100 years. The mail causes of soil erosion remain inappropriate agricultural practices, deforestation, overgrazing, forest fires and construction [8, p.16]. Because erosion is a serious problem for productive

agricultural land, an idea was born to combine these two paper maps into one interactive for better visual spatial analysis.

Based on previous experience in creating physical and thematic maps for the above-mentioned atlas, it can be hypothesized, that the spatial data and geovisualization tools [9, 10] previously used to create paper maps can be used to build an interactive map too. To support this hypothesis, the detailed technological scheme of the atlas creation was also studied [11]. In general, the creating a paper map lifecycle consists of four steps: page design, mapping, preparing for printing and printing on a printing house [12, p. 92]. The Page Design includes determination of mapping territory boundaries, its placement relative to page frames, legend and, if it is required, additional small-scale maps, explanation text, graphs and diagrams. During this process, technical conditions are taken into account too. It means that standard paper sizes for printing, visual equilibrium of page elements are carefully studied. Besides especially important requirements aimed at correctly displaying of idea and usability of map [13, p. 119]. The next step GIS mapping refers to the process by which geo-located data are charted onto maps using different cartographic methods. The most frequently used cartographic methods from Salichev classification [14] are cartogram, carto diagram, qualitative background method, linear method and Map Icons. Preparing for printing require some processing before printing or electronic distribution. For example, preparing of text and graphic elements of pages that meet output requirements. The last step of creating of a paper geographical atlas is printing on a Typography printing house. This process is the shortest from all the paper map lifecycle, but is the most responsible one. This is because errors that editors did not notice earlier can be identified on Typography's specimen, corrected and not replicated for many hundreds or thousands of copies.

Mapping is the only one common step for web mapping and creation of paper map. Page design may be replaced with creation of dashboards. At the first stage, there is a need to add the creation of a geodatabase, at the last - data sharing relationships.

So, it became necessary to determine the methods, procedures and principles for creation of thematic web maps for schools, because, for example, various spelling for a place-name always present a problem [15, p. 62]. It is hypothesized that names from web base map can be used for mapping.

The aim of this paper is to explore the methods of creating and sharing of interactive web map of Moldova using ArcGIS Tools.

2. Materials and Methods

There were used tools from ArcGIS Data Management Toolbox to develop, manage, and maintain feature classes, datasets, layers, and raster data structures. To simplify the task for data storage, a decision was made to use cloud-based mapping ArcGIS Online. With cloud storage, there is no need to rack and stack servers. In the cloud, businesses can scale workloads based on certain metrics as needed - in literally a few clicks - using built-in features. In the course of work, a free version of ArcGIS Online was used to test the map.

Table 1 gives an overview of the applications and tools used for Land Use map creation.

The first phase of the data lifecycle is the creation of Geodatabase in ArcCatalog Application with two types of data: Feature classes and Tables.

Next step is to relate attribute table of polygon layer of Moldova's districts with Excel Table which contains Land Use information using tool Join Field from ArcToolbox. As a result, automatically indicators of Land Use are added to be marked on the map at the next step.

Table 1

Applications and tools used for mapping

	Application/Tools	Purpose
1	ArcCatalog 10.4.1	Collect data to Geodatabase
2	ArcMap 10.4.1, ArcToolbox, Representation	Map Design
3	ArcGIS Online	Create cloud-based interactive map
4	ArcGIS API for JavaScrip	Create and customize Dashboard

Next step is Map Design. Taking into account the fact that base map has been provided on ArcGIS Online by Esri free of charge, there is no need to create Layers of cities, hydrography, etc. For the Land Use of Moldova map there was created only one feature class with area objects of the Moldova's districts, each of which in its table of attributes keeps information on the percentage of land damaged by erosion, percentage of vineyards, arable land, orchards and pastures in the total area of the district (Figure 1).

Raion_Name	ravene	arabil	Livezi	Vii	pasuni
Anenii Noi	1	65.28	5.44	6.89	11.89
Basarabeasca	3	67.49	2.02	10.14	19.76
Briceni	1	78.38	9.33	0.24	11.47
Cahul	4	74.29	2.07	14.06	8.45
Călăraşi	5	47.19	11.29	21.77	18.65
Cantemir	4	67.28	3.91	10.25	15.89
Căuşeni	3	74.66	5.46	6.25	12.89
Cimişlia	3	71.68	2.92	8.98	15.67
Criuleni	2	74.4	5.07	4.19	9.9
Criuleni	2	74.4	5.07	4.19	9.9
Donduşeni	1	71.2	10.65	0.16	16.89
Drochia	2	82.42	2.62	0.26	13.55
Dubăsari	2	77.14	6.44	3.56	11.71
Dubăsari	2	77.14	6.44	3.56	11.71
Edineţ	1	79.58	6.21	0.16	13.81

Figure 1. Attribute table of Thematic Layer.

All this information from the attribute table has been indicated on the map by two different cartographic methods. To indicate the degree of damage to the land of the district by erosion, the cartographic method of cartogram was selected. Also there was created the carto diagram with land use structure on districts. Chart shares are percentages of area used for arable agriculture, area used for orchards, area used for vineyards and area used for pastures.

In Table 2, data and data sources for Land Use map are presented, followed by a discussion on how these are represented on map.

When the attribute table is filled with all necessary information, cartogram and carto diagram are created, it is time to transfer the data to the online ArcGIS space and to add the created thematic layer to the base map. Next step is to create ArcGIS Online account and to indicate the purpose of it. For free it is easy to get account to test the web map.

Next step is to add the map from computer to Gallery (Figure 2) and to click Apps – Dashboard on the left side panel.

Table 2

Sources and types of data

	Data	data format	data display	data source
1.	Number of population	numeric	numeric	Wikipedia
2.	Soil erosion data	1-4	colour	Laboratory of Geomorphology and Ecopedology, Institute of Ecology and Geography of Republic of Moldova
3.	Share of land area used for arable agriculture	%	chart pie	
4.	Share of land area used for orchards	%	chart pie	
5.	Share of land area used for vineyards	%	chart pie	
6.	Share of land area used for pastures	%	chart pie	
7.	Settlements	-	point	Esri Romania, Esri, Here Technology, Garmin, Foursquare, Food and Agriculture Organization (FAO), National Aeronautics and Space Administration (NASA), United States Geological Survey (USGS)
8.	Administrative districts	-	polygon	
9.	Roads	-	line	
10.	Railroads	-	line	
11.	State borders	-	line	

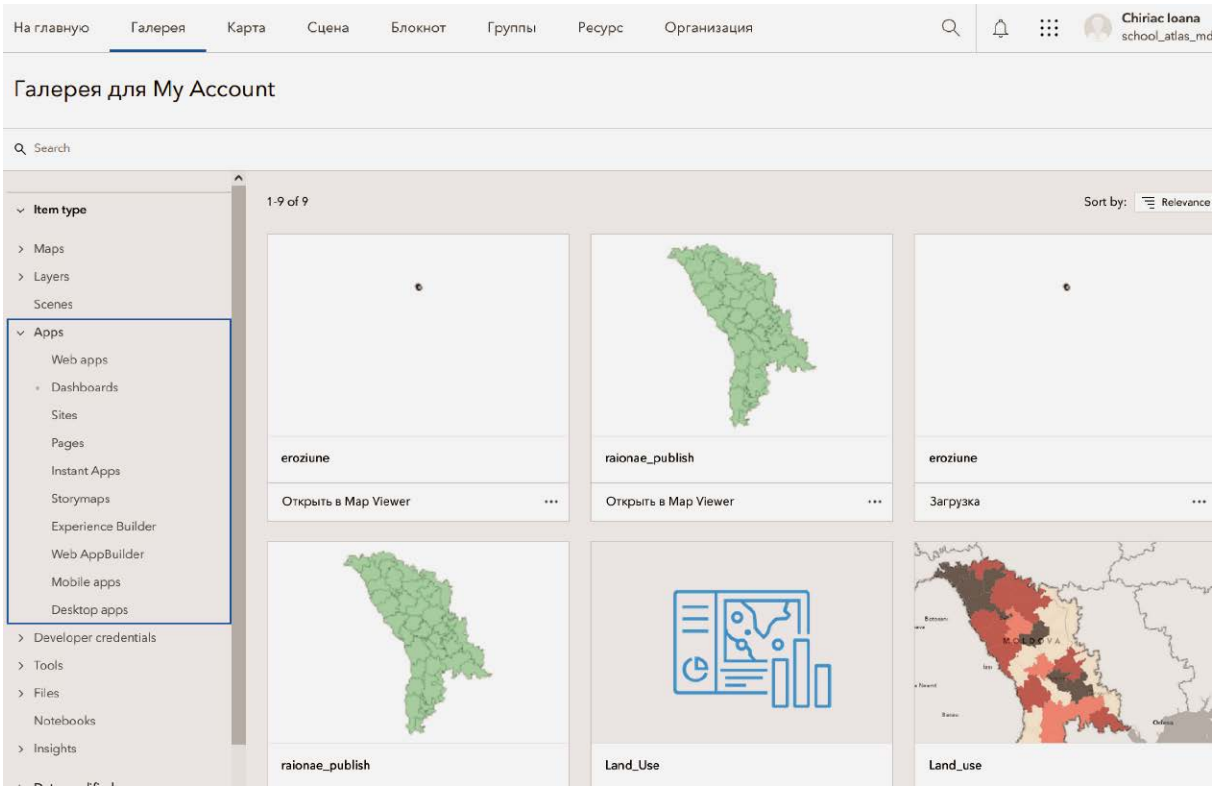

Figure 2. ArcGIS Online Gallery.

Dashboard is the app builder of map. It is very convenient that Dashboards are designed to display multiple visualizations that work together on a single screen.

Configurable elements include maps, lists, charts, gauges, indicators, and tables, and occupy 100 % of the application browser window.

3. Results

The results of the study include Land Use Web Map of Moldova and methodology suitable for creating any other thematic interactive map. In Table 3 there is made an attempt to present steps based on the workflow previously described.

Table 3

Overview of ArcGIS components and their functions

	Component of ArcGIS	Purpose
1.	ArcCatalog	Creating a new file geodatabase. Import or creation of feature class.
2.	ArcToolbox	Adding data to attribute table.
3.	ArcMap	Mapping. Geovisualization of data using different cartographic methods.
4.	ArcGIS Online	Account Creation. Downloading data on ArcGIS Online.
5.	Dashboard	Dashboard design. Data sharing.

The process of map abstraction includes at least five major (interdependent) steps: creating of Personal Geodatabase, adding data to attribute table, geovisualization of data using different cartographic methods, downloading data on ArcGIS Online and data sharing. A personal geodatabase is a Microsoft Access database that can store, query, and manage data. Using right-click on the file folder in the ArcCatalog tree, there is a possibility to select the place, where new file geodatabase will be created. Data with Moldova's districts was imported from another geodatabase. Using the geospatial tool "Join" information about erosion and land use was added to attribute table of feature class of districts. Next step is geovisualization of data in ArcMap using classification in proprieties of selected Layer. After the design of the map is ready, it is possible to publish the map.

The result of the study in the form of an interactive map is presented in Figure 3. The cartogram with its intensity of the color indicates the degree of damage to the land by erosion processes. On the left side there is presented list of districts of Moldova. By clicking on the name of the district in the list or on its configuration on the map, the Land Use diagram appears. The chart includes the percentage of arable land, pastures, orchards and vineyards in the selected district. The name of land use and its percentage in total area of district appears when the mouse pointer comes over the share of the diagram. This way of displaying information was selected not to overload the map interface with text information.

On the right side of the interactive map (Figure 3), there is a Land Use graph of Moldova. This graph clearly shows that most of the land in Moldova is used for growing crops. If Full Screen for Republic of Moldova is selected, then entire territory of Moldova fits on the monitor screen and only names of countries and districts are presented on the map.

Zooming in reveals more details on the map (Figure 4). For example, communes, localities and their names, hydrography, and road networks. Thus, a very detailed informative map at one scale can also become very concise at another scale. This is one of the main advantages of an interactive map over a paper one, which usually shows only the largest geographic features.

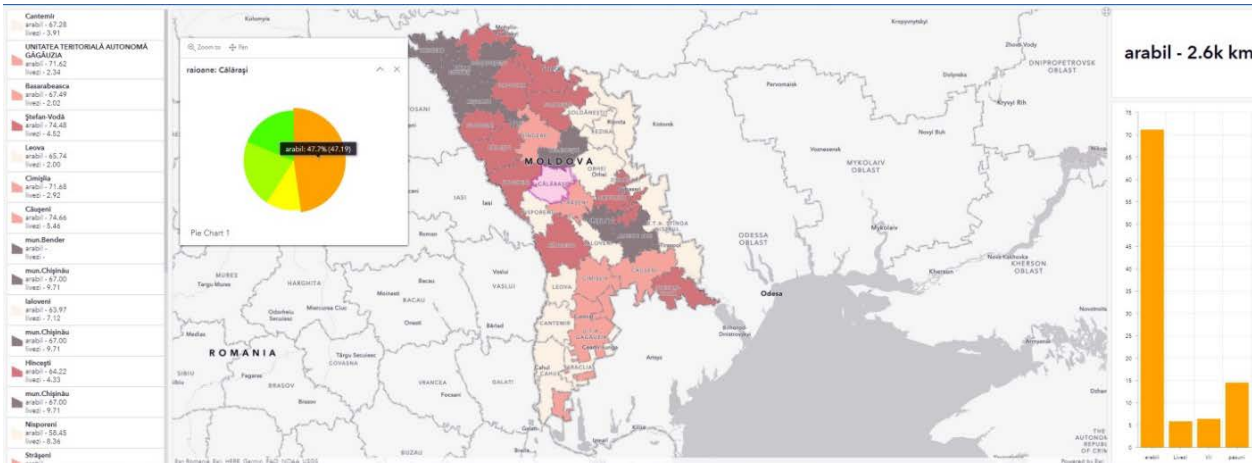

Figure 3. Land Use web map of Republic of Moldova.

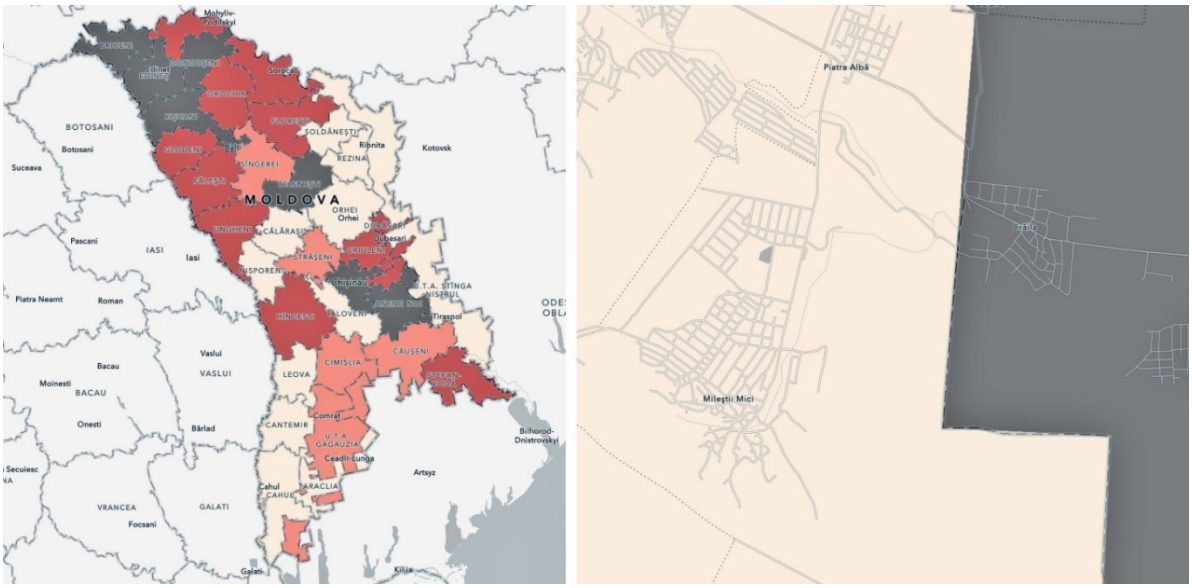

a) b)

Figure 4. Land Use Map at different scales: a) scale 1:1500000; b) scale 1:10000.

Internet-based GIS have been developed in which all the individual layers are separated thus allowing many students to access and visualize the geo-data at the same time. Data editing on Geography lessons should not be available to students. However, on the lessons about geodatabase, it makes sense to demonstrate the fact that data changes by one student will be displayed on all computers in the class in real time.

The application has been designed in such way that information is easy to find, quickly to access and available for students whenever they require it. All the tools offered does help the secondary school student to find what they need for their objectives of lesson.

4. Discussion

The long way to the applying of Geographic Information System Mapping Technology in school education in Republic of Moldova began 15 years ago. In 2008, the possibilities and prospects of using GIS for paper atlas producing in Republic of Moldova where proposed [3]. During 2013-2016, the production of paper atlases using GIS technologies was launched at State Enterprise "INGEOCAD" [5]. In this period of time, it was found that ArcGIS is a mapping platform that enables to create interactive maps and apps to share within organization or publicly. Based on above-mentioned experience in paper maps production, there were

proposed methods for creation of interactive maps [12]. As a logical consequence, the paper you are reading, provides step-by-step instruction for interactive map creation. It should also be noted that this instruction can be used to create other interactive thematic maps.

Future research directions include the study of results after the integration of interactive maps in school education. The significant improvement in grades would be a positive outcome of this study. It would be useful to explore the possibilities of other mapping software, except ArcGIS. There perhaps exists free GIS software, which is also fully compatible with the school education. It would also be interesting to explore how interactive maps can be assembled into a coherent atlas system.

5. Conclusions

There will be a significant increase in the use of the Internet by schools over the next five years. Young geography teachers and school students who grew up with gadgets in their hands will obviously find paper atlases irrelevant. New system of education with faster paced and interactive learning is required. Interactive maps are suitable for these purposes. WebGIS is a special GIS tool that uses the Internet as a means to access and transmit data, present GIS results and conduct analysis. Similar to web maps and web layers, dashboard is the part of the ArcGIS geo informational model. In addition, dashboards offer filtering capabilities, which enable a refined set of data to be presented to the intended audience.

The transition from the use of paper atlases to interactive ones will saves printing costs and will reduce the financial costs of the parents. However, the budget item must be included for information technology so that the expenditure for acquisition is part of the scholar planning process. Every organization using the ArcGIS platform can take advantage of ArcGIS Dashboards for a fee.

The main conclusion, based entirely on the results of the research is the fact that the data, geospatial tools and flowsheet used before to create paper maps, now can be used to create interactive thematic maps of Republic of Moldova. Compared to the process of creating paper atlases, the web mapping is much simpler. The development environment for web based GIS application is greatly simplified with easy-to-use ArcGIS tools. A dashboard's layout can be configured in various ways to be as effective as possible. Page format, map scale, geographic projection are no longer limiting factors for the amount of geographic information added to a map. In addition, the line features (boundaries, rivers) and labels accepted in the international geographical community are used as a base map and exclude errors. Various spelling for a place-name is not a problem anymore. On ArcGIS Online names are spelled according to official practice in the local language. For names in language written in non-roman alphabets, the U. S. Board of Geographic Names transliteration system were followed as well as local official systems where they exist.

The methodology of Land Use Web map creating described by steps in this article maybe used to create any other thematic interactive maps. Creating a cartogram is the best way to map contiguous geographic phenomena. For example, Land Use Web map gives a good overview of the structure of the Moldovan land fund by its diagrams and degree of soil damage by erosion by its cartogram. The dark colours of the cartogram, covering more than half of the territory of Moldova, indicate that agricultural activities in these areas are under threat. Soil erosion by water, wind and tillage affects both agriculture and the natural environment.

Getting an access to workflow-specific apps, maps and data from around the globe and tools gives an opportunity for being equally mobile in the classroom and at homeschooling or in quarantine.

Conflicts of Interest: The author declares no conflict of interest.

References

1. Slocum, T.A.; McMaster, R.B. Thematic Cartography and Geovisualization. 3rd ed., Pearson Prentice Hall: Upper Saddle River, NJ, United States, 2009; p. 442.
2. Peterson, M. Maps and Internet. Elsevier, Amsterdam, 2003; p. 357.
3. Constantinov, T.; Syrodoev, G. Geographic information systems – tool of geographic research. Akademos 2008, p. 82 [in Romanian].
4. Chiriac, I.; Nistor-Lopatenco, L.; Vlasenco, A. Spatial information management in creating of Digital Atlas of Moldova. RevCAD 2022, 32, pp. 41-50.
5. Cazanteva, O.; Sirodoev, G. Atlas. Physical and human geography of the Republic of Moldova; SI INGEOCAD: Chisinau, Republic of Moldova, 2015, p. 23 [in Romanian].
6. Bodea, C.; Constantinescu L.; Pascu S.; Trebici, V.; Tufescu V. Historical-Geographical Atlas. Romania. Editura Academiei Romane, Bucuresti, Romania, 1996, p. 149.
7. Virga, V. Cartographia: Mapping Civilizations, 3rd ed.; Little Brown and Company, Singapore, 2008; p. 248.
8. Ptacek P.; Ruffini F. V. Atlas of the Carpathian Macroregion. Palasky University Olomouc, Czech Republic, 2009, p. 16.
9. Koua, E.L.; MacEachren, A.M.; Kraak, MJ. Evaluating the usability of visualization methods in an exploratory geovisualization environment. Int. J. Geogr. Inf. Sci. 2006, pp. 425–448.
10. Chen, J.; Lengerich, E.J.; MacEachren,; Meyer, H.G.; A.M.Robinson, A.C. Combining usability techniques to design geovisualization tools for epidemiology; Cartogr. Geogr. Inf. Sci. 2005, pp. 243–255.
11. Chiriac, I. Production of digital school atlas using geographic information system. In: The technical-scientific conference of students, masters and doctoral students, Chisinau, Republic of Moldova, 1-3 aprilie 2020, p.177.
12. Chiriac, I. Analysis of mapping methods for creating electronic maps. In: International scientific and practical Internet conference Trends and prospects for the development of science and enlightenment in the minds of globalization, 31 June 2020, Pereyaslav, 2020, 61, p. 92 [in Russian].
13. Chiriac, I.; Syrodoev, G.; Syrodoev I. Experience in creation of the Ecological River Dniester Basin Atlas. In: *Modern achievements of geodetic science and production, Proceedings of the National atlases in the formation of the global information space Conference*, Ukraine, September 13-15, 2012; Publishing House of Lviv Polytechnic National University: Lviv, Ukraine, 2012; p. 118 [in Russian].
14. Salishchev, K. Mapping. 2nd ed. Moscow University Press, Moscow, 1990, p. 80 [in Russian].
15. Wilbur, E. G. National Geographic Atlas of the World. 5th edition; National Geographical Society:Washington D. C., 1981, p. 62 [in Russian].

Citation: Chiriac, I. Land use web map of Moldova creating using web-based mapping software ArcGIS online. *Journal of Engineering Science* 2023, 30 (2), pp. 117-125. https://doi.org/10.52326/jes.utm.2023.30(2).11.

Publisher's Note: JES stays neutral with regard to jurisdictional claims in published maps and institutional affiliations.

Submission of manuscripts: jes@meridian.utm.md

Journal of Engineering Science *Vol. XXX, no. 2 (2023), pp. 126 - 134*
Fascicle *Architecture, Civil and Environmental Engineering* *ISSN 2587-3474*
Topic *Architecture, Urbanism and Cadaster* *eISSN 2587-3482*

https://doi.org/10.52326/jes.utm.2023.30(2).11
UDC 332.6:72(479.22+458.2)

COMPUTING HERITAGE VALUES: A CASE FOR GEORGIA AND MALTA

Lino Bianco[1,2*], ORCID: 0000-0001-8779-2351

[1]*University of Malta, MSD 2080 Msida, Malta*
[2]*University of Architecture, Civil Engineering and Geodesy, 1, Hristo Smirnenski Blvd, 1046 Sofia, Bulgaria*
*Corresponding author: Lino Bianco, *lino.bianco@um.edu.mt*

Received: 03. 24. 2023
Accepted: 05. 03. 2023

Abstract. Value criteria and dimensions of heritage are two aspects on which the heritage value is calculated. The Heritage Value Calculation is effectively a computation whereby the heritage value for given site is established. This method was applied to two seminal contemporary architectural case studies, namely, the Palace of Rituals (Georgia) and the Manikata Church (Malta). The heritage value computed for each provides insight into their essential features whilst allowing a comparison of the sites – Georgia and Malta are spiritually linked through the same religious faith. Although the Palace of Rituals scored slightly higher in the dimensions of materiality, function, and spirit and memory, the Manikata Church obtained considerably higher scores for design, location and context, and traditions and techniques, thus ending up with a higher overall final heritage value score.

Keywords: *Palace of Ceremonies, Wedding Palace, Palace of Rituals, Manikata Church, heritage values.*

Rezumat. Criteriile de valoare și dimensiuni sunt două aspecte pe baza cărora se calculează valoarea patrimoniului. Calculul valorii patrimoniului este un calcul efectiv prin care se stabilește valoarea patrimoniului pentru un anumit sit. Această metodă a fost aplicată la două studii de caz arhitecturale contemporane fundamentale, anume - Palatul Ritualurilor (Georgia) și Biserica Manikata (Malta). Valoarea patrimoniului, calculată pentru fiecare obiect, oferă o idee despre principalele caracteristici esențiale, și în același timp permite comparația site-urilor – Georgia și Malta, care sunt legate spiritual prin aceeași credință religioasă. În timp ce Palatul Ritualurilor a obținut un scor mai mare la parametrii de materialitate, funcționalitate, spiritualitate și memorabilitate, Biserica Manikata a obținut un scor semnificativ mai mare la expresivitatea arhitecturală, locație și context, precum și prin tradiții și procedee, obținând astfel în general un punctaj mai mare în evaluarea patrimoniului.

Cuvinte cheie: *Palatul Ceremoniilor, Palatul Nunții, Palatul Ritualurilor, Biserica Manikata, valori ale patrimoniului.*

1. Introduction

A recent study developed a heritage value calculation based on multicriteria mathematical analysis [1]. It takes into account a number of dimensions of heritage – design,

materiality, function, location and context, traditions and techniques, and spirit and memory – with respect to the following heritage value criteria: form and physicality, socio-cultural, economic and use, and informational. These dimensions and criteria are used to compute the final heritage value of a given cultural site. Similar to the analysis undertaken in [2], the aim of this paper is to apply this formula to compute the heritage value of the Palace of Rituals and the Manikata Church, two iconic contemporary buildings of outstanding architectural importance rooted in the spirit of place, located in Georgia and Malta, the main island of the of the Maltese archipelago, respectively (Figure 1). Although in a geographical sense these two buildings are situated in different locations on the globe – Georgia, the mythological land of the Golden Fleece, occupying part of the eastern coast of the Black Sea whilst Maltese archipelago, the island of Gozo is the mythical Ogygia, lies nearly at the center of the Mediterranean Sea – both nations were among the first to be exposed to Christianity, the former by the apostles Andrew and Simon [3, 4] and, recalling *The Acts of the Apostles* 28, 1-11 [5], the latter by the apostle Paul.

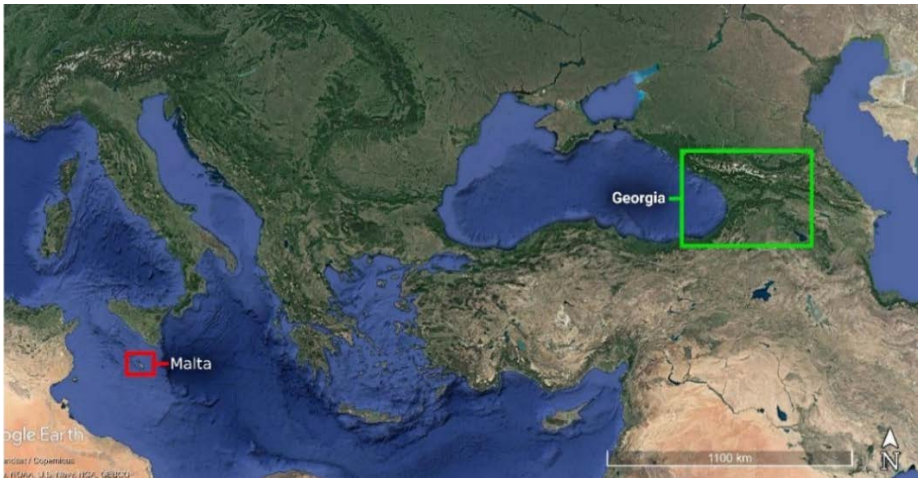

a)

b)

c)

Figure 1. Site location (online version is in colour): a) the Mediterranean Sea and the Black Sea showing the location of Malta and its dependencies, and Georgia; b) Manikata, Malta; and c) Tbilisi, Georgia (© Google Earth).

2. Theoretical background

Based on the evaluation of leading publications studied by Mason [6], Yung and Chan [7], de la Torre [8], Doğan [9], Chen and Li [10] and Olukoya [11], 24 heritage value typologies were identified which formed the baseline for assessing a given heritage site through the Heritage Value Calculation [1]. These typologies – classified into four categories (N): (i) form

and physicality, (ii) socio-cultural, (iii) economic and use, and (iv) informational value – are tabulated against six heritage dimensions (K) – design, materiality, function, location and context, tradition and techniques, and spirit and memory – forming a heritage value grid whereby all the dimensions of heritage and heritage values carry equal weighting. For a given heritage site, the final heritage value, F, is defined by:

$$\mathrm{F} = \frac{1}{\mathrm{K}} \sum_{k=1}^{K} y_k$$

where y_k, the outer average of a given heritage dimension, is defined by:

$$y_k = \frac{1}{\mathrm{N}} \sum_{i=1}^{\mathrm{N}} z_i^k$$

where z_i^k, the average within the value category of each dimension, defined by:

$$z_i^k = \frac{1}{\mathrm{M}_i} \sum_{j=1}^{\mathrm{M}_i} x_{ij}$$

and where M_1 = 7, M_2 = 7, M_3 = 4, M_4 = 6, which respectively corresponds to (i) form and physicality, (ii) socio-cultural, (iii) economic and use, and (iv) informational values.

3. Materials and Methods

The Palace of Rituals, also referred to as the Palace of Ceremonies or the Wedding Palace, was erected in 1984 as a wedding venue (Figure 2).

a)

b)

Figure 2. The Palace of Rituals (online version is in colour): a) site location map (© Google Earth); and b) view from the south-west (© Roman Geber / CCBY-SA 4.0).

It is one of 90 case studies Chaubin considers representative of Brezhnev-era architecture [12, p. 268-269]. Its design, the work of Georgian architect Victor Djorbenadze (1925–1999) and his assistant Vazha Orbeladze (1941–2022), is reminiscent of Georgian ecclesiastical architecture through an architectural language akin to the German avant-garde expressionism of the early twentieth century [13]. In the words of Djorbenadze, it is a "cathedral" [14, p. 14]; its plan is an abstraction of a drawing retrieved from a gynaecological book in Djorbenadze's mother library. Recalling Bostanashvili [15], the Palace of Ceremonies restored "the forgotten meaning of the city as a spiritual link between the heavens and the underworld, and integrates the symbolic with the functional. It is a place where the ritual of marriage … is celebrated" [16, p. 462]. Famous individuals and members of the general public have tied the knot in this building. The place, often visited by celebrities, was purchased in 2002 and used as a private residence until it was leased to a private events company in 2013. It currently serves, once again, as a venue for weddings and other social functions.

The Manikata Church was completed a decade prior to the Palace of Rituals according to the 1962 design by Maltese architect Richard England (Figure 3).

a)

b)

Figure 3. The Manikata Church (online version is in colour): a) site location map (© Google Earth); and b) view from the west (© credit to the Archdiocese of Malta – Ian Noel Pace).

Although inspired by modernist traditions, it is grounded in the geocultural context of the site and thus, in terms of its style, it complies with critical regionalism. The form is an abstraction of the traditional corbelled masonry hut common in rural Malta known as a girna [17]. Its configuration evokes the Megalithic temples of the Maltese archipelago, which predate the pyramids of Egypt by a millennium [17] and were listed as UNESCO World Heritage sites of outstanding universal value in 1980 [18]. Aware of the major reforms set in motion by the Second Vatican Council and the innovative church of Notre-Dame du Haut executed to the design of the Franco-Swiss architect Le Corbusier in 1955, England's design departed from the Baroque-inspired churches which dominate the landscape of Malta, embracing instead the local cultural and natural environs. The church is an embodiment of the "successful cohesion of human spirituality within the peacefulness of its natural environment" [19]. Together with a number of other parish churches, it was scheduled in 2011 as a Grade 1 monument [20].

4. Results and Discussion

A binary valuation was applied to the Heritage Value Calculation [1] – that is, if a dimension of heritage fits one of the criteria, a value of 1 is allocated, otherwise 0 is assigned. The resultant heritage value criteria scores for both case studies are given in Table 1 and their combined heritage value grids are given in Table 2 and Table 3.

Table 1

Binary scoring of heritage value: design, materiality and function

Dimensions of Heritage	Heritage Value Criteria							
	Form and Physicality		Socio-Cultural		Economic and Use		Informational	
	PR*	MC**	PR*	MC**	PR*	MC**	PR*	MC**
Design	1	1	1	1	0	1	0	0
	1	1	0	1	1	1	1	1
	0	0	0	1	1	1	0	
	0	1	0	0	1	0	0	0
	1	1	0	0			1	1
	1	1	1	1			0	0
	1	1	1	1				
z_i^1	0.714	0.857	0.429	0.714	0.75	0.75	0.333	0.333
Materiality	1	1	0	0	0	0	1	0
	1	1	0	0	0	0	1	1
	0	0	0	0	0	0	0	0
	1	0	0	0	0	0	0	0
	0	0	0	0			1	1
	0	1	0	0			0	0
	1	1	0	0				
z_i^2	0.571	0.571	0.000	0.000	0.000	0.000	0.500	0.333
Function	0	0	1	1	1	1	1	1
	0	0	1	1	0	0	0	0
	0	0	1	1	0	0	0	0
	0	0	1	1	1	0	0	0

Continuation Table 1

	1	0	1	1			0	0
	0	0	1	1			0	0
	1	1	1	1				
z_i^3	0.286	0.143	1.000	1.000	0.500	0.250	0.167	0.167

* Palace of Rituals, ** Manikata Church

The Heritage Value Calculation allocates the final value of a heritage site in a multifaceted way, where aspects such as the informational value resulting from the function of the building has as much weighting as aspects such as design aesthetics. In the design dimension, the Manikata Church scored higher overall in comparison to the Palace of Rituals. It scored slightly higher in the category of form and physicality and considerably higher in the socio-cultural value category, scoring five out of the seven value benchmarks in this category compared to the Palace of Rituals, which scored only three out of seven. Both sites obtained equal scores in the economic and use and informational value categories.

In terms of the materiality dimension, the Palace of Rituals obtained an overall higher score. Both sites obtained similar scores in the form and physicality value category, as well as scoring zero in the socio-cultural and economic and use categories of this dimension. The Palace of Rituals received a higher rating for informational values, scoring three out of the six value benchmarks in the informational category, compared to the Manikata Church's two out of six value benchmarks.

The Palace of Rituals scored higher overall than the Manikata Church in the dimension of function, with higher scores in the subdimensions of form and physicality, and economic and use; the two sites received comparable scores in the remaining categories. In terms of location and context, the Manikata Church scored considerably higher overall, scoring three out of the seven value benchmarks in the form and physicality category whilst the Palace of Rituals obtained a zero. It also scored higher in the socio-cultural and informational value categories; however, both sites obtained scores of one in the economic and use category.

Table 2

Binary scoring of heritage value: location, traditions and memory

Dimensions of Heritage	Heritage Value Criteria							
	Form and Physicality		Socio-Cultural		Economic and Use		Informational	
	PR*	MC**	PR*	MC**	PR*	MC**	PR*	MC**
Location and Context	0	1	0	1	1	1	0	1
	0	0	1	1	1	1	0	0
	0	1	1	1	1	1	0	1
	0	1	0	0	1	1	0	0
	0	0	0	0			0	1
	0	0	0	0			1	1
	0	0	0	0				
z_i^4	0.000	0.429	0.286	0.429	1.000	1.000	0.167	0.667
Traditions and Techniques	0	0	1	1	0	0	0	0
	1	1	1	1	0	0	1	1
	0	0	0	0	0	0	0	0

Continuation Table 2

	0	1	0	0	1	0	0	0
	0	1	0	0			1	1
	0	1	1	1			0	0
	1	1	1	1				
z_i^5	0.286	0.714	0.571	0.571	0.250	0.000	0.333	0.333
Spirit and Memory	1	1	1	1	0	0	1	1
	1	1	1	1	0	0	0	0
	0	0	1	1	0	0	0	0
	0	1	1	1	1	0	0	0
	1	1	0	0			0	0
	1	1	1	1			0	0
	1	1	1	1				
z_i^6	0.714	0.857	0.857	0.857	0.250	0.000	0.167	0.167

* Palace of Rituals, ** Manikata Church

In the dimension of traditions and techniques, once again the Manikata Church scored higher overall. The Palace of Rituals scored slightly higher in the economic and use category – one out of the four value benchmarks – whilst the Manikata Church was allocated a zero for this category. However, in the form and physicality category, the church obtained a considerably higher value: five out of the seven value benchmarks in comparison to two out of seven for the palace. Both were weighted equally in the socio-cultural and informational value categories.

In terms of the spirit and memory dimension, the Palace of Rituals scored slightly higher, although comparably to the Manikata Church. The latter obtained a slightly higher score for the form and physicality category, with six out of seven value benchmarks, compared to five out of seven for the palace. In the economic and use category, the Palace of Rituals scored one of the four value benchmarks whereas the Manikata Church obtained a zero. In the socio-cultural and informational categories, both sites obtained equal scoring. The final heritage value (F) for the Palace of Rituals was 0.422, and that for the Manikata Church was 0.464 (see Table 3).

Table 3

Heritage value grid

Case study	Dimensions of Heritage	Heritage Value Criteria					
		Form and Physicality	Socio-Cultural	Economic and Use	Informational	y_k	F
Palace of Rituals	Design	0.714	0.429	0.75	0.333	0.557	0.422
	Materiality	0.571	0.000	0.000	0.500	0.268	
	Function	0.286	1.000	0.500	0.167	0.488	
	Location and Context	0.000	0.286	1.000	0.167	0.363	
	Traditions and Techniques	0.286	0.571	0.250	0.333	0.360	
	Spirit and Memory	0.714	0.857	0.250	0.167	0.497	

Continuation Table 3

Manikata Church	Design	0.857	0.714	0.750	0.333	0.664	0.464
	Materiality	0.571	0.000	0.000	0.333	0.226	
	Function	0.143	1.000	0.250	0.167	0.390	
	Location and Context	0.429	0.429	1.000	0.667	0.631	
	Traditions and Techniques	0.714	0.571	0.000	0.333	0.405	
	Spirit and Memory	0.857	0.857	0.000	0.167	0.470	

5. Conclusions

The Heritage Value Calculation provides a relative value to determine the heritage value of a specific site in comparison with another or number of others, preferably of identical typology. Applying a binary scoring system to the sites under study resulted in final heritage values (F) of 0.422 and 0.464 for the Palace of Rituals and the Manikata Church, respectively. Although the former scored slightly higher in the materiality, function, and spirit and memory dimensions, the latter obtained a considerably higher scoring in the dimensions of design, location and context, and traditions and techniques, thus giving it a higher overall final value. One may argue that the scores obtained for both buildings were relatively comparable and similar in value. In the proposed binary scoring system, where $0 < F < 1$, even a minor difference in the final value indicates a notable difference in heritage value. Moreover, the quantifiable results would have been more accurate if a non-binary valuation had been undertaken.

Acknowledgements. This article is based on a presentation by the author at the XIth edition of the International Conference 'Current problems in urban planning and architecture', held on 15-17 November 2022 at the Faculty of Urbanism and Architecture, Technical University of Moldova, Chisinau, marking the 50th anniversary of the faculty's foundation. The author would like to thank Nadine Zammit for her critical input with respect the interpretation of the findings. Furthermore, credit is due to Roman Geber and the Archdiocese of Malta – Ian Noel Pace, authors of Figure 2 (bottom) and Figure 3 (bottom), respectively.

Conflicts of Interest: The author declares no conflict of interest.

References

1. Zammit, N.; Bianco, L. Computation of heritage values: Towards a holistic method to assess built heritage. In: *Heritage and Sustainable Development*, 2022, 4(2), pp. 101-110. https://doi.org/10.37868/hsd.v4i2.117
2. Zammit, N.; Bianco, L. The heritage value of the auberges of the Order of St John in Valletta, Malta. In: *Terra Sebus. Acta Musei Sabesiensis*, 2022, 14(1), pp. 259-315. Available online: https://www.cclbsebes.ro/wp-content/uploads/2023/05/12_N_Zammit_L_Bianco.pdf (accessed on 30.04.2023).
3. Paphlagonis, N. *Orations*, IV. In *Patrologia Graeca*, Migne J.P., Ed.; Imprimerie Catholique, Paris, 1862, Volume 105, col. 64.
4. Preud'homme, N. Andrew the Apostle and Samżivari: A crossing of traditions in Georgia. Conference (3 November 2021), Centre for Advanced Studies 'Beyond Canon', University of Regensburg. Available online: https://www.academia.edu/60159301/Andrew_the_Apostle_and_Sam%C5%BCivari_A_crossing_of_traditions_in_Georgia (accessed on 11.12.2022).
5. Wansbrough, H. *The New Jerusalem Bible*. London, Darton, Longman & Todd, 1985, pp. 1844-1845.

6. Mason, R. Assessing values in conservation planning: Methodological issues and choices. In: *Assessing the values of cultural heritage: Research report*, Los Angeles, 2002, pp. 5-13.
7. Yung, E.H.K.; Chan, E.H.W. Evaluation for the conservation of historic buildings. In: *Facilities*, 2013, 31(11-12), pp. 542-564. https://doi.org/10.1108/F-03-2012-0023
8. de la Torre, M. Values and heritage conservation. In: *Heritage & Society*, 2013, 6(2), pp. 155-166. https://doi.org/10.1179/2159032X13Z.00000000011
9. Doğan, H.A. Perception of the modern movement in architecture as cultural heritage. In: *Art History & Criticism / Meno istorija ir kritika*, 2020, 16(1), pp. 65-78. https://doi.org/10.2478/mik-2020-0004
10. Chen, D.; Li, J. Process-led value elicitation within built heritage management: A systematic literature review between 2010 and 2020. In: *Journal of Architectural Conservation*, 2021, 27(1-2), pp. 1-16. https://doi.org/10.1080/13556207.2021.1909900
11. Olukoya, O.A.P. Framing the values of vernacular architecture for a value-based conservation: A conceptual framework. In: *Sustainability*, 2021, 13(9), 4974. https://doi.org/10.3390/su13094974
12 Chaubin, F. *CCCP: Cosmic Communist Constructions Photographed*. Cologne: Taschen, 2011, pp. 268-269.
13. Wheeler, A.; Shioshvili, V. *Beyond the Ruin: Soviet Georgian architecture in context*. 2016. Available online: https://www.academia.edu/30963679/Beyond_the_Ruin_Soviet_Georgian_Architecture_in_Context (accessed on 14.12.2022).
14. Wheeler, A. *Socialist in Form, National in Content: Preserving late Soviet culture at Tbilisi Palace of Rituals*. M.Sc. dissertation, Columbia University, New York, 2016. Available online: https://academiccommons.columbia.edu/doi/10.7916/D88W3DFD (accessed on 16.12.2022)
15. Bostanashvili, S.; Bostanashvili, D. *Butza: Architect Victor Jorbenadze*. Tbilisi: Ltd Universal, 2012, pp. 73-105,
16. Bianco, L. Butza: Architect Victor Jorbenadze. In: *The Journal of Architecture*, 2016, 21(3), pp. 459-464. https://doi.org/10.1080/13602365.2016.1183384
17. Knevitt, C. *Manikata: The making of a church*. Malta: Manikata Parish Church, 1980, pp. 7-17.
18. UNESCO. *Megalithic Temples of Malta*. 1980. Available online: https://whc.unesco.org/en/list/132/ (accessed on 11.12.2022).
19. Anon. St Joseph in Manikata. In: *Times of Malta*, 13 October 2011. Available online: https://timesofmalta.com/articles/view/St-Joseph-in-Manikata.388896 (accessed on 11.12.2022).
20. Department of Information. Government Notice 782: Environment and Development Planning Act, 2010 (Article 81) – Scheduling of property: parish churches. In: *The Malta Government Gazette*, 26 August 2011, 18796, pp. 10131-10146.

Citation: Bianco, L. Computing heritage values: a case for Georgia and Malta. *Journal of Engineering Science* 2023, 30 (2), pp. 126-134. https://doi.org/10.52326/jes.utm.2023.30(2).11.

Submission of manuscripts: jes@meridian.utm.md

Journal of Engineering Science *Vol. XXX, no. 2 (2023), pp. 135 - 143*
Fascicle *Architecture, Civil and Environmental Engineering* *ISSN 2587-3474*
Topic *Civil Engineering and Management* *eISSN 2587-3482*

https://doi.org/10.52326/jes.utm.2023.30(2).12
UDC 625.7:624.138.26:69.059

INTERVENTION SOLUTIONS ON LANDSLIDES IN ROAD AREAS. CASE STUDY

Diana-Nicoleta Dima[1], ORCID: 0000-0002-2217-4330,
Răzvan Chirilă[2], ORCID: 0000-0001-8490-3300,
Gelu-Răzvan Gimiga[1], ORCID: 0000-0002-6798-1793

[1]*Gheorghe Asachi Technical University of Iasi-Romania, Department of Transportation Infrastructure and Fundations, Blvd. Mangeron, No. 1, 700050, Iasi, Romania*
[2] *GeotehnIS Concept S.R.L., Iasi, Romania*
*Corresponding author: Diana-Nicoleta Dima, *diana-nicoleta.dima@academic.tuiasi.ro*

Received: 03. 22. 2023
Accepted: 04. 28. 2023

Abstract. In our country, there is a large variety of foundation soils, some of them having inferior characteristics to those necessary for the proper support of a communication path. This raises some of the most common problems in the field of road infrastructures, namely the sliding of slopes in the area related to road construction. This phenomenon appears more and more frequently, especially after some periods with accentuated atmospheric instability, sometimes leading to the partial inability to use the affected infrastructure sector. In some cases, the development of this phenomenon can lead to the traffic blockage and the isolation of the communities in the area, to the destruction of a well-defined road sector and even to the loss of human lives. In order to maintain the quality requirements imposed by the law and to limit the risk of reaching the limit state of normal operation, respectively of compromising the structure, the administrators and the staff who are directly involved in the maintenance and the expertise of the affected area, achieve direct examination works or investigation by means of specific observation and measurement. In the current practice, these works are part of the technical expertise of the affected area, being made by a specialized team, led by an authorized technical expert in the field.

Keywords: *consolidation solutions with drilled piles, investigations, landslide, monitoring, road sector.*

Rezumat. În țara noastră sunt prezente o gamă largă de pământuri de fundare, unele dintre ele prezentând caracteristici inferioare celor necesare susținerii corespunzătoare a unei căi de comunicații. Acest lucru ridică unele dintre cele mai frecvente probleme din domeniul infrastructurilor rutiere, respectiv a alunecării versanților din arealul aferent execuției drumurilor. Aceste fenomene apar din ce în ce mai frecvent, mai ales în urma unor perioade cu instabilitate atmosferică accentuată, conducând uneori la incapacitatea parțială de utilizare a sectorului de infrastructură afectat. În unele cazuri, dezvoltarea fenomenului poate conduce la blocarea circulației și izolarea comunităților din zonă, până la distrugerea unui sector de drum bine definit și chiar la pierderi de vieți omenești. În scopul menținerii cerințelor de calitate

impuse prin lege și a limitării riscului de atingere a stării limită de exploatare normală, respectiv de compromitere a structurii, administratorii, împreună cu personalul implicat direct în întreținerea sau expertizarea zonei afectate, realizează lucrări de examinare directă sau investigare prin mijloace de observare și măsurare specifică. În practica curentă, aceste lucrări fac parte din expertizarea tehnică a zonei afectate, fiind realizate de către o echipă specializată, condusă de un Expert tehnic autorizat în domeniu.

Cuvinte cheie: *sector de drum, alunecare de teren, investigații, monitorizare, soluții de consolidare cu piloți forați*.

1. Introduction

Landslides causes traffic disruptions have been one of the threats to the normal operation of regional roads [1-4] and are erosive actions of the soil that can lead to the displacement of a large volume of soil, changes in the slope of the land and even significant changes in the relief. They are caused by triggering factors such as torrential rains, water leaks, earthquakes or human interventions on the relief, due to lower characteristic parameters of the soils. Landslides can trigger suddenly, being dangerous to people, properties and communication routes, causing property damage or even loss of human lives [5-9]. The prevention and management of landslides requires continuous planning and monitoring, as well as rapid physical interventions to stabilize the area, through the construction of various support structures or through technical interventions on the foundation soils.

In this article, the authors focus on determining the causes of soil instability phenomena for a local road sector in the Moldova region and the solutions for consolidating, developing and monitoring the behaviour of the consolidated area during operation. The meteorological phenomena that have taken place in recent years have strongly affected the investigated road sector through rainwater runoff, which engaged soil particles in the immediate vicinity, resulting in a landslide with a length of 40 m.

2. Current situation on site. Characteristics of the analyzed area. Causes of the degradations

Due to the occurrence of a strong landslide, the road administrator ordered a specialist study for emergency intervention in the disaster area.

Along the analyzed route, a slope was identified with stability issues (Figure 1), unevenness, and potholes caused by the lack of drainage and maintenance systems, as well as erosion forms on the sloping areas, given that the road embankment was supported by a structure made of gabions. The area belongs to the high-risk area for soil collapse or landslide, with a high probability of primary landslide occurrence.

Intense weather conditions have heavily impacted the road sector, causing a 40 meters length landslide along the road embankment. Successive break steps were observed that threaten the overall stability of the road.

In the partially forested upstream slope, saturation areas were formed due to precipitation which softened to the point of flow. The flowing material and water from the slope are uncontrolledly discharged onto the road. Upstream zones of counter-slope have also been identified, which have favored the flooding of precipitation.

At the base of the excavation slope there is no walled ditch for collecting the waters, and the existing bridge is silted and does not have a drop chamber for collecting upstream and trench water.

Figure 1. The analyzed landslide.

The road surface is inadequate because it presents counterslope and discharge areas due to excessive water. The road's viability is affected, so that road and pedestrian traffic cannot take place under normal conditions.

During dry periods, the existing road structure generates a lot of dust, and during rainy periods mud is formed and the road becomes impassable. Precipitation waters flow down and the road does not have a rainwater collection system to ensure controlled drainage of these waters. The road shoulder is made of earth and is structurally degraded.

2.1. Geologic, geomorphologic and hydrological characteristics

The analyzed sector is located in the Central Moldovan Hills, with elevations up to 200 m, wide valleys with lakes and slopes with numerous landslides. A small part of the sector belongs to the orogenic region and the rest to the platform region.

In the investigated geotechnical area, the Cetățuia River is the collector of the entire hydrographic network in the site area.

2.2. Seismic Characteristics

In terms of seismic activity (Figure 2), our country's territory is divided into macrozones with seismic intensities of 6, 7, 8, and 9 degrees. The analyzed area fits into grade 7.1 on the Medvedev, Sponhauer, Karnik (MSK) scale [10] and is located in the southwestern extremity of the Russian-Moldovan Platform that shows positive movements of 5 mm per year.

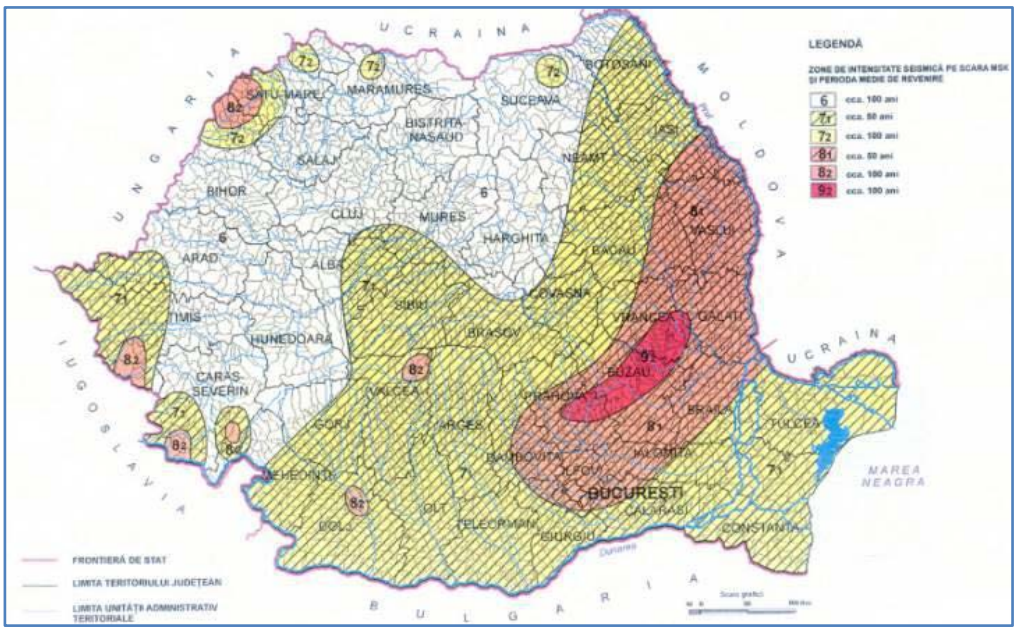

Figure 2. Seismic zoning. Macrozoning of the territory of Romania [10].

For earthquakes with an average recurrence interval of 225 years (IMR = 225 years), with a 20% probability of exceedance in 50-year (Figure 3), the seismic coefficient value, named ag in Romanian standard, is 0.25 g, and the control period (corner), name Tc in Romanian standard, is 0.70 s (Figure 4) [11].

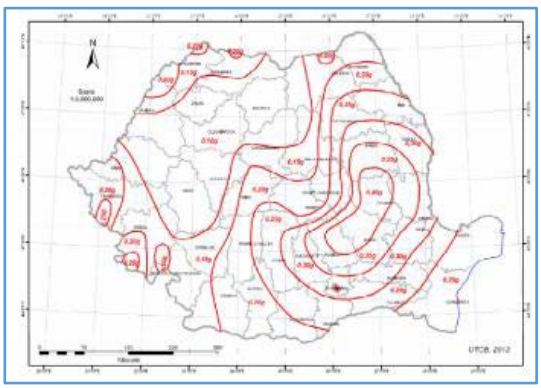

Figure 3. Zoning of peak ground acceleration values for design ag with IMR = 225 years and 20% probability of exceedance in 50 years according to [11].

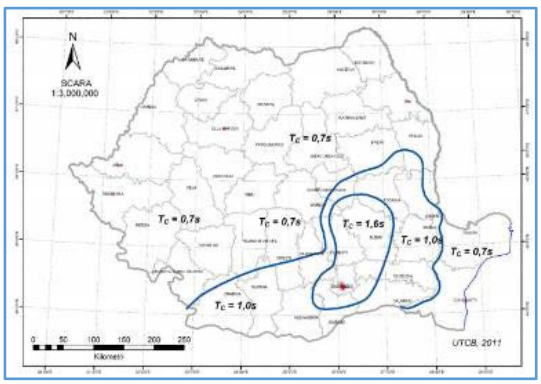

Figure 4. Zoning of the Romanian territory in terms of the control period (corner), named TC (control periods) in Romanian standard of the response spectrum [11].

The analyzed sector is located in the temperate-continental climate zone with Baltic influences. Annual precipitation is 500-700 mm with lower values in January, February, and March and higher values (600-700) in June and July. The area is characterized by average annual temperatures of 9-10°C, with the minimum air temperature dropping to -20 °C in

winter months and reaching +39°C in summer months. According to [12], the maximum depth of frost in the studied area is 80-90 cm (Figure 5). The reference wind pressure is 0.70 kPa [13], and the snow load on the ground is 2.50 kN/m^2, as stated in [14].

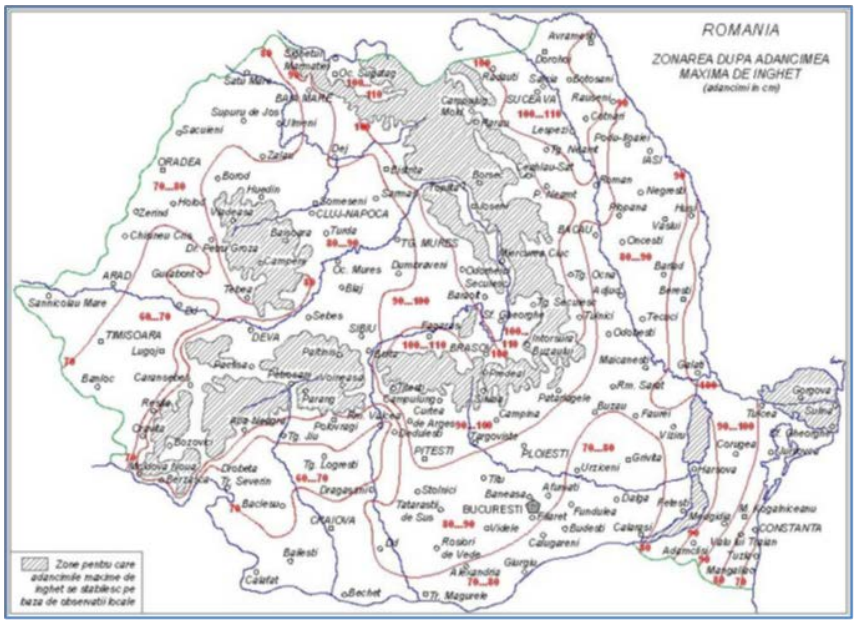

Figure 5. Maximum depths of frost. Zoning of the territory of Romania according to [12].

3. Geotechnical conditions. Methods, equipment and apparatus

The foundation ground was geotechnically investigated in the landslide area by performing a dynamic cone penetration test with a depth of 14.0 m (Figure 7) and two drillings: one in the road body at a depth of 15.0 m and the other downstream -2.70 m below the road elevation at a depth of 8.0 m.

The geotechnical drillings were carried out with a semi-mechanized drill, with disturbed and undisturbed samples taken. The drill diameter is 100 mm.

The system used for drilling (Figure 6) consists of:

- percussion hammer with internal combustion engine on gasoline
- hydraulic extractor - pulling power of 10 tons
- drill bits with diameters between 36 - 100 mm and lengths between 1.0 and 2.0 m
- connecting rods with lengths between 1.0 and 2.0 m
- utility vehicle used for mobilization on site, equipment transport, and maintenance on site
- wooden boxes for transporting samples to the laboratory
- stands and pipes for collecting undisturbed samples
- electric generator and concrete/asphalt corer - to cross any concrete/asphalt platforms.

The samples were collected manually, in plastic bags for moisture preservation, transported in soil sample boxes, and stored in an exicator in the laboratory to maintain the initial site conditions.

In order to complete the geotechnical information and determine derived geotechnical indices, a dynamic cone penetration test was performed using a Heavy Dynamic Penetrometer (DPH) cone, the results are briefly presented in Figure 6.

To determine the best intervention solutions, the following aspects were taken into account:

Figure 6. Heavy Dynamic Cone Penetrometer Equipment [15-17].

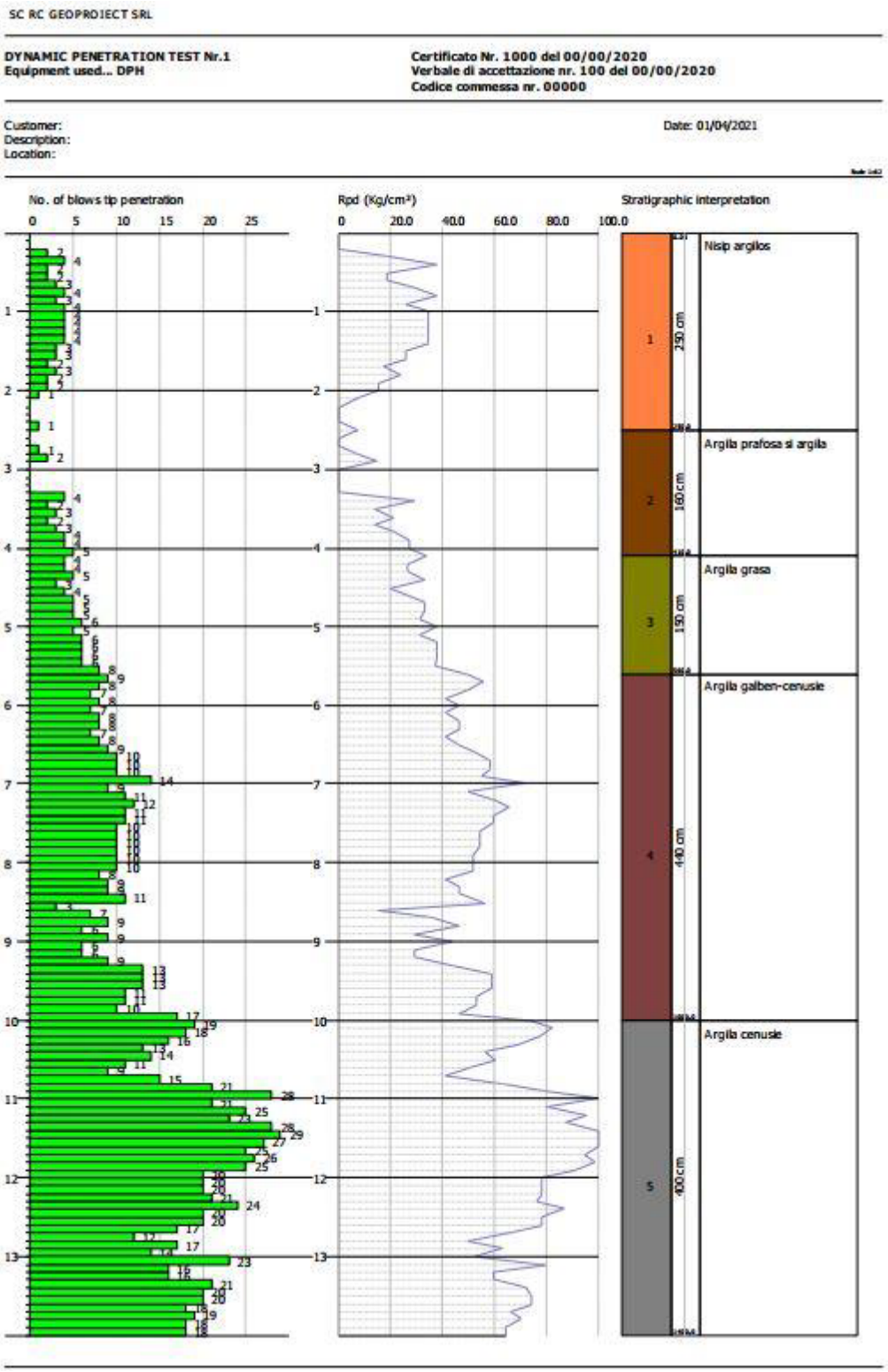

Figure 7. Dynamic penetration test graph.

- a sliding phenomenon occurred on the site
- the main elements of a landslide are visible (ebulment, landslide body, rupture steps and crown)
- under the action of disruptive factors, there is a risk that the phenomenon will develop upstream and affect the communal road sector in its entirety.

Thus, it was necessary to carry out a stability analysis with the help of calculation programs (Fellenius and Bishop method), through methods that admit the limit equilibrium conditions, in which to highlight the potential sliding planes (Figure 8), respectively the risk of advancing the sliding to the body of the road.

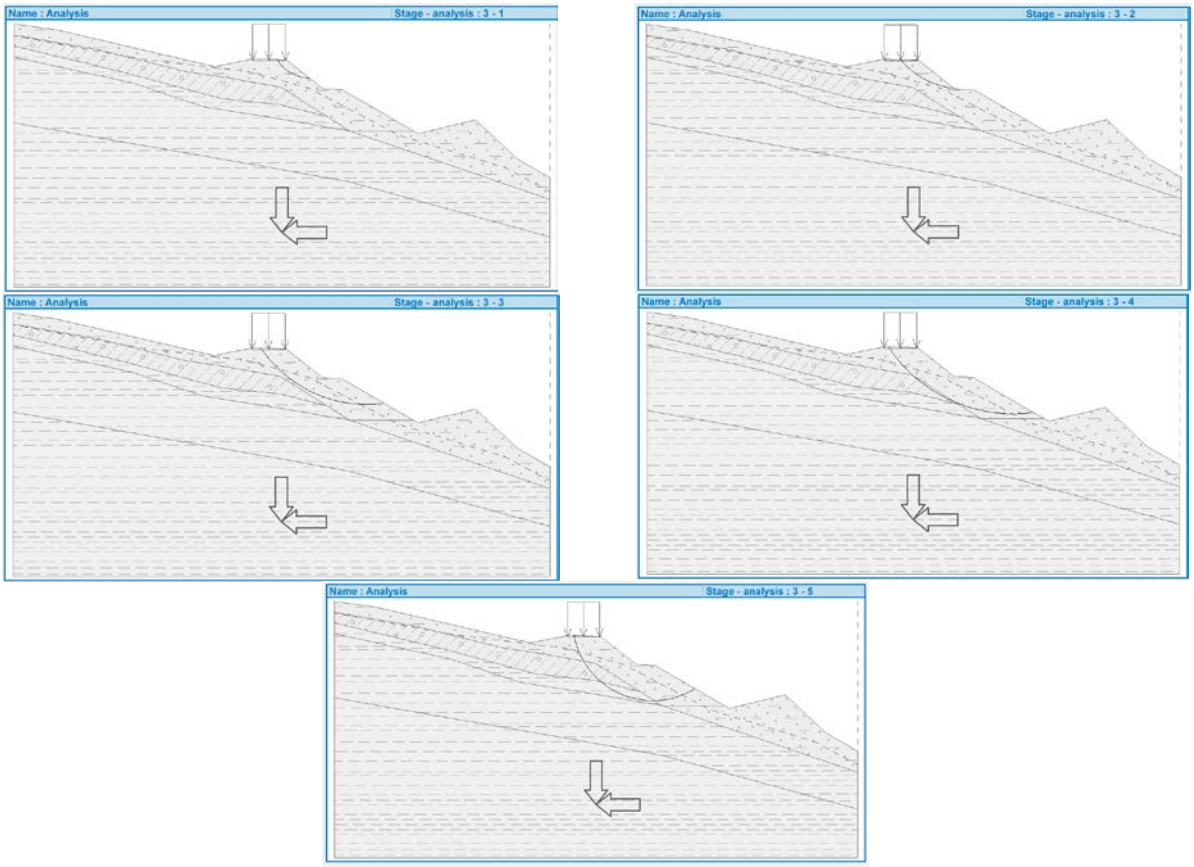

Figure 8. Potential sliding surfaces.

3. Conclusions and recommendations

The following conclusions can be drawn from the analysis of the stratification of the land revealed by geotechnical drilling and from the results of the stability analyses:

- In natural conditions (static loads), the road embankment does not have guaranteed stability. Potential sliding surfaces have been identified that highlight the active nature of the landslide with small periods of relative stabilization (phenomenon given by the natural balance of internal forces following a new configuration of the land).
- In seismic conditions (dynamic loads) it can be observed that the safety factors are sub-unit for the sliding surfaces that intersect only the first layers.
- Therefore, under the action of disturbing factors, slide planes can form in depth up to the contact with the resistance layer (approximately - 4.50 m compared to the existing road elevation).
- Considering the stratification of the land and the microrelief conditions, it can be estimated that the sliding surfaces will develop successively - rotationally, both upstream -

horizontally, and in depth - vertically, until the contact with the resistance layer. This will lead to the total damage of the road sector covered by the present study.

- The time factor gives the landslide an active alternative character - partially stable, but with the possibility of reactivation, with slide planes that started from shallow depths, with deep development.
- The main recommendations aim to eliminate all possibilities of water infiltration into the land and its wetting with a negative effect on the construction, respectively:
- The arrangement of a reinforcement structure made of drilled piles with a minimum diameter of 600 mm, at a minimum depth of 14.0 m. The piles will be spatially positioned, at a distance in the plan, calculated so that the earth does not flow between the piles.
- The arrangement of a horizontal drainage system under the bottom of the ditch to collect the water from seepage. The depth of the drain will be at least 2.00 m. It will have a minimum length of 40 m.
- Restoration of the water discharge bridge. It is recommended that the bridge foundation rests on the reinforcement structure in the downstream area.
- Development of the torrential valley on the upstream and downstream area for a minimum of 25-30 m. An initial systematization of the land both downstream and upstream is recommended, then protection with gabion mattresses/geocells filled with concrete.
- Restoring the road body and ensuring the designed width.
- Ensuring adequate storm water collection and drainage systems to avoid their infiltration into the road system, which can have a negative effect on the appearance of subsidence and cracks in the road body. They can be trapezoidal ditches, triangular ditches, rectangular ditches, etc.
- Unclogging and maintenance of existing ditches - on the extended area along the road, activity aimed at reducing the risk of destructive phenomena.
- Vegetation of the entire slope with perennial plants and trees with deep roots, in order to eliminate the risk of surface slides and erosion due to rainwater falling directly on the surface of the slope.
- Placement of a reinforced ditch on the drainage area, with the aim of eliminating the risk of soil flow in the area of the ditches. Behind the support structure, a drainage system will be created that can have a common body with the horizontal drain, with the aim of taking over the infiltration waters that come to the surface on the slope of the embankment.
- Ensuring the safety of traffic through the provision of indicators and metal protective parapets.
- Geotechnical monitoring with at least 2 boreholes equipped with inclinometer and tracking program of movements that may occur inside the slope and the consolidation structure. The inclinometers will be placed in the reinforcement piles.

By rehabilitating and modernizing the investigated sectors, the aim is to increase the load-bearing capacity of the road system, increase traffic safety, increase the viability of the streets according to the current and prospective traffic.

This work is part of a large research program in the field of slope instability, wanting to raise an alarm signal regarding the need to complete the work within the term considered in the design stage, with the aim of minimizing the damage caused by the impact of environmental factors and execution delay on the viability of the work. The program is

developed by the Faculty of Construction and Installations of the "Gheorghe Asachi" Technical University in Iasi.

Conflicts of Interest: The authors declare no conflict of interest.

References

1. Liu, Q.; Zhang, B.; Tang, A. Landslide risk of regional roads: Consider the road mileage of expected losses. *Transportation Research Part D: Transport and Environment* 2023, 120, 103771.
2. Pantelidis, L. A critical review of highway slope instability risk assessment systems. *Bulletin of Engineering Geology and the Environament* 2011, 70, pp. 395-400.
3. Argyroudis, S.A.; Mitoulis, S.A.; Winter, M.G.; Kaynia, A.M. Fragility of transport assets exposed to multiple hazards: State-of-the-art review toward infrastructural resiliance. *Reliability Engineering&System safety* 2019, 191, 106567.
4. Saleh, M.; Hashemian, L. Addressing Climate Change Resiliance in Pavements: Major Vulnerability Issues and Adaptation Measures. *Sustainability* 2022, 14(4), doi.org/10.3390/su14042410.
5. Nappo, N.; Mavrouli, O.; Nex, F.; van Westen, C.; Gambillara, R.; Michetti, A.M. Use of UAV-based photogrammetry products for semi-automatic detection and classification of asphalt road damage in landslide-affected areas. *Engineering Geology* 2021, 294, 106363.
6. Bordoni, M.; Persichillo, M.G.; Meisina, C.; Crema, S.; Cavalli, M.; Bartelletti, C.; Galanti, Y.; Barsanti, M.; Giannecchini, R.; Avanzi, G.A. Estimation of the susceptibility of a road network to shallow landslides with the integration of the sediment connectivity. *NHESS* 2018, 18, 1735-1758.
7. Mavrouli, O.; Corominas, J.; Ibarbia, I.; Alonso, N.; Jugo, I.; Ruiz, J.; Luzuriaga, S.; Navarr, J.A. Integrated risk assessment due to slope instabilities in the roadway network of Gipuzkoa. Basque Country. *NHESS* 2019, 19, 399-419.
8. Postance, B.; Hillier, J.; Dijkstra, T.; Dixon, N. Extending natural hazard impacts: an assessment of landslide disruptions on a national road transportation network. *Environ. Res. Lett.* 2017, 12, doi: 10.1088/1748-9326/aa5555.
9. van Westen, C.J.; van Asch, T.W.J.; Soeters, R. Landslide hazard and risk zonation - why is it still so difficult?. *Bull. Eng. Geol. Environ.* 2006, 65 (2), 167-184.
10. SR 11100/1-93 – Seismic zoning. Macrozoning of the territory of Romania
11. Normative P100-1/2013 – Normative for the anti-seismic design of social-cultural, agro-zootechnical and industrial housing constructions
12. STAS 6054-77 – Foundation land. Maximum frost depths. Zoning of the territory of the Socialist Republic of Romania
13. CR 1-1-4/2012 – Design code. Assessment of wind action on buildings
14. CR 1-1-3/2012 - Design code. Evaluation of the action of snow on constructions
15. cptools.ro. Available online: https://cptools.ro/project/set-prelevare-probe-geotehnice/ (accessed on 01/06/2023)
16. stitz-gmbh.de. Available online: https://www.stitz-gmbh.de/en_window_sampling.html (accessed on 01/06/2023)
17. directindustry.com. Available online: https://www.directindustry.com/prod/von-oertzen-gmbh/product-107869-1730862.html (accessed on 01/06/2023)

Citation: Dima, D.-N.; Chirilă, R.; Gimiga, G.-R. Intervention solutions on landslides in road areas. Case study. *Journal of Engineering Science* 2023, 30 (2), pp. 135-143. https://doi.org/10.52326/jes.utm.2023.30(2).12.

Publisher's Note: JES stays neutral with regard to jurisdictional claims in published maps and institutional affiliations.

Submission of manuscripts: jes@meridian.utm.md

Journal of Engineering Science *Vol. XXX, no. 2 (2023), pp. 144 - 157*
Fascicle *Food Engineering* *ISSN 2587-3474*
Topic *Food Technologies and Food Processes* *eISSN 2587-3482*

https://doi.org/10.52326/jes.utm.2023.30(2).13
UDC [664.162.82+667.27]:664.14

QUALITY ASSESSMENT OF THE TOFFEE WITH SWEETENERS AND DYE FROM WALNUT SEPTUM OR KERNEL'S PELLICLE

Valentina Bantea-Zagareanu *, ORCID: 0000-0003-4886-2980,
Iuliana Sandu, ORCID: 0000-0003-1266-3154,
Alexei Baerle *, ORCID: 0000-0001-6392-9579,
Pavel Tatarov, ORCID: 0000-0001-9923-8200

Technical University of Moldova, 168 Stefan cel Mare Blvd., Chisinau, Republic of Moldova

*Corresponding authors: Valentina Bantea-Zagareanu, *valentina.bantea@tpa.utm.md;*
Alexei Baerle, *alexei.baerle@chim.utm.md*

Received: 05. 04. 2023
Accepted: 06. 16. 2023

Abstract. Reduction of "bad" carbohydrates in sweets is a complex issue, because carbohydrates provide important sensory, physical and textural properties of food. This research illustrated the possible use of the colorant Brown 7 (0.6...1.0%) in combination with sucralose and isomalt for alerting the functional quality of toffee candies. Sensory and physicochemical properties, microbiological indicators and color parameters were analyzed for four samples of toffee. The combination of sweetener with anti-crystallizer and Brown 7 significantly improves the color of toffees. It was established by HPLC that during thermal processing the Casuarictin from Brown 7 transforms into Ellagic acid. These transformations lead to an increase in the intensity of the brown color in the toffee. The addition of Brown 7 contributes to the decrease of titratable acidity from 0.28 ± 0.08 in the control to 0.21 ± 0.06 degrees of acidity in the sample which contain 1.0% dye. The chromatic parameters L*, a*, b* of the toffee sample with 0.6% Brown 7 content are the closest to the classic toffee parameters. Use of colorant in combination with sweetener illustrates a potential synergy of sensorial properties. This help to increase the intake of natural bioactive compounds and to decrease carbohydrates in sweets, promising health benefits.

Keywords: *Brown 7, CIELab, color, HPLC, pellicle, RGB, sweeteners, toffee candies, walnut.*

Rezumat: Reducerea carbohidraților „răi" din dulciuri este o problemă complexă, deoarece carbohidrații oferă proprietăți senzoriale, fizice și texturale importante ale alimentelor. Această cercetare a ilustrat posibila utilizare a colorantului Brown 7 (0.6...1.0%) în combinație cu sucraloză și izomalt pentru a mări calitatea funcțională a bomboanelor de tip toffee. Proprietățile senzoriale și fizico-chimice, indicatorii microbiologici și parametrii de culoare au fost analizate pentru patru mostre de toffee. Combinația de îndulcitor cu anticristalizant și Brown 7 îmbunătățește semnificativ culoarea produsului. Sa stabilit prin HPLC că în timpul procesării termice, casuarictină din Brown 7 se transformă în acid ellagic. Aceste transformări duc la o creștere a intensității culorii maro din toffee. Adăugarea Brown 7 contribuie la

scăderea acidității titrabile de la 0.28 ± 0.08 în proba de control la 0.21 ± 0.06 grade de aciditate în proba cu 1.0% colorant. Parametrii cromatici L*, a*, b* ai probei de caramel cu 0.6% conținut Brown 7 sunt cei mai apropiați de parametrii de caramel clasic. Utilizarea colorantului Brown 7 în combinație cu îndulcitorul ilustrează o potențială sinergie a proprietăților senzoriale. Acest lucru contribuie la creșterea aportului de compuși bioactivi naturali și la scăderea carbohidraților din dulciuri, promițând beneficii pentru sănătate.

Cuvinte-cheie: *Brown 7, CIELab, culoare, HPLC, peliculă, RGB, îndulcitori, bomboane toffee, nucă.*

1. Introduction

The color is the first quality indicator of the food product, to which the consumer draws attention. Sweets, which contain synthetic dyes are beloved by little children, but because of their possible negative effect on health, the question arises of replacing synthetic dyes with natural ones. Among the sources of perspective for obtaining yellow and brown dyes can be mentioned the parts of the walnut Juglans regia L. fruit - septum and kernel's pellicle. In tandem, the Republic of Moldova and Romania annually produce about 1500-3000 tons of septum. The septum contains significant amounts of polyphenols with expressed physiological properties [1], which, in addition to their physiological activity, have the ability to generate deep-brown color.

In the confectionery production, natural colorants are used, which include carotenoids [2], anthocyanins (E163i, the extract of black currants, rosehips, aronia, and the enoch dye produced from the processing of winemaking waste [3]), flavonoids (Brown 7) and chlorophylls (E140m from spirulina, chlorella) etc. Caramel dye E150 is used in various food systems as a substitute for brown synthetic dye and as an antioxidant. FAO/WHO Expert Group on Food Additives divides the caramel color into 4 classes, depending on the preparation method and physical properties. But this dye can be toxic in large quantities [4]. Available studies of other authors [5] support the conclusion that caramel colors are not genotoxic or carcinogens, so, the intake of caramel colors and constituents does not present safety risks. A synthetic brown dye, similar with color of old walnut pellicle is Brown HT or E155 [6]. These dyes are used in the confectionery industry in combination with other color influencing factors [7-10].

A distinctive feature of the toffee is the amorphous or microcrystalline structure obtained from boiled mass of caster sugar, glucose syrup, dairy products [11]. The milk and butter provided in the toffee recipe determine not only its nutritional value, but also the taste, aroma, color and structure of the products. Toffee has recently been highlighted as a potential antioxidant due to its high sugar content [12]. In order to expand the range of fortified products with increased biological value, in the complete absence of synthetic additives in the composition of the recipe, it was proposed to add Lavitol-M antioxidant premix, powder of viburnum berries, schisandra, Amur grape berries and powders from preserved reindeer antlers containing a unique complex of vitamins and minerals [13]. In order to increase the biological value of the drawn toffee, a recipe composition was proposed in which carrot puree and whey were added, which contribute significantly to increasing the content of dietary fiber, carotenes, essential amino acids (lysine, methionine) and minerals [14]. Also known are sugar-based toffee varieties with fillings containing molasses, condensed milk, invert syrup, dehydrated milk fat, vegetable fats, glycerin, strawberry juice, lecithin [15]. When using guava pulp in toffee preparation technology, changes in the chemical composition and sensory properties of toffee during storage at ambient temperature (27 ± 2°C), as well as under

refrigerated conditions (5 ± 2°C), for 90 days [16]. A similar study focused on the preparation of toffee with the addition of a mixture of Aonla pulp (Emblica officinalis Gaertn.) and ginger extract, which contains vitamin C, is intensely energizing and has a strong beneficial antioxidant activity in the body. Toffee prepared using an 80:20 g/g mixture (Aonla pulp: ginger extract) was found to be superior to other mixtures in terms of yield, organoleptic properties and nutritional quality during 90 days of storage at different temperatures [17].

The major problem eating toffee is its high sugar content. Great efforts have been made to replace the sugar in toffee with bioactive ingredients. The sugar content in toffee was replaced with jojoba powder at concentrations of 20-100% [18, 19]. Examples of classic technologies and with the replacement of sucrose in confectionery products with various sweeteners are known. A method was proposed for the production of semi-hard toffee with the substitution of sugar with 85.7 - 83.4% isomalt or lactitol, with the addition of powdered milk, melted fat, emulsifier and vanilla flavor. The obtained toffee contained reduced carbohydrates - 15% and a reduced energy value - 260 kcal, due to the absence of sucrose in the recipe [20]. Therefore, the objective of the present work is to select the necessary amount of colorant, the optimal quantities of sweetener and the method of their administration, to expand the range of marketed toffee with dietary and diabetic properties, with a low carbohydrate content. To accomplish this task, sugar was replaced with sucralose and glucose syrup with isomalt - products that serve both as anti-crystallizers and sweeteners. In order to improve the nutritional value and sensorial aspect of the finished product, natural Brown coloring obtained from walnuts was added.

2. Materials and Methods

2.1. Extraction of Brown 7 from walnut fruit pellicle and septum

The walnuts of the "Kogâlniceanu" variety, harvested in 2020-2022, were used. The walnut core was treated with a 1.0% sodium carbonate solution, 15.0% ethanol and 0.02% pectolytic enzyme at a temperature of 18...20 °C, in 5 repetitions. Extracts were united in one and filtered. After filtration, the solution was concentrated at 60-70 °C at a rotary speed of 150-200 rpm. About 150 mL of ethanol were added to the obtained dark-brown (almost black) viscous paste to separate a very viscous mass. This mass was dried under vacuum at 60 – 70 °C and 90-100 mbar. The obtained powder was kept cold (4.0 ± 1.0 °C) [21]. Because the mass part of the pellicle in the kernel is max. 10%, in turn, the content of extractable substances is equal to 10.0%. Respectively, the yield of the dye, recalculated to the walnut kernel, was 1.0 ± 0.2%. The septum was separated from the walnut core and placed in an ultrasonic bath (22 ± 2°C, 37 kHz, 10...15 min*)*. Separation of the dye from the septum in powder form takes place under similar conditions. The dye yield was 4.0 ± 0.2%.

2.2. RGB-analysis method

The determination and digitization of the sample colors in solid dry state is usually performed by the CIELab method [22, 23]. At the same time, determining the exact shade of the color of the samples in the wet state represents some difficulties. This led us to develop our own method, based on the use of the three-bytes Red-Green-Blue (RGB) code, in which the intensity of the respective component is rendered by 1 byte of information [24]. Sample images were processed with the help of the application, which determines the RGB codes of the chosen pixels [25]. To reduce the inevitable color inhomogeneity, the RGB codes were recorded in three equidistant points. The arithmetic mean, calculated for each byte, is only rounded to a whole number, given the fact that the RGB code consists exclusively of whole numbers.

2.3. High-Performance Liquid Chromatography with Photodiode Array (HPLC-PDA)

Analysis of extracts, dyes, and food products were performed on the „Shimadzu LC2030 3D Plus" instrument, using the reverse-phase column C_{18} „Phoenomenex" (150 mm×4.6 mm×5 μm×80 nm) and biphasic gradient elution. **Phase A**: Water / Acetic Acid 0.1%. **Phase B:** MeCN / Acetic acid 0.1 %. The temperature of the samples in the autosampler – 15.0 °C. Constant flow rate 0.5 mL/min. Phase B content in the extremes of the gradient curve from 5 % to 90%, column temperature 25 °C, PDA detection cell temperature of 30 °C [26, 27].

2.4. Toffee-candies producing

Toffee candies were prepared according to the classic method using in the manufacturing recipe: concentrated milk, sugar, glucose syrup, whipped cream and essence [28, 29]. The toffee production method provides for the tempering of glucose syrup to a temperature of 45...50 °C, concentrated milk to 30 °C and fats to 33...36 °C. The classic manufacturing recipe does not contain water. The materials were mixed until a homogeneous mass was obtained. In order to avoid worsening the properties of the mass (excess caramelization of sugars), the heating of the mixture took place gradually: in the first stage, up to a dry substance content of 84.0 ± 0.1 %, and in the second stage boiling of toffee mass up to the temperature of 120 ± 2 °C and dry substance content of 91.0 ± 1 %. When mixture is heated and boiled, various processes of sugars and proteins transformation take place: inversion, monosaccharide decomposition, sugar-amine reactions. There is an increase in reducing substances, change in acidity, color, taste and aroma. This is mainly due to the melanoidin formation reaction [30]. Milk proteins are essential for the color and flavor of toffee masses by the Maillard reaction [31]. Constant stirring of the mixture ensures a distribution of fat throughout the mass, prevents protein coagulation and burning [20], the toffee mass acquires a fuller milky taste and a caramel color. Then, in the toffee mass rapidly cooled to the 60 ± 1 °C, the essence was added and mixed for 4...6 minutes to obtain a homogeneous product [32]. The confectionery masses were molded using a toffee forming unit, then cooled, dried at ambient temperature, packaged in a moisture and grease resistant label and stored at 18 ± 3 °C and ϕ = 75 ± 1 % [11].

2.5. Preparation of toffee for HPLC analysis

The toffee samples of 1.000 ± 0.002g were dissolved in 5mL of distilled water and placed in the 37MHz ultrasound bath at room temperature for 10 minutes. Obtained dispersed samples were filtered through filter paper and then through a 0.22-micron polytetrafluorethylene (PTFE) syringe filter and immediately placed in cooled autosampler.

2.6. Moisture content

Samples were dried at 105 ± 1 °C to obtain constant weight [33, 34].

2.7. Ash content

Ash content was measured by complete combustion of organic substances with the aim of obtaining the residue of mineral substances at a temperature of 550 ± 5 °C.

2.8. Titrable acidity

Dispersed samples of toffee candies were titrated with a 0.1 mol/L potassium hydroxide solution in the presence of phenolphthalein indicator until a pale pink color, which did not disappear for one minute [35].

2.9. Reductants content

The iodometric method, based on the ability of the sugar carbonyl groups to reduce potassium ferrocyanide in alkaline solution, was used [33].

2.10. Fat content

Fats were extracted from weighted toffee probes with hexane as solvent using „VELP Scientifica" fat extraction system.

2.11. Water activity (a_w)

It was measured using "Rotronic Hygro Palm" system [36].

2.12. CIELab color parameters

CIELab color parameters were measured using "Chroma Meter CR-400" [37, 38]. Luminosity (L*), red/green component (a*), yellow/blue component (b*), hue angle (H*) were measured. Total color difference was calculated using Eq. (1) [39]:

$$\Delta E^* = \sqrt{(\Delta L^*)^2 + (\Delta a^*)^2 + (\Delta b^*)^2} \quad (1)$$

2.13. Microbiological analysis

It was performed in accordance with the "Rules on microbiological criteria for foodstuffs" [40, 41].

2.14. Sensory analysis

It was performed according to [42, 43] by 9 trained evaluators. The individual score was given according to the deviations from the sensory requirements (Table 1) [11].

Table 1

Scoring 5-point scale of the deviation from the official sensory requirements

Points	Description of the evaluation stage
5	No deviation from sensory quality requirements
4	Minimal non-conformities from sensory quality requirements
3	Visible nonconformities from sensory quality requirements
2	Obvious/considerable non-conformities from sensory quality requirements
1	Very obvious/considerable non-conformities from the sensory quality requirements
0	The product cannot be analyzed from a sensory point of view

2.15 Statistical analysis

Confidence intervals were calculated for significance P = 95%, by "2σ-rule", $X = \langle X \rangle \pm 2\sigma$. The statistical analysis of the results was carried out with the application of Microsoft Excel 2017 programs. To exclude results with accidental errors and those with high levels of uncertainty, three parallel measurements were performed.

3. Results and Discussion

3.1. Brown 7 quality and composition

Brown 7 analysis by the RGB-method requires the scanning of more than 3 experimental points sufficient for wet samples or solutions [44], due to the "play of lights and shadows" in the image of powder. In Table 2 are shown RGB data and colors for 7 random points of the image, as well as the "average" of the RGB bytes and color.

Table 2

Detected RGB values and corresponding color for Brown 7 in powder form

Analysed image	R (red)	G (green)	B (blue)	Color
	81	70	57	
	39	30	19	
	67	61	49	
	29	21	12	
	61	51	40	
	34	25	14	
	47	40	30	
	Average values, rounded to closest integer			<Color>
	51	43	32	

3.2. Evaluation of the nutritional and functional characteristics of the toffee candies

Reducing the sugars in foods is a complex issue because sugars contribute to important sensory and physical food properties. Near the 20-50% of sugar can be reduced or replaced by several ingredients without affecting sensory acceptance [45, 46]. Two commonly used sweeteners, sucralose and isomalt have been proposed to replace sugar in toffee masses. The amount of sweetener, sucralose and isomalt, were calculated in relation to the sweetness index of sucrose: sucrose – 100 c.u., sucralose – 600 c.u., isomalt – 50 c.u. The glucose syrup in the recipe was substituted with a quantity of isomalt, resulting from the sweetness of the glucose syrup – 75 c.u. [45].

The control sample without sugar (TSIM) was prepared similarly to the sample with sugar (TZGS), dissolving the sweetener and anti-crystallizer in an amount of water of 35...40% of the mass of the mixture of dry components, without dye. In this case, the masses were obtained with a slightly pronounced color due to the lack of sucrose that contributes to the process of caramelization of the mass. To improve the color of the mass, the Brown 7 from the walnut pellicle was used, in a proportion of 0.6 and 1.0% compared to the amount of sugars, giving birth to TSIB_0.6 and TSIB_1.0. Colorant was added with the essence at the stage of the toffee's cooling at continuous stirring until a homogeneous mass was obtained. The obtained samples (Figure 1) were analyzed according to sensory, physicochemical, textural and microbiological quality indicators (Table 3).

Figure 1. Toffee samples: TZGS – control with sugar and glucose syrup, TSIM – control with sucralose and isomalt, TSIB_0.6 – with sucralose, isomalt and 0.6% Brown 7, TSIB_1.0 – with sucralose, isomalt, 1.0% Brown 7.

Table 3

Physicochemical indicators of toffee samples

Parameters	TZGS	TSIM	TSIB_0.6	TSIB_1.0
Moisture content, %	8.10 ± 0.03	8.50 ± 0.03	8.93 ± 0.03	10.05 ± 0.04
Titratable acidity, degrees	0.32 ± 0.01	0.28 ± 0.08	0.27 ± 0.08	0.21 ± 0.06
Reducing substances, %	19.40 ± 0.17	17.23 ± 0.19	21.02 ± 0.22	20.90 ± 0.20
Ash content, %	0.038 ± 0.003	0.032 ± 0.002	0.036 ± 0.003	0.050 ± 0.004
Fat content, %	7.7 ± 0.1	7.0 ± 0.1	5.9 ± 0.1	6.2 ± 0.1
Water activity (a_w), c. u.	0.608 ± 0.002	0.622 ± 0.002	0.640 ± 0.001	0.732 ± 0.003

Note: TZGS – toffee with sugar and glucose syrup; TSIM – toffee with sucralose and isomalt; TSIB_0.6, TSIB_1.0 – toffee with sucralose, isomalt and 0.6 or 1.0% of Brown 7.

Water content is an important factor for confectionery quality, influencing texture, and is often the limiting parameter during storage that controls shelf life. This parameter can be controlled by the boiling point of toffee masses during manufacturing [47].

The TZGS control sample has a lowest value of 8.10 ± 0.03% due to the presence of sugar in the recipe [48]. At the temperature of 160 °C, the caramelization of the sugars takes place, which begins with the melting of the sugar at high temperatures followed by foaming (boiling). Sucrose is first broken down into glucose and fructose. This is followed by a condensation step, where the individual sugars lose water and react with each other [49, 50].

Table 3 demonstrates that the substitution of sugar in the recipe and the addition of Brown 7 increase the moisture content of the products comparing with the control samples. For TSIM and TSIB_0.6 they constituted 8.50 ± 0.03% and 8.93 ± 0.03%, respectively. In the TSIB_1.0 the value of this quality indicator increased 1.3 times compared to the control sample and was 10.05 ± 0.04%. According to Moldovan Government Decision 204/2007 the mass fraction of moisture in acidulated toffee should be maximum of 9.0%, and for non-acidulated masses up to 10.0%. Only TSIB_1.0 does not correspond the required value. Was reported that due to the presence of non-hygroscopic isomalt in the recipe, there is no absorption of moisture by the product and there is no recrystallization of crystals with the formation of larger ones. It was found that the obtained toffee retains a fine-crystalline consistency for a longer time compared to commercial toffee obtained by traditional sucrose-based technology [20].

In the control sample TZGS the ash content was 0.038 ± 0.003%, while in the control sample with sweeteners, TSIM, it was 0.032 ± 0.002% and increases with the increase in the concentration of Brown 7, ranging from 0.032 ± 0.002% to 0.050 ± 0.004%. The content of reducing substances correspond to the permitted regulated values up to max. 22.0% [11]. The fat content for all products is between 7.7 ± 0.1% and 6.2 ± 0.1%. The acidity correlate with the concentration of Brown 7, showing a decreasing trend, from 0.32 ± 0.01 for TZGS to 0.21 ± 0.06 degrees of acidity for TSIB_1.0. The reduction in titratable acidity may occur due to the basicity of the quinones in Brown 7 [21]. Many sugar-free labeled sweets are high in food acids and have teeth-erosive potential. Applying an in vitro dental erosion test of surface microhardness modification, it was found that 56% of sugar-free sweets (even some with "Tooth friendly" message) contain high concentrations of food acids and low pH [51]. The lower acidity values and higher pH of our experimental samples suggests that they are safety for the teeth.

3.3. Transformation of Brown 7 during the toffee production

In time of the heat treatment profound changes occur in the composition of carbohydrates, proteins and fats of the toffee [30]. The dark brown color of the toffee mass is due to the formation of melanoidins [52].

Table 4

HPLC data for different systems with Brown 7

Compound	R_T	λ, nm	Area	Area, %	Summ, %
Brown 7 dye from walnut fruit septum					
Catechin	15.175	278	503031	86.770	100
Epicatechin	16.488	278	76696	13.230	
Casuarictin	17.096	366	498754	39.657	100
Ellagic Acid	18.795	366	758899	60.343	
Brown 7 dye from walnut kernel pellicle					
Casuarictin	17.625	366	98562	75.644	100
Ellagic Acid	18.831	366	31735	24.356	
TSIB**_0.6 with Brown 7 from walnut kernel pellicle**					
Casuarictin	17.693	366	3739	15.311	100
Ellagic Acid	18.896	366	20679	84.689	
TSIB**_1.0 with Brown 7 from walnut kernel pellicle**					
Casuarictin	17.645	366	7562	10.906	100
Ellagic Acid	18.841	366	61775	89.094	

From data presented in the Table 4, it follows that during the production of toffee there is an increase in the Ellagic Acid / Casuarictin ratio from 1/3 up to 9/1 (Figure2).

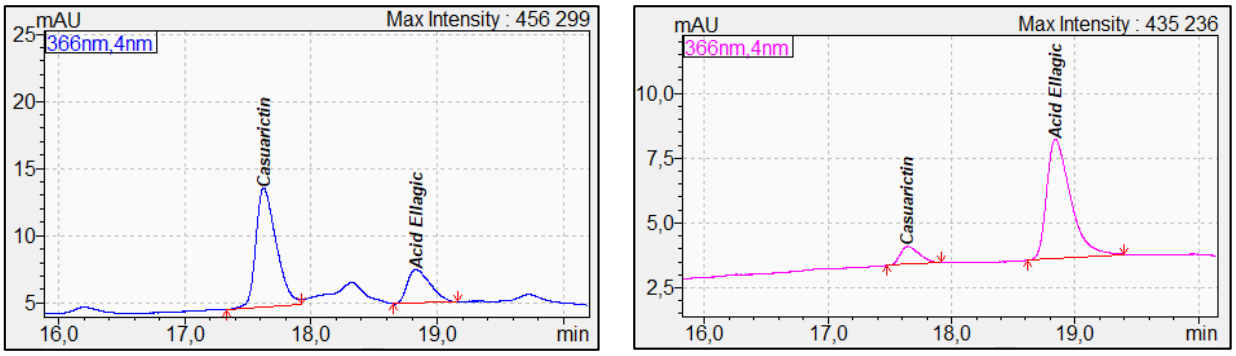

a) b)

Figure 2. Phenols relationship: a) in powdered Brown 7; b) in TSIB_0.6.

This change allows us to propose the mechanism of the transformation of Casuarictin into Ellagic Acid (Figure 3). Both Gallic and Ellagic Acids are converted to brown quinones upon oxidation [53], which enhances the effect of the Brown 7 dye.

Water activity is a critical parameter related to candy stability and the main controlling characteristic of microbial growth in sugar confectionery [31]. Toffee has a water activity between 0.60-0.65 c.u. [54, 55].

Sugar-free samples show increasing aw values, from 0.622 ± 0.002 c.u. (TSIM) to 0.732 ± 0.003 c.u. (TSIB_1.0). It is considered that the sample values do not exceed the range determined for the quality and safety of food for sweets [56].

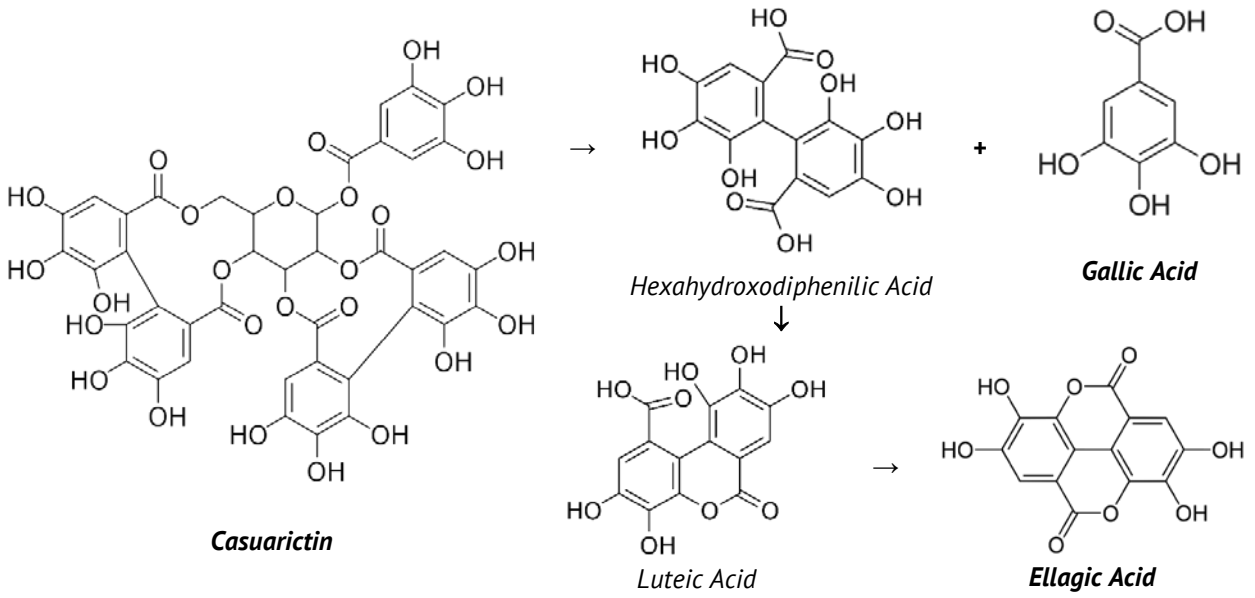

Figure 3. Casuarictin hydrolysis scheme during the toffee heat treatment.

The total number of germs (TNG) in the experimental samples was reduced, with a maximum of 5 ± 1 CFU/g, therefore they are in accordance with the values allowed by the regulations [36]. Was reported an antimicrobial activity of tannins and flavonoids against pathogenic bacteria [57]. This was also confirmed by other authors [58], who indicate that the total content of phenolics and flavonoids inhibited bacterial and fungal growth, reduced cell viability, showed free radical scavenging capacity and inhibited the formation of superoxide anions. Polyphenol content of walnut extract is more than 4000 mg/100 g and 24 compounds from the group of flavonoids, phenolic acids and juglone derivatives were identified [59]. A strong correlation between polyphenol content and antioxidant capacity and cytotoxic activity was observed. In addition, the toffee is processed at temperatures above 93 °C, which proves that the growth and survival of vegetative cells of bacteria, yeasts and molds will be stopped and the samples will be stable during storage.

Toffee rarely suffers microbial spoilage if properly prepared, packaged and stored. The source of microorganisms in toffee products can be taken from the raw materials used in production. Another source of contamination can be air, equipment, workers and improper humidity [60]. Microorganisms that can be identified in toffee masses include *Bacillus spp.* and Clostridium spp. Other microorganisms that can be observed are introduced post-processing.

The most common primary microorganisms associated with the alteration of sugar confectionery products were identified as *Zygosaccharomyces rouxii* and *Brettanomyces bruxellensis* yeasts [61]. Other studies demonstrate detectable mold genera such as *Aspergillus*, *Penicillium*, *Verticillium*, *Rhizopus*, *Mucor* and *Trichothecium*. The authors argue that this could be due to increased humidity and water activity [62, 63]. Controlling moisture content will prevent the spoilage of sugar confectionery products most susceptible to mold growth [64].

CIELab chromatic parameters were analyzed for the toffee samples. The results show that the TZGS control sample is characterized by the highest L* (luminosity) value of 48.22 (Table 5).

Table 5

CIELab chromatic parameters of toffee candies

Toffee sample	Luminosity, L*	Red/Green, a*	Yellow/Blue, b*	Hue angle, H*,°	Total color difference, ΔE*
TZGS	48.2 ± 1.3	8.27 ± 0.42	20.4 ± 1.2	67.9 ± 1.2	6.7 ± 1.3
TSIM	46.8 ± 1.3	3.84 ± 0.60	12.0 ± 1.1	72.2 ± 1.1	6.27 ± 0.17
TSIB_0.6	41.8 ± 1.1	5.07 ± 0.57	12.9 ± 0.9	68.57 ± 0.83	9.2 ± 1.5
TSIB_1.0	34.27 ± 0.88	4.7 ± 1.2	9.2 ± 0.5	52.79 ± 0.82	17.2 ± 1.1

Note: TZGS – toffee with sugar and glucose syrup; TSIM – toffee with sucralose and isomalt; TSIB_0.6, TSIB_1.0 – toffee with sucralose, isomalt and 0.6 or 1.0% of Brown 7.

The hue angle H* of 67.89 °, is in the first trigonometric quadrant, in which the orange hue predominates. With the removal of sugar from the recipe, it is not possible to obtain the caramel color. In the case of the addition of the Brown 7 dye, it was observed that the hue angle remains in the first trigonometric quadrant, but with the addition of a larger amount of dye, the values reduced from 72.20 to 52.79. In the TSIM sample a low color intensity and the presence of the gray shade, presenting a combination of unpleasant colors. The closest to the control sample with TZGS sugar, was the TSIB_0.6 sample, which was characterized by a suitable color, generates chromatic harmony, provides a state of well-being and pleasure.

The sensory analysis, carried out by nine specialists in the field, a clearly defined sweet taste, caramel color and a pleasant smell of sugar characteristic of the product were observed in the sugar-based control sample (figure 4). Addition of Brown 7 significantly led to change in sensory characteristics, especially color and texture. The samples with 0.6% and 1.0% addition (TSIB_0.6 and TSIB_1.0) obtained a darker color with the increase of the amount of Brown 7, having a pleasant and homogeneous shade. The change in color is explained by the content of polyphenols present in the walnut skin, which when homogenized with other components in the recipe and after heat treatment lead to a change in the color of the finished product [65].

The texture of toffee masses [66] is determined by factors such as chemical composition and cooling rate. Milk protein, especially casein, denatures in the heat treatment process, forming a viscoelastic structural network throughout the candy mass, that gives the following textural properties: rigidity, texture and chewability [31].

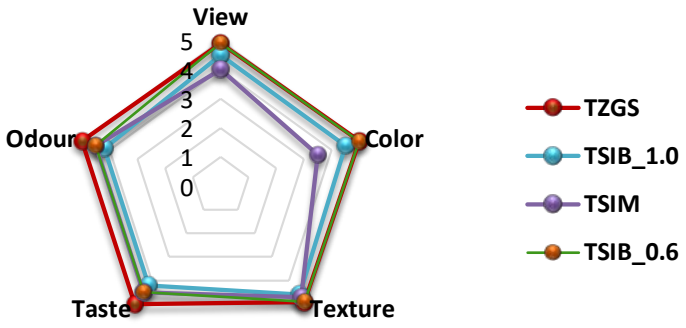

Figure 4. Toffee candies sensorial profiles.

Processing conditions also affect the crystallization of fats [67], thus having an effect on their functional properties. The effects of cooling rate on the macroscopic properties of a network of fat crystals were studied by crystallization of anhydrous milk fat (5 °C/min,

Newtonian cooling) or slowly (0.1 °C/min, step cooling). The microstructure was also different between the two treatments. When they crystallized rapidly, the crystallites were numerous and small, while a smaller number of larger crystallites were observed when they crystallized slowly.

The color of a translucent sample will change when the length of the light path through it changes. The path length must be fixed with a fixed white background [68]. The control sample with sugar and glucose syrup (TZGS) scored 4.96 out of 5 points. The control sample with sucralose and isomalt (TSIM) was degraded, accumulating 4.24 points, it was characterized by an opaque color with a gray tint that can be seen entirely by reflected light.

The highest total sensory score was accumulated by TSIB_0.6 (23.8), followed by TSIB_1.0 (22.0), compared to TSIM control sample (21.2). The sample with 0.6% Brown 7 dye shown an optimal combination as it reported the most pleasant color, flavor and texture, similar to the sugar control sample (TZGS). It was also characterized by a soft texture, viscous consistency, with a sweet taste due to the substitution of sugar in the recipe.

4. Conclusions

Extracts and powders from *Juglans regia* are sources of natural dyes of a polyphenolic nature, which, in addition to color, can provide food products with some functional properties.

The possibility of correcting the color of confectionery products with a reduced amount of sugar, by adding the natural brown dye, obtained from the walnut kernel's pellicle or from walnut septum, has been confirmed. The toffee samples were obtained by replacing sugar with sucralose and isomalt, and the addition of the natural dye Brown 7 allowed to obtain the characteristic color of the product obtained by the classic technology (with sugar). The incorporation of the Brown 7 dye in concentrations from 0.6% to 1.0% contributes to the formation of the product with optimal sensory characteristics.

It was confirmed by HPLC, that during thermal processing, the composition of the polyphenols in the natural dye Brown 7 changes, which is expressed by increasing the Ellagic Acid / Casuarictin ratio from 1/3 to 9/1. Since the thermal hydrolytic transformation products of Casuarictin (Gallic, Hexahydroxydiphenylic, Luteic, Ellagic Acids; Glucose) are harmless, the natural dye Brown 7 can be used in sweets, especially in the case when long heat treatments take place in the technological production process.

Acknowledgements: Express our gratitude for the financial and logistical support within the framework of the State Research Project 20.80009.5107.09 – "Improving the quality and safety of food products using biotechnology and food technology" funded by the Moldovan Government. Also express thanks to Ms. Aliona Ghendov-Moșanu, Ms. Rodica Sturza and Mr. Artur Macari.

Conflicts of Interest: The authors declare no conflict of interest.

References

1. Rusu, M.E.; Fizesan, I.; Pop, A.; Mocan, A.; Gheldiu, A.M.; Babota, M.; Vodnar, D.C.; Jurj, A.; Berindan-Neagoe, I.; Vlase, L.; Popa, D.S. Walnut (Juglans regia L.) Septum: Assessment of Bioactive Molecules and In Vitro Biological Effects. *Molecules* 2020, 25(9), 2187.
2. Cmirnov, Ye. V. *Pishchevyye krasiteli*. Spravochnik. Professiya, Sankt-Peterburg, Rossija, 2009, 352 p.
3. Bolotov, V.M.; Nechayev, A.P.; Sarafanova, L.A. *Pishchevyye krasiteli: klassifikatsiya, svoystva, analiz, primeneniye*. GIORD, Sankt-Peterburg, Rossija, 2008, 240 p.
4. Garima, S.; Harish, K. S. Food caramels: Review. *J Food Sci Technol*. 2014, 51(9), pp. 1686-1696.
5. Thomas, A. Caramel color safety - An update Review *Food Chem Toxicol*. 2018, 111(1), pp. 578-596.

6. Decision of the Government of the Republic of Moldova No. 229 of 29.03.2013. Regarding the Approval of the Sanitary Regulation on Food Additives. 2013. Available online: https://www.legis.md/cautare/getResults?doc_id=109707&lang=ro (accessed on 22 December 2022).
7. Bantea-Zagareanu, V.; Sandu, Iu.; Baerle, A. Changing the ratio of biologically active compounds in the nut kernel film in sweets. *Perspectives and Problems of Integration in the European Research and Education Area* 2022, 9(1), Cahul: USC, pp. 377-378.
8. Bantea-Zagareanu, V. Use of walnuts (*Juglans regia L.*) waste from physical extraction of oil to produce flour and sweets. *Food and Environment Safety Journal* 2018, 27(1), pp. 74-80. Available online: http://fens.usv.ro/index.php/FENS/article/view/562/537 (accessed on 1.03.2023).
9. Ghendov-Moşanu, A.; Bantea-Zagareanu, V.; Tatarov, P. The use of walnut flour (*Juglans regia L.*) in the manufacture of Amaretti biscuits. *Meridian Engineering* 2016, 3, pp. 62-65.
10. Breahna, N.; Sturza, M.; Dodon, A.; Bantea-Zagareanu, V. Aspects of the use of spirulina in the confectionery industry. In: *Materials of the Technical-Scientific Conference of Collaborators, PhD Students and Students*. Tehnica-UTM, Chisinau, 2018, 2, p. 13-16.
11. Decision of the Government of the Republic of Moldova no. 204 of 11.03.2009. Regarding the approval of the Confectionery Products, Technical Regulation. Official Gazette. Published: 20-03-2009 no. 57-58 art. 254.
12. Khvorost, O. P.; Malyy, V. V.; Serbin, A. G. Ellagovaya kislota, rasprostranennost' v rastitel'nom mire i aspekty biologicheskogo *Provizor. zhurn.* 1998, 22, pp. 36–37.
13. Frolova, N.A.; Peznichenko, I.Yu. Kompozitsiya ingrediyentov dlya prigotovleniya obogashchennogo konditerskogo izdeliya tipa irisa tirazhennogo. Patent RU2687459C1.
14. Bas'kina, V.A.; Kondratova, I.I.; Tadeush, A.I. Sposob proizvodstva irisa i kompozitsiya dlya yego osushchestvleniya. Patent 4374.
15. Merkushkin, A.N.; Murav'yev, A.S.; Gruzintsev, A.P.; Gyatkova, S.P. Sposob proizvodstva irisa s nachinkoy Pravoobladateli Otkrytoye aktsionernoye obshchestvo Lamzur. Patent 219.016.BF36.
16. Chavan, U.D.; Shegade, S.L.; Karma, B.R.; Dalvi, U.S. Studies on Preparation of Toffee from Guava. Int. *J. Adv. Res. Biol. Sci* 2016, 3(1), pp. 99-111.
17. Domale, J.N.; Kotecha, P.M.; Pawar, V.D. Studies on preparation of toffee from Aonla pulp. *Beverage and Food World* 2008, 35(9), pp. 39-40.
18. Bahrasemani, K.M.; Sahari, M.A.; Barzegar, M. The effect of jujube powder incorporation on the chemical, rheological, and sensory properties of toffee. *Food Sci Nutr.* 2018, pp. 1–11. https://doi.org/10.1002/fsn3.912.
19. Koohestani, M. B.; Sahari, M. A.; Barzegar, M. The effect of jujube powder incorporation on the chemical, rheological, and sensory properties of toffee. *Food Sci Nutr.* 2018, 19,7(2), pp. 678-688. doi: 10.1002/fsn3.912.
20. Krylova, E. N.; Savenkova, T. V.; Mavrina, Ye. N. Sposob proizvodstva tirazhennogo irisa. Patent 216.012.
21. Baerle, A.; Tatarov, P.; Sandu, Iu. Polyphenols and naphthoquinones extraction from walnuts pellicula: the impact on kernels quality. *Journal of Engineering Science* 2020, 27 (2), pp. 145-153. doi: 10.5281/zenodo.3784368.
22. Ghendov-Moșanu, A.; Cristea, E.; Sturza, R.; Niculaua, M.; Patraș, A. Synthetic dye's substitution with chokeberry extract in jelly candies. *Journal of food science and technology* 2020, 57(12), pp. 4383–4394.
23. Radu, O. Food compositions based on walnut oil (Juglans regia L.) resistant to oxidative degradation. Doctoral thesis in technology. UTM, Chisinau, 2020, p.150
24. Zelazko, A. RGB colour model. *Encyclopedia*, Britannica, 2022. Available online: https://www.britannica.com/science/RGB-colour-model (accessed on 1.04.2023).
25. Color picker, calculator and generator with high precision and contrast test. Available online: http://colorizer.org/. (accessed on 25.04.2021).
26. Gurev, A.; Dragancea, V.; Baerle, A.; Netreba, N.; Boestean, O.; Haritonov, S; Gaina, B. Properties of winemaking by-products of *Feteasca Neagra* grape seeds. *Chemistry Journal of Moldova - General, Industrial and Ecological Chemistry*, 2022, 17(2), pp. 50-61.
27. Popescu, L.; Ghendov-Moşanu, A; Baerle, A.; Savcenco, A.; Tatarov, P. Color stability of yogurt with yellow food dye from safflower (Carthamus tinctorius L.). *Journal of Engineering Sciences* 2022, 29 (1), pp. 142 – 150.
28. Pavlova N.S. Sbornik osnovnykh retseptur sakharistykh konditerskikh izdeliy. GIORD, Sankt-Peterburg, Rossija, 2000, 232 p.
29. Smirnova, M. K.; Ivanushko, L. S. *Retseptury na konfety i iris*. Pishchevaya promyshlennost', 1971, 824 p.
30. Sengar, G.; Sharma, H. K. Food caramels: a review. *J Food Sci Technology* 2014, 51(9), pp. 1686-1696. doi: 10.1007/s13197-012-0633-z.

31. Mendenhall, H.; Hartel, R. W. Protein content affects caramel processing and properties. *Journal of Food Engineering* 2016, 186, pp. 58-68. https://doi.org/10.1016/j.jfoodeng.2016.04.013.
32. Proizvodstvo irisa. Available online: https://msd.com.ua/texnologiya-konditerskogo-proizvodstva/proizvodstvo-irisa/?fbclid=IwAR2DHq8Z1fhN_6K94aWLkm7xMLdl8P9qRzpqJwGlZvwCXg6SS8hwLz5eo5g (accessed on 25.04.2022).
33. AOAC. Official Methods of Analysis, 18th ed.; Association of Official Analytical Chemists: Washington, DC, USA, 2000.
34. GOST 5900-73. *Izdeliya konditerskiye. Metody opredeleniya vlagi i sukhikh veshchestv*
35. ISO 750:1998. Fruit and vegetable products- In Determination of Titratable Acidity. International Organization for Standardization: Geneva, Switzerland, 1998.
36. Sandulachi, E. *Water activity in food products:* Monograph. Tehnica-UTM, Chisinau, Moldova, 2020, 208 p.
37. Pankaj, B. P.; Umezuruike, L. O.; Fahad, Al-Julanda.; Al-Said. Color Measurement and Analysis in Fresh and Processed Foods. *Food and Bioprocess Technology,* 2013, (6), pp. 36–60. doi:10.1007/s11947-012-0867-9.
38. Konica Minolta Chroma Meter CR-400/410 instruction manual. 2013, 9222-1878-20. http:// www.konicaminolta.com/instruments/download/instruction_manual/color/pdf/cr-400-410_instruction_eng.pdf
39. ISO 12647-2:2004/Amd.1:2007(E) 2007-04-15 Available online: https://cielab.xyz/ (accessed on 1.04.2023).
40. ISO 4833-2:2013/COR 1:2014. In Microbiology of the Food Chain—Horizontal Method for the Enumeration of Microorganisms—Part 2: Colony Count at 30 °C by the Surface Plating Technique—Technical Corrigendum 1; International Organization for Standardization: Geneva, Switzerland, 2014.
41. Decision of the Government of the Republic of Moldova No. 221 of 16.03.2009. Regarding the approval of the Rules regarding the microbiological criteria for food products. 2009, pp. 59-61. Available online: https://www.legis.md/cautare/getResults?doc_id=119439&lang=ro (accessed on 25 April 2022).
42. ISO 6658:2017. Sensory Analysis – Methodology - General Guidance. International Organization for Standardization: Geneva, Switzerland, 2017.
43. Popescu, L.; Bantea-Zagareanu, V.; Gudima, A. *Sensory analysis of food products*. Tehnica-UTM, Chişinau, Moldova, 2020, 84 p.
44. Baerle A.; Savcenco A.; Tatarov P.; Fetea F.;, Ivanova R.; Radu O. Stability limits of a red Carthamin–cellulose complex as a potential food colourant. *Food & Funcions* 2021, 2, pp. 8037-8043.
45. McKenzie, E.; Lee, Soo-Yeun. Sugar reduction methods and their application in confections: a review. *Food Sci Biotechnology* 2022, 31(4), pp. 387-398. doi: 10.1007/s10068-022-01046-7.
46. Mayhew, E. J.; Schmidt, S. J.; Lee, S. Y. Sensory and Physical Effects of Sugar Reduction in a Caramel Coating System. *Journal of food science* 2017, 82(8), pp. 1935-1946. https://doi.org/10.1111/1750-3841.13785
47. Ergun, R.; Lietha, R.; Hartel, R W. Moisture and shelf life in sugar confections. Review. *Crit Rev Food Sci Nutr.* 2010, 50(2), pp. 162-92. doi: 10.1080/10408390802248833.
48. Bantea-Zagareanu, V. Assurance of quality and shelf life of marmalade. Scientific papers Horticulture Series, USAMV Iași. 2018, 61(2), pp. 405-414.
49. Burluc, R. *Technology and quality control of sugar products*. Galatians. 2009, 120 p.
50. Ghendov-Moşanu, A. Biologically active compounds of horticultural origin for functional foods: Monograph. Chisinau: Tehnica-UTM, 2018. 236 p.
51. Shen, P.; Walker G. D.; Yuan, Y., Reynolds, C.; Stacey, M.A.; Reynolds, E.C. Food acid content and erosive potential of sugar-free confections. *Australian Dental Journal* 2017, 62(2), pp.215-222. doi: 10.1111/adj.12498.
52. Tatarov, P.G. *Food chemistry*. Tehnica-UTM, Chişinau, Moldova, 2017, 450 p. [in Romanian].
53. Evtyugin, D.D.; Magina, S.; Evtuguin, D.V. Recent Advances in the Production and Applications of Ellagic Acid and Its Derivatives. A Review. *Molecules* 2020, 25(12), 2745.
54. Sarafanova, L. A. Primeneniye pishchevykh dobavok v konditerskoy promyshlennosti. Professiya, Sankt-Peterburg, Rossija, 2010, c. 73-74.
55. Sarafanova, L. A. Pishchevyye dcbavki, Entsiklopediya. GIORD, Sankt-Peterburg, Rossija, 2004, c.193-195.
56. Wills, D. Water Activity and its Importance in Making Candy. *The Manufacturing Confectioner*, 1998, pp.71.
57. Machado, T. B.; Leal, I.C.R.; Amaral, A.C.F.; Santos, K.R.N.; Silva M.G.; Kuster, R.M. Antimicrobial ellagitannin of Punica granutum fruits. J. Braz. Chem. 2002, 13 (5), pp. 606-610. https://doi.org/10.1590/S0103-50532002000500010

58. D'Angeli, F.; Malfa, G. A.; Garozzo, A.; Volti, G. L.; Genovese, C.; Stivala, A.; Nicolosi, D.; Attanasio, F.; Bellia, F.; Ronsisvalle, S.; Acquaviva, R. Antimicrobial, Antioxidant, and Cytotoxic Activities of Juglans regia L. Pellicle Extract. Antibiotics (Basel) 2021, 10(2), 159. doi: 10.3390/antibiotics10020159.
59. Żurek, N.; Pawlowska, A.; Pycia, K.; Grabek-Lejko, D.; Kapusta I. T. Phenolic Profile and Antioxidant, Antibacterial, and Antiproliferative Activity of *Juglans regia* L. Male Flowers. *Molecules* 2022, 27(9), 2762. doi: 10.3390/molecules27092762.
60. Dragoni, J.; Balzaretti, C; Ravaretto, R. Seasonality of the microflora in environments of confectionery production. *Industrie Alimentari* 1989, 28, pp. 481–486.
61. Lenovich, L. M.; Konkel, P.J. Confectionery products. In: *Compendium of methods for the microbiological examination of foods*. Vanderzant, C.; Splittstoesser, D.F. (Eds.). Washington, DC: American Public Health Association, 1992, 3, pp. 1007–1018.
62. Hopko, I. *Food hygienic aspects of the confectionery industry*. Edesipar, 1979, 30, 8 (in Hungarian).
63. Thompson, S. Microbiological Spoilage of High-Sugar Products Food Microbiology and Food Safety book series (FMFS). Compendium of the Microbiological Spoilage of Foods and Beverages, 2009, pp. 301-324. Available online: https://link.springer.com/chapter/10.1007/978-1-4419-0826-1_11. Accessed on 1.03.2023.
64. Bantea-Zagareanu, V. Application of walnut oil cake in sweets manufacturing. In: *The international conference Biotechnologies, present and perspective* 2017, Suceava, Romania, 2017, pp. 9.
65. Bantea-Zagareanu, V. Effects of defatted walnut meal as a potential ingredient in bread: physicochemical, rheological, functional and sensory properties. *Journal of Engineering Science* 2023, 30(1), pp. 187–206.
66. Steiner, A. E.; Foegeding, E. A.; Drake, M. Descriptive analysis of caramel texture. *Journal of Sensory Studies* 2007. https://doi.org/10.1111/j.1745-459X.2003.tb00390.x.
67. Campos, R; Narine S.S.; Marangoni A.G. Effect of cooling rate on the structure and mechanical properties of milk fat and lard. *Food Research International* 2002, 35(10), pp. 971-981 https://doi.org/10.1016/S0963-9969(02)00159-X.
68. James, G. Color Measurement in Foods. *Laboratory Food technology*, 2003.

Citation: Bantea-Zagareanu, V.; Sandu, Iu.; Baerle, A.; Tatarov, P. Quality assessment of the toffee with sweeteners and dye from walnut septum or kernel's pellicle. *Journal of Engineering Science* 2023, 30 (2), pp. 144-157. https://doi.org/10.52326/jes.utm.2023.30(2).13.

Submission of manuscripts: jes@meridian.utm.md

Journal of Engineering Science *Vol. XXX, no. 2 (2023), pp. 158 - 172*
Fascicle *Food Engineering* *ISSN 2587-3474*
Topic *Food Technologies and Food Processes* *eISSN 2587-3482*

https://doi.org/10.52326/jes.utm.2023.30(2).14
UDC 579.8:634.8

MICROBIAL DIVERSITY ON GRAPE SURFACE AND ITS RESEARCH STATUS

Meiling Yao*, ORCID:0000-0001-5531-5518

Technical University of Moldova, 168 Stefan cel Mare Blvd., Chisinau, Republic of Moldova
*Corresponding author: Meiling Yao, *meiling.yao@saiem.tm.md*

Received: 05. 03. 2023
Accepted: 06. 11. 2023

Abstract. The microbial diversity of grape surfaces, also known as "microbial terroir", plays a critical role in winemaking and has applications in crop health and plant protection. Next-generation Sequencing (NGS) has revolutionized our understanding of grape surface microbiota by providing insights into the complex and dynamic microbial communities present on grape berries. NGS studies have confirmed the existence of distinct regional differences in grape surface microbial diversity, highlighting the concept of microbial terroir. This diversity is influenced by various natural and human factors, such as soil type, climate, vineyard management practices, and grapevine genetics, which contribute to the unique microbial terroir of each location. The application of NGS in studying microbial terroir has not only advanced our knowledge of grape and wine science, but also has implications in crop health and plant protection. The identification and characterization of microbial communities using NGS can help to develop sustainable and eco-friendly strategies for managing grapevine diseases and pests. The ongoing research in this area is expected to further expand our understanding of microbial terroir and its applications, contributing to the advancement of grape and wine science, and promoting environmentally responsible grape production practices. Based on bibliometric analysis, the current research focuses on the selection autochthonous *S. cerevisiae*, non-*Saccharomyces* and LAB. Plant growth-promoting bacteria considered as a new agroecological manageme. Interest in the role of natural microbial diversity in winemaking remains high.

Keywords: *Microbial terroir, microbial diverstiy, grape, non-saccharomysis yeast, biological control agents, bibliometric analysis.*

Rezumat. Diversitatea microbiană de pe suprafața strugurilor, cunoscută și ca "terroir microbian", joacă un rol crucial în procesul de producție a vinului și are aplicații în sănătatea și protecția plantelor. Secvențierea noii generații (Next-generation Sequencing - NGS) a revoluționat percepția asupra microbiotei suprafeței strugurelui, oferind informații despre comunitățile complexe și dinamice de microorganisme prezente. Studiile NGS au confirmat existența diferențelor regionale distincte în diversitatea microbiană a suprafeței boabelor de strugure, evidențiind conceptul de terroir microbian. Această diversitate este influențată de diferiți factori naturali și umani, precum tipul de sol, climatul, practicile de gestionare a viței de vie și genetica strugurilor, care contribuie la terroirul microbian unic al fiecărei locații.

Aplicația NGS în studiul terroirului microbian nu numai că a avansat cunoștințele în domeniul științei strugurilor și vinului, dar are și implicații în sănătatea plantelor și protecția plantelor. Identificarea și caracterizarea comunităților microbiene utilizând NGS pot contribui la dezvoltarea de strategii durabile și prietenoase cu mediul pentru gestionarea bolilor și dăunătorilor la vița de vie. Cercetarea continuă în acest domeniu este așteptată să extindă în continuare înțelegerea noastră asupra terroirului microbian și a aplicațiilor acestuia, contribuind la avansarea științei despre struguri, vinuri și promovarea practicilor responsabile de producție a strugurilor în concordanță cu mediul înconjurător. Pe baza analizei bibliometrice, cercetarea curentă se concentrează pe selecția de *S. cerevisiae* autohtone, non-*Saccharomyces* și LAB. Bacteriile care promovează creșterea plantelor sunt considerate o nouă metodă de gestionare agroecologică. Interesul pentru rolul diversității microbiene naturale în producția de vin rămâne ridicat.

Cuvinte cheie: *Terroir microbian, diversitate microbiană, strugure, drojdii non-saccharomyces, agenți de control biologic, analiză bibliometrică.*

1. Introduction

Wine production is characterized by distinct regional characteristics known as "terroir." With the advancements in biological technology, particularly high-throughput sequencing technology, also known as Next Generation Sequencing (NGS), there is increasing evidence supporting the role of microbial communities or microbial diversity in shaping the concept of "microbial terroir" in the wine industry. NGS has helped numerous countries and regions identify the microbial terroir of their wines and wine grapes [1-3].

The winemaking process is a complex interplay of microbial activities, with grape berries being a crucial source of microorganisms. Apart from enology applications, the study of microbial diversity also holds significant importance in plant protection. As concerns about environmental pollution and food safety rise, many traditional vineyards are transitioning to organic practices. In this context, research has shown that grape surfaces harbor numerous microorganisms that can be harnessed for local antagonism, providing an environmentally friendly alternative to pesticides and mitigating food safety concerns arising from pesticide residues [4-5].

Based on research conducted over the past two decades, this work highlights the importance of studying microbial diversity on grape surfaces, the advancements in research technology, and the microbial terroirs of various countries. Furthermore, a bibliometric analysis of 453 papers from Web of Science was conducted to analyze the current status and prospects of research on microbial diversity on grape surfaces.

2. Microbes on the grape surface

The surface of grape berries constitutes a complex microbial habitat, inhabited by epiphytic microorganisms such as bacteria, yeast, and filamentous fungi [6-8]. These microorganisms play a crucial role in crop health and can also interfere with the winemaking process, potentially exerting a significant impact on wine quality [9].

2.1. The role of microbes on grape surface

Numerous microorganisms are involved in the winemaking process, with *Saccharomyces cerevisiae* being the main organism responsible for converting grape juice into wine. However, native yeasts have been found to play a crucial role in shaping the chemical

and organoleptic properties of wine. Non-*Saccharomyces* yeasts, in particular, are known to produce more complex aromas through their metabolic activities, this conclusion already confirmed by lots of researches, which are listed in Table 1. The ecology of natural yeast flora is therefore an important factor that can significantly impact wine quality [10].

Table 1

The main influence of non-saccharomyces on sensory characteristics

Non-*saccharomyces*	Metabolite	Sensory characteristics	Reference
Hanseniaspora/Kloeckera	2-Phenylethyl acetate, Mannas	Floral rose petals hints, mannoproteins	[11-12]
Hanseniaspora vineae	Benzyl acetate	Floral jasmine aroma	[13]
Lachancea thermotolerans	2-Phenylethyl acetate, Ethyl lactate, Lactic acid	Floral, rose petals hints, strawberry, toffee, Citric acidity	[14]
Metschinikowia pulcherrima	2-Phenylethanol, Monoterpens	Rose-like odour, Floral	[15]
Pichia kuyveri	Mercapthohexanol, Mercaptohexyl acetate	Grapefruit, passion fruit,	[16]
Schizosaccharomyves pombe	Mannoproteins	Softening astringency	[17]
Torulaspora delbrueckii	3-Phenylethyl acetate, Ehyl hexanoate, 3-Ethoxy-1-propanol	Flower, honey, apple, black currant, solvent	[18]
Wickerhamomyces anomalus	2-phenylethyl acetate, Isoamyl acetate, Ethyl acetate	Flower, honey, banana, fruity	[19]

The ascomycete *Botrytis cinerea*, *Aspergillus carbonarius*, and *Penicillum expansum* are considered the most destructive fungi in viticulture [20]. The traditional approach to combat them is the use of fungicides. However, repeated use of fungicides can lead to resistance in *Ascomycetes*, negatively impact the natural microbial community, and result in chemical residues on grape berries and vineyards [21]. Furthermore, due to increasing concerns over food security and environmental protection, the European Union has imposed strict restrictions on the use of fungicides [22].

As an effective alternative to fungicides, biological control agents (BCA) act on pathogenic agents through three pathways: (i) competition for space and nutrients, (ii) production of bioactive molecules, and (iii) induction of defense-related responses in grapevines [23]. Yeasts of the genera *Metschnikowia*, *Pichia*, or *Candida*, which are commonly used as BCAs in viticulture, are part of the natural microbiome of grape berries [20]. Table 2 lists the known grape pathogenic microorganisms and their BCA.Therefore, understanding

the structural and functional diversity of microbial communities on grape berry skins is crucial for the development of native antagonists.

Table 2

The pathogenic microbe and biological control agents

Pathogenic microbe	Grape disease	Biological control agent	Reference
Botrytis cinerea	Gray mold	*Bacillus sp. C. membranifasciens, M. guilliermondii, Ralstonia sp, Issatchenkia terricola, Aureobasidium pullulans, Metschnikowia pulcherrima, Pichia guilliermondii*	[24]
Penicillium expansum	Blue mold	*Rahnella aquatillis, Cryptococcus laurentti, M. pulcherrima*	[24]
Aspergillus niger	Asperigillus rot, ochratoxin	*Issatchenkia orientalis, M.pulcherrima, Issatchenkia terricola, C. incommunis.*	[25]
Aspergillus carbonarius	Black mold	*Aureobasidium pullulans, Metschnikowia pulcherrima, Kluyveromyces thermotolerans, Issatchenkua orientalis, Candida sake*	[26]

2.2 The factors impact on grape microbial diversity

Grape microbial diversity can be influenced by various factors, including human-related factors and natural factors. Among human-related factors, vineyard management, particularly fungicide usage, has been frequently reported. In recent years, there has been a growing interest in organic and biodynamic vineyard management in viticulture, and this trend is also reflected in studies on grape microbial diversity. A research carried out between conventional and biodynamic vineyards revealed that farming practices shape the fungal community influencing wine traits linking the wine with the viti-vinicultural area of origin [27]. Besides, the microorganism of grape from organic vineyard had advantages in fermentation speed and wine sensory quality [28].

The active ingredients and application modalities of fungicides, such as contact, superficial or systemic, can influence the structure of yeast communities on grape berry surfaces [29]. In a long-term study on fungicide use in vineyards, it was observed that yeasts other than *Metschnikowia pulcherrima* had higher tolerance to sulfur compared to penconazole, suggesting that sulfur-based fungicides had little effect on yeast community structure. As sulfur-based fungicides are permitted in organic vineyards, low doses of sulfur-based fungicides could be used as a strategy for organic vineyard management. Barba [21] reported that sulfur-based fungicides had no negative effects on yeast, while copper-based

fungicides significantly inhibited the growth of *Saccharomyces cerevisiae*. However, studies by Massieux et al. [30] Hengst et al. [31], and Merrington et al. [32] suggested that copper-based fungicides could impact microbial structure.

Furthermore, a study by Neza Cadez [33] found that fungicides containing active ingredients such as iprodione, pyrimethanil, and fludioxonil plus cyprodinil had effects only on specific microbial species, and that their impact on the microbiome was minimal after a safety interval, even if the microbiome changed during application. In the same study, researcher figured out that a fungicide containing pyrimethanil suppressed the growth of all basidiomycetous yeast species, while the sporadically occurring fermentative yeasts were unaffected.

Rocio Escribano-Viana [34] found that the use of bio-fungicides has no significant effect on the structure of microbial communities. Similarly, a study utilizing NGS sequencing methods also reported no discernible differences in the microbial community composition on grape surfaces among organic, conventional, and biodynamic vineyards, with the cultivation mode only influencing certain microbial abundances [35].

As a result, the management of vineyards and viticultural practices that regulate the presence or absence of microorganisms are considered crucial for sustainable grape production in the region. Climatic factors, such as temperature, ultraviolet light, and rainfall, can impact the number and diversity of microorganisms, but understanding the specific effects of these factors on the microbial community is challenging due to the complexity of the interactions [36-37]. For instance, previous studies have reported conflicting findings, with some suggesting that higher rainfall leads to higher microorganism populations, while others propose the opposite [38].

Most of the research in this field has primarily focused on bacteria of oenological interest, such as acetic acid bacteria (AAB) and lactic acid bacteria (LAB), which are commonly found on grape berries [39-40]. However, these studies were limited by the methodologies available at the time. The advent of high-throughput sequencing methods has significantly advanced the understanding of other bacteria in the grapevine microbiota.

It is evident that the influence of climate on microorganisms is multifaceted and not yet fully elucidated. Multiple studies have shown that the microbial community is influenced by various factors, including variety, vintage, and geography [41-43]. Unlike human factors, natural factors' impact on the microbial community has received less attention, with researchers typically conducting statistical analyses on the microbial community grouped by different natural factors that are concluded to be statistically significant.

In Dimitrois' study [44], location was found to have a more significant impact on yeast populations than grape variety and stage of ripening. Currently, most studies only report the composition of grape microbial diversity in specific production areas, which is commonly referred to as the concept of "microbial terroir" [45-46].

2.3 Microbial terroir

The International Organisation of Vine and Wine (OIV) defines "Terroir" as an area where the collective knowledge of interactions between human and natural factors shape the unique characteristics of the wine produced [47]. However, earlier research on terroir has often overlooked the role of microbes in this complex interplay of factors.

Microbes play a crucial role in crop nutrient availability, influencing biogeochemical cycles, rhizosphere-root interactions, and plant growth and health. Recent advancements in

high-throughput sequencing technology have provided deeper insights into the complex bacterial and fungal community structures associated with soil, rhizosphere, plant phyllosphere, and fruit surface. In the past decade, there has been extensive scientific research on the microbial composition of vineyards, revealing evidence of regional microbial communities that contribute to the characterization and typicity of regional wines [48].

The concept of 'microbial terroir', including 'yeast terroir', has been proposed to describe the link between microbial biogeography and regional wine characteristics [49]. This has significantly advanced our understanding of the factors that influence the microbial structure and diversity of vineyards within the context of terroir, which encompasses both natural and human factors. However, despite progress, there is still limited scientific evidence on the "potential microbial influence" on wine composition within the terroir concept, and many questions remain unresolved. These include the functional characteristics of microbial communities and their impact on plant physiology and grape composition, the role of vineyard microbiota origin and interannual stability, and their influence on wine sensory attributes [50-51]. Further research is needed to fully comprehend the complex interplay between microbes, terroir, and wine production.

3. The grape microbial diversity research

3.1 Identification method

Since the discovery of microorganisms in grape must by Louis Pasteur in the 19th century, conventional microbiological methods such as biochemical characterization, cultivation on agar media, and microscopic observation have been used to study microbial diversity associated with grapes. However, these traditional methods have limitations as they cannot provide species-level identification and may result in incorrect identification [52].

With the advent of polymerase chain reaction (PCR) technique, various PCR-based techniques such as PCR-Fingerprint, Droplet Digital PCR (ddPCR), PCR-denaturing gradient gel electrophoresis (PCR-DGGE), PCR-Restriction Fragment Length Polymorphism, and others have been employed for grape microbial diversity research. The bacterial small subunit ribosomal RNA gene (16S rRNA) and fungal ITS1-5.8S rRNA-ITS2 gene have been recognized as the gold standard for estimating phylogenetic diversity in microbial communities. Among the PCR-based techniques, RFLP and DGGE are commonly used methods [53, 54], their advantages and disadvantages are listed in Table 3.

PCR-RFLP is unable to provide population-level results, but direct PCR-RFLP analysis, which involves sampling random colonies on agar plates, can provide an idea of the proportion of different species. Although RFLP is often considered a culture-independent method, it is combined with culture methods in almost all researches related to grape microbial diversity [55].

On the other hand, DGGE is a culture-independent method that utilizes the different melting behaviors of DNA in different concentrations of denaturants to separate DNA fragments with the same size but different base composition, thereby allowing for the analysis of complex mixed microorganisms in grape samples. However, in practice, most studies on grape microbial diversity still combine culture methods with RFLP [56].

As a result, over the past three decades, molecular techniques targeting rRNA genes have been used in conjunction with culture-dependent methods to identify microorganisms after isolation and growth in pure cultures. Traditional culture-based methods have led to the isolation and identification of around 50 bacterial species and 70 genera of filamentous fungi.

PCR-DGGE is often considered suitable for less species-rich environments such as grape must, but it has low sensitivity and may not detect populations present at a relative abundance of less than 1% of the population, as reported by Andorrà et al. in 2010 [57].

Table 3

The advantage and disadvantage of main PCR based method

	Advantage	Disadvantage
PCR-DGGE	Culture-independent, directly applied to samples.	Low sensitive, only intense and well-seperated bands can be sequenced
PCR-RFLP	Easily to applied to large number of samples	Difficult to use for complex communities

The advent of high-throughput, short-amplicon sequencing has revolutionized our ability to study microbial diversity within and across complex biomes. This cutting-edge technology, also known as next-generation sequencing (NGS), allows for the direct measurement and sequencing of PCR products from genes in specific regions, resulting in millions or even hundreds of millions of gene sequences. Some of the commonly used high-throughput sequencing platforms include 454 Life Sciences, ABI, Illumina, Pacific Biosciences' single-molecule sequencing technology, and Helicos Heliscope [58].

Compared to traditional sequencing methods, high-throughput sequencing is cost-effective and efficient, as it uses chip sequencing to simultaneously read and sequence millions of data points. These sequencing platforms generate massive amounts of data, with the HiSeq2000 sequencer from Solexa Technology, for example, capable of producing over 300G of data within just two weeks, equivalent to sequencing the human genome 100 times over [59].

Although high-throughput sequencing is a relatively new technology in grape microbial diversity research, emerging within the past decade, it has revealed a greater diversity than previously reported, even identifying several species that were previously unknown [60]. This method has made it possible to describe the microbial terroir, or the unique microbial community associated with the specific environmental conditions, on the surface of grapes [9]. Microbial terroir has been identified in various grape-growing regions around the world as Table 4 shows, shedding new light on the complex interactions between grapes and their surrounding microbial communities.

Table 4

The microbial terroir identified by NGS in the world

Country	Main genus identified	Reference
Spain	*Aureobasidium, Metschnikowia, lachancea, Candida, Pichia, Zygoascus, Hanseniaspora, Debaromyces, Cryptococcus, Rhodotorula, Sporobolomyces*	[61]
USA	*Alternaria, Aspergillus, Cladosporium, Coniothryium, Epicoccum, Filobasidium, Lewia, Lophiostoma, Metschnikowia, Stemphylium, Ulocladium, Wickerhamomyce*	[62]

Continuation Table 4

Australia	*Alternaria, Aureobasidium, Botrytis, Candida, Cladosporium, Cystofilobasidium, Didymosphaeria, Epicoccum, Hanseniaspora, Kazachstania, Lophiostoma, Metschnikowia, Pichia, Rhynchogastrema, Saccharomyces, Saccharomycopsis, Seimatosporium, Torulaspora*	[63]
Italy	*Mycosphaerella, Sporobolomyves, Articulospora, Pyrenophora, Cadophora, Coprinellus, Phodosporidiobolus, Fusarium, Sphaeropsis, Coprinopsis, Sporisorium, Crepidotus, Saccharomyves*	[64]
Portugal	*Zygoascus, Metschnikowia, Vishniacozyma, Mycosphaerella, Filobasidium, Botrytis, Stemphylium, Cladosporium, Altemaria, Aureobasidium, Sporobolomyces, Rhodotorula, Hanseniaspora, Pichia*	[65]
Slovakia	*Aspergillaceae, Hanseniaspora, Kazachstania, Lachancea, Metschnikowia, Pichia, Pleosporineae, Saccharomyves, Saccotheciaceae, Starmerella*	[66]
China	*Massilia, Pantoea, Pseudomonas, Halomonas, Corynebacterium, Bacillus, Anaerococcus, Acinetobacterm Brevundimonas, Peptoniphilus, Paracoccus, Sphingomonas, Ginegoldia, Bifidobacterium, Staphylococcus*	[67]

4. The current research status

A bibliometric analysis was conducted to explore the current research status of microbial diversity in grape berries. The search was performed using the following keywords: "((grape* OR wine*) AND (microb* OR bacter* OR fung* OR microorg* OR yeast) AND (berry* OR skin* OR surface*) AND (diversity* OR community* OR abundance* OR richness* OR eco*))" on Web of Science, resulting in 1,875 records. From these records, 453 papers published within the past five years (2021-2023) were selected for further analysis.

The bibliometric analysis involved identifying high-frequency keywords (mentioned more than 30 times) using VOS viewer, and the co-occurrence of these keywords was examined. Figure 1 presents the relationship between the 27 high-frequency keywords obtained from the analysis, as shown in the co-occurrence network. This analysis provides insights into the key research areas and trends in the study of microbial diversity in grape berries, highlighting the interconnectedness of various concepts in this field.

The co-occurance network is divided in to 3 clusters, the details are shown in Table 5. Cluster 1 (in red color) consists of 12 keywords, this group of key words relates to various aspects of microbial communities and their role in wine fermentation.

S. cerevisiae is usually considered the most important microorganism, which converts sugar into alcohol. Many commercial strains of the *S. cerevisiae* species are used around the world in the wine industry, while the use of native yeast strains is highly recommended for their role in shaping specific, terroir-associated wine characteristics [68-69].

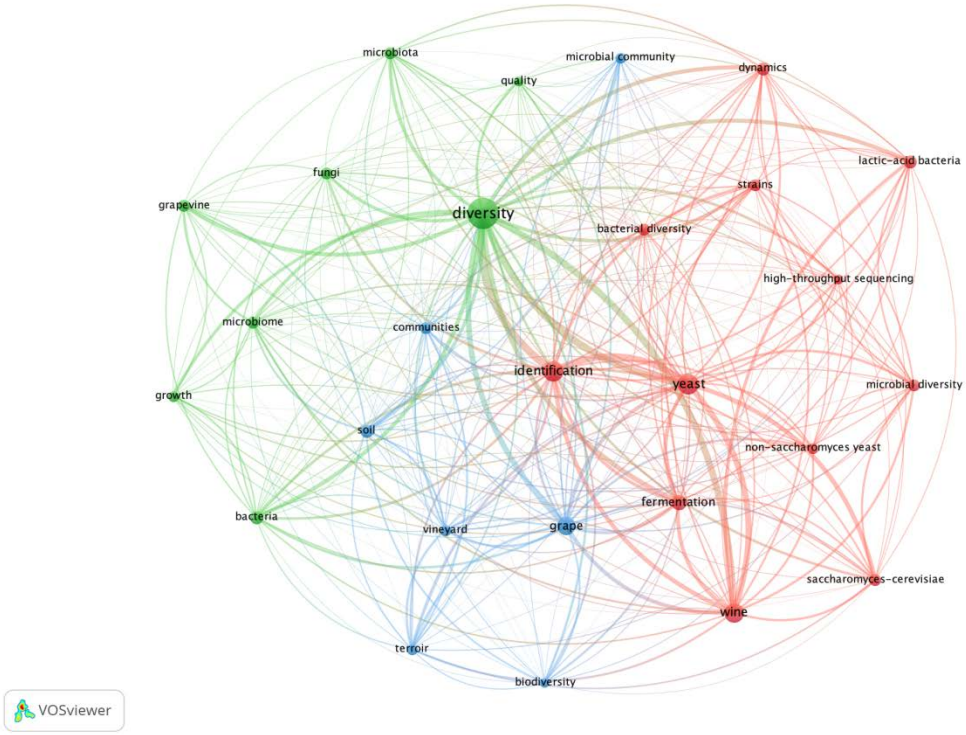

Figure 1. The bibliometric analysis.

Co-fermentation by non-*Saccharomyces* yeasts with S. *cerevisiae* has been widely used to improving sensory properties of wine [70-71]. Recently, researchers noticed that their effect on the biogenic amines (BAs) and Glutathione (GSH). BAs widely exist in the wine, which are often linked with off-odor, and they are harmful to health of human. The combination of two non-*Saccharomyces yeast* : *S. pombe* and *L. thermotolerans* can significantly reduce BAs levels in wine [72]. GSH is a non-protein thiol which has a strong antioxidant activity to reduce the SO_2 usage in the winemaking. It present in grape berries and produced by yeasts during fermentation [73]. These new discoveries about *non-Sacchromyces* yeast could provide new strategies for improving the quality of wine. Except *S. cerevisia*e, LAB also has a fundamental role in determining the quality chemical and aromatic properties of wine, especially red wine. Its by-products have important enzymatic activities that can release volatile aromatic compounds during malolactic fermentation [74], winemakers have attempted to replace commercially *O.oeni* with autochthonous LAB to obtain wines with more terroir and improve the wine quality[75-76]. In addition, searching for bacteria to use as BCA has become a research focus [77].

It can be observed the high-throughput sequencing is still the most frequency identification method for grape microbial diversity. There is another high frequency key word "dynamics", the current dynamics of microbial diversity are not limited to grape ripening [78], but also include microbial diversity dynamic during winemaking [79].

Cluster 2 (in green color) consists of 8 keywords, most of which are similar to the Cluster 1, however, "grapevine" and "growth" are totally different. Under these key words, more on topic of plant protection and disease control. Grapevine offers different habitats for microorganisms, such as: roots, leaves, fruits, each of which is unique [80]. As it mentioned previously, researchers are funding the plant growth-promoting bacteria (PGPB) as new agroecological management [81]. It has been proven that PGPB are an excellent option to

prevent grey mould, and specific composition and functions of the rhizosphere microbial community contribute to the enhanced tolerance of some grapevines to salt stress [82].

Table 5

The clusters of key words

Cluster number	Key words number	Key words
Cluster1	12	Bacteria diversity, dynamics, fermentation, high-throughput sequencing, identification, lactic-acid bacteria, microbial diversity, non-saccharomyces yeast, saccharomyces-cerevisae, strains, wine, yeast
Cluster2	8	Bacteria, diversity, fungi, grapevine, growth, microbiome, microbiota, quality
Cluster3	7	Biodiversity, communities, grape, mirobial community, soil, terroir, vineyard

Cluster 3 (in blue color) consists of 7 words, in which, “terroir’ is more attractive. The concept of terroir was discussed previously, however, the biodiversity of vineyard is an important composition of terroir [83]. Under this topics, researchers are intersted in promoting cultivation and fermentation management strategies, advocate natural terroir attributes for grapes and wines [84-85].

5. Conclusions

The concept of "microbial terroir" refers to the unique microbial communities that are present on the surface of grape berries, and this concept has gained significant attention in recent years. The application of Next Generation Sequencing (NGS) in studying microbial terroir has provided valuable insights into the complex interactions between microbes and grapevines, with implications for both oenology and plant protection.

One of the key applications of microbial terroir is in exploring local wine styles. By studying the microbial communities on grape surfaces in different regions, researchers can gain a deeper understanding of how local environmental factors, such as soil type, climate, and vineyard management practices, influence the composition and activity of the microbial populations. This knowledge can provide a theoretical basis for developing unique wine styles that are characteristic of specific regions, known as "terroir wines". For example, certain microbial species may contribute to the production of specific aroma compounds or metabolites that are responsible for the unique sensory characteristics of wines from certain regions. This understanding of microbial terroir can help winemakers in their decision-making processes, such as grape selection, fermentation techniques, and aging practices, to enhance the quality and distinctiveness of their wines.

In addition to its significance in oenology, microbial terroir also has implications in the domain of plant protection. Understanding the diversity and dynamics of microbial communities on grape surfaces can provide valuable insights into the natural defense mechanisms of grapevines against pathogens. Some microbial species found on grape surfaces have been shown to possess biocontrol properties, inhibiting the growth of pathogenic microorganisms and reducing the need for chemical interventions. Therefore, studying microbial terroir can help in the development of safer and more environmentally friendly management strategies for grapevine diseases and pests. For instance, the

identification of specific beneficial microorganisms from local microbial terroir can lead to the development of biocontrol agents that can be used as alternatives to chemical pesticides, reducing the environmental impact and promoting sustainable grape production practices.

Despite the significant progress made in studying microbial terroir using NGS, our knowledge of grape-associated bacteria is still limited. There is a vast diversity of microbial species that inhabit the grape surface, and many of them may have important roles in grapevine health and wine production. Further research utilizing advanced NGS technologies and bioinformatics tools can help uncover the complex interactions and dynamics of microbial communities on grape berries, leading to a deeper understanding of microbial terroir and its applications in oenology and plant protection.

In summary, the analysis of the co-occurrence network reveals three clusters: Cluster 1 focuses on the role of mircoorganisms in wine fermentation, selection autochthonous *S. cerevisiae* , non-*Saccharomyces* and LAB are the trend. Cluster 2 explores plant protection and disease control in grapevines, including the use of plant growth-promoting bacteria. Cluster 3 emphasizes the importance of terroir and vineyard biodiversity in wine production. These findings provide insights into improving wine quality, sustainability, and understanding the complex interactions in grape microbial communities.

Acknowledgments: The author is supported by China Scholarship Council, and the author would like to thank dr. hab. Arpentin Gheorghe for reviewing the paper.

Conflicts of Interest: The author declares no conflict of interest.

References

1. Kazou, M.; Pagiati, L.; Dotsika, E.; Proxenia, N.; Kotseridis, Y.; & Tsakalidou, E. The Microbial Terroir of the Nemea Zone Agiorgitiko cv.: A First Metataxonomic Approach. *Aust. J. Grape Wine Res.* 2023, ID 8791362.
2. Shimizu, H.; Kamada, A.; Koyama, K.; Iwashita, K.; Goto-Yamamoto, N. Yeast diversity during the spontaneous fermentation of wine with only the microbiota on grapes cultivated in Japan. *J. Biosci. Bioeng.* 2023, pp. 35-43.
3. Zambianchi, S.; Patrone, V.; Becchi, P. P.; Callegari, M. L.; Stagnati, L.; Lucini, L.; Busconi, M. Metagenomic bacterial diversity and metabolomics profiling of Buttafuoco wine production. *Food Control*. 2023, 148, 109657.
4. Esteves, M.; Lage, P.; Sousa, J.; Centeno, F.; de Fátima Teixeira, M.; Tenreiro, R.; Mendes-Ferreira, A. Biocontrol potential of wine yeasts against four grape phytopathogenic fungi disclosed by time-course monitoring of inhibitory activities. *Front. Microbiol*. 2022, 14, 1146065.
5. Ayogu, P.; Teixeira, A.; Gerós, H.; Martins, V. Identification of grape berry indigenous epiphytic yeasts with in vitro and in vivo antagonistic activity towards pathogenic fungi. *OENO One* 2023, 57(1), pp. 253-264.
6. Costantini, A.; Vaudano, E.; Pulcini, L.; Boatti, L.; Gamalero, E.; Garcia-Moruno, E. Yeast biodiversity in vineyard during grape ripening: comparison between culture dependent and NGS analysis. *Processes* 2022, 10(5), 901.
7. Lorenzini, M.; & Zapparoli, G. Epiphytic bacteria from withered grapes and their antagonistic effects on grape-rotting fungi. *Int. J. Food Microbiol.* 2020, 319, 108505.
8. Martiniuk, J. T.; Hamilton, J.; Dodsworth, T.; Measday, V. Grape-associated fungal community patterns persist from berry to wine on a fine geographical scale. *FEMS Yeast Res.* 2023, 23.
9. Liu, D.; Zhang, P.; Chen, D.; & Howell, K. From the vineyard to the winery: how microbial ecology drives regional distinctiveness of wine. *Front. Microbiol.* 2019, 10, 2679.
10. Carrau, F.; Boido, E.; & Ramey, D. Yeasts for low input winemaking: microbial terroir and flavor differentiation. *Adv. Appl. Microbiol.* 2020 ,111, pp. 89-121.
11. Giorello, F.; Valera, M.J.; Martin, V.; Parada, A.; Salzman, V.; Camesasca, L.; Fariña, L.;Boido, E.;Medina, K.; Dellacassa, E.; Berna, L. Genomic and transcriptomic basis of Hanseniaspora vineae's impact on flavor diversity and wine quality. *Appl. Environ. Microbiol.* 2019, 85(1), e01959-18.
12. Testa, B.; Coppola, F.; Lombardi, S. J.; Iorizzo, M.; Letizia, F.; Di Renzo, M.; Tremonte, P. Influence of Hanseniaspora uvarum AS27 on chemical and sensorial characteristics of aglianico wine. *Processes* 2021, 9(2), 326.

13. Del Fresno, J. M.; Escott, C.; Loira, I.; Herbert-Pucheta, J. E.; Schneider, R.; Carrau, F.; Morata, A. Impact of Hanseniaspora vineae in alcoholic fermentation and ageing on lees of high-quality white wine. *Fermentation* 2020, 6(3), 66.
14. Morata, A.; Bañuelos, M.A.; Vaquero, C.; Loira, I.; Cuerda, R.; Palomero, F.; González, C.; Suárez-Lepe, J.A.; Wang, J.; Han, S.; Bi, Y. Lachancea thermotolerans as a tool to improve pH in red wines from warm regions. *Eur. Food Res. Technol.* 2019, 245, pp. 885-894.
15. Varela, C.; Bartel, C.; Espinase Nandorfy, D.; Bilogrevic, E.; Tran, T.; Heinrich, A.; Borneman, A. Volatile aroma composition and sensory profile of Shiraz and Cabernet Sauvignon wines produced with novel Metschnikowia pulcherrima yeast starter cultures. *Aust. J. Grape Wine Res.* 2021, 27(3), pp. 406-418.
16. Paup, V. D.; Aplin, J. J.; Potter, R. I.; Edwards, C. G.; Lee, J.; Ross, C. F. Sensory properties of 6-and 18-month-stored wines made with pectinase-producing non-Saccharomyces yeasts. *J. Food Sci.* 2023, 88(1), pp.462-476.
17. Wang, Y.; Sheng, W.; Li, M.; Mi, L.; Jiang, Y.; Wang, J. (2019). Effect of sequential fermentation with Lachancea thermotolerans and Schizosaccharomyces pombe on the quality of Merlot dry red wine. *Shipin Kexue/Food Science* 2019, 40(8), pp. 102-111.
18. Zhang, B.; Liu, H.; Xue, J.; Tang, C.; Duan, C.; Yan, G. Use of Torulaspora delbrueckii and Hanseniaspora vineae co-fermentation with Saccharomyces cerevisiae to improve aroma profiles and safety quality of Petit Manseng wines. *LWT* 2022, 161, 113360.
19. Lee, S. B.; & Park, H. D. Isolation and investigation of potential non-Saccharomyces yeasts to improve the volatile terpene compounds in Korean Muscat Bailey A wine. *Microorganisms*. 2020, 8(10), 1552.
20. Di Canito, A.; Mateo-Vargas, M. A.; Mazzieri, M.; Cantoral, J.; Foschino, R.; Cordero-Bueso, G.; Vigentini, I. The role of yeasts as biocontrol agents for pathogenic fungi on postharvest grapes: A review. *Foods* 2021, 10(7),. 1650.
21. Gava, A.; Emer, C. D.; Ficagna, E.; Fernandes de Andrade, S.; Fuentefria, A. M. Occurrence and impact of fungicides residues on fermentation during wine production–A review. *Food Addit. Contam. Part A Chem. Anal Control Expo Risk Assess.* 2021, 38(6), pp. 943-961.
22. Costantini, E.; La Torre, A. Regulatory framework in the European Union governing the use of basic substances in conventional and organic production. *J. Plant Di.s Prot.*2022,129(4), pp.715–743.
23. Carmona-Hernandez, S.; Reyes-Pérez, J. J.; Chiquito-Contreras, R. G.; Rincon-Enriquez, G.; Cerdan-Cabrera, C. R.; & Hernandez-Montiel, L. G. Biocontrol of postharvest fruit fungal diseases by bacterial antagonists: a review. *Agronomy*. 2019, 9(3), 121.
24. Zhang, H.; Godana, E.A.; Sui, Y.; Yang, Q.; Zhang, X.; Zhao, L. Biological control as an alternative to synthetic fungicides for the management of grey and blue mould diseases of table grapes: a review. *Crit. Rev. Microbiol.* 2020, 46(4), pp.450-462.
25. Li, Q.; Li, C.; Li, P.; Zhang, H.; Zhang, X.; Zheng, X.; Yang, Q.; Apaliya, M.T.; Boateng, N.A.S.; Sun, Y. The biocontrol effect of Sporidiobolus pararoseus Y16 against postharvest diseases in table grapes caused by Aspergillus niger and the possible mechanisms involved. *Biol. Control*. 2017, 113, pp.18-25.
26. Senthil, R.; Prabakar, K.; Rajendran, L.; Karthikeyan, G.Efficacy of different biological control agents against major postharvest pathogens of grapes under room temperature storage conditions. *Phytopathol. Mediterr.* 2011, 50(1), pp.55-65.
27. Perpetuini, G.; Rossetti, A. P.; Battistelli, N.; Zulli, C.; Cichelli, A.; Arfelli, G.; Tofalo, R.Impact of vineyard management on grape fungal community and Montepulciano d'Abruzzo wine quality. *Food Research Intl.* 2022, 158, pp. 111577.
28. Xu, W.; Liu, B.; Wang, C.; Kong, X. Organic cultivation of grape affects yeast succession and wine sensory quality during spontaneous fermentation. *LWT*. 2020, 120, 108894
29. Milanović, V.; Comitini, F.; Ciani, M. Grape berry yeast communities: influence of fungicide treatments. *Int. J. Food Microbiol.* 2013, 161(3), pp.240-246.
30. Massieux, B.P.J.C.; Boivin, M.E.Y.; Van Den Ende, F.P.; Langenskiold, J.; Marvan, P.; Barranguet, C.; Admiraal, W.; Laanbroek, H.J.; Zwart, G. Analysis of structural and physiological profiles to assess the effects of Cu on biofilm microbial communities. *Appl. Environ. Microbiol.* 2004, 70(8), pp.4512-4521.
31. Hengst, M.B.; Andrade, S.; González, B.; Correa, J.A. Changes in epiphytic bacterial communities of intertidal seaweeds modulated by host, temporality, and copper enrichment. *Microb. Ecol.* 2010, 60, pp.282-290.
32. Merrington, G.; Rogers, S.L.; Van Zwieten, L. The potential impact of long-term copper fungicide usage on soil microbial biomass and microbial activity in an avocado orchard. *Soil Res.* 2002, 40(5), pp.749-759.
33. Čadež, N.; Zupan, J.; Raspor, P. The effect of fungicides on yeast communities associated with grape berries 2010. *FEMS Yeast Res.* 2010, 10(5), pp.619-630.

34. Escribano-Viana, R.; López-Alfaro, I.; López, R.; Santamaría, P.; Gutiérrez, A.R.; González-Arenzana, L. Impact of chemical and biological fungicides applied to grapevine on grape biofilm, must, and wine microbial diversity. *Front. Microbiol*. 2018, 9, pp.59.
35. Kecskeméti, E.; Berkelmann-Löhnertz, B.; Reineke, A.Are epiphytic microbial communities in the carposphere of ripening grape clusters (Vitis vinifera L.) different between conventional, organic, and biodynamic grapes? *PloS one.* 2016, 11(8), e0160852.
36. Rivas, G. A.; Guillade, A. C.; Semorile, L. C.; Delfederico, L. Influence of climate on soil and wine bacterial diversity on a vineyard in a non-traditional wine region in Argentina. *Front. Microbio* .2021, 12, pp. 726384.
37. Liu, D.; Howell, K. Community succession of the grapevine fungal microbiome in the annual growth cycle. *Environ. Microbiol.* 2021, 23(4), pp. 1842-1857.
38. Barata, A.; Malfeito-Ferreira, M.; Loureiro, V. The microbial ecology of wine grape berries. *Int. J. Food Microbiol*. 2012, 153(3), pp. 243-259.
39. Jiang, L.; Shi, X. Isolation and identification of acetic acid bacteria and optimization of acid-producing conditions from grape skins of Xinjiang wine grape. *China Condiment* 2019, 44(4), pp. 75-79.
40. Franco, W.; Benavides, S.; Valencia, P.; Ramírez, C.; Urtubia, A. Native yeasts and lactic acid bacteria isolated from spontaneous fermentation of seven grape cultivars from the maule region (Chile). *Foods* 2021, 10(8), 1737.
41. Bao, L.; Sun, B.; Wei, Y.; Xu, N.; Zhang, S.; Gu, L.; Bai, Z. Grape cultivar features differentiate the grape rhizosphere microbiota. *Plants* 2022,11(9), 1111.
42. Oyuela Aguilar, M.; Gobbi, A.; Browne, P. D.; Ellegaard-Jensen, L.; Hansen, L. H.; Semorile, L.; Pistorio, M. Influence of vintage, geographic location and cultivar on the structure of microbial communities associated with the grapevine rhizosphere in vineyards of San Juan Province, Argentina. *PLoS One* 2020, 15(12), e0243848.
43. Castrillo, D.; Blanco, P. Influence of vintage, geographical location and agricultural management on yeast populations in Galician grape musts (NW Spain). *OENO One* 2022, 56(4), pp. 65-79.
44. Kioroglou, D.; Kraeva-Deloire, E.; Schmidtke, L.M.; Mas, A.; Portillo, M.C. Geographical origin has a greater impact on grape berry fungal community than grape variety and maturation state. *Microorganisms* 2019, 7(12), 669.
45. Mas, A.; Portillo, M. C. Strategies for microbiological control of the alcoholic fermentation in wines by exploiting the microbial terroir complexity: A mini-review. *Int J Food Microbiol.* 2022, 109592.
46. Gao, F.; Chen, J.; Xiao, J.; Cheng, W.; Zheng, X.; Wang, B.; Shi, X. Microbial community composition on grape surface controlled by geographical factors of different wine regions in Xinjiang, China. *Food research intl.* 2019, 122, pp. 348-360.
47. Van Leeuwen, C. Terroir: The effect of the physical environment on vine growth, grape ripening, and wine sensory attributes. In: *Managing Wine Quality (Second Edition),* 2022.
48. Gilbert, J.A.; van der Lelie, D.; Zarraonaindia, I. Microbial terroir for wine grapes. *Proc. Natl. Acad. Sci. U.S.A.* 2014, 111(1), pp. 5-6.
49. Chalvantzi, I.; Banilas, G.; Tassou, C.; Nisiotou, A.Biogeographical regionalization of wine yeast communities in Greece and environmental drivers of species distribution at a local scale. *Front. Microbiol.* 2021, 12, 705001.
50. Sare, A. R.; Jijakli, M. H.; & Massart, S. Microbial ecology to support integrative efficacy improvement of biocontrol agents for postharvest diseases management. *Postharvest Biol. Technol.* 2021, 179, 111572.
51. Romano, P.; Giacomo B.; Gabriella S.; Francesca P.; Rosalba L. Role of yeasts on the sensory component of wines. *Foods* 2022, 13, 1921.
52. Awad, M.; Giannopoulos, G.; Mylona, P. V.; Polidoros, A. N. Comparative Analysis of Grapevine Epiphytic Microbiomes among Different Varieties, Tissues, and Developmental Stages in the Same Terroir. *Appl. Sci.* 2023, 13(1), 102.
53. Ye, Q.; Zhang, W.; Jia, J.; Li, X.; Zhou, Y.; Han, C.; Wu, X.; Yan, J. Fungal pathogens associated with black foot of grapevine in China. *Phytopathol. Mediterr.* 2021, 60(2), pp. 303-312.
54. Rivas, G. A.; Valdes La Hens, D.; Delfederico, L.; Olguin, N.; Bravo-Ferrada, B. M.; Tymczyszyn, E. E.; Brizuela, N. S. Molecular tools for the analysis of the microbiota involved in malolactic fermentation: From microbial diversity to selection of lactic acid bacteria of enological interest. *World J. Microbiol. Biotechnol.* 2022, 38(2), 19.
55. Diguta, C.F.; Vincent, B.; Guilloux-Benatier, M.; Alexandre, H.; Rousseaux, S. PCR ITS-RFLP: a useful method for identifying filamentous fungi isolates on grapes. *Food Microbiol.* 2011, 28(6), pp. 1145-1154.

56. Renouf, V.; Strehaiano, P.; Lonvaud-Funel, A. Yeast and bacteria analysis of grape, wine and cellar equipments by PCR-DGGE. *OENO One*. 2007, 41(1), pp. 51-61.
57. Andorrà, I.; Landi, S.; Mas, A.; Esteve-Zarzoso, B.; Guillamón, J.M. Effect of fermentation temperature on microbial population evolution using culture-independent and dependent techniques. *Food Res. Int.* 2010, 43(3), pp.773-779.
58. Baldrian, P.; Větrovský, T.; Lepinay, C.; Kohout, P. High-throughput sequencing view on the magnitude of global fungal diversity. *Fungal Diversity*. 2022, 114(1), pp. 539-547.
59. Nilsson, R. H.; Anslan, S.; Bahram, M.; Wurzbacher, C.; Baldrian, P.; Tedersoo, L. Mycobiome diversity: high-throughput sequencing and identification of fungi. *Na. Rev. Microbiol*. 2019, 17(2), pp. 95-109.
60. Singh, P.; Santoni, S.; This, P.; Péros, J.P. Genotype-environment interaction shapes the microbial assemblage in grapevine's phyllosphere and carposphere: an NGS approach. *Microorganisms* 2018, 6(4), 96.
61. Mezzasalma, V.; Sandionigi, A.; Guzzetti, L.; Galimberti, A.; Grando, M.S.; Tardaguila, J.; Labra, M. Geographical and cultivar features differentiate grape microbiota in Northern Italy and Spain vineyards. *Front. Microbiol*. 2018, 9, 946.
62. Wang, X.; Schlatter, D.C.; Glawe, D.A.; Edwards, C.G.; Weller, D.M.; Paulitz, T.C.; Abatzoglou, J.T.; Okubara, P.A. Native yeast and non-yeast fungal communities of Cabernet Sauvignon berries from two Washington State vineyards, and persistence in spontaneous fermentation. *Int. J. Food Microbiol*. 2021, 350, 109225.
63. Varela, C.; Cuijvers, K.; Van Den Heuvel, S.; Rullo, M.; Solomon, M.; Borneman, A.; Schmidt, S. Effect of aeration on yeast community structure and volatile composition in uninoculated chardonnay wines. *Fermentation* 2021, 7(2), 97.
64. Costantini, A.; Vaudano, E.; Pulcini, L.; Boatti, L.; Gamalero, E.; Garcia-Moruno, E.; Yeast biodiversity in vineyard during grape ripening: comparison between culture dependent and NGS analysis. *Processes* 2022, 10(5), 901.
65. Fernandes, P.; Afonso, I. M.; Pereira, J.; Rocha, R.; Rodrigues, A. S. Epiphitic Microbiome of Alvarinho Wine Grapes from Different Geographic Regions in Portugal. *Biology* 2023, 12(2), 146.
66. Böhmer, M.; Smoľak, D.; Ženišová, K.; Čaplová, Z.; Pangallo, D.; Puškárová, A.; Szemes, T. Comparison of microbial diversity during two different wine fermentation processes. *FEMS Microbiol. Lett.* 2020, 367(18), 150.
67. Zhu, F.; Li, T.; Xu, X.; Shi, X. Wang, B. Succession of fungal communities at different developmental stages of cabernet sauvignon grapes from an organic vineyard in xinjiang. *Front. Microbiol*. 2021, 12, 718261.
68. Williams, M.; Khan, W.; Ntushelo, N.; & Hart, R. An indigenous Saccharomyces cerevisiae yeast strain isolated from Paarl regional Shiraz grapes to enhance Shiraz wine typicity. *Oeno One* 2021, 55 (2), pp. 209-225
69. Karampatea, A.; Tsakiris, A.; Kourkoutas, Y.; Skavdis, G. Molecular and Phenotypic Diversity of Indigenous Oenological Strains of Saccharomyces cerevisiae Isolated in Greece. *Engineering Proceedings* 2021, 9(1), 7.
70. Zhang, B.; Tang, C.; Yang, D.; Liu, H.; Xue, J.; Duan, C.; Yan, G. Effects of three indigenous non-Saccharomyces yeasts and their pairwise combinations in co-fermentation with Saccharomyces cerevisiae on volatile compounds of Petit Manseng wines. *Food Chem* 2022, 368, 130807.
71. Lai, Y. T.; Hsieh, C. W.; Lo, Y. C.; Liou, B. K.; Lin, H. W.; Hou, C. Y.; Cheng, K. C. Isolation and identification of aroma-producing non-Saccharomyces yeast strains and the enological characteristic comparison in wine making. *LWT* 2022, 154, 112653.
72. Wang, B.; Tan, F.; Chu, R.; Li, G.; Li, L.; Yang, T.; Zhang, M. The effect of non-Saccharomyces yeasts on biogenic amines in wine. *Trends Food Sci Technol* 2021, 116, pp.1029-1040.
73. Binati, R. L.; Larini, I.; Salvetti, E.; Torriani, S. Glutathione production by non-Saccharomyces yeasts and its impact on winemaking: A review. *Food Res. Int.* 2022, 111333.
74. Capozzi, V.; Tufariello, M.; De Simone, N.; Fragasso, M.; Grieco, F. Biodiversity of oenological lactic acid bacteria: Species-and strain-dependent plus/minus effects on wine quality and safety. *Fermentation*, 2021, 7(1), 24.
75. Jin, G.; Jiranek, V.; Hayes, A. M.; Grbin, P. R. Isolation and characterization of high-ethanol-tolerance lactic acid bacteria from Australian Wine. *Foods* 2022, 11(9), 1231.
76. Virdis, C.; Sumby, K.; Bartowsky, E.; Jiranek, V. Lactic acid bacteria in wine: Technological advances and evaluation of their functional role. *Front. Microbiol*. 2021, 11, 612118.
77. Sun, D.; Qu, J.; Huang, Y.; Lu, J.; Yin, L. Analysis of microbial community diversity of muscadine grape skins. *Food Res. Int.* 2021, 145, 110417.
78. Ding, Y.; Wei, R.; Wang, L.; Yang, C.; Li, H.; Wang, H. Diversity and dynamics of microbial ecosystem on berry surface during the ripening of Ecolly (Vitis vinifera L.) grape in Wuhai, China. *World J. Microbiol. Biotechnol.* 2021, 37, pp. 1-14.

79. Wang, H. L.; Hopfer, H.; Cockburn, D. W.; Wee, J. Characterization of microbial dynamics and volatile metabolome changes during fermentation of Chambourcin hybrid grapes from two Pennsylvania regions. *Front. Microbiol*. 2021, 11, 614278.
80. Ranade, Y.; Sawant, I.; Saha, S.; Chandrashekar, M.; Pathak, P. Epiphytic microbial diversity of Vitis vinifera fructosphere: Present status and potential applications. *Curr. Microbiol*., 2021, 78, pp. 1086-1098.
81. Orozco-Mosqueda, M. D. C.; Kumar, A.; Fadiji, A. E.; Babalola, O. O.; Puopolo, G.; Santoyo, G. Agroecological management of the grey mould fungus Botrytis cinerea by plant growth-promoting bacteria. *Plants* 2023, 12 (3), 637.
82. Wang, B.; Wang, X.; Wang, Z.; Zhu, K.; Wu, W. Comparative metagenomic analysis reveals rhizosphere microbial community composition and functions help protect grapevines against salt stress. *Front. Microbiol.* 2023, 14, 1102547.
83. Nanetti, E.; Palladino, G.; Scicchitano, D.; Trapella, G.; Cinti, N.; Fabbrini, M.; Rampelli, S. Composition and biodiversity of soil and root-associated microbiome in Vitis vinifera cultivar Lambrusco distinguish the microbial terroir of the Lambrusco DOC protected designation of origin area on a local scale. *Front. Microbiol.* 2023, 14, 1108036.
84. Ding, Y.; Wei, R.; Wang, L.; Wang, W.; Wang, H.; Li, H. Exploring the ecological characteristics of natural microbial communities along the continuum from grape berries to winemaking. *Food Res. Int.* 2023, 167, 112718.
85. Hawkins, D. L.; Ryder, J.; Lee, S. A.; Parish-Virtue, K.; Fedrizzi, B.; Goddard, M. R.; Knight, S. J. Mixed yeast communities contribute to regionally distinct wine attributes. *FEMS Yeast Res.* 2023, 23, foad005.

Citation: Yao, M. Microbial diversity on grape surface and its research status. *Journal of Engineering Science* 2023, 30 (2), pp. 158-172. https://doi.org/10.52326/jes.utm.2023.30(2).14.

Submission of manuscripts: jes@meridian.utm.md

Journal of Engineering Science *Vol. XXX, no. 2 (2023), pp. 173 - 184*
Fascicle *Food Engineering* *ISSN 2587-3474*
Topic *Biotechnologies, Food Chemistry and Food Safety* *eISSN 2587-3482*

https://doi.org/10.52326/jes.utm.2023.30(2).15
UDC 665.3:[547.562.1:663.26]

THE EFFECT OF GRAPE SEED OIL FORTIFICATION WITH EXTRACTS OF NATURAL ANTIOXIDANTS

Veronica Dragancea, ORCID: 0000-0002-5938-0410,
Angela Gurev*, ORCID: 0000-0001-8493-5257,
Rodica Sturza, ORCID: 0000-0002-2412-5874,
Svetlana Haritonov, ORCID: 0000-0002-9244-8982,
Natalia Netreba, ORCID: 0000-0003-4200-1303,
Olga Boeștean, ORCID: 0000-0002-0390-3550

Technical University of Moldova, 168 Stefan cel Mare Blvd., Chisinau, Republic of Moldova
*Corresponding author: Angela Gurev, *angela.gurev@chim.utm.md*

Received: 03. 29. 2023
Accepted: 04. 28. 2023

Abstract. Grape seed oil (GSO) consists mostly of triglycerides of polyunsaturated fatty acids, which are sensitive to oxidation and to the high temperatures. The aim of this research was to study the effect of GSO fortification with hydroalcoholic extracts of antioxidants from grape seeds, up to and after 12 months. It was established that the immediate effect of the oil fortification was the increase of the total polyphenol content (TPC) in the oil, by up to 141.34 mg GAE/kg of oil, and the increase of the DPPH• antioxidant activity by up to 0.580 mmol TE/kg (in the control sample, refined grape oil, these values were 1.57 mg GAE/kg and 0.003 mmol TE/kg, respectively). After 12 months, TPC and DPPH• antioxidant activity decreased nearly 10-fold in all of the fortified oil samples. The difference between the oxidative status of the oil was assessed (UV-Vis). In the case of the GSO sample, treated with *n*-octyl gallate, the absorbances remained unchanged after 12 months. When compared to the synthetic antioxidant *n*-octyl gallate, grape seed polyphenolic extracts were found to have a less protective effect on the oil during storage under environmental conditions.

Keywords: *antioxidant activity, extract of polyphenols*, *grape seed*, *octyl gallate, oil, UV-Vis*.

Rezumat. Uleiul din semințe de struguri conține în mare parte din trigliceride ale acizilor grași polinesaturați, sensibile la oxidare și la acțiunea temperaturilor înalte. Scopul cercetărilor a fost de studia efectul fortificării uleiului cu extracte hidroalcoolice de antioxidanți din semințe de struguri. Fortificarea uleiului are ca efect imediat creșterea conținutului total de polifenoli (TPC) cu până la 141.34 mg GAE/kg de ulei și a activității antioxidante DPPH• cu până la 0.580 mmol TE/kg (în proba martor, ulei de struguri rafinat, aceste valori erau de 1.57 mg GAE/kg și 0.003 mmol TE/kg, respectiv). După 12 luni, TPC și activitatea antioxidantă DPPH• au scăzut aproape de 10 ori în toate probele de ulei fortificate. A fost observată diferența dintre starea oxidativă a uleiului (UV-Vis): în cazul probei GSO tratată cu *n*-octil galat, absorbanțele au rămas neschimbate după 12 luni. Extractul de polifenoli din semințe

de struguri are un efect protector mai redus asupra uleiului pe perioada depozitării, în condiții ambientale, comparativ cu antioxidantul sintetic *n*-octil galat.

Cuvinte cheie: *activitate antioxidantă, extract de polifenoli, octil galat, semințe de struguri, ulei, UV-Vis*.

1. Introduction

Grape seed oil is mainly composed of unsaturated fatty acids, which account for 85-90% of the total fatty acid content. Of these, linoleic acid (C18:2 *ω*-7) accounts for up to 70% [1, 2]. The glycerides composed from polyunsaturated fatty acids (PUFA) have a short shelf life as they are very sensitive to oxidation and to high temperatures [3]. Depending on the storage conditions, they can undergo oxidative degradation, hydrolysis, polymerization, etc. with the formation of unwanted products, the concentration of which increases with the period of oil storage [4]. Research shows that oil with an increased content of antioxidants, such as tocopherols, carotenes, and phenolic compounds, is more stable to oxidative processes and has a longer shelf life [5, 6].

The phenolic compounds in edible oils have several health benefits, being responsible for capturing free radicals and for antibacterial, antiviral, anti-inflammatory, antitumor, cardioprotective, neuroprotective and antidiabetic properties [7-11], nevertheless, grape seed oil contains a very low concentration of the aforementioned compounds. Maier et al. [12] determined a very low quantity of total polyphenols (TPC), of only 2.90 mg GAE/kg (which represents 0.0003%), in cold pressed grape seed oil; the content of catechins and epicatechins reached 1.30 mg/kg, and *trans*-resveratrol was of 0.30 mg/kg. Heat treatments and rigorous purification considerably reduce the content of antioxidants in the oil. At the same time, the amount of total extractable polyphenols, in the hydrophilic extracts of grape seeds, differs depending on the variety, ranging between 42.9 and 114.8 g per kilogram of dry seeds [13-15].

Grape seed oil also includes approximately 0.8-1.5% of compounds that do not undergo saponification - tocopherols and sterols (campesterol, beta-sitosterol, sigmasterol). The content of vitamin E, another important antioxidant, is between 1 and 53 mg per 100 g of oil [17]. In the grape oil extracted by the Soxhlet and Folch methods, researchers determined the following compounds: gallic acid 3.70 and 14.02 mg/kg; caffeic acid 5.20 and 8.42 mg/kg; ellagic acid 1.50 and 3.50 mg/kg, respectively, as well as chlorogenic, 4-hydroxybenzoic, 3,5-dihydroxybenzoic, protocatechuic, genistic acids, etc. [18].

Nowadays, the following synthetic antioxidants are used to stabilize vegetable oils: butylated hydroxytoluene, butylated hydroxyanisole, tertiary butylhydroquinone, *α*-tocopherol, propyl gallate, *n*-octyl gallate (OG), etc. [19]. Concurrently, some synthetic antioxidants have been banned, as their negative effect on the human body has been demonstrated [20, 21]. In the last decades, to meet the demands of the modern consumer, research is being focused on replacing synthetic antioxidants with harmless, natural additives [22], such as tocopherols, polyphenols, carotenoids, pigments, etc., which are found in plants, in agro-industrial waste and can be extracted by different methods.

It was reported that the fortification of oils with hydrophilic and lipophilic antioxidants, of plant origin, has an oxidative stabilization effect, similar to that exhibited by synthetic antioxidants. Roschel et al. [23] proved that the hydrophilic mixture of sinapic, ascorbic, and citric acids, was more effective in stabilizing oxidatively the linseed oil, compared to the lipophilic mixture of tocopherol, ascorbyl palmitate, and citric acid. The hydrophilic mixture introduced into the oil had an effect comparable to the one of tertiary

butyl hydroquinone (TBHQ), in preventing the formation of primary and secondary oxidation products. Mohanan et al. [24] had also determined the effect of natural antioxidants, of various polarity (tannic acid, tocopherol and ascorbyl palmitate), on the improvement of the linseed oil stability during long-term storage. The antioxidant protection of the ascorbyl palmitate was comparable to TBHQ, while tannic acid did not prevent lipid oxidation. Gülmez et al. [25] assessed the oxidative stability of hazelnut oil treated with natural gallic acid or *β*-carotene. In the dark, for 80 days under environmental conditions, the gallic acid increased the shelf life of the enriched oil nearly 3 times, compared to the untreated sample. Moreover, TPC increased by 77%. Manzano et al. [26] fortified soybean oil with polyphenols (0.02% and 0.04% *w/w*) extracted from *Theobroma cacao* and determined that only higher concentrations (0.04%) of phenolic compounds inhibited the generation of free fatty acids and oxidation products. Oil fortification increased 20 times the antioxidant activity against the DPPH radical (2,2-diphenyl-1-picrylhydrazyl), after frying.

Other authors have observed that the antioxidant activity of extracts from *Rosa woodsii* fruits, added to canola oil, depends on the concentration of polyphenols. Adding 200 µ*g* GAE/g to the oil has a marginal efficiency, but at a higher concentration, of 500 µ*g* GAE/g (or 0.5%), the antioxidant activity is significantly greater, compared to butylated hydroxytoluene, under the rancimat conditions and during frying. Probably, the higher temperatures encourages a better distribution of the polyphenols in the oil, allowing all the phenolic components in the extract to display their antioxidant properties. The authors determined that the protective effect of phenolic antioxidants is not significant during the storage period [27]. However, research did not mention what quantity of hydrophilic antioxidants can be delivered from vegetable matter or from extracts of polyphenols in the hydrophobic phase.

The purpose of this research was to dose spectrophotometrically the total content of polyphenols in grape seed oil fortified with hydroalcoholic extracts of grape seeds, at the initial stage and after 12 months; to elucidate the influence of polyphenols on the antioxidant activity of the oil, and to observe the difference in the oxidative status of the oil according to absorbances in UV-Vis before and after storage.

2. Materials and Methods

2.1. Materials

Commercial refined grape seed oil, produced on 12.06.2020, valid until 12.06.2021.

Folin-Ciocalteu phenol reagent was provided by Chem-Lab NV (Belgium). The 6-hydroxy-2,5,7,8-tetramethylchromane-2-carboxylic acid (Trolox) and 1,1-diphenyl-2-picrylhydrazyl-hydrate (DPPH) were provided by Alpha Aesar (U.S.A.). Gallic acid (GA) was purchased from Sigma-Aldrich (St. Louis, MO, U.S.A.); *n*-octyl gallate (OG) from Alpha Aesar (Germany). Ethanol, methanol, *n*-hexane, sodium carbonate, and chloroform purchased from Chemapol (Czech Republic). All reagents were of analytical or chromatographic grade.

2.2. Methods

2.2.1. Extraction of antioxidants from grape seeds

The hydroalcoholic extract of native grape seeds (GSE) was obtained in the following way: 50 g of grape seeds, separated from the fermented pomace and dried at 70°C for 2 hours (humidity 6.63±0.02%), were crushed and macerated at room temperature for 24 hours in 65% aqueous ethyl alcohol solution, with a liquid:solid ratio (LSR) of 5 (*v/m*). The macerated mixture was subjected to ultrasound-assisted extraction (ISOLAB Laborgeräte GmbH), for 30 min, at a temperature of 40°C (37 kHz). The next steps consisted of centrifugation (5000 rpm

for 10 min), collection of the supernatant, vacuum evaporation of the solvent at a temperature of 60°C, and drying of the residue in a vacuum oven at 60°C. As a result, 3.985 g of GSE, with a greasy appearance, were obtained.

The hydroalcoholic extract of defatted grape seeds (DGSE) was obtained as follows: 50 g of seeds, dried and crushed, were extracted with *n*-hexane, LSR of 3 (*v/m*), whilst heated on a water bath at 50°C, for 60 min. The mixture was filtered through filter paper, the extraction was performed in two repetitions. The degreased sample was further extracted with hydroalcoholic solution, according to the procedure described above. As a result, 2.792 g of DGSE were obtained. The total polyphenol content of GSE and DGSE, was determined (Table 1).

2.2.2. Sample preparation

Six samples of refined GSO were weighed (100 g). Grape seed antioxidant extracts were added to four oil samples. The GSE and DGSE extracts in dry form and in dissolved form (GSE_{EtOH}, $DGSE_{EtOH}$) in 96% ethyl alcohol, were added, with the theoretically calculated concentration of 4 g GAE/kg of oil (or 0.4% TPC in the oil sample). For a better distribution of the biologically active substances from the extracts in the oil, the ultrasound-assisted method (ISOLAB Laborgeräte GmbH, Germany) was applied (30 min, 50°C, 37 kHz); followed by centrifugation (5000 rpm for 10 min) and sediment separation. Ethyl alcohol was distilled under vacuum at a temperature of 60°C. Refined grape seed oil (GSO) and oil with addition of synthetic antioxidant *n*-octyl gallate (GSO+OG), in a concentration of 200 mg GAE/kg of oil (or 0.02% in the oil sample), served as reference samples.

In June of 2021, the oil samples were scanned with a DR 5000 spectrophotometer (HACH- Lange GmbH, USA-Germany), the TPC was dosed and the DPPH• antioxidant activity was determined. The samples were stored at room temperature, in a cupboard (without access to light), in polystyrene containers, closed with plugs. After 12 months of storage in ambiental conditions (June of 2022), the same determinations were made.

2.2.3. Extraction of the polyphenols from oil

The hydrophilic fractions were obtained with 1.5 mL of aqueous solution of 60% MeOH from the 1.25 g of oil dissolved in 2.5 mL of *n*-hexane [28]. Hydrophilic and hydrophobic phases were separated by centrifugation (3500 rpm for 10 min). The procedure was repeated twice. The methanolic extracts were combined and analyzed.

2.2.4. UV-Vis spectroscopic analysis of oil samples

The absorbances of the oil samples (2% of oil in hexane) were recorded on a DR5000 spectrophotometer (HACH- Lange GmbH, USA-Germany).

2.2.5. Determination of the total content of polyphenols (TPC)

The TPC was dosed by the Folin-Ciocalteu method [29, 30] according to the calibration curve (0-500 mg/L, R^2= 0.9977) of the gallic acid (GA) standard. The results were expressed in milligrams equivalent of GA per gram of grape seed extract dry weight (mg GAE/g DW) or per kilogram of oil (mg GAE/kg).

2.2.6. DPPH• Free Radical Scavenging Activity

The antioxidant activity of the hydrophilic fractions was determined according to the procedure [31]. The calibration curve was made with Trolox in various concentrations (3.95 - 500 µmol/L). The absorbance of the solutions was measured at 515 nm, using the spectrophotometer mentioned above, the results were expressed in millimoles Trolox

equivalent per kilogram of oil (mmol TE/kg). DPPH• radical scavenging ability was calculated using formula (1):

$$DPPH \bullet \ (\%\ inhibition) = \frac{(A_0 - A_1)}{A_0} \cdot 100\ \% \qquad (1)$$

where A_0 is the absorbance of the control sample and A_1 is the absorbance of all extract samples and reference samples. All assays were performed in triplicate and results were averaged.

2.2.7. Statistical processing of experimental data

The statistical analysis of the results was carried out with the application of IBM SPSS Statistics 23 and Microsoft Excel 2010 programs. The level of significance of the results was 95% (q<0.05). To exclude results with accidental errors and those with high levels of uncertainty, three parallel measurements were performed [32].

3. Results and Discussion

In this study, attempts were made to fortify refined grape seed oil (GSO) with extracts from native grape seeds (GSE) and defatted grape seeds (DGSE), separated from fermented pomace. Research has shown that hydrophilic and lipophilic extracts of grape seeds are rich in phenolic antioxidants [33], with valuable potential for different fields [34]. Hydroalcoholic extracts from grape seeds contain polyphenolic compounds mostly in the form of monomers - gallic acid, catechin, epicatechin; in the form of oligomeric proanthocyanidins (PAC) - dimers, trimers and tetramers of catechin, epicatechin, epigallocatechin, and epicatechin gallate [16, 35]. The extraction of grape seeds was carried out with an 65% aqueous solution of ethyl alcohol, considered a harmless solvent for obtaining nutraceuticals [36]. In both dry extracts, GDE and DGSE, the total content of polyphenols (TPC) was measured spectrophotometrically by the methods described in the literature, Table 1 [29, 30]. Hydroalcoholic extracts of native GSE seeds have a lower TPC due to the lipophilic components contained. The results show that after defatting seeds with *n*-hexane, the second extraction, with hydrophilic solvent, solubilizes better the phenolic compounds from the solid matrix of the degreased seeds, and the TPC reaches 978.37 mg GAE/g DW in the DGSE extract.

Table 1

Mass fraction of hydroalcoholic grape seed extracts and their total polyphenol content

Extracts	*GSE*	*DGSE*
The mass fraction of the extract, % DW seeds	7.97±0.68	5.58±0.47
TPC, mg GAE/g DW extract	516.43±11.15	978.37±23.36

Note: GSE - grape seeds extract; DGSE - defatted grape seeds extract; DW - dry weight; TPC - total polyphenol content. Values represent the means of three replicates ± standard deviation.

The physicochemical properties of the refined grape seed oil (GSO) were within the data presented in the bibliography [37, 38]. The refractive index of the oil was determined (1.4794, 25°C) at ABBE Refractometer (ISOLAB Laborgeräte, Germany); the relative density (0.921 kg/dm^3); the acidity index (0.85 mg KOH/g of oil) and the peroxide value (2.44 mEqO_2/kg) were determined according to the known methods [39].

The experimental samples were named as follows: GSO - control sample, refined grape seed oil; GSO+OG - oil fortified with *n*-octyl gallate; GSO+GSE oil fortified with dry grape seed extract; GSO+GSE_{EtOH} - fortified oil with grape seed extract solubilized in ethyl alcohol;

GSO+DGSE - fortified oil with dry extract of defatted grape seeds; GSO+DGSE$_{EtOH}$ - fortified oil with defatted grape seed extract, solubilized in ethyl alcohol. The amount of GSE was calculated to obtain the theoretical concentration of 0.4% polyphenols in oil (or 4 g GAE/kg of oil). The addition of GSE did not change the colour of the oil.

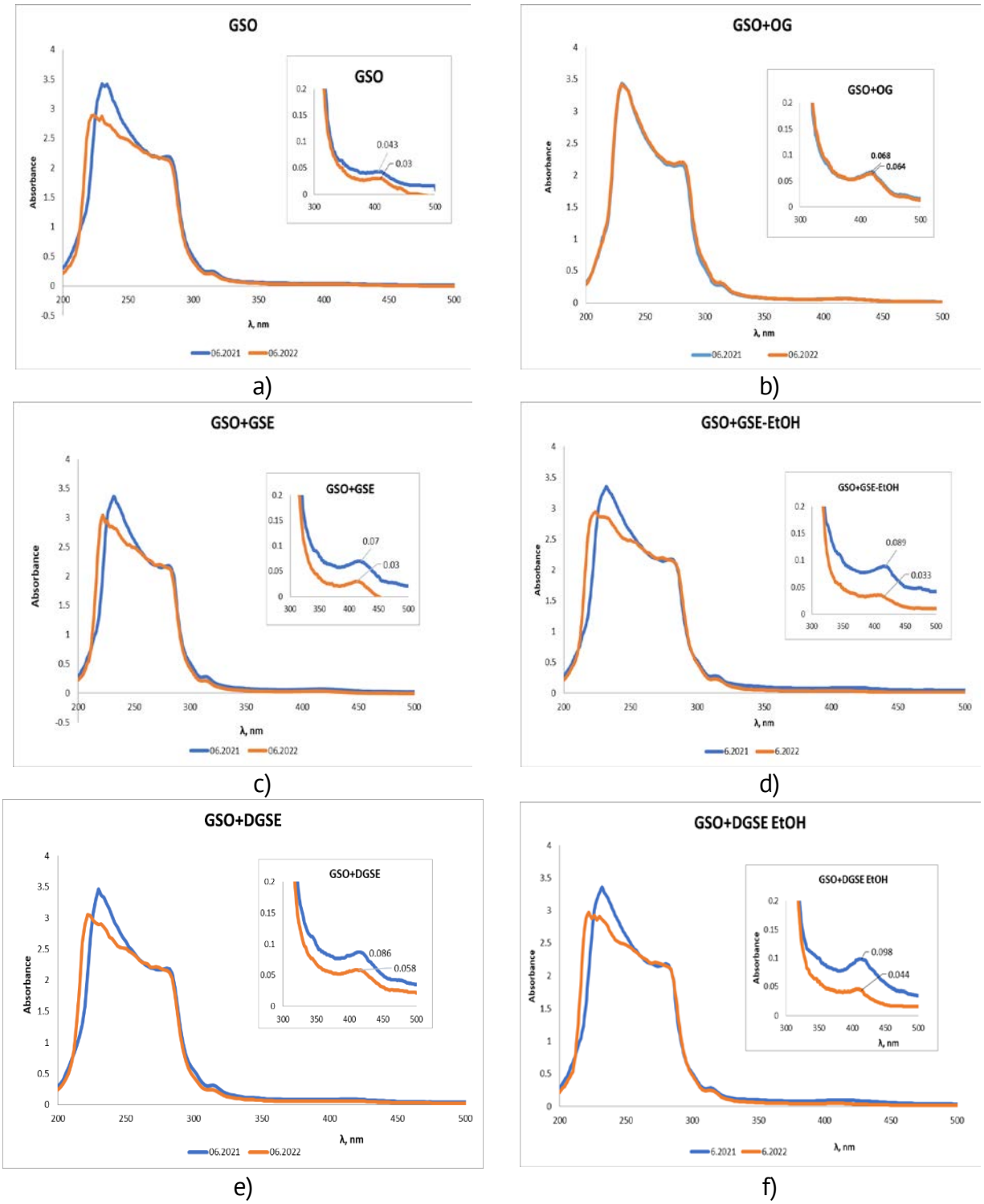

Figure 1. UV-Vis spectra of oil samples:
a) grape seed oil; b) oil fortified with n-octyl gallate; c) oil fortified with dry extract of grape seed oil; d) oil fortified with grape seed extract solubilized in ethyl alcohol; e) oil fortified with dry extract of defatted grape seeds; f) oil fortified with defatted grape seed extract solubilized in ethyl alcohol.

The UV-Vis spectrum was recorded before and after 12 months of storage for all of the fortified oil samples. In the refined GSO control sample, after storage, the absorbances decreased the most in the 200-250 nm wavelength ranges, due to the reduction in the concentration of triglycerides, free fatty acids and the formation of some secondary oxidation products in the oil (Figure 1).

Vegetable oils with a high content of polyunsaturated acids, at the end of one year of storage in dark, environmental conditions, accumulate secondary oxidation products - alkenals with *cis*- or *trans*- configurations at the double bonds, epoxides, ketones, hydrocarbons, dimers and polymers of PUFA, and triglycerides [40, 41].

The best oxidative stabilization and preservation effect of grape seed oil was recorded for synthetic antioxidant *n*-octyl gallate. The UV-Vis absorbances of the GSO+OG sample after 12 months of storage in polystyrene containers, in dark, environmental conditions, remained unchanged (Figure 1, b). The decrease of the UV-Vis absorbance, in the 280-450 nm range, in all samples except for GSO+OG, is a consequence of the decrease in the concentration of biologically active substances, such as phenolic compounds, carotenoids, tocopherols, phytosterols, *etc*.

In the case of the fortified samples, the absorbance values in the 200-500 nm range show that the grape seed extracts have a weak protective effect on the oil during storage under environmental conditions (Figure 1, a, c - f). After 12 months, in all samples of oil fortified with grape seed extracts, the hydrophilic phenolic compounds formed a sediment. Mentioned by other authors as well, it suggests a more complex interaction between the hydrophilic phenolic compounds used for fortification during the storage period. Research has shown that the antioxidant effect of the polyphenols manifests itself at higher temperatures, under the rancimat conditions and while frying oil [26,27].

By the spectrophotometric method, polyphenols (TPC) were dosed in the hydrophilic fractions of the oil samples before and after the 12 months of storage. As seen in Table 2, before the storage, the GSO control sample has an insignificant TPC of 1.57 mg GAE/kg of oil, due to the refining processes applied during production.

The bibliographic study shows that the TPC in unrefined grape seed oil is of 2.9 mg GAE/kg [12]. Other research has shown that TPC in cold-pressed grape seed oil ranged from 48 to 153 mg GAE/kg of oil [15].

Table 2

Total content of polyphenol (TPC) in oil samples

Sample	TPC (06.2021) mg GAE/kg	TPC (06.2022) mg GAE/kg
GSO	1.57 ± 0.12	0.05 ± 0.01
GSO+OG	222.30 ± 3.64	117.94 ± 2.20
GSO+GSE	38.28 ± 0.95	4.10 ± 0.17
GSO+GSE$_{EtOH}$	127.42 ± 0.98	10.32 ± 0.56
GSO+DGSE	56.86 ± 1.35	6.54 ± 0.45
GSO+DGSE$_{EtOH}$	141.34 ± 1.06	19.67 ± 0.85

Note: GSO - grape seed oil; GSO+OG - oil fortified with n-octyl gallate; GSO+GSE - oil fortified with dry extract of grape seed oil; GSO+GSE$_{EtOH}$ - oil fortified with grape seed extract solubilized in ethyl alcohol; GSO+DGSE - oil fortified with dry extract of defatted grape seeds; GSO+DGSE$_{EtOH}$ - oil fortified with defatted grape seed extract solubilized in ethyl alcohol. Values represent the means of three replicates ± standard deviation.

In the fortified oil samples, GSO+GSE and GSO+DGSE, the initial dosed total polyphenol content, is of 38.2 and 56.8 mg GAE/kg of oil. Although the amount of introduced antioxidants was theoretically calculated to obtain a TPC of 4.0 g GAE/kg oil, a TPC almost 100 times lower was dosed spectrophotometrically in the fortified oil (Table 2). Almost 1.5% of the introduced polyphenols were incorporated into the oil, which represents a very small amount.

The synthetic antioxidant *n*-octyl gallate (*n*-octyl 3,4,5-trihydroxybenzoate, E 311) was added to GSO in an amount of 200 mg GAE/kg, as per The European Food Safety Authority's accepted norms (200-300 mg GAE/kg of oil) [42]. By the spectrophotometric method, a TPC of 222.3 mg GAE/kg was dosed in the GSO+OG sample, which, being fat-soluble, was completely incorporated into the oil, unlike the polar polyphenolic compounds from the grape seed extracts (Table 2).

The solubilization of GSE and DGSE extracts in ethyl alcohol aids the better distribution of polar compounds in the lipophilic phase. The samples of GSO+GSE_{EtOH} and GSO+$DGSE_{EtOH}$ have a higher TPC, of 127.4 and 141.3 mg GAE/kg of oil, compared to the GSO+GSE and GSO+DGSE samples (Table 2). Calculations show that 3.5% of phenolic compounds, out of the 4.0 g GAE/kg initially introduced, were incorporated into the GSO+$DGSE_{EtOH}$ oil sample.

The spectrophotometrically dosed TPC [28-30] in the GSO samples, fortified with grape seed extracts, is lower compared to unrefined olive oil, which contains on average from 250 to 574 mg GAE/kg, depending on the method of obtaining [43]. The low values of TPC dosed in the fortified oil are due to the hydrophilic character of GSE and DGSE, which were extracted with hydroalcoholic solution of EtOH (65%) from grape seeds. These extracts contain phenolic compounds with increased polarity, more in the form of glycosides [16], which are delivered in a reduced amount in the hydrophobic oil.

The fortification of the oil with extracts of phenolic antioxidants has as an immediate effect the significant increase of the DPPH• scavenging effect, compared to the control sample. The highest antioxidant activity was determined for the GSO+OG sample, of 0.698 mmol TE/kg. In case of GSO+$DGSE_{EtOH}$, the DPPH• radical inhibition capacity of 0.580 mmol TE/kg is close to the antioxidant activity of *n*-octyl gallate, Table 3.

Table 3

Antioxidant activity of oil samples

Sample	DPPH• (06.2021)	DPPH• (06.2022)
	Concentration, mmol TE/kg	Concentration, mmol TE/kg
GSO	0.003 ± 0.001	n.d.
GSO+OG	0.698 ± 0.002	0.396 ± 0.003
GSO+GSE	0.078 ± 0.003	0.026 ± 0.001
GSO+GSE_{EtOH}	0.481 ± 0.004	0.047 ± 0.001
GSO+DGSE	0.295 ± 0.004	0.035 ± 0.001
GSO+$DGSE_{EtOH}$	0.580 ± 0.002	0.055 ± 0.001

Note: GSO - grape seed oil; GSO+OG - oil fortified with n-octyl gallate; GSO+GSE - oil fortified with dry extract of grape seed oil; GSO+GSE_{EtOH} - oil fortified with grape seed extract solubilized in ethyl alcohol; GSO+DGSE - oil fortified with dry extract of defatted grape seeds; GSO+$DGSE_{EtOH}$ - oil fortified with defatted grape seed extract solubilized in ethyl alcohol, n.d. - data not determined. Values represent the means of three replicates ± standard deviation.

The bibliographic study shows that the antioxidant capacity of the hydrophilic fractions in vegetable oils is lower compared to that of the lipophilic fractions. For example, the DPPH• antioxidant activity of the hydrophilic fraction of sesame oil is 0.50 mmol TE/kg, and that of the lipophilic fraction is 1.15 mmol TE/kg [44].

Manzano et al. [26] proved that the introduction of high concentrations (0.04%) of polyphenols in soybean oil delayed the release of fatty acids and the formation of peroxides; increased 20-fold the antioxidant activity against the DPPH• radical after roasting.

After 12 months of storage, TPC decreased in all of the fortified oil samples by approximately 10 times, except for GSO+OG, where TPC decreased nearly twice (Table 2).

The same effect, of significant reduction of DPPH• antioxidant activity, is observed in all of the samples (Table 3). The oil treated with OG, after storage under environmental conditions, exhibited a fairly good antioxidant activity (0.396 mmol TE/kg).

4. Conclusions

The effect of grape seed oil fortification with hydroalcoholic extracts of antioxidants from grape seeds (GSE), was studied up to and after 12 months. Research has shown that due to the hydrophilic nature of grape seed extracts, a small number of phenolic compounds have been incorporated into the oil. It was established that oil fortification with GSE has the immediate effect of increasing the total polyphenol content (TPC) in the oil by up to 141.34 mg GAE/kg and increasing the DPPH• antioxidant activity by up to 0.580 mmol TE/kg (in the control sample, grape oil refined, these values were 1.57 mg GAE/kg and 0.003 mmol TE/kg, respectively). After 12 months, TPC and DPPH• antioxidant activity decreased nearly 10-fold in all GSE-fortified oil samples. In the oil treated with *n*-octyl gallate, after 12 months, TPC values and antioxidant activity decreased twice. The difference between the oxidative status of the oil was observed according to the absorbances in UV-Vis; absorbances of the GSO+OG sample, up to and after 12 months, remained unchanged. It was determined that the extract of phenolic antioxidants from grape seeds had a lower protective effect on the oil during storage under ambient conditions compared to the synthetic antioxidant *n*-octyl gallate.

Acknowledgments: The research was carried out with the support of the Moldova State project 20.80009.5107.09 Improvement of food quality and safety by biotechnology and food engineering.

Conflicts of Interest: The authors declare no conflict of interest.

References

1. Garavaglia, J.; Markoski, M.; Oliveira, A.; Marcadenti, A. Grape Seed Oil Compounds: Biological and Chemical Actions for Health. *Nutr and Metabolic Insights* 2016, 9, pp. 59-64. doi: https://doi.org/10.4137/NMI.S32910.
2. Messina, C.M.; Manuguerra, S.; Catalano, G.; Arena, R.; Cocchi, M.; Morghese, M.; Montenegro, L.; Santulli, A. Green biotechnology for valorisation of residual biomasses in nutraceutic sector: Characterization and extraction of bioactive compounds from grape pomace and evaluation of the protective effects in vitro. *Nat Prod Res* 2021, 35(2), pp. 331-336. https://doi.org/10.1080/14786419.2019.1619727.
3. Yun, J.M.; Surh, J. Fatty Acid Composition as a Predictor for the Oxidation Stability of Korean Vegetable Oils with or without Induced Oxidative Stress. *Prev Nutr Food Sci* 2012, 17(2), pp.158–165. doi: 10.3746/pnf.2012.17.2.158.
4. Liu, H; White, PJ; (1992) Oxidative stability of soybean oils with altered fatty acid compositions. *J Am Oil Chem Soc* 1992, 69, pp. 528–532. https://doi.org/10.1007/BF02636103).
5. Prescha, A., Grajzer, M., Dedyk, M. The Antioxidant Activity and Oxidative Stability of Cold-Pressed Oils. *J Am Oil Chem Soc* 2014, 91 (8), pp.1291–1301. https://doi.org/10.1007/s11746-014-2479-1.

6. Psomiadou, E.; Tsimidou, M. Stability of Virgin Olive Oil. 2. Photo-Oxidation Studies. *J Agr and Food Chem* 2020, 50 (4), pp.722–27. https://doi.org/10.1021/jf010847u.
7. Xu, C., Yagiz, Y., Hsu, W., Simonne, A., Lu, J., Marshall, M.R. Antioxidant, antibacterial, and antibiofilm properties of polyphenols from muscadine grape (Vitis rotundifolia Michx.) pomace against selected foodborne pathogens. *J Agr Food Chem* 2014, 62, pp. 6640–6649. DOI: 10.1021/jf501073q.
8. Iannone, M.; Mare, R.; Paolino, D.; Gagliardi, A.; Froiio, F.; Cosco, D.; Fresta, M. Characterization and in vitro anticancer properties of chitosan-microencapsulated flavan-3-ols-rich grape seed extracts. *Int J Biol Macrom* 2017, 104, pp.1039–1045. DOI: 10.1016/j.ijbiomac.2017.07.022.
9. Ferri, M.; Rondini, G.; Calabretta, M.M.; Michelini, E.; Vallini, V.; Fava, F.; Roda, A.; Minnucci, G.; Tassoni, A. White grape pomace extracts, obtained by a sequential enzymatic plus ethanol-based extraction, exert antioxidant, anti-tyrosinase and anti-inflammatory activities. *New Biotech* 2017, 39, pp. 51–58. DOI: https://doi.org/10.1016/j.nbt.2017.07.002.
10. Vaisman, N.; Niv, E. Daily consumption of red grape cell powder in a dietary dose improves cardiovascular parameters: A. double blind, placebo-controlled, randomized study. *Int J Food Sci Nutr* 2015, 66, pp. 342–349. DOI: http://dx.doi.org/10.3109/09637486.2014.1000840.
11. Wesseler, A.R; Bast, A. Masquelier's grape seed extract: from basic flavonoid research to a well-characterized food supplement with health benefits. *Wesseler and Bast Nutr J* 2017, 16(5), pp. 1-19. DOI: https://nutritionj.biomedcentral.com/articles/10.1186/s12937-016-0218-1.
12. Maier, T.; Schieder, A.; Kammerer, D.R.; Carle, R. Residues of grape (*Vitis vinifera* L.) seed oil production as a valuable source of phenolic antioxidants. *Food Chem* 2009, 112, pp. 551–559. DOI: https://doi.org/10.1016/j.foodchem.2008.06.005.
13. Weidner, S.; Powałka, A.; Karamac, M.; Amarowicz, R. Extracts of Phenolic Compounds from Seeds of Three Wild Grapevines Comparison of Their Antioxidant Activities and the Content of Phenolic Compounds. In: *Int. J. Mol. Sci*. 2012, 13, pp. 3444-3457. https://doi.org/10.3390/ijms13033444
14. Lachman, J.; Hejtmánková, A.; Hejtmánková, K.; Horníčková, S; Pivec, V.; Skala, O.; Dědina, M.; Přibyl, J. Towards complex utilisation of winemaking residues: Characterisation of grape seeds by total phenols, tocols and essential elements content as a by-product of winemaking. *Ind Crops Prod* 2013, 49, pp. 445–453. https://doi.org/10.1016/j.indcrop.2013.05.022.
15. Rombaut, N.; Savoire, R.; Thomasset, B.; Castello, I.; Van Hecke, E.; Lanoisellè, J.L. Optimization of oil yield and oil total phenolic content during grapeseed cold screw pressing. *Ind Crops Prod* 2015, 63, pp. 26–33. DOI: http://dx.doi.org/10.1016/j.indcrop.2014.10.001.
16. Gurev, A.; Dragancea, V; Baerle, A.; Netreba, N.; Boestean, O.; Haritonov, S.; Gaina, B. *Chem J Mold* 2022, 17(2), pp. 50-61. DOI: 10.19261/cjm.2022.946.
17. Assumpção, C.F.; Nunes I.L.; Mendonça, L.; Jablonski, A. The Quality, Stability, and Bioactive Compound Composition of Virgin and Refined Organic Grape Seed Oil. *J Am Oil Chem Soc* 2014, 91, pp.2035–2042, DOI 10.1007/s11746-014-2548-5.
18. Usman, A. S; Farooq, A.; Muhammad, T. A.; Rahman, Q.; Sadaf, Z.; Iram, S.; Ghulam, S.; Farzana, S.; Anuchita, M. Variations in Physico-Chemical and antioxidant Attributes of Grape Seed Oil as Function of Extraction Techniques. *Sains Malaysiana* 2022, 51(7), pp. 2087-2096. http://doi.org/10.17576/jsm-2022-5107-12.
19. Carocho, M.; Ferreira, I.C.F.R. A review on antioxidants, prooxidants and related controversy: Natural and synthetic compounds, screening and analysis methodologies and future perspectives. *Food Chem Toxicol* 2013, 51, pp. 15–25. doi: 10.1016/j.fct.2012.09.021
20. Rangan, C.; Barceloux, D.G. Food Additives and Sensitivities. *Dis. Mon.* 2009, 55 (5), pp. 292–311. DOI: 10.1016/j.disamonth.2009.01.004.
21. European Commission. Commission Regulation (EU) No 1129/2011 of 11 November 2011 amending Annex II to Regulation (EC) No 1333/2008 of the European Parliament and of the Council by establishing a Union list of food additives. *J Eur Union* 2011, 295, pp. 1–177.
22. Rozin, P.; Spranca, M.; Krieger, Z.; Neuhaus, R.; Surillo, D.; Swerdlin, A.; Wood, K. Preference for natural: Instrumental and ideational/moral motivations, and the contrast between foods and medicines. *Appetite* 2004, 43, pp. 147–154. DOI: 10.1016/j.appet.2004.03.005.
23. Roschel, G.G.; da Silveira, T.F.F.; Cajaiba, L.M.; Castro, I.A. Combination of hydrophilic or lipophilic natural compounds to improve the oxidative stability of flaxseed oil. *Eur J Lipid Sci Technol* 2019, 121, 1800459. DOI: 10.1002/ejlt.201800459.

24. Mohanan, A; Nickerson, M.T.; Ghosh, S. Oxidative stability of flaxseed oil: Effect of hydrophilic, hydrophobic and intermediate polarity antioxidants. *Food Chem* 2018, 15, 266, pp. 524-533. https://doi.org/10.1016/j.foodchem.2018.05.117
25. Özge, G.; ¸Sahin, S. Evaluation of oxidative stability in hazelnut oil treated with several antioxidants: Kinetics and thermodynamics studies. *LWT Food Sci Technol* 2019, 111, pp. 478–483. DOI: 10.1016/j.lwt.2019.05.077.
26. Manzano, P.; Hernández, J.; Quijano-Avilés, M.; Barragán, A.; Chóez-Guaranda, I.; Viteri, R.; Valle, O. Polyphenols extracted from Theobroma cacao waste and its utility as antioxidant. *Emir J Food Agric* 2017, 29, pp. 45–50. DOI: 10.9755/ejfa.2016-04-388.
27. Aladedunye, F.; Kersting, H.J.; Matthäus, B. Phenolic extract from wild rose hip with seed: Composition, antioxidant activity, and performance in canola oil. *Eur J Lipid Sci Technol* 2014, 116(8), pp. 1025-1034, https://doi.org/10.1002/ejlt.201300255
28. Gutfinger, T. Polyphenols in olive oils. *J Amer Oil Chem Soc* 1981, 1, pp. 966-968. DOI: https://doi.org/10.1007/BF02659771.
29. Bouyahya, A.; Dakka, N.; Talbaoui, A.; Moussaoui, N.E.; Abrini, J.; Bakri, Y. Phenolic contents and antiradical capacity of vegetable oil from Pistacia lentiscus (L). *J Mat Env Sci* 2018, 9(5), pp. 1518-1524. DOI: https://doi.org/10.26872/jmes.2018.9.5.167
30. Singleton, V.; Rossi, J. Colorimetry of total phenolic compounds with phosphomolybdic-phosphotungstic acid reagents. *Amer J Enol and Vit* 1965, 16, pp. 144-158. DOI: http://garfield.library.upenn.edu.
31. Paulpriya, K.; Packia Lincy, M.; Tresina Soris, P.; Veerabahu Ramasamy, M. *In vitro* antioxidant activity, total phenolic and total flavonoid contents of aerial part extracts of *Daphniphyllum neilgherrense* (wt.) Rosenth. *J Bio Innov* 2015, 4(6), pp. 257–268.
32. *ISO 5725*-1:*1994*. Accuracy (trueness and precision) of measurement methods and results. International Organization for Standardization: Geneva, Switzerland, 1994. Available online: https://www.iso.org/standard/11833.html (accessed on 21.02.2023).
33. Mandic, A.I; Dilas, S.M.; Ćetković, G.S.; Čanadanović-Brunet, J.M.; Tumbas, V.T. Polyphenolic composition and antioxidant activities of grape seed extract. *Int J Food Prop* 2008, 11(4), pp. 713–726. DOI: https://doi.org/10.1080/10942910701584260.
34. Patel, S. Grape seeds: Agro-industrial waste with vast functional food potential. In: *Emerging Bioresources with Nutraceutical and Pharmaceutical Prospects*. Ed. Patel, S., Springer International Publishing AG, 2015, 3, pp. 53–69. DOI: 10.1007/978-3-319-12847-4_6.
35. Lucarini, M.; Durazzo, A.; Kiefer, J.; Santini, A.; Ginevra Lombardi-Boccia, G.; Eliana B. Souto, E.B.; Romani, A.; Lampe, A.; Ferrari, S.N.; Gabrielli, P.; Bevilacqua, N.; Campo, M.; Morassut, M.; Cecchini, F. Grape Seeds: Chromatographic Profile of Fatty Acids and Phenolic Compounds and Qualitative Analysis by FTIR-ATR Spectroscopy. *Foods* 2020, 9, 10, pp.1-14. DOI: 10.3390/foods9010010
36. FDA. Food Additive Status List. 2021. Available online: https://www.conceptsforhealth.com/healthyarticles/Food%*20 Additive*%20Status%*20 List*%20_%20FDA.pdf (accessed on 21.02.2023).
37. Pal, U. S.; Patra, R. K.; Sahoo, N. R.; Bakhara, C. K.; Panda, M. K. Effect of refining on quality and composition of sunflower oil. *J Food Sci Technol* 2015, 52(7), pp. 4613–4618. https ://doi.org/10.1007/s1319 7-014-1461-0.
38. Codex Standard for Named *Vegetable Oils* (CODEX-STAN 210 - 1999). Essential Composition and *Quality* Factors. Codex Alimentarius 1999. Report of the 16th Session of the Codex Committee on Fats and Oils, ALINORM 99/17. Available online: file:///C:/Users/User/Downloads/CXS_210e_2015.pdf (accessed on 21.02.2023).
39. Oils and Fats. Manual of Methods of Analysis of Foods. *AOAC 17th ed., 2015,* 96 p. Available online: https://old.fssai.gov.in/Portals/0/Pdf/Draft_Manuals/OILS_AND_FAT.pdf (accessed on 21.02.2023).
40. Choe, E.; Min, D.B. Mechanisms and Factors for Edible Oil Oxidation. *Comprehensive reviews in Food Science and Food Safety* 2006, 5(4), pp.169-186. https://doi.org/10.1111/j.1541-4337.2006.00009.x .
41. María D. Guillén, M.D.; Goicoechea, E. Detection of Primary and Secondary Oxidation Products by Fourier Transform Infrared Spectroscopy (FTIR) and ^{1}H Nuclear Magnetic Resonance (NMR) in Sunflower Oil during Storage. J. Agric. Food. Chem. 2007, *55*(26), pp. 10729-10736. https://doi.org/10.1021/jf071712c
42. EFSA ANS Panel (EFSA Panel on Food Additives and Nutrient Sources Added to Food), 2015. Scientific Opinion on the re-evaluation of octyl gallate (E 311) as a food additive. *EFSA Journal* 2015, 13 (10), pp. 4248. https://*doi*.org/*10.2903/j.efsa.2015.4248*.

43. Gutfinger, T. Polyphenols in olive oils. *J Am Oil Chem Soc* 1981, 1, pp. 966-968. DOI: https://doi.org/10.1007/BF02659771
44. Prescha, A.; Grajzer, M.; Dedyk, M.; Grajeta, H. The Antioxidant Activity and Oxidative Stability of Cold-Pressed Oils. *J Am Oil Chem Soc* 2014, 91, pp. 1291–1301. https://doi.org/10.1007/s11746-014-2479-1

Citation: Dragancea, V.; Gurev, A.; Sturza, R.; Haritonov, S.; Netreba, N.; Boeștean, O. The effect of grape seed oil fortification with extracts of natural antioxidants. *Journal of Engineering Science* 2023, 30 (2), pp. 173-184. https://doi.org/10.52326/jes.utm.2023.30(2).15.

Submission of manuscripts: jes@meridian.utm.md

Journal of Engineering Science *Vol. XXX, no. 2 (2023), pp. 185 - 195*
Fascicle *Food Engineering* *ISSN 2587-3474*
Topic *Biotechnologies, Food Chemistry and Food Safety* *eISSN 2587-3482*

https://doi.org/10.52326/jes.utm.2023.30(2).16
UDC 664.66.019

BREAD ROPE SPOILAGE DEVELOPMENT

Iurie Rumeus*, ORCID: 0000-0002-6392-7343

Cahul State University "Bogdan Petriceicu Hasdeu",
1 Independence Square, Cahul, MD-3901, Republic of Moldova
*Corresponding author: Iurie Rumeus, *rumeus.iurie@usch.md*

Received: 05. 06. 2023
Accepted: 06. 12. 2023

Abstract. Rope spoilage of bread is produced by bacteria belonging to *Bacillus* genus. Insufficient cleaning of the wheat before the milling operation contributes to obtaining flour with a high degree of contamination with these bacteria which produce thermoresistant endospores and further maintain their viability in the baking process. After baking, thermoresistant endospores can pass into the vegetative form and can multiply, causing spoilage of bread, which is manifested by the occurrence of an unpleasant odour, and the core of the bread becomes sticky. In this study, samples of bread from second-grade wheat flour were obtained. The kinetics of bacterial growth in the core of the thermostated bread at 37 °C for 84 hours was determined. It was found that immediately after baking the degree of contamination of the bread core was $1.28 \cdot 10^4$ cfu/g, and after 40 hours of thermostating the degree of contamination of the bread core increased by 2.85 logarithmic cycles, at this bread sample were observed the first signs of the rope spoilage (unpleasant odour). Thus, bread obtained from highly contaminated flour can contain a very large number of bacteria belonging to *Bacillus* genus, having no signs of rope spoilage, and thus the consumption of this bread may be dangerous to the consumer's health.

Keywords: *bread, bacteria grow, unpleasant odor, sticky core.*

Rezumat. Boala întinderii a pâinii este produsă de bacteriile aparținând genului *Bacillus*. Curățarea insuficientă a grâului înainte de operația de măcinare contribuie la obținerea făinii cu un grad ridicat de contaminare cu aceste bacterii, care produc endospori termorezistenți și astfel își păstrează ulterior viabilitatea în procesul de coacere. După coacere, endospori termorezistenți pot trece în formă vegetativă și se pot înmulți, cauzând astfel alterarea pâinii, care se manifestă prin apariția unui miros neplăcut, și miezul pâinii devine lipicios. În această cercetare au fost obținute probe de pâine din făină de grâu de calitatea a doua. S-a determinat cinetica creșterii bacteriilor în miezul pâinii termostatate la 37 °C timp de 84 de ore. S-a constatat că imediat după coacere gradul de contaminare a miezului pâinii a fost de $1.28 \cdot 10^4$ u.f.c./g, iar după 40 de ore de termostatare gradul de contaminare a miezului pâinii a crescut cu 2.85 cicluri logaritmice, la această probă de pâine s-au observat primele semne ale bolii întinderii (mirosul neplăcut). Astfel, pâinea obținută din făină foarte contaminată poate conține un număr foarte mare de bacterii din genul *Bacillus*, neavând semne ale bolii întinderii, și astfel consumul acestei pâini poate fi periculos pentru sănătatea consumatorului.

Cuvinte cheie: *pâine, creșterea bacteriilor, mirosul neplăcut, miezul lipicios.*

1. Introduction

There are many species of microorganisms that can cause the spoilage of bakery products. Rope spoilage is the most important and most common defect of bread caused by the activity of bacteria. The microbial agents that produce the alteration are part of the genus *Bacillus*, highlighting the following species: *Bacillus subtilis* [1-3], *Bacillus subtilis* subsp. *mesentericus* [4-7]. In some research, the important role of *Bacillus licheniformis* [8] and *Bacillus amyloliquefaciens* [9] bacteria in the production of this defect is highlighted. Some researchers consider that the initiators of rope spoilage in bakery products are also bacteria of the species *Bacillus cereus* [10], *Bacillus mycoides*, *Bacillus pumilus*, *Bacillus polymyxa*, *Bacillus sonorensis*, *Bacillus megaterium*, *Paenibacillus polymyxa*, but their role is less important [2, 8, 11].

Bacteria that cause rope spoilage in bakery products are not part of the epiphytic microbiota of cereal plants and do not have the possibility to grow on their surface. The concentration of bacteria of the genus *Bacillus* on the surface of cereal plants is very low (approximate 5 cfu/g), but these bacteria are present in the soil, where their concentration can reach 10^5 cfu/g soil, and the main way in which they get to the grain mass is represented by the dust particles that attach to the grains during the harvesting and primary processing of the wheat. Additionally, during storage under improper conditions, when the cereals undergo the process of self-heating, the number of bacteria of the genus *Bacillus* increases considerably. Therefore, the concentration of these bacteria in the mass of cereals can exceed $3 \cdot 10^4$ cfu/g [11]. Subsequently, these bacteria, which become part of the cereal microbiota, pass into the flour in the process of milling the grains. Insufficient cleaning of the grain surface before the grinding operation contributes to the obtaining of flour with a high degree of microbial contamination [6, p. 231].

Flour is widely known as the main source of rope-producing bacteria in dough intended for manufacturing bakery products [12]. It is also considered that the flours with a higher degree of extraction (especially wholemeal flour), which contain more particles from the grain shell, are more contaminated with bacteria that produce the rope spoilage in bread, than those with a lower degree of extraction (white flour) [13]. Moreover, the environment of processing (air, the working surface of the equipment) or other raw materials such as yeast or additives may also be contaminated with *Bacillus* [14]. The application of hygiene procedures in the bread-making section is an important condition for preventing the ropiness in bread [7].

Bacteria of the species *Bacillus subtilis* are gram-positive, and bacillary in shape, the length and the width of cells are 2–5 μm and 0,4–0,6 μm. Have the ability to form oval-shaped spores smaller than the cell size, and centrally located [1, 15]. The colonies of bacteria, that cause rope spoilage in bakery products, have an irregular shape, sometimes circular, and have different sizes when cultured on Nutrient agar medium. The surface of the colonies is smooth, with a buttery sheen, slightly wrinkled. The color of the colonies is white, sometimes pink, translucent, or milky. The margin of the colonies is wavy or lobed [16]. The species of bacteria that cause the rope spoilage in bread are amylase producers, and thus, are characterized by amylolytic capacity [8,12]. At the same time, bacteria from the *Bacillus subtilis* species have the ability to produce enzymes, which catalyze protein hydrolysis. Thus, the degradation of the starch and proteins in the core of the bread under the action of these bacteria is considered the main cause of the occurrence of the signs of spoilage [6, p. 232].

Rope spoilage occurs more frequently in bakery products during the warm period of the year [6, p. 232; 4, p. 441]. Spores of bacteria, that cause rope spoilage of bread, are resistant to heat treatment, and because the temperature in the bread core achieves usually values of 95-100 °C for several minutes, these bacteria can survive [14]. Ropiness occurs particularly when warm (25-30 °C) and humid (water-activity, ⩾0.95) environmental conditions allow spore germination [1]. The first signs of this alteration, which can occur after 24-48 hours of bread storage, can be observed by changing the odour of the bread, which becomes uncharacteristic for the product. If the spoilage progresses, then the odour intensifies and becomes rotten; outbreaks of bacteria that appear as yellow-brown or pink-brown spots can be observed in the core; the porous structure of the core deteriorates, gaps appear, and the core becomes sticky and when broken it stretches into very thin mucilaginous wires, that is why this alteration is named „rope spoilage" or „ropiness". At the strong development of the spoilage, the core turns into a compact and dark mass, with a specific pungent and unpleasant smell, from which the name „potato disease" comes [6, p. 232; 5, p. 441; 17, 18]. In addition to the change of sensory properties of bread, the growth and development of rope-producing bacteria (*Bacillus cereus*, *Bacillus subtilis*, *Bacillus licheniformis*) are accompanied by an accumulation of toxins, which can pose safety risks for consumers and can be implicated in producing of foodborne diseases [19].

The aims of the present study were to demonstrate the rate of bacterial growth in the bread core and to establish the correlation between bacterial growth and the occurrence of the signs of rope spoilage.

2. Materials and Methods

2.1 Study of the rate of colonial growth of bacteria isolated from the spoiled bread core

The rate of colonial growth of bacteria that cause rope spoilage in bread was determined by harvesting of bacteria cells with a loop from an outbreak in the core of spoiled bread, introduction into saline and obtaining the suspension of bacteria, placing a drop of this suspension in the center of Petri plate with the nutrient medium distributed preventively and solidified, thermostating of the sample at 37 °C with simultaneous video recording for 22 hours and visual observation of the size of the colony. Nutrient agar (Peptic digest of animal tissue 5.00 g/L; sodium chloride 5.00 g/L; beef extract 1.50 g/L; yeast extract 1.50 g/L; agar 15.00 g/L) (HiMedia Laboratories Pvt. Ltd., Mumbai, India) was used to cultivate the bacterial colony. Thermostating of the sample was performed in the thermostat ST1 (Pol-Eko-Aparatura, Poland). Video recording was made with the camera Logitech C270 placed in the thermostat.

2.2 Preparation of the bread samples and thermostating

Bread samples were obtained by the standard baking method [20; 21, p 18]. The mass of the bread samples was determined by weighing on a balance BSN-60D1.3 (Alex S&E, Republic of Moldova). The temperature of the bread core was measured by injecting the digital thermometer SH-113V1 (IsoLab, Germany) immediately after baking.

To obtain the bread samples, second-grade wheat flour, from the batch of flour received at the Cahulpan bread-making company (Cahul, Republic of Moldova), was used. This type of flour is used to manufacture the assortment of bread with a lower price compared to bread obtained from highest-grade wheat flour. At the same time, the bread prepared from the second-grade wheat flour is characterized by a higher content of dietary fiber due to the

higher content of bran particles. But the higher the bran content in the flour, the higher the degree of contamination of the flour with sporulated bacteria can be, that is why this type of flour was chosen in this research. The following properties of the flour were determined: acidity by titrating the aqueous suspension with sodium hydroxide in the presence of the indicator phenolphthalein [22]; humidity by drying to the constant mass [23]; wet gluten content by manually washing the piece of dough [24]; ash content by complete burning of the sample at 600 °C for 6 hours [25]; the total number of sporulated bacteria by preparing the wash by mixing 10 g of flour with 90 cm^3 of sterile saline and agitating with an orbital shaker for 10 minutes at the rotation 250 min^{-1} and pasteurizing it at 85 °C for 10 minutes, preparing dilutions, inoculating the samples and cultivating on Nutrient agar medium at 37 °C for 48 hours [26].

For the preparation of dough, its were also used: baking yeast (species Sacharomycess cerevisiae, „Livivski Drijdji", „Compania Enzim" company, Lviv, Ukraine), salt (for food use, „Arteomsoli" company, Soledar, Ukraine), potable water (from the aqueduct, Cahul). The quality of the raw materials used in this research is regulated in legislative acts of the Republic of Moldova [27, 28].

The recipe presented in table 1 was used to prepare the dough.

Table 1

The recipe for the preparation of the bread samples

Raw materials	Amount, %
Second-grade wheat flour	100
Baking yeast	3
Salt	1,5

The amount of water required for the preparation of the dough was calculated according to the total content of dry substances in the raw materials and the desired humidity of the dough equal to 45%.

After the baking process, the bread samples, have been cooled for 1 hour and packed in polyethylene bags, placed in the thermostat, and kept for 88 hours at the temperature of 37 °C.

The following utensils and equipment were used: laboratory mixer FIMAR 7/SN TR 1 V CE, thermostat BJPX - Diego, leavening cabinet UNOX XLT 133, laboratory oven UNOX XFT 133, laboratory glassware and utensils.

2.3. Determination of the number of bacteria in the bread core

The determination of the number of bacteria in the core of bread was performed immediately after baking and after each approximately 12 hours of thermostating of the samples. The bread sample has been cut; the core of the bread has been chopped using the crusher First FA-5481-1. An aliquot of 10 g of the chopped bread core have been transferred into a flask and mixed for 10 minutes in 90 cm^3 of sterile saline using the orbital shaker OS-10 at the rotation 250 min^{-1}. Decimal dilutions were prepared from the obtained suspension according to standard methods of microbiological analysis [26]. Inoculations have been made from the last two or three dilutions (two from each dilution). The bacteria have been cultured in the thermostat ST1 (Pol-Eko-Aparatura, Poland) at the temperature 37 °C.

2.4. The test for the occurrence of the rope spoilage

After about every 12 hours of thermostating, one of the bread samples has been analyzed organoleptically for unpleasant odours and other signs of rope spoilage, such as

sticky and changed color core [21, p 20]. For each analysis, the bread sample has been unpacked, it has been broken in two halves, and immediately the core has been smelled. After this, the appearance and colour uniformity of the core has been examined. The stickiness of the core has been examined by the touch.

2.5. Calculation methods

The Excel programme from the Office 2010 suite was used to process experimental data. The necessary calculations were performed using this application, the data obtained from the microbiological analysis of the bread samples were graphically represented and the function was chosen for the mathematical description of the kinetics of bacterial growth in the core of bread.

3. Results

3.1. Colonial growth rate of bacteria isolated from spoiled bread core

Figure 1 represents images showing an increase in the size of the bacteria colony every two hours of thermostating.

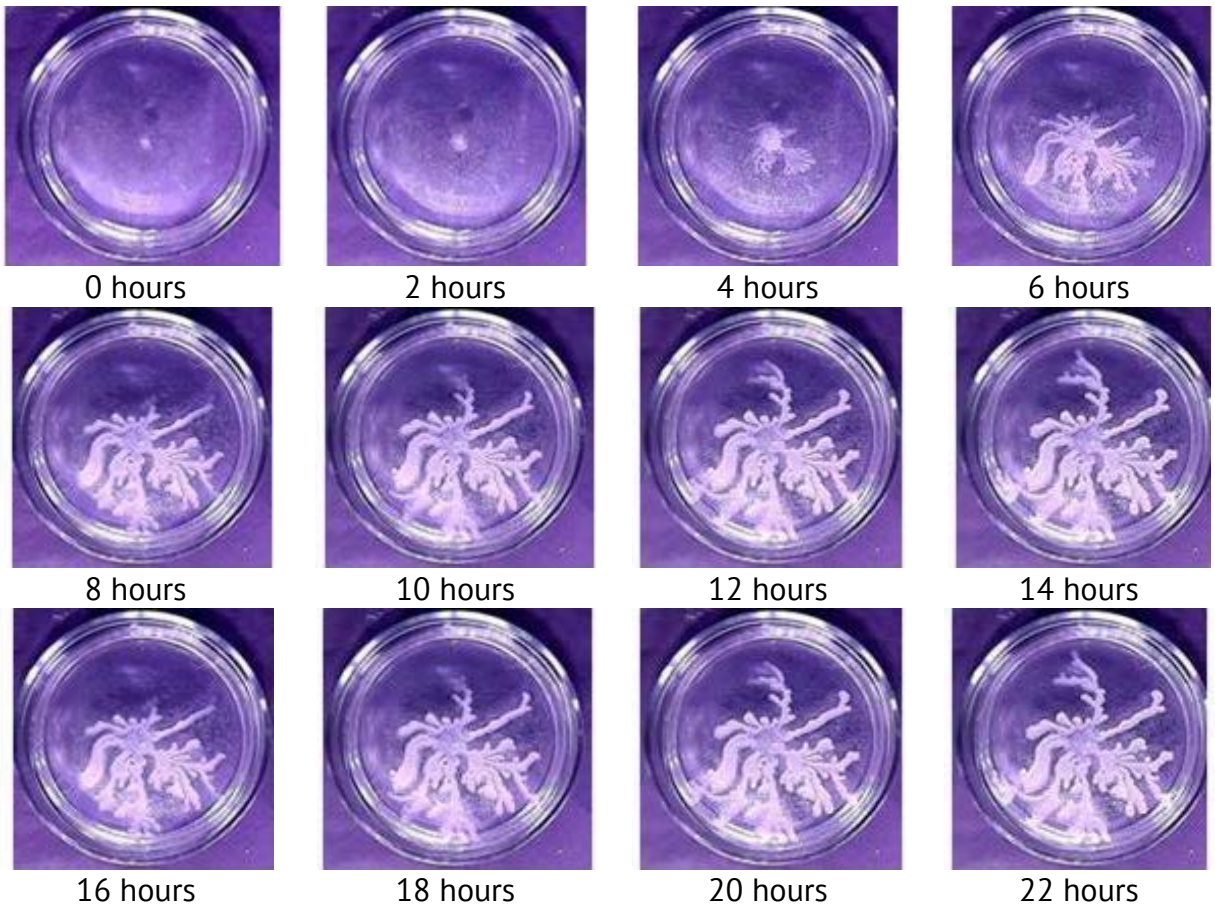

Figure 1. Colonial growth of bacteria isolated from spoiled bread core.

It was found that after 6 hours of thermostating the size of the colony reached about 50 mm in diameter, and after 22 hours it occupied the entire surface of the Petri plate, which demonstrates the high growth rate of these bacteria and proves that the number of bacteria in the core of the bread can quickly reach a level sufficient to produce rope spoilage in a very short time (sometimes even after a few hours) [6, p. 232; 12].

3.2. The bread samples and the properties of the flour

Eight bread samples of prismatic shape were obtained, each with a mass of 450 ± 4 g. The temperature in the core of the bread immediately after baking reached values of 96 ± 0.5 °C.

Table 1 shows values for the main properties of the flour used in the baking tests. Values of the physicochemical indices of flour (acidity, humidity, wet gluten content and ash content) are within the limits provided in the regulations for wheat flour in the Republic of Moldova [29].

At the same time, it was found that the total number of sporulated bacteria is more than 10^3 cfu/g, which means that this sample of flour is characterized as being heavily contaminated [30, p. 78].

Table 2

Properties of the flour used in baking tests

Properties and units of measure	Value	Permissible rates
Acidity, degrees of acidity	2.7 ± 0.1	max. 3.8
Humidity, %	12.8 ± 0.2	max. 15
Wet gluten content, %	33.8 ± 0.2	min. 20
Ash content, %	0.79 ± 0.1	max. 1.25
Total number of sporulated bacteria, cfu/g	$1.5 \cdot 10^3$	-

3.3. The kinetics of the growth of bacteria in the core of bread and the occurrence of signs of the rope spoilage

Figure 2 shows the kinetics of bacterial growth in the core of bread. It was found that the number of bacteria in about 90 hours of thermostating increases by 6.7 logarithmic cycles. The degree of core contamination at the end of thermostating was $6.98 \cdot 10^{10}$ cfu/g. Kinetics of increasing the number of bacteria in the core of bread is characterized by an exponential function, the value of the square of Pearson's correlation coefficient being greater than 0.9.

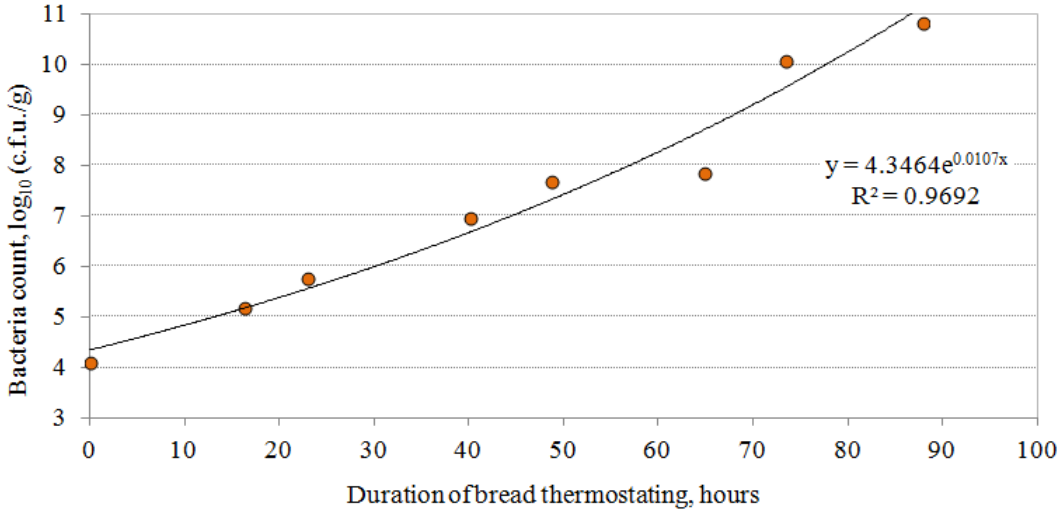

Figure 2. Kinetics of bacterial growth in the core of spoiled bread.

It was also observed that the initial degree of contamination of the bread core was $1.28 \cdot 10^4$ cfu/g. And because bacteria of the genus *Bacillus* are considered pathogenic, bread with a high degree of microbial contamination can represent a risk to consumer health. These bacteria can be involved in the production of diseases with mixed etiology (intoxication and

infection), and can produce emetic syndrome (nausea, vomiting) observed after 1-5 hours after consumption of the product [4, p. 441; 6, p. 28; 19].

At the same time, it was found that the first signs of bread rope spoilage occurred after 40 hours of thermostating – the organoleptic analysis of the bread revealed the characteristic odour of the alteration (Table 2).

Table 2

Correlation between the degree of bread core contamination and the occurrence of signs of rope spoilage

Duration of bread samples thermostating, hours	0	16	23	40	49	65	73	88
The occurrence of signs of the rope spoilage	-	-	-	±	+	+	+	+
The total number of bacteria in the core of the bread, cfu/g	$1.3 \cdot 10^4$	$1.5 \cdot 10^5$	$5.9 \cdot 10^5$	$9.0 \cdot 10^6$	$5.0 \cdot 10^7$	$6.9 \cdot 10^7$	$1.2 \cdot 10^{10}$	$6.9 \cdot 10^{10}$

Note: – no signs of rope spoilage; ± poor signs of rope spoilage (unpleasant odour); + pronounced signs of alteration (unpleasant odour and sticky core).

Analyzing the correlation between the degree of contamination of the bread core and the occurrence of the signs of rope spoilage, it was found that the unpleasant odour, characteristic to this alteration, appears at a fairly high degree of core contamination (10^6 cfu/g), which means that a person, who does not feel the odour of rope spoilage, can eat bread heavily contaminated with bacteria of the genus *Bacillus* and be at risk of food poisoning.

At a longer thermostating of the bread samples, there was an intensification of the unpleasant odour, the local change of the colour of the core and the occurrence of outbreaks of bacterial growth (zones of yellow-brown sticky core) (Figure 3).

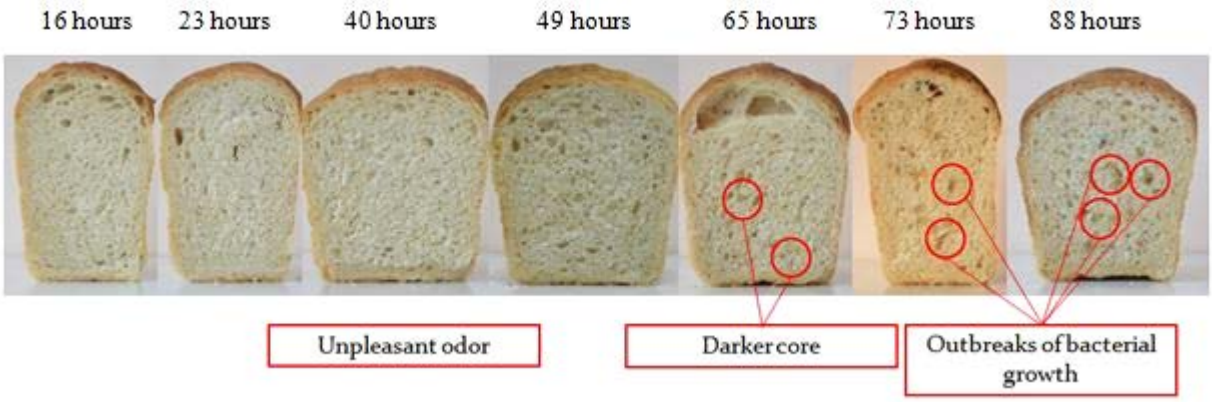

Figure 3. Signs of the occurrence of the rope spoilage in bread samples.

These changes were observed at the values of degree of microbial contamination of the bread core of 10^7-10^{10} cfu/g.

4. Discussion

In this research, it was observed that the characteristic odour of rope spoilage of bread occurs at a very high degree of bacterial contamination of the core, and since the rope-producing bacteria possess the property of releasing toxins into the product in which they grow, there is a risk that after consuming of such bread some people will suffer from poisoning. Thus, to avoid the risk of ropiness in bread and minimize the risk of intoxication, the microbiological control of the quality of the received flour must be applied at the bakery factories and to avoid the use of flour heavily contaminated with bacteria of the genus *Bacillus* in the bread making process, this flour can be directed for the obtaining of other products such as dry pretzels or breadcrumbs (which during the manufacture are treated with high temperatures and are characterized by a low moisture content, which makes it impossible for these bacteria to survive). Dilution of the heavily contaminated flour batches with uncontaminated flour batches can also be applied [7].

At the same time, the classical methods of preventing the rope spoilage of bread can be applied, such as the use of sourdough [31-39], calcium propionate [40], and other bakery improvers [41], the effectiveness of which was demonstrated in many scientific papers.

Unconventional methods can also be applied, such as the treatment of the surface of wheat grains with continuous ultraviolet light, or light pulses, with the aim to reduce the contamination degree of the grains before milling [16].

Electromagnetic radiation with wavelengths range 200–280 nm (UV-C light) is called bactericidal or germicidal light because by treatment with radiation in this range, bacteria and viruses are effectively inactivated [42]. The inactivation of microbial cells, by treatment with ultraviolet light, is based on the damage of nucleic acids [43], which is the cause of the loss of ability of microorganisms to reproduce. Nucleic acids absorb ultraviolet light in the wavelength range between 200 and 310 nm. Absorbed ultraviolet light causes the breaking of bonds and the formation of pyrimidine, thymine, or cytosine dimers in the same strand of DNA or RNA. These dimers change the helical structure of the DNA, which disturbs the cell replication process; therefore, the microorganisms become inactive [42; 44].

The treatment with light pulses is an effective method used to destroy both vegetative forms and spores of microorganisms [45-47]. This technology uses short pulses of intense white light with wavelengths from 100 nm in the UV range to about 1100 nm in the near-infrared region. The inactivation of microorganisms by light pulses treatment is attributed to the effect of the high energy of a pulse and the UV component, which represents about 25% of the light pulse spectrum [45]. The biological mechanism of microorganisms' inactivation includes restructuring nucleic acids, denaturation of proteins, and damage to other cellular components [42].

5. Conclusions

Bacteria of the genus *Bacillus* can be characterized by a high rate of reproduction, which can be the cause of the rapid occurrence of signs of rope spoilage in bread when the flour is with a high degree of contamination. Bread obtained from flour with a high degree of contamination with sporulated bacteria can represent a risk to consumers because signs of the rope spoilage in bread (unpleasant odour, sticky core) appear when the degree of core contamination is over 10^6 cfu/g, thus at the degree of contamination below 10^6 cfu/g the consumer is not warned that the bread is contaminated. Bacteria of the species *Bacillus subtilis* are considered conditionally pathogenic and can cause gastroenteritis, therefore, in

order to prevent the risk of food poisoning it is necessary to prevent contamination of flour with sporulating bacteria, or to apply the methods of inactivation of them during the bread making process.

Acknowledgments: This research was carried out with the financial support of the innovation and technology transfer project no. 22.80015.5107.260T Ensuring the food safety of bakery products by sanitizing the work surfaces of equipment used in the preparation of dough.

Acknowledgments for Mrs. Pușnei Irina, Ph.D. in Philology, for her contribution to linguistic correction.

Conflicts of Interest: This research represents the continuation of the doctoral studies and contains in the introductory part some information taken from the doctoral thesis entitled "Improvement of the bread quality as a result of wheat decontamination by non-conventional methods" and carried out under the direction of scientific coordinator, Mrs. Turtoi Maria, Prof. Dr. Eng.

References

1. Widyasari, A.A.; Magdalena, S.; Widiyati, L.B. Isolation and identification of bacteria from raw materials contaminated by rope-producing bacteria. *Microbiology* 2015, 9(3), pp. 113–119. doi: 10.5454/mi.9.3.3.
2. Erem, F.; Certel, M.; Karakaş, B. Identification of *Bacillus* species isolated from ropey breads both with classical methods and API identification kits. *Akdeniz Üniversitesi Ziraat Fakültesi Dergisi* 2009, 22(2), pp. 201–210.
3. Sorokulova, I.B.; Reva,O.N.; Smirnov, V.V.; Pinchuk, I.V.; Lapa, S.V.; Urdaci, M.C. Genetic diversity and involvement in bread spoilage of *Bacillus* strains isolated from flour and ropy bread. *Letters in Applied Microbiology* 2003, 37, pp. 169–173.
4. Puchkova, L.I.; Polandova, R.D.; Matveeva, I.V. *Tekhnologiya hleba, konditerskih i makaronnyh izdelij*, chast 1, Giord, Sankt-Peterburg, 2005, 559 p. [in Russian].
5. Bordei, D. *Modern bakery technology*. Agir, Bucharest, Romania, 2005, 448 p. [in Romanian].
6. Dan, V. *Microbiology of food products*. Alma, Galati, Romania, 2000, vol. 2, 318 p. [in Romanian].
7. Polandova, R.D.; Bogatyreva, T.G.; Sidorova, O.A.; Zelinskij, G.S.; Shuhnov, A.F.; Tereshkova, L.P.; Novikova, S.V.; Svyahovskaya, I.B. *Instrukciya po preduprezhdeniyu kartofelnoj bolezni hleba*. Izd. GOSNIIHP, Moskva, 1998 [in Russian].
8. Pereira A.P.; Stradiotto G.C.; Freire, L; Alvarenga V.O.; Crucello A.; Morassi L.L.; Silva F.P.; Sant'Ana A.S. Occurrence and enumeration of rope-producing spore forming bacteria in flour and their spoilage potential in different bread formulations. *LWT - Food Science and Technology* 2020, 133, 110108.
9. Valerio, F.; Di Biase, M.; Huchet, V.; Desriac, N.; Lonigro, S. L.; Lavermicocca, P. Comparison of three *Bacillus amyloliquefaciens* strains growth behaviour and evaluation of the spoilage risk during bread shelf-life. *Food Microbiology* 2015, 45, pp. 2–9.
10. Yibar, A.; Cetinkaya, F.; Soyutemiz, G.E. Detection of rope-producing *Bacillus* in bread and identification of isolates to species level by Vitek 2 System. *J. Biol. Environ. Sci.* 2012, 6(18), pp. 243-248.
11. Lvova, L.S.; Yaickih A.V. Istochniki zagryazneniya zerna sporoobrazuyushchimi bakteriyami vozbuditelyami kartofelnoj bolezni hleba. *Hleboprodukty* (2013, 9, pp. 57–59. [in Russian].
12. Pepe, O.; Blaiotta, G.; Moschetti, G.; Greco, T.; Villani F. Rope-producing strains of *Bacillus* spp. from wheat bread and strategy for fheir control by lactic acid bacteria. *Applied and Environmental Microbiology* 2003, pp. 2321–2329.
13. Rumeus, I.; Turtoi M. The occurrence of the rope spoilage of bread at Cahulpan bread-making company. *Economic and Engineering Studies* 2020, 2(8), pp. 107-116.
14. Valerio, F.; De Bellis, P.; Di Biase, M.; Lonigro, S. L.; Giussani, B.; Visconti, A.; et al. Diversity of spore-forming bacteria and identification of *Bacillus amyloliquefaciens* as a species frequently associated with the ropy spoilage of bread. *International Journal of Food Microbiology* 2012, 156, pp. 278–285.
15. Sandulachi, E.; Bulgaru, V.; Ghendov-Mosanu, A.; Sturza R. Controlling the risk of *Bacillus* in food using berries. *Food and Nutrition Sciences* 2021, 12, pp. 557-577.

16. Rumeus I. Improvement of the bread quality as a result of wheat decontamination by non-conventional methods. Doctoral thesis, „Dunarea de Jos" University of Galati, Romania, 2019.
17. Yudina, M.A.; Mustafin, A.H.; Feoktistova, N.A.; Vasilev, D.A.; Merkulov, A.V.; Baharovskaya, E.O. Diagnostika kartofelnoj bolezni hleba vyzyvaemoj bakteriyami vidov *Bacillus subtilis* i *Bacillus mezentericus*. *Vestnik Ulyanovskoj Gosudarstvennoj Selskohozyajstvennoj Akademii* 2011, 3, pp. 61–67 [in Russian].
18. Saranraj, P.; Sivasakthivelan P. Microorganisms involved in spoilage of bread and its control measures. In: Bread and Its Fortification: Nutrition and Health Benefits. Taylor & Francis Group, LLC, 2016, pp. 132-149.
19. De Bellis, P.; Minervini, F.; Di Biase, M.; Valerio, F.; Lavermicocca, P.; Sisto, A. Toxigenic potential and heat survival of spore-forming bacteria isolated form bread and ingredients. *International Journal of Food Microbiology* 2015, 197, pp. 30–39.
20. GOST 27669-88. Muka pshenichnaya hlebopekarnaya. Metod probnoj laboratornoj vypechki hleba; Standartinform, Moskva, 2007, 10 p. [in Russian].
21. SR 90: 2007. Wheat flour. Methods of analysis; Edition 7, Romanian Standardization Association (ASRO), Bucharest, Romania, 2007, 22 p. [in Romanian].
22. GOST 27493-87. Muka i otrubi. Metod opredeleniya kislotnosti po boltushke; Standartinform, Moskva, 2007, 4 p. [in Russian].
23. GOST 9404-88. Muka i otrubi. Metod opredeleniya vlazhnosti; Standartinform, Moskva, 2007, 5 p. [in Russian].
24. GOST 27839-2013. Muka pshenichnaya hlebopekarnaya. Metod opredeleniya kolichestva i kachestva klejkoviny; Standartinform, Moskva, 2014, 20 p. [in Russian].
25. GOST 27494-2016. Muka i otrubi. Metody opredeleniya zolnosti; Standartinform, Moskva, 2016, 14 p. [in Russian].
26. GOST 26972-86. Zerno, krupa, muka. Metody mikrobiologicheskogo analiza; IPK Izdatelstvo standartov, Moskva, 2003, 16 p. [in Russian].
27. Sanitary regulation on food salt. Annex no. 2 to the Decision of the Government of the Republic of Moldova no. 596 of 03 August 2011, Version in force from 29.12.22 based on the amendments by HG959 of 28.12.22, MO438-439/29.12.22 art.1048 [in Romanian].
28. Law no. 182 of 19-12-2019 regarding the quality of drinking water. Published: 03-01-2020 in Official Gazette No. 1-2 art. 2. [in Romanian].
29. The technical regulation "Flour, semolina and cereal bran", approved by the Decision of the Government of the Republic of Moldova no. 68 of January 29, 2009, Version in force from 02.11.18 based on amendments by HG956 of 03.10.18, MO410-415/02.11.18 art.1109 [in Romanian].
30. Dan, V.; Oancea, I.; Kramer, C.; Zara, M.; Tofan C. Microbiological control of food products. "Dunărea de Jos" University from Galati, Romania, 1991, 115 p. [in Romanian].
31. Rumeus, I.; Turtoi M. Influence of sourdough use on rope spoilage of wheat bread. *Journal of Agroalimentary Processes and Technologies* 2013, 19(1), pp. 94–98.
32. Clarke, C.I.; Arendt, E.K. A review of the application of sourdough technology to wheat breads. *Advances in Food and Nutrition Research* 2005, 49(1), pp. 137–161.
33. Lacaze, G.; Wick, M.; Cappelle, S. Emerging fermentation technologies: Development of novel sourdoughs. *Food Microbiology* 2007, 24(2), pp. 155–160.
34. Corsetti, A.; Settani, L. Lactobacilli in sourdough fermentation. *Food Research International* 2007, 40(5), pp. 539–558.
35. Arendt, E.K.; Ryan, L.A.; Dal Bello, F. Impact of sourdough on the texture of bread. *Food Microbiology* 2007, 24(2), pp. 165–174.
36. Brandt, M.J. Sourdough products for convenient use in baking. *Food Microbiology* 2007, 24(2), pp. 161–164.
37. Valerio, F.; De Bellis, P.; Lonigro, S.L.; Visconti, A.; Lavermicocca, P. Use of *Lactobacillus plantarum* fermentation products in bread-making to prevent *Bacillus subtilis* ropy spoilage. *International Journal of Food Microbiology* 2008, 122(3), pp. 328–332.
38. Decock, P.; Cappelle, S. Bread technology and sourdough technology. *Trends in Food Science & Technology* 2005, 16(1-3), pp. 113-120.
39. Ryan, L.A.M.; Dal Bello, F.; Arendt, E.K. The use of sourdough fermented by antifungal LAB to reduce the amount of calcium propionate in bread. *International Journal of Food Microbiology* 2008, 125(3), pp. 274–278.
40. Rumeus, I.; Turtoi, M. Prevention of stretching disease in bakery products using calcium propionate. In: *Scientific-practical conference Innovation - factor of social-economic development, B. P. Hasdeu State University of Cahul, Faculty of Economics, Engineering and Applied Sciences*, 2017, pp. 124–131 [in Romanian].

41. Pacher, N.; Burtscher J.; Johler, S.; Etter, D.; Bender, D.; Fieseler, L.; Domig KJ. Ropiness in bread - a re-emerging spoilage phenomenon. *Foods* 2022, 11, 3021.
42. Koutchma, T.; Forney, L.J.; Moraru, C.I. *Ultraviolet Light in Food Technology: Principles and Applications*. CRC Press, Taylor & Francis Group, New York, SUA, 2009, 300 p.
43. Kowalski W. UVGI for air and surface disinfection. In: *Ultraviolet germicidal irradiation handbook*. Springer, Heidelberg, 2009, 504 p.
44. Lado, B.H.; Yousef, A.E. Alternative food-preservation technologies: efficacy and mechanisms. *Microbes Infection* 2002, 4(4), pp. 433–440.
45. Dunn, J.; Ott, Th.; Clark, W. Pulsed-light treatment of food and packaging. *Food Technology* 1995, 49(9), pp. 95-98.
46. Elmnasser, N.; Guillou, S.; Leroi, F.; Orange, N.; Bakhrouf, A.; Federighi, M. Pulsed-light system as a novel food decontamination technology: A review. *Canadian Journal of Microbiology* 2007, 53(7), pp. 813–821.
47. Oms-Oliu, G.; Martín-Belloso, O.; Soliva-Fortuny, R. Pulsed light treatments for food preservation. A review. *Food and Bioprocess Technology* 2010, 3(1), pp. 13–23.

Citation: Rumeus, Iu. Bread rope spoilage development. *Journal of Engineering Science* 2023, 30 (2), pp. 185-195. https://doi.org/10.52326/jes.utm.2023.30(2).16.

Submission of manuscripts: jes@meridian.utm.md